Asymptotic Behavior of the Gell-Mann–Low Function in Quantum Field Theory

D. I. Kazakov[1, 2] and V. S. Popov[1]

[1] *Institute of Theoretical and Experimental Physics, ul. Bol'shaya Cheremushkinskaya 25, Moscow, 117259 Russia*
[2] *Joint Institute for Nuclear Research, Dubna, Moscow region, 141980 Russia*
e-mail: kazakovd@thsun1.jinr.ru
e-mail: markina@beron.itep.ru
Received March 25, 2003

The reconstruction of the Gell-Mann–Low function in quantum field theory from its asymptotic series, whose first terms are calculated using perturbation theory, is discussed. This mathematical problem cannot be solved uniquely. Nevertheless, the desired function can be reconstructed in a certain finite range of coupling constant g under reasonable assumptions about this function. However, attemps to determine the behavior of the function for $g \longrightarrow \infty$ are, in our opinion, groundless. Conditions under which the sum of the divergent perturbation series can rapidly decrease at infinity are determined. © 2003 MAIK "Nauka/Interperiodica".

PACS numbers: 03.70.+k; 11.10.Jj

1. The asymptotic behavior of the Gell-Mann–Low function (GLF) $\beta(g)$ at $g \longrightarrow \infty$ is of great interest in quantum field theory [1, 2], because it determines the invariant-charge behavior at small distances. The presently available information about the GLF is obtained using perturbation theory (PT) in the form of the asymptotic series in powers of the coupling constant g

$$\beta(g) \sim \sum_{n=2}^{\infty} \beta_n(-g)^n, \tag{1}$$

where the first several coefficients β_n are calculated from Feynman diagrams and the higher order asymptotic terms $\bar{\beta}_n$ for $n \longrightarrow \infty$ are also known. The asymptotic terms can be represented in the form

$$\bar{\beta}_n = \Gamma(n + 1/2) a^n n^b c, \tag{2}$$

where the constants a, b, and c are determined by the steepest descent method [3].

Although the available information is, strictly speaking, insufficient for uniquely reconstructing the function $\beta(g)$, it was originally thought that matching the asymptotic term $\bar{\beta}_n$ and the exact first coefficients would be helpful in reconstructing the GLF with an acceptable accuracy over a wide range of the coupling constant g and even in the strong-coupling limit $g \longrightarrow \infty$.

Many authors undertook such attempts by using various methods of summing divergent PT series. However, all these attempts showed that this program can be implemented only in a certain limited g range and not for $g \longrightarrow \infty$ (see, e.g., [4–8] and references therein). This conclusion is commonly accepted in the literature.

Recently, Suslov [9–13] attempted to revise these results. His works are based on the interpolation of the PT β_n coefficients to the intermediate n values. In [9] (p. 11), he wrote, "A reasonable formulation of the problem corresponds to approximately specifying all β_n, after which $\beta(g)$ can be reconstructed with a certain accuracy. Thus, a necessary stage in solving the problem consists in interpolating the coefficient function, which naturally implies that this function is analytic."

Then, the interpolation procedure is optimized with respect to parameters. According to [9], this procedure determines the asymptotic behavior of the desired function for $g \longrightarrow \infty$. Applying this procedure, Suslov [9–12] obtained asymptotic behavior of the GLF at $g \longrightarrow \infty$ for a number of models of quantum field theory, including the $\phi^4_{(4)}$ theory, QED, and QCD. Moreover, he stated that zero charge is absent in the $\phi^4_{(4)}$ theory and QED. This statement contradicts the previous results of other authors, which were obtained by summing asymptotic PT series [6–8].

As was mentioned in [14], the procedure applied in [9–12] is insufficiently justified for definite conclusions to be drawn. Moreover, we believe that it is reasonable to discuss the possibility of reconstructing the function from its asymptotic behavior (under the assumption about the analytic properties of the function) only in a certain range, wider than that in PT, of the expansion constant g but not for $g \longrightarrow \infty$. Corresponding arguments were presented in [14]. The publication of Suslov's new paper [12] concerning the asymptotic behavior of GLF in QCD has motivated us to return to this problem.

2. An important feature of QCD is that its PT series (1) is of constant sign. Therefore, it cannot be summed by the Borel method, which is used in almost all approaches to the summation of asymptotic series. To overcome this difficulty, Suslov [12] substituted $g \longrightarrow -g$ in the PT series and assumed that the asymptotic behaviors of the function $\beta(g)$ at $g \longrightarrow \pm\infty$ coincide with each other. This assumption is obviously unjustified. Moreover, it is physically clear that, if the coupling constant changes sign, the system completely changes; it becomes unstable and collapses. Owing to this circumstance, the $g = 0$ point is an essentially singular point in the complex plane and, because of this, the PT series is asymptotic [15]. As is known, since the PT series for QCD is of constant sign, the vacuum in QCD is degenerate and there are contributions proportional to the exponential of the inverse coupling constant, which are not reproduced by the perturbation theory. At the same time, these contributions are not necessarily suppressed for a large coupling constant. For this reason, the method in which the sign of the expansion constant is changed and the series becomes alternating, after which the answer is extended to the series of constant sign, is, in our opinion, fully unjustified and, generally speaking, incorrect.

To illustrate this statement, we consider the following example. Let two functions $f_1(g)$ and $f_2(g)$ be specified by the formulas

$$f_1(g) \sim \frac{e^g \sum a_n g^n + e^{-g} \sum b_n g^n}{e^g + e^{-g}}, \qquad (3)$$

$$f_2(g) \sim \frac{e^{-g} \sum a_n (-g)^n + e^g \sum b_n (-g)^n}{e^{-g} + e^g}, \qquad (4)$$

where $a_n \sim \Gamma(n + a)$ and $b_n \sim \Gamma(n + b)$. Then, the functions $f_1(g)$ and $f_2(g)$ have the same asymptotic series at $g \longrightarrow 0$ but with opposite signs of the coupling constant:

$$f_1(g) \sim \sum f_n g^n, \quad f_2(g) \sim \sum f_n (-g)^n,$$

where $f_n \simeq a_n + b_n$ for $n \gg 1$. Nevertheless, these functions can behave independently at $g \longrightarrow \infty$:

$$f_1(g) \sim \sum a_n g^n \sim g^\alpha, \quad f_2(g) \sim \sum b_n (-g)^n \sim g^\beta. \quad (5)$$

We emphasize that $f_2(g) \neq f_1(-g)$, as might appear at first glance, because the function $f_1(-g)$ need not to exist and the analytic continuation from the positive to the negative semiaxis usually leads to the appearance of imaginary part [15], which is absent in $f_2(g)$.

It is easy to present many more such examples. The asymptotic form of an analytic function at infinity is not, as a rule, an analytic function and has discontinuities (Stocks phenomenon), which is well known in the theory of special functions. We can also mention the semiclassical wave functions that change their form both upon passing from the classically admissible

region to the subbarrier region and upon crossing the Stocks line in the complex plane [16].

Thus, the assumption that two functions specified by the same asymptotic series but with different signs of g behave identically is by no means obvious and requires additional arguments, which were absent in [12].

Even under this assumption, the application of Suslov's method to an alternating series gives very ambiguous results (see Fig. 1 in [12]); the presence of numerous χ^2 minima seems to be an artefact of the procedure that is used for a small number of the initial terms of the PT series. Moreover, since the coefficient of the leading term in the asymptotic series is estimated at $\beta_\infty \sim 10^5$ with an error of several orders of magnitude (in fact, it varies from 1 to 10^{10}; see Fig. 2b in [12]), this asymptotic behavior is determined quite unreliably.

3. There are other arguments against the asymptotic behavior presented in [12]. Indeed, let us consider a function specified by the asymptotic series

$$f(g) \sim \sum_{n=0}^{\infty} f_n (-g)^n, \quad f_n \sim \Gamma(n + b) \text{ at } n \longrightarrow \infty. \quad (6)$$

Assume that the series can be summed in the Borel sense[1] and apply the Borel transformation

$$f(g) = \int_0^\infty dx e^{-x} \sum_{n=0}^\infty \frac{f_n}{n!} (-gx)^n = \int_0^\infty dx e^{-x} B(gx), \quad (7)$$

where the function $B(x)$ specified by a convergent series is called the Borel transform of the function $f(g)$.

Without loss of generality, we assume that $B(x) \sim x^\alpha$ at $x \longrightarrow \infty$. Then, the function $f(g)$ at $g \longrightarrow \infty$ behaves as

$$f(g) \sim \begin{cases} \Gamma(\alpha + 1)g^\alpha, & \alpha > -1 \\ \log g/g, & \alpha = -1 \\ c_1 g^{-1}, & \alpha < -1, \end{cases} \quad (8)$$

where $c_1 = \int_0^\infty dx B(x) < \infty$. The last equality can easily be obtained by substituting $x = t/g$ in integral (7) and turning g to infinity.

At first glance, the function $f(g)$ cannot decrease faster than $1/g$. However, this is not the case. If the first N moments of the Borel transform vanish, i.e.,[2]

$$c_i = \int_0^\infty dx x^{i-1} B(x) = 0, \quad i = 1, \dots, N, \quad (9)$$

---

[1] This assumption is reasonable because otherwise the PT series are not strictly defined in quantum mechanics and field theory. This assumption was also used in [9–12].

[2] Accordingly, the Borel transform must oscillate and have N zeros in the range $0 < x < \infty$.

then

$$f(g) \sim c_{N+1} g^{-(N+1)}, \quad g \longrightarrow \infty \qquad (10)$$

at $0 < |c_{N+1}| < \infty$. Otherwise (if $c_{N+1} = \infty$), the exponent for the asymptotic behavior of the function $f(g)$ lies between $-N$ and $-(N+1)$ or $f(g) \sim \ln g / g^{N+1}$.

Therefore, to obtain a decrease of the g^{-13} order (see [12]), it is required that the first 12 moments of the function $B(x)$ vanish. Taking into account that only four terms of series (1) are currently known, this statement seems to be unjustified.

The same property of the function is seen for the modified Borel transform used, in particular, in [12]:

$$f(g) = \int_0^\infty dx\, e^{-x} x^{\beta-1} \sum_{n=0}^\infty \frac{f_n}{\Gamma(n+\beta)} (-gx)^n$$
$$= \int_0^\infty dx\, e^{-x} x^{\beta-1} B_\beta(gx), \quad \beta > 1. \qquad (11)$$

In this case, the asymptotic behavior of the Borel transform depends on β. In particular, for $\beta = b$ from Eq. (6) one has $B_b(x) \sim c_1/x$ and

$$f(g) \sim c_1 \Gamma(b-1) g^{-1}, \quad \text{if} \quad c_1 \neq 0.$$

Otherwise, changing $x \longrightarrow x/g$ in integral (11), we obtain[3]

$$f(g) = \frac{1}{g^\beta} \int_0^\infty dx\, e^{-x/g} x^{\beta-1} B_\beta(x)$$
$$\sim \frac{1}{g^\beta} \int_0^\infty dx\, x^{\beta-1} B_\beta(x) \quad g \longrightarrow \infty. \qquad (12)$$

Setting sequentially $\beta = 1, 2, \dots, N$, we conclude that, to obtain the asymptotic behavior $f(g) \sim 1/g^N$, the lower moments must vanish, i.e.,

$$\int_0^\infty dx\, x^{j-1} B_k(x) = 0, \quad k \le j \le N-1;$$
$$k = 1, 2, \dots, N-1. \qquad (13)$$

Thus, the GLF can, in principle, decrease rapidly, as $\beta(g) \sim g^{-N}$, but only with many [N and $N^2/2$ for Eqs. (9) and (13), respectively] additional constrains on the Borel transform. Evidently, the knowledge of four or five PT coefficients cannot guarantee these conditions. At the same time, the above analysis shows that the asymptotic expression increasing at infinity or decreasing no faster than $1/g$ is much less restrictive.

4. We now comment on "remark" [13] to our paper [14]. In this remark, Suslov presented the zero-dimensional $\phi^4_{(0)}$ model

$$J(g) = \frac{1}{\sqrt{2\pi}} \int_\infty^\infty d\phi \exp\left\{-\frac{1}{2}\phi^2 - \frac{g}{4!}\phi^4\right\}$$
$$\sim \sum_{k=0}^\infty (-g)^k \frac{\Gamma(2k+1/2)}{\Gamma(k+1)\Gamma(1/2)6^k} \qquad (14)$$

and stated that the method developed in [9] allows the use of only one (!) coefficient of the PT series to determine the asymptotic exponent $J(g) \propto g^\alpha$ with a 10% accuracy: $-0.271 < \alpha < -0.218$ (exact value is $\alpha = -0.25$). Further, he wrote, "This result refutes the main statement made in [14] stipulating a large number of expansion coefficients." However, this example is very specific because of the following reasons.

(i) Even the first coefficients of the PT series approach rapidly their asymptotic values (see $D = 0$ column in Table 1). Such a behavior occurs neither in quantum mechanics ($D = 1$ column) nor, all the more, in all models of field theory (see, e.g., [7, 14] and Table 1).

(ii) The calculation with 50 coefficients of the PT series instead of one coefficient yields the exponent $\alpha = -0.235 \pm 0.025$ [9], which virtually coincides with the above estimate. Thus, the inclusion of many coefficients of the PT series, which give the only new information about the desired function, does not improve the accuracy of determining the exponent α. This fact testifies to the poor convergence of the method used in [9].

(iii) Model example (14) does not possess the property that is characteristic of field theory, where the ratio $\bar{\beta}_n/\beta_n$ depends on the renormalization scheme (*MOM* or $\overline{MS}$, see Table 1). This dependence also shows that the calculated coefficients β_n are still far from their asymptotic form at $n \longrightarrow \infty$.

Thus, zero-dimensional model (14) is too simplified to provide any general conclusions about the number of PT coefficients necessary for reconstructing the GLF.

5. The situation in the Yang–Mills theory is even less definite than in the scalar field theory. In the former theory, four expansion coefficients of the GLF are calculated [17]. They increase rapidly in magnitude: $\beta_2 = -11$, $\beta_3 = -102$, $\beta_4 = -1428.5$, and $\beta_5 \approx -29243$. In addition, the asymptotic term

$$\beta_n \sim c\Gamma(n+35/2) \qquad (15)$$

at $n \longrightarrow \infty$ was found in [13, 18].

Since the coefficient c is unknown in this case,[4] we present in Table 2 the ratios $\sigma_n = \rho_{n+1}/\rho_n$, where $\rho_n =$

---

[3] We assume that integral (11) converges, which imposes upper limit on the parameter β.

[4] Similar to [12], we consider the case $N_c = 3$ and $N_f = 0$, i.e., pure gluodynamics without quarks.

Table 1. Ratios $\rho_n = \bar{\beta}_n / \beta_n$ for the $\phi^4_{(D)}$ model

n	$D = 0$	1	3	4(*MOM*)	4($\overline{MS}$)
2	1.0317	2.005	0.019	0.0978	0.0075
3	1.0210	1.897	0.085	0.659	0.0505
4	1.0157	1.718	0.166	1.072	0.097
5	1.0126	1.562	0.252	1.554	0.128
6	1.0104	1.443	0.322	–	0.139
7	1.0090	1.354	0.379	–	–
10	1.0063	1.203	–	–	–
20	1.0031	1.078			
30	1.0021	1.049			
50	1.0013	1.028			
75	1.0008	1.018			
a	2/3	3	0.1477	1	1
b	−1/2	0	4	4	4

Note: The case $D = 0$ corresponds to integral (14), $D = 1$ corresponds to the ground-state energy of a one-dimensional anharmonic oscillator [23], and $D = 3$ and 4 correspond to the GLF in scalar field theory. In the last case, the ρ_n values are presented in two renormalization schemes, *MOM* or $\overline{MS}$. The lower two rows give the parameters of asymptotic formula (2).

Table 2. Ratios $\sigma_n = \rho_{n+1}/\rho_n$ for the $\phi^4_{(D)}$ model and for the Yang–Mills theory for $N_c = 3$ and $N_f = 0$

n	$D = 0$	$D = 1\ \phi^4$	$D = 1\ \phi^4\ MOM$	$D = 1\ \phi^4\ (\overline{MS})$	YM ($\overline{MS}$)
2	0.9896	0.9459	6.738	6.733	177.089
3	0.9948	0.9063	1.627	1.921	24.935
4	0.9969	0.9090	1.450	1.320	7.810
5	0.9978	0.9235	–	1.086	–
10	0.99943	0.9769	–	–	–
50	0.99998	0.9994	–	–	–
75	0.99999	0.9998	–	–	–

$\bar{\beta}_n / \beta_n$, to illustrate the convergence for an anharmonic oscillator, $\phi^4_{(4)}$ theory, and Yang–Mills theory. According to the asymptotic formula

$$\beta_n = \bar{\beta}_n\left(1 + \frac{c_1}{n} + \frac{c_2}{n^2} + \dots\right) \quad \text{at} \quad n \longrightarrow \infty, \quad (16)$$

the ratios σ_n (independent of c) behave as

$$\sigma_n = 1 + \frac{c_1}{n^2} - \frac{c_1^2 + c_1 - 2c_2}{n^3} + O(1/n^4). \quad (17)$$

Therefore, if the coefficients β_n reached their asymptotic values, σ_n must rapidly approach unity with $n \longrightarrow \infty$. This is indeed the case for the anharmonic oscillator. In the scalar field theory, the convergence of σ_n to unity is

already seen. However, in the Yang–Mills theory, the values of σ_n with $n \leq 4$ are still far from unity.

In this case, $a = 1$ and $b = 17$ in asymptotic term (2), and, for $n \ll b$, there is a sharp dependence on the form of the asymptotic coefficients. For example,

$$\delta_n \equiv \frac{\Gamma(n + b + 1/2)}{\Gamma(n + 1/2)n^b} = 1 + \frac{b^2}{2n} + \frac{3b^4 - 4b^3 + b}{24n^2} + \dots (18)$$

In particular, $\delta_2 \sim 2 \times 10^{11}$, $\delta_3 \sim 10^9$, and $\delta_5 \sim 6 \times 10^6$ for $b = 17$. Hence, the coefficients β_n do not yet approach their asymptotic form, so that the corrections in powers of $1/n$, which underlie the algorithm developed in [9–12], depend strongly on the chosen form of asymptotic coefficients.

For this reason, we are still of the opinion [14] that the statements made in [9–12] about the asymptotic

behavior of the GLF at $g \longrightarrow \infty$ in the field theory are doubtful. As was shown in [14], to reliably reconstruct the GLF in the strong-coupling regime ($g \gg 1$ but not at $g \longrightarrow \infty$), many terms of the PT series must reach their asymptotic values. The situation is considerably complicated if there is an intermediate asymptotic form [14] or if the asymptotic form contains logarithm, in addition to powers of g. In these cases, the asymptotic regime occurs much later. A particular example is provided by the problem of a hydrogen atom in a strong electric [14] or magnetic [19] field.

We emphasize that the Borel resummation method and similar methods give very reliable results for alternating series (see, e.g., [8, 20, 21], where the critical exponents of the second-order phase transitions were calculated). At the same time, no commonly accepted methods exist for series of constant sign, because the existence of such a series implies ground-state degeneracy and the presence of contributions that cannot be reproduced by perturbation theory. In this case, the reconstruction of the function requires additional information that is lacking in the perturbative field theory. A good example is a degenerate anharmonic oscillator, considered in [22].

We would not like the readers of papers [9–12] to be under the impression that the asymptotic behavior of the GLF in quantum field theory at $g \longrightarrow \infty$ can be obtained by processing the first few terms of the PT series without invoking additional nonperturbative information, which is not currently available.

REFERENCES

1. M. Gell-Mann and F. E. Low, Phys. Rev. **95**, 1300 (1954).

2. N. N. Bogolyubov and D. V. Shirkov, *Introduction to the Theory of Quantized Fields*, 4th ed. (Nauka, Moscow, 1984; Wiley, New York, 1980), Chap. 9.

3. L. N. Lipatov, Pis'ma Zh. Éksp. Teor. Fiz. **25**, 116 (1977) [JETP Lett. **25**, 104 (1977)]; Zh. Éksp. Teor. Fiz. **72**, 411 (1977) [Sov. Phys. JETP **45**, 216 (1977)].

4. V. S. Popov, V. L. Eletsky, and A. V. Turbiner, Phys. Lett. B **72**, 99 (1977); Zh. Éksp. Teor. Fiz. **74**, 445 (1978) [Sov. Phys. JETP **47**, 232 (1978)].

5. V. L. Eletsky and V. S. Popov, Phys. Lett. B **77**, 411 (1978).

6. D. I. Kazakov, O. V. Tarasov, and D. V. Shirkov, Teor. Mat. Fiz. **38**, 15 (1979).

7. D. I. Kazakov and D. V. Shirkov, Fortschr. Phys. **28**, 465 (1980).

8. Yu. A. Kubyshin, Teor. Mat. Fiz. **58**, 137 (1984).

9. I. M. Suslov, Pis'ma Zh. Éksp. Teor. Fiz. **71**, 315 (2000) [JETP Lett. **71**, 217 (2000)]; Zh. Éksp. Teor. Fiz. **120**, 5 (2001) [JETP **93**, 1 (2001)].

10. I. M. Suslov, Pis'ma Zh. Éksp. Teor. Fiz. **74**, 211 (2001) [JETP Lett. **74**, 191 (2001)].

11. I. M. Suslov, Zh. Éksp. Teor. Fiz. **117**, 659 (2000) [JETP **90**, 571 (2000)].

12. I. M. Suslov, Pis'ma Zh. Éksp. Teor. Fiz. **76**, 387 (2002) [JETP Lett. **76**, 327 (2002)].

13. I. M. Suslov, Zh. Éksp. Teor. Fiz. **122**, 696 (2002) [JETP **95**, 601 (2002)].

14. D. I. Kazakov and V. S. Popov, Zh. Éksp. Teor. Fiz. **122**, 675 (2002) [JETP **95**, 581 (2002)].

15. F. J. Dyson, Phys. Rev. **85**, 631 (1952).

16. J. Heading, *An Introduction to Phase-Integral Methods* (Methuen, London, 1962; Mir, Moscow, 1965).

17. T. van Ritbergen, J. A. M. Vermaseren, and S. A. Larin, Phys. Lett. B **400**, 379 (1997).

18. E. B. Bogomolny and V. A. Fateev, Phys. Lett. B **71**, 93 (1977).

19. H. Hasegawa and R. E. Howard, J. Phys. Chem. Solids **21**, 179 (1961).

20. J. C. Le Guillou and J. Zinn-Justin, Phys. Rev. Lett. **39**, 95 (1977); Phys. Rev. B **21**, 3976 (1980); J. Zinn-Justin, *Quantum Field Theory and Critical Phenomena*, 2nd ed. (Clarendon Press, Oxford, 1993), Chap. 25.

21. A. A. Vladimirov, D. I. Kazakov, and O. V. Tarasov, Zh. Éksp. Teor. Fiz. **77**, 1035 (1979) [Sov. Phys. JETP **50**, 521 (1979)].

22. J. Zinn-Justin, *Quantum Field Theory and Critical Phenomena*, 2nd ed. (Clarendon Press, Oxford, 1993), Chap. 40.

23. C. M. Bender and T. T. Wu, Phys. Rev. **184**, 1231 (1969).

Translated by R. Tyapaev

Constraints on Nonsinglet Polarized Parton Densities
from the Infrared-Renormalon Model¶

A. L. Kataev

Institute for Nuclear Research, Russian Academy of Sciences, Moscow, 117312 Russia
e-mail: kataev@ms2.inr.ac.ru

Using the infrared-renormalon approach, we obtain the constraints on the next-to-leading order nonsinglet polarized parton densities. The advocated feature follows from the consideration of the effect revealed in the process of the next-to-leading order fits to the data for the asymmetry of polarized lepton–nucleon scattering, which result in the approximate nullification of the $1/Q^2$-correction to $A_1^N(x, Q^2)$. © 2003 MAIK "Nauka/Interperiodica".

PACS numbers: 13.60.Hb; 12.38.Bx; 12.39.-x; 13.88.+e

The study of the QCD predictions for the photon–nucleon asymmetry $A_1^N = (\sigma_{1/2} - \sigma_{3/2})/(\sigma_{1/2} + \sigma_{3/2})$, where subscripts denote the total angular momentum of the photon–nucleon pair along the incoming lepton's direction, plays the essential role in the analysis of polarized deep inelastic scattering (DIS) (see, e.g., [1]). It is related to the well-known structure function g_1^N of polarized DIS by

$$A_1^N(x, Q^2) = (1 + \gamma^2)\frac{g_1^N(x, Q^2)}{F_1^N(x, Q^2)}, \qquad (1)$$

where the kinematic factor γ is defined as $\gamma = 4M_N^2 x^2/Q^2$ and $g_1^N(x, Q^2)$ is the structure function (SF) of polarized DIS, while $F_1^N(x, Q^2)$ SF enters into the cross-section of unpolarized charged lepton–hadron DIS (see, e.g., [2]). Quite recently, several procedures of the study of the Q^2 behavior of A_1^N were discussed in the literature (see [3–6]). Moreover, in [2, 5, 6], by fitting existing data for polarized DIS obtained at the accelerators of the CERN, DESY, and SLAC scientific centers in the kinematical region $0.005 \leq x \leq 0.75$ and $1 \text{ GeV}^2 \leq Q^2 \leq 58 \text{ GeV}^2$, the $1/Q^2$ dynamical power correction to A_1^N was extracted. In general, it gives an additional contribution to the perturbation theory part of $(A_1^N)_{PT}$ and can be parameterized as

$$A_1^N(x, Q^2) = (A_1^N(x, Q^2))_{PT} + h^{A_1}(x)/Q^2. \qquad (2)$$

It is interesting that, in the process of the fits of [2, 5, 6], it was found that the x shape of $h^{A_1}(x)$ is consistent with zero (see, e.g., the figure from [2]).

In this note, we describe the possible consequences of this effect in the nonsinglet (NS) approximation, which is valid for the x-cut $x \gtrsim 0.25$. Our consideration
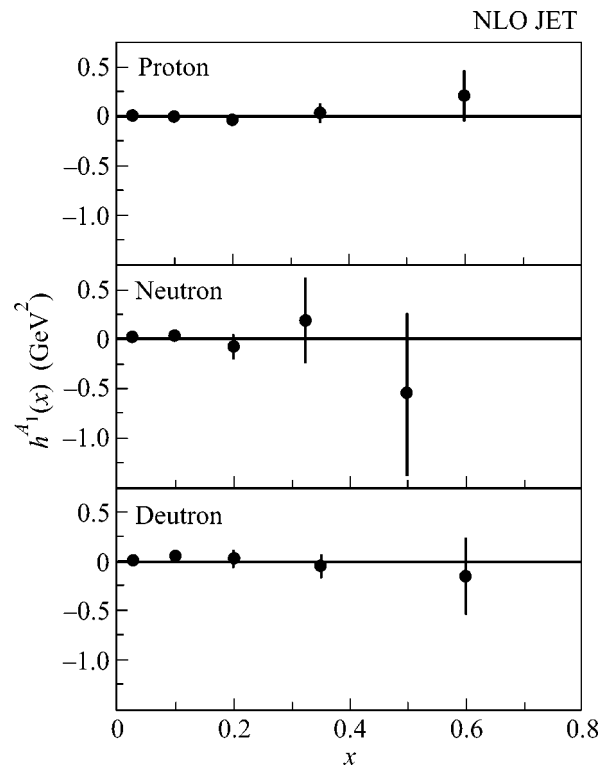
The results of extraction of $h^{A_1}(x)$ from the next-to-leading order fits of [2] in the JET scheme [7].

¶ This article was submitted by the author in English.

will be based on the infrared-renormalon (IRR) approach, developed in QCD in [8] and reviewed in detail in [9]. This approach was used in [10] to study the behavior of the $1/Q^2$ corrections to the NS contributions to F_2 and F_1 SFs of unpolarized DIS of charged leptons on nucleons and the pure NS xF_3 SF of vN DIS using $\overline{MS}$-scheme calculations.[1] It is interesting that the x shape of the IRR induced power corrections to xF_3 predicted in [10] was supported in [12, 13] by the leading order (LO) and next-to-leading order (NLO) fits to CCFR'97 data (a detailed description and refinements of the fits of [12] are given in [14, 15]. Therefore, it is worth considering the consequences of calculations of the IRR contributions to the NS part of g_1^N SF of polarized deep-inelastic scattering, which was also performed in [10].

Let us rewrite Eqs. (1), (2) in the following way:

$$A_1^N = (1 + \gamma^2)\frac{g_1^N(x, Q^2)\left(1 + \dfrac{h^{g_1}(x)}{Q^2 g_1^N(x, Q^2)}\right)}{F_1^N(x, Q^2)\left(1 + \dfrac{h^{F_1}(x)}{Q^2 F_1^N(x, Q^2)}\right)}, \quad (3)$$

where $h^{g_1}(x)/Q^2$ and $h^{F_1}(x)/Q^2$ are the model-independent parameterizations for the twist-4 contributions to g_1^N and F_1^N SFs, which in general are nonzero. Using the above-mentioned effect of approximate nullification of the twist-4 correction to A_1^N, we get

$$\frac{h^{g_1}(x)}{Q^2 g_1^N(x, Q^2)} \approx \frac{h^{F_1}(x)}{Q^2 F_1^N(x, Q^2)}. \quad (4)$$

At the next step, we will use the existing inequality for $g_1^N(x, Q^2)$ SF, namely,

$$\left| g_1^N(x, Q^2) \right| \le F_1^N(x, Q^2). \quad (5)$$

Combining it with Eq. (4), we arrive at the bound

$$\left| h^{g_1}(x) \right| \le \left| h^{F_1}(x) \right|. \quad (6)$$

It should be stressed that the calculations of [10] predict that, in the NS approximation (or in the valence-quarks approximation), the contributions of the $1/Q^2$ corrections to F_1 and xF_3 SFs are the same. Indeed, the corresponding results of [10] can be rewritten in the following way:

$$h^{F_1}(x, \mu^2) = h^{F_3}(x, \mu^2) = A_2'\int\limits_x^1 \frac{dz}{z}C_1(z)q^{NS}(x/z, \mu^2), \quad (7)$$

---

[1] Note that we avoid considerations of the IRR renormalon free expansions in QCD coupling constants with the "freezing-type" behavior at small Q^2 (see [11]).

where

$$C_1(z) = -\frac{4}{(1-x)_+} + 2(2 + x + 2x^2) \\ - 5\delta(1 - x) - \delta'(1 - x), \quad (8)$$

the "+" prescription, for any test function, is defined as

$$\int\limits_0^1 F(x)_+ f(x)dx = \int\limits_0^1 F(x)[f(x) - f(1)]dx, \quad (9)$$

and

$$q^{NS}(x, \mu^2) \\ = \sum_{i=1}^{n_f}\left(e_i^2 - \frac{1}{n_f}\sum_{k=1}^{n_f}e_k^2\right)(q_i(x, \mu^2) + \bar{q}_i(x, \mu^2)) \quad (10)$$

are the NS parton densities, μ^2 is the normalization point of order 1 GeV^2, and A_2' is the IRR model parameter, to be extracted from the fits to the concrete data. Its value was extracted from the low-energy xF_3 data, collected by the IHEP–JINR neutrino detector at the IHEP 70 GeV proton synchrotron [16] (see also [17] for a review). The result of [16] $A_2' = -0.10 \pm 0.09$ (experimental) GeV^2 is in agreement with the value extracted from the NLO analysis of the CCFR'97 xF_3 data [18], namely, with $A_2' = -0.125 \pm 0.053$ (statistical) GeV^2 [15]. It should be noted that the identity of Eq. (7) does not contradict the point of view, expressed in [3, 4], that to study the Q^2 behavior of $A_1(Q^2)$ in the NS approximation it might be convenient to use the concrete xF_3 data instead of the theoretical expression for F_1^N.

Consider now the case of g_1^N SF of polarized DIS. In general, the IRR contributions to g_1^N were studied in [19]. In the NS approximation, the IRR contributions to g_1^N were calculated in [10], where the following result was obtained:

$$h^{g_1}(x, \mu^2) = A_2\int\limits_x^1 \frac{dz}{z}C_1(z)\Delta^{NS}(x/z, \mu^2). \quad (11)$$

Here, $\Delta^{NS}(x, \mu^2)$ are the NS polarized parton densities, namely,

$$\Delta^{NS}(x, \mu^2) \\ = \sum_{i=1}^{n_f}\left(e_i^2 - \frac{1}{n_f}\sum_{k=1}^{n_f}e_k^2\right)(\Delta q_i(x, \mu^2) + \Delta\bar{q}(x, \mu^2)), \quad (12)$$

and the IRR model coefficient function $C_1(z)$ is the same as in the case of the IRR model contributions to the $1/Q^2$ corrections for F_1 and xF_3 SFs of unpolarized

deep-inelastic scattering (see Eq. (8)). As to the IRR model parameter A_2, in general one should not expect that it has the same value as the parameter A_2' in Eq. (7). In principle, it should be extracted from the separate fits to g_1 data in the NS approximation. However, it is worth stressing that in the NS approximation the IRR contributions to g_1^N and F_1^{vN} are closely related (a similar feature was revealed while comparing IRR model contributions to the Bjorken sum rule for g_1^N SF [20] and still unmeasured Bjorken sum rule for F_1^{vN} SF [21]).

Using now Eqs. (6), (7) and Eq. (11), we get the following constraint:

$$\left| A_1 \Delta^{NS}(x, \mu^2) \right| \leq \left| A_2' q^{NS}(x, \mu^2) \right| \qquad (13)$$

which is valid at both the LO and the NLO. This constraint is the main result of our note. The consequences for its Q^2 dependence can be further studied using the machinery of the DGLAP equations [22].

It is rather impressive that the NLO constraint of Eq. (13) is similar to the well-known LO bound of [1], namely,

$$\left| \Delta(x, Q^2) \right| \leq q(x, Q^2). \qquad (14)$$

Moreover, Eq. (13) can also be transformed to the LO relation between the IRR model parameters of Eq. (3) and Eq. (7), namely,

$$\left| A_2 \right| \sim \left| A_2' \right|. \qquad (15)$$

We hope that it will be possible to check the relation of Eq. (15) using the fits of the concrete data for g_1 SF.

REFERENCES

1. G. Altarelli, S. Forte, and G. Ridolfi, Nucl. Phys. B **534**, 277 (1998); hep-ph/9806345.

2. E. Leader, A. V. Sidorov, and D. B. Stamenov, hep-ph/0212085; Phys. Rev. D (in press).

3. A. V. Kotikov and D. V. Peshekhonov, Pis'ma Zh. Éksp. Teor. Fiz. **65**, 9 (1997) [JETP Lett. **65**, 7 (1997)]; hep-ph/9612319.

4. A. V. Kotikov and D. V. Peshekhonov, Eur. Phys. J. C **9**, 55 (1999); hep-ph/9810224.

5. E. Leader, A. V. Sidorov, and D. B. Stamenov, in *Proceedings of 9th Lomonosov Conference on Elementary Particle Physics: Particle Physics on the Boundary of the Millenium, Moscow, 1999*, Ed. by A. I. Studenikin (World Sci., Singapore, 2001), p. 78.

6. E. Leader, A. V. Sidorov, and D. B. Stamenov, Eur. Phys. J. C **23**, 479 (2002); hep-ph/0111267.

7. R. D. Carlitz, J. C. Collins, and A. H. Mueller, Phys. Lett. B **214**, 229 (1988); M. Anselmino, A. Efremov, and E. Leader, Phys. Rep. **261**, 1 (1995); Err.: Phys. Rep. **281**, 399 (1997)]; hep-ph/9501369; D. Muller and O. V. Teryaev, Phys. Rev. D **56**, 2607 (1997); hep-ph/9701413.

8. V. I. Zakharov, Nucl. Phys. B **385**, 452 (1992).

9. M. Beneke, Phys. Rep. **317**, 1 (1999); hep-ph/9807443.

10. M. Dasgupta and B. R. Webber, Phys. Lett. B **382**, 273 (1996); hep-ph/9604388.

11. N. V. Krasnikov and A. A. Pivovarov, Mod. Phys. Lett. A **11**, 835 (1996); hep-ph/9602272; D. V. Shirkov and I. L. Solovtsov, Phys. Rev. Lett. **79**, 1209 (1997); hep-ph/9704333; Y. A. Simonov, Yad. Fiz. **65**, 140 (2002) [Phys. At. Nucl. **65**, 135 (2002)]; hep-ph/0109081.

12. A. L. Kataev, A. V. Kotikov, G. Parente, and A. V. Sidorov, Phys. Lett. B **417**, 374 (1998); hep-ph/9706534.

13. S. I. Alekhin and A. L. Kataev, Phys. Lett. B **452**, 402 (1999); hep-ph/9812348.

14. A. L. Kataev, G. Parente, and A. V. Sidorov, Nucl. Phys. B **573**, 405 (2000); hep-ph/9905310.

15. A. L. Kataev, G. Parente, and A. V. Sidorov, Fiz. Elem. Chastits At. Yadra **34**, 43 (2003) [Phys. Part. Nucl. **34**, 20 (2003)]; hep-ph/0106221.

16. S. I. Alekhin, V. B. Anykeyev, A. A. Borisov, *et al.*, Phys. Lett. B **512**, 25 (2001); hep-ex/0104013.

17. A. L. Kataev, hep-ph/0107247; in *Proceedings of 15th les Recontre de Physique de la Vallee d'Aosta: Results and Perspectives in Particle Physics*, Ed. by M. Greco (2001), Frascati Physics Series, Vol. 22, p. 205.

18. W. G. Seligman, C. G. Arroyo, L. de Barbaro, *et al.*, Phys. Rev. Lett. **79**, 1213 (1997).

19. E. Stein, M. Maul, L. Mankiewicz, and A. Schafer, Nucl. Phys. B **536**, 318 (1998); hep-ph/9803342.

20. D. J. Broadhurst and A. L. Kataev, Phys. Lett. B **315**, 179 (1993); hep-ph/9308274.

21. D. J. Broadhurst and A. L. Kataev, Phys. Lett. B **544**, 154 (2002); hep-ph/0207261.

22. V. N. Gribov and L. N. Lipatov, Yad. Fiz. **15**, 781 (1972) [Sov. J. Nucl. Phys. **15**, 438 (1972)]; G. Altarelli and G. Parisi, Nucl. Phys. B **126**, 298 (1977); Y. L. Dokshitzer, Zh. Éksp. Teor. Fiz. **73**, 1216 (1977) [Sov. Phys. JETP **46**, 641 (1977)].

Effect of Injection of C-band ASE on L-band Erbium-Doped Fiber Amplifier[¶]

S. W. Harun*, N. Tamchek, P. Poopalan, and H. Ahmad

Photonics Laboratory, Department of Physics, University of Malaya, 50603 Kuala Lumpur, Malaysia
*e-mail: wadi72@yahoo.com
Received March 13, 2003

The effect of injecting conventional band (C-band) amplified spontaneous emission on the performance of long-wavelength band erbium-doped fiber amplifier (L-band EDFA) is demonstrated. It uses a circulator and broadband fiber Bragg grating (FBG) to route C-band ASE from a C-band EDFA. Injection of a small amount of ASE (attenuation of 20 dB or above) improves the small signal gain with a negligible noise figure penalty compared to that of an amplifier without the ASE injection. A maximum gain improvement of 3.5 dB is obtained at an attenuation of 20 dB. At very large amounts of ASE injection (attenuation of 0 dB), the gain of the amplifier is clamped at 15.2 dB from –40 to –10 dBm with a gain variation of less than 0.3 dB. The saturation power is also increased from –8 dBm (for without ASE injection) to 2 dBm (VOA = 0 dB) with a slight noise figure penalty. These results show that the ASE injection technique can be used either for gain improvement or for gain clamping in L-band EDFA. © 2003 MAIK "Nauka/Interperiodica".

PACS numbers: 42.60.Da; 42.81.Uv; 42.81.Wg

INTRODUCTION

The erbium-doped fiber amplifier (EDFA) moved very quickly from invention in 1987 to the cornerstone of high-speed long-haul networks. The need to extend the bandwidth of dense wavelength division multiplexing systems has resulted in research aimed at transmitting outside the conventional wavelength band (also known as the C-band, ranging from 1530 to 1565 nm). Transmission in the region 1570–1610 nm (referred to as the L-band), which effectively doubles the potential bandwidth, has been reported [1]. The L-band EDFA can be combined with a C-band EDFA in parallel configuration to increase the range of amplification wavelength region. However, the L-band lies at the tail of the erbium amplification window, where the inversion rate is low. Therefore, various research efforts have been explored to enhance the amplification characteristics in the L-band EDFA [2, 3].

As the complexity of the networks increases in multiplex system networking, a major potential problem associated with the amplifier is a need for the control of the gain of EDFAs due to circumstances such as faults, adding and dropping of wavelengths, and rerouting. In these cases, the total input signal power to the amplifier varies abruptly, causing the dynamics of the population inversion to change accordingly. Therefore, the amplifier gain increases or decreases with the potential to cause receiver saturation or bit error rate increment. Thus, a gain-clamping mechanism is desired. To date, there have been various research efforts to clamp the

gain in C- and L-band EDFA [4, 5]. In this paper, we demonstrate the effect of injecting C-band ASE on L-band EDFA. This ASE injection technique shows a possible application either for gain improvement or for gain clamping in L-band EDFA.

EXPERIMENTAL SETUP

The experimental setup is shown in Fig. 1. The erbium-doped fiber (EDF) used in the experiment is commercially available and has a numerical aperture of 0.22, cut-off wavelength of 920 nm, and peak absorption of 6.1 dB/m at 1531 nm. The length of EDF is fixed at 50 m. A 980-nm laser diode is used as a pump source with a maximum pump power of 92 mW at the EDF input end. The wavelength selective coupler (WSC) combines the input test signal and the 980-nm pump into the EDF. The C-band ASE from a C-band EDFA is fed into the EDF section using an optical circulator and a fiber Bragg grating. At the amplifier input end, a broadband fiber Bragg grating with a center wave-
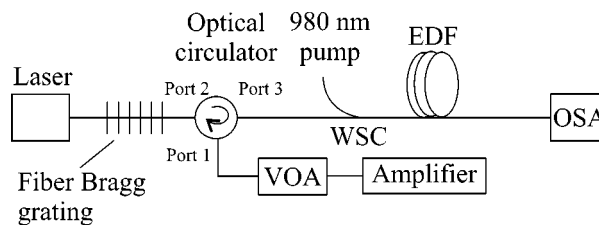

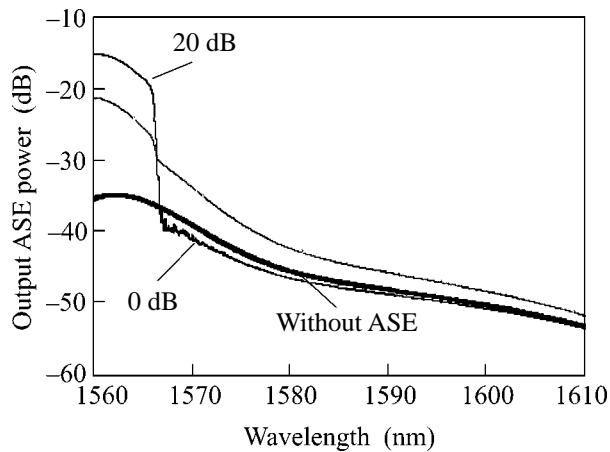**Fig. 1.** Experimental setup.

Fig. 2. ASE spectra of the amplifier with and without C-band ASE.

length, bandwidth, and reflectivity of 1545 nm, 40 nm, and 99%, respectively, is employed as a broadband reflector. The forward ASE light from the C-band EDFA is routed by the optical circulator, reflected by the grating, and then copropagates with the signal. A variable optical attenuator (VOA) is used to control the power level of the launched C-band ASE. A tunable laser source is used for the evaluation of the amplifier performance in conjunction with an optical spectrum analyzer (OSA), which uses the interpolation technique to evaluate noise figure.

RESULT AND DISCUSSION

Figure 2 depicts the ASE spectra of the amplifier with and without injection of C-band ASE, where the
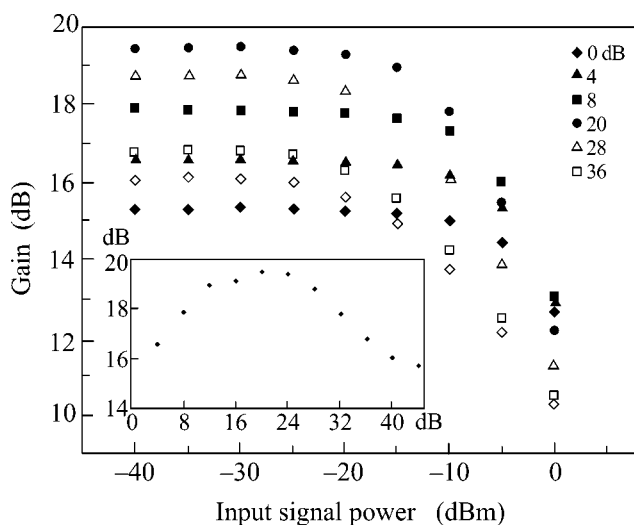
thick line represents the amplifier without injection of C-band ASE. The pump power is fixed at 92 mW. As apparent in the figure, the amplifier with a large amount of ASE injection (VOA = 0 dB) shows a lower L-band ASE than that of the amplifier without ASE injection, at L-band region (above 1567 nm). This reduction of L-band ASE is obtained due to the injection of a large amount of C-band (1525 to 1567 nm) ASE that causes limitation of population inversion in the longer wavelength region. However, the injection of low power of ASE (VOA = 20 dB) dramatically increases the ASE level in the L-band region. The ion population inversion is increased by this amount of ASE through energy transfer from short wavelengths to longer wavelengths.

Figures 3 and 4 show the optical gain and noise figure characteristics, respectively, at 1580 nm as a function of input signal power against the VOA losses. The pump power is fixed at 92 mW. The characteristic of the amplifier without the injection of backward ASE is also shown for comparison. Inset of Figs. 4 and 5 shows the small signal gain and noise figure against the VOA loss, respectively, when input signal and wavelength are fixed at –30 dBm and 1580 nm. At attenuations of 20 dB or above, the gain level increases with the amount of the injected ASE power as shown in Fig. 3. The small signal gain improvement of 3.5 dB is obtained for the attenuation of 20 dB compared to the amplifier without the ASE injection. Figure 5 shows an injected ASE spectrum at attenuations of 0 and 20 dB. The ASE power is –40 dBm at 1531 nm for the attenuation of 20 dB. This amount of ASE increases the population ion inversion at the input end of the EDF and hence improves the L-band signal gains. This technique shows that the injection of C-band ASE (total power should be less than –14.1 dBm) can be utilized to enhance the L-band performance. Besides gain
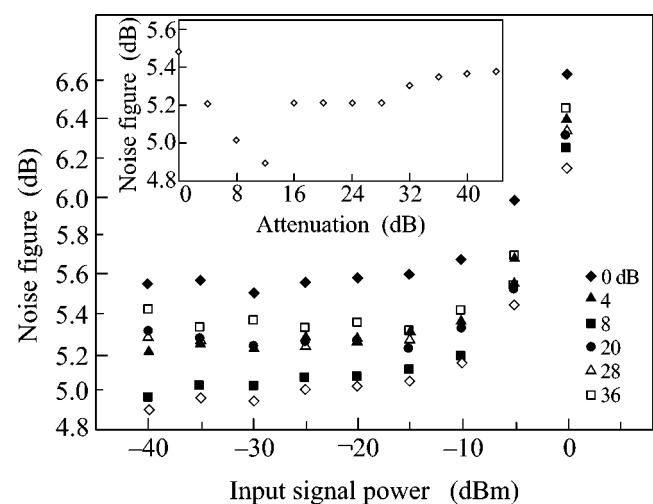

Fig. 3. Gain as a function of input signal power at various VOA losses (◇—without ASE). Inset: Gain against the VOA loss.

Fig. 4. Noise figure as a function of input signal power at various VOA losses (◇—without ASE). Inset: Noise figure against the VOA loss.
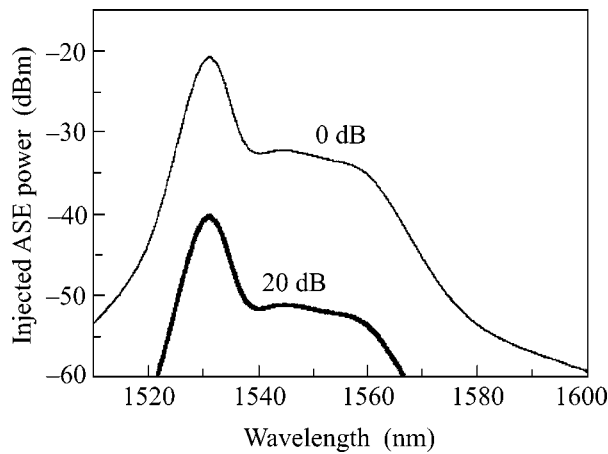
Fig. 5. Injected C-band ASE spectrum at attenuations of 0 and 20 dB.

improvement, this technique also produces almost negligible noise figure penalties, as shown in Fig. 4. However, the gain level is decreased for higher amounts of ASE (<20 dB of attenuation). At attenuation of 0 dB (total ASE power of 6 dBm), the gain is clamped at 15.2 dB from –40 to –10 dBm with gain variation of less than 0.3 dB. The saturation power also increases from –8 dBm (for without ASE injection) to 2 dBm (VOA = 0 dB). The ASE power is measured to be –20 dBm at 1531 nm for attenuation of 0 dB, as shown in Fig. 5. The L-band amplification mechanism is made possible by the intra-Stark level multiphonon transitions and reabsorptions that transfer energy from the short wavelength (C-band) to the longer wavelength (L-band). Therefore, injecting a large amount C-band ASE into EDF depletes the number of ions in the ground state. This limits the population inversion, which in turn reduces gain, thereby clamping the gain. A lower VOA loss enables a higher injected ASE power, which severely degrades the amount of available inversion. The noise figure for the gain clamped amplifier (VOA = 0 dB) is slightly higher at an average value of 5.5 dB, compared to the unclamped amplifier (without injection of ASE). A large amount of injected ASE induces an incomplete population inversion in the EDF as given by the inversion parameter $n_{sp} = \{\sigma_e(\lambda)N_2\}/\{\sigma_e(\lambda)N_2 - \sigma_a(\lambda)N_1\}$, where σ_e is the emission cross section, σ_a is the absorption cross section, N_2 is the population density of the upper state, and N_1 is the population density of the lower state, which leads to the noise figure degradation.

CONCLUSION

The effect of injecting C-band ASE on a L-band EDFA is demonstrated in this paper. Compared to the amplifier without ASE injection, the L-band EDFA has shown a small signal gain improvement of 3.5 dB at attenuation of 20 dB with a negligible noise figure penalty. With the ASE injection at attenuation of 0 dB, the gain of the amplifier is clamped at 15.2 dB from –40 to –10 dBm with gain variation less than 0.3 dB. The saturation power is increased from –8 dBm (for without ASE injection) to 2 dBm (VOA = 0 dB) with slight noise figure penalty. This ASE injection technique has shown a possible application either for gain improvement or for gain clamping in L-band EDFA.

REFERENCES

1. Y. Sun, J. W. Sulhoff, A. K. Srivastava, *et al.*, Electron. Lett. **33**, 1965 (1997).
2. S. W. Harun, P. Poopalan, and H. Ahmad, IEEE Photonics Technol. Lett. **14**, 196 (2002).
3. J. Lee, U.-C. Ryu, S. J. Ahn, and N. Park, IEEE Photonics Technol. Lett. **11**, 42 (1999).
4. T. Subramaniam, M. A. Mahdi, P. Poopalan, *et al.*, IEEE Photonics Technol. Lett. **13**, 785 (2001).
5. S. W. Harun, N. Tamchek, P. Poopalan, and H. Ahmad, Jpn. J. Appl. Phys. **41** (7B), L836 (2002).

Self-Induced Transparency of Circularly Polarized Femtosecond Pulses

A. A. Zabolotskiĭ

Institute of Automatics and Electrometry, Siberian Division, Russian Academy of Sciences,
Universitetskiĭ pr. 1, Novosibirsk, 630090 Russia
* e-mail: zabolotskii@iae.nsk.su
Received March 20, 2003

The phenomenon of self-induced transparency in a two-level medium is studied using a new integrable set of evolution equations for the optical pulses with a duration on the order of the energy-transition oscillation period. A mathematical apparatus is developed for the inverse scattering problem and used to obtain solitonic solutions to the model. The characteristics of linearly and circularly polarized pulses are compared with each other. © 2003 MAIK "Nauka/Interperiodica".

PACS numbers: 42.50.Md; 42.65.Tg; 02.30.Ik

The generation and evolution of femtosecond optical pulses with a characteristic duration close to the oscillation period $2\pi/\omega_0$, where ω_0 is the transition frequency, are of constant interest because of their applications in various areas of physics (see, e.g. reviews [1, 2]). The range of parameters of such pulses is limited by the requirement that photoionization be absent, i.e., that the field amplitude be no larger than $\sim 10^8$–10^9 W/cm and the lower bound for the soliton duration be $\sim 10^{-15}$–10^{-16} s [3, 4]. The conditions for the applicability of a two-level model require that the working transition be well isolated from other transitions [5–8]. These conditions become less stringent if the chosen dipole-transition moment is greater than those for the nearby transitions [4].

In the models used for studying the optical femtosecond range, the approximation of slowly varying field amplitude and phase does not apply, because the pulse duration τ_p comprises several oscillation periods $\tau_p \sim \pi/\omega_0$. Below, these pulses will be referred to as "nearly ultrashort pulses" (NUSPs). The simplifying approximation $\tau_p \ll \pi/\omega_0$ corresponding to the ultrashort pulses (USPs), which was used in some theoretical works, e.g., in [5–8], is unrealistic in the optical range.

The most detailed information on the pulse evolution can be gained in the integrable models by the method of inverse scattering problem (ISP) [9]. Among these are the well-studied Maxwell–Bloch (MB) equations for the dynamics of quasi-monochromatic pulses [2]. The self-induced transparency of a nondegenerate two-level medium was studied for NUSPs in [10], where it was shown that the initial set of equations can be transformed to the reduced MB (RMB) equations, to which the ISP method can be applied. Instead of the slow-envelope approximation, the RMB equations

were derived in [10] using the low-density active-medium approximation, which corresponds to a unidirectional wave propagation. However, these results relate to a linearly polarized field and do not apply to the transitions with a ±1 change in the magnetic quantum number and to the circular NUSP polarization. To my knowledge, the particular solitonic solution found in [7] to the MB equations for a circularly polarized USP in a nondegenerate two-level medium is the only exception. At the same time, the study of many-soliton and other self-similar dynamics of a circularly polarized NUSP is also no less topical. Evidently, the conditions for the applicability of the NUSP theory are much less stringent than for an USP. Moreover, using the results presented below, one can easily show that the theory of NUSP includes the USP theory and the theory of quasi-monochromatic pulses as limiting cases.

In this work, the interaction dynamics between a femtosecond NUSP and a two-level medium consisting of atoms with the σ transition, i.e., with a change in the magnetic quantum number by unity ($\Delta m = \pm 1$), is studied. The corresponding dipole-transition matrix element is complex, $d = d_x \mathbf{e}_x - i d_y \mathbf{e}_y$ [11]. Here, $\mathbf{e}_x$ and $\mathbf{e}_y$ are unit vectors along the x and y axes of the Cartesian coordinate system. The pulse field interacting with the transition is circularly polarized [11].

The corresponding set of Bloch equations for a two-level medium has the form

$$\partial S_x/\partial t = -\omega_0 S_y + \omega_0 f_y \mathscr{E}_y S_z, \tag{1}$$

$$\partial S_y/\partial t = \omega_0 S_x - \omega_0 f_x \mathscr{E}_x S_z, \tag{2}$$

$$\partial S_z/\partial t = \omega_0 (f_x \mathscr{E}_x S_y - f_y \mathscr{E}_y S_x), \tag{3}$$

where $f_{x(y)} = d_{x(y)}\hbar^{-1}\omega_0^{-1}$, ω_0 is the transition frequency, and ε_x and ε_y are the corresponding projections of the electric-field vector. The components of Bloch vector **S** are expressed through the elements of the medium density matrix as $\hat{\rho}$: $S_z = \frac{1}{2}(\rho_{11} - \rho_{22})$, $S_x = \frac{1}{2}(\rho_{12} + \rho_{21})$, and $S_y = \frac{i}{2}(\rho_{12} - \rho_{21})$, where $S_z^2 + S_x^2 + S_y^2 = 1$.

The Maxwell equations for the field components are obtained by projecting onto the corresponding axis,

$$\frac{\partial^2 \mathscr{E}_x}{\partial t^2} - c^2 \frac{\partial^2 \mathscr{E}_x}{\partial z^2} = \frac{4\pi d_x n}{c^2} \frac{\partial^2 S_x}{\partial t^2}, \tag{4}$$

$$\frac{\partial^2 \mathscr{E}_y}{\partial t^2} - c^2 \frac{\partial^2 \mathscr{E}_y}{\partial z^2} = \frac{4\pi d_y n}{c^2} \frac{\partial^2 S_y}{\partial t^2}, \tag{5}$$

where c is the speed of light in a medium with density n.

The density of active atoms or molecules in real media can often be assumed to be small. In such a situation, one can use the familiar hydrodynamic approximation of unidirectional waves. In nonlinear optics, it was used in [10] to derive the reduced MB equations. A low density of active atoms corresponds to the formal approximate equality $\partial_z \approx -c^{-1}\partial_t + \mathbb{O}(\epsilon)$, where ϵ is a small parameter. The normalized density of two-level atoms or molecules is on the same order of smallness as the derivative $\partial_z + c^{-1}\partial_t$ with respect to the field polarization components.

If the condition for unidirectional pulse propagation is fulfilled, the set of Eqs. (1)–(5) reduces to

$$\partial S_x / \partial \tilde{\tau} = -S_y + E_y S_z,$$

$$\partial S_y / \partial \tilde{\tau} = S_x - E_x S_z,$$

$$\partial S_z / \partial \tilde{\tau} = E_x S_y - E_y S_x, \tag{6}$$

$$\partial E_x / \partial \chi = \frac{\partial S_x}{\partial \tilde{\tau}},$$

$$\partial E_y / \partial \chi = r^2 (\partial S_y / \partial \tilde{\tau}),$$

where $r = d_y/d_x$, $E_{x(y)} = f_{x(y)}\mathscr{E}_{x(y)}$, $\tilde{\tau} = \omega_0(t - c^{-1}z)$, and $\chi = z 2\pi n d_x^2 (c\hbar)^{-1}$.

The set of Eqs. (6) is a new integrable set of equations. Its Lax representation $\forall r \in \mathbb{R}$ has the form

$$\partial_{\tilde{\tau}} \Phi = \frac{1}{2} \begin{pmatrix} -i\text{cn}\,\text{dn} & \text{dn}\,E_x - i\text{cn}\,E_y \\ -\text{dn}\,E_x - i\text{cn}\,E_y & i\text{cn}\,\text{dn} \end{pmatrix} \Phi, \tag{7}$$

$$\partial_\chi \Phi = \frac{1}{2\text{sn}^2} \begin{pmatrix} -i\text{cn}\,\text{dn}\,S_z & \text{dn}\,S_x - i\text{cn}\,S_y \\ -\text{dn}\,S_x - i\text{cn}\,S_y & i\text{cn}\,\text{dn}\,S_z \end{pmatrix} \Phi, \tag{8}$$

where sn = $\text{sn}(\zeta, r)$, cn = $\text{cn}(\zeta, r) = \sqrt{1 - \text{sn}^2}$, and dn = $\text{dn}(\zeta, r) = \sqrt{1 - r^2\text{sn}^2}$ are the Jacobi elliptic functions, ζ is the spectral parameter, and r is the module of Jacobi functions.

The algebraic parameterization of the Lax representation is more preferential for the ISP method. It can be obtained for nonoverlapping r values: in the isotropic case, $r^2 = 1$; in the limit of infinite anisotropy, $r = 0$; and in the intermediate case, $r^2 \neq 0, 1$.

In the isotropic case, Eq. (7) reduces to the Kaup–Newell problem [12] with spectral parameter $\lambda = \text{cn} = \text{dn}$, and, for $r = 0$, it amounts to the Zakharov–Shabat problem [9] with the addition $-i\lambda E_y$, where E_y is an arbitrary function of τ.

Let us consider the intermediate case in more detail. For $r^2 \neq 1$ and $r \neq 0$, the following substitution of spectral parameter is possible: $\text{cn}(\zeta, r) = \sqrt{1 - r^2}(\xi - \xi^{-1})(2r)^{-1}$, after which one obtains the following Lax representation of the set (6):

$$\partial_\tau \Phi = \begin{pmatrix} -i\left(\xi^2 - \frac{1}{\xi^2}\right)\xi E^* + \frac{1}{\xi}E \\ -\xi E - \frac{1}{\xi}E^* \quad i\left(\xi^2 - \frac{1}{\xi^2}\right) \end{pmatrix} \Phi, \tag{9}$$

$$\partial_x \Phi = \frac{2r^2(1 - r^2)^{3/2}\xi^2}{4r^2 - [(1 - r^2)\xi^2 - 1 - r^2]}$$

$$\times \begin{pmatrix} -i\frac{a}{r}\left(\xi^2 - \frac{1}{\xi^2}\right)S_z & \xi S^* + \frac{1}{\xi}S \\ -\xi S - \frac{1}{\xi}S^* & i\frac{a}{r}\left(\xi^2 - \frac{1}{\xi^2}\right)S_z \end{pmatrix} \Phi \equiv \hat{A}\Phi, \tag{10}$$

where ξ is the new spectral parameter, $a = \sqrt{1 - r^2}/2$, $E = rE_x/a + iE_y/a$, $S = S_x + iS_y/r$, and $\tau = a^2\tilde{\tau}/(2r)$.

In the theory of integrable systems, the spectral problem (9) likely arises for the first time. However, the corresponding ISP apparatus has much in common with the apparatus developed earlier for the related spectral problems arising when solving the Thirring equation [13], the nonlinear differential Schödinger equation [12], and the set of MB equations taking into account the nonlinear Stark effect [14]. For this reason, we will discuss only the key elements of the ISP apparatus for a potential E that decreases sufficiently quickly at infinity.

The solutions to Eq. (9) possess the following symmetry property:
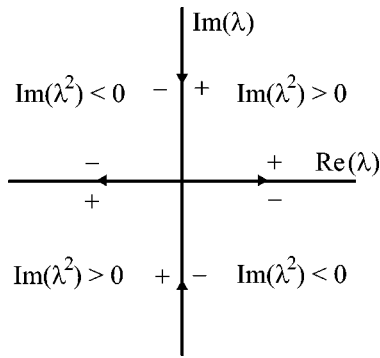
$$\Phi = \hat{M}\Phi(\xi^*)^*\hat{M}^{-1}, \tag{11}$$

Fig. 1. Integration contour Γ.

where

$$\hat{M} = \begin{pmatrix} 0 & 1 \\ -1 & 0 \end{pmatrix}$$

and

$$\Phi(\xi^*)^* = \Phi(\xi^{-1}). \tag{12}$$

Following the standard procedure, we introduce the Jost functions $\Phi^\pm$ (solutions to Eq. (9)) with asymptotic behavior

$$\Phi^\pm = \exp(-i\omega\sigma_3\tau), \quad \tau \longrightarrow \pm\infty, \tag{13}$$

where $\omega = \xi^2 - \xi^{-2}$. Symmetry property (11) corresponds to the following matrix form of the Jost functions:

$$\Phi^\pm = \begin{pmatrix} \psi_1^\pm & -\psi_2^{\pm*} \\ \psi_2^\pm & \psi_1^{\pm*} \end{pmatrix}.$$

These solutions are related by the scattering matrix $\hat{T}$:

$$\Phi^- = \Phi^+\hat{T}. \tag{14}$$

The dependence of scattering data on χ is given by the formula

$$\partial_\chi\hat{T} = -\hat{T}e^{-i\sigma_3\omega\tau}\hat{A}(\tau = -\infty)e^{i\sigma_3\omega\tau}$$
$$+ e^{-i\sigma_3\omega\tau}\hat{A}(\tau = \infty)e^{i\sigma_3\omega\tau}\hat{T}. \tag{15}$$

The Jost function can be represented in the form

$$\Phi^+(\tau) = e^{-i\hat{\sigma}_3[\omega\tau + \mu(\tau)]}$$

$$+ \int_\tau^\infty \begin{pmatrix} [Q_1(\tau, s) + \xi^{-2}Q_2(\tau, s)]e^{-i\mu(\tau)} & -[\xi\tilde{K}_1(\tau, s) + \xi^{-1}K_2(\tau, s)]e^{-i\mu(\tau)} \\ [\xi K_1(\tau, s) + \xi^{-1}\tilde{K}_2(\tau, s)]e^{i\mu(\tau)} & [Q_1^*(\tau, s) + \xi^{-2}Q_2^*(\tau, s)]e^{i\mu(\tau)} \end{pmatrix} e^{-i\hat{\sigma}_3\omega s}ds. \tag{16}$$

Here, $\hat{\sigma}_3$ is the Pauli matrix and $\mu(\tau)$ is a function to be determined below. From the symmetry properties of the Jost functions, it follows that $\tilde{K}_{1,2} = K_{1,2}^*$ and $\mu^* = \mu$.

The kernels $K_{1,2}$ and $Q_{1,2}$ must satisfy the conditions

$$\lim_{s \to \infty} K_{1,2}(\tau, s) = 0, \tag{17}$$

$$\lim_{s \to \infty} Q_{1,2}(\tau, s) = 0. \tag{18}$$

After inserting Eq. (16) into Eq. (9), one obtains the following relation between the potential and kernels:

$$E(\tau, \chi) = -2K_2(\tau, \tau, \chi)\exp(-2i\mu), \tag{19}$$

$$E^*(\tau, \chi) = -2K_1^*(\tau, \tau, \chi)\exp(-2i\mu). \tag{20}$$

By substituting the components of the function Φ in Eq. (14), integrating the resulting expressions with respect to ξ with weights $\xi^m\exp(i\omega\tau)$ ($m = 0, -2$) along the contour Γ shown in Fig. 1, and using the equalities

$$\int_\Gamma \xi^m\exp(i\omega\tau)d\xi = 4\pi\delta(\tau), \quad m = 1, -3, \tag{21}$$

$$\int_\Gamma \xi^m\exp(i\omega\tau)d\xi = 0, \quad m = -1/2, 0, \pm1, \pm2, \ldots, \tag{22}$$

one arrives at the Marchenko equations

$$K_1^*(\tau, y) = F_0(\tau + y)$$
$$+ \int_\tau^\infty [Q_1(\tau, s)F_0(s + y) + Q_2(\tau, s)F_{-1}(s + y)]ds, \tag{23}$$

$$K_2(\tau, y) = F_{-1}(\tau + y)$$
$$+ \int_\tau^\infty [Q_1(\tau, s)F_{-1}(s + y) + Q_2(\tau, s)F_{-2}(s + y)]ds, \tag{24}$$

$$Q_1^*(\tau, y) = -\int_\tau^\infty [K_1(\tau, s)F_1(s + y)$$
$$+ K_2^*(\tau, s)F_0(s + y)]ds, \tag{25}$$

$$Q_2^*(\tau, y) = -\int_\tau^\infty [K_1(\tau, s)F_0(s + y)$$
$$+ K_2^*(\tau, s)F_{-1}(s + y)]ds, \tag{26}$$

where $y \geq \tau$. The kernel F has the form

$$F_m(y, \chi) = \int_{-\infty}^{\infty} \frac{b(\chi)\xi^{2m}e^{-i\omega y}}{a(\chi)} \frac{d\xi}{2\pi} - i\sum_k \frac{\xi_k^{2m}c_k(\chi)e^{-i\omega_k y}}{a'(\xi_k, \chi)}, \quad (27)$$

where $\omega_k = \xi_k^2 - \xi_k^{-2}$.

The simplest solitonic solution corresponds to a single pole ξ_1 lying in the first (third) quadrant and satisfying conditions $E(\pm\infty, \chi) = 0$ and $S_z(0, \chi) = -1$. Due to symmetry property (12), the values of ξ_1 are restricted by the condition $|\xi_1| = 1$. We take $\xi_1 = \exp(i\phi_1)$, where $\phi_1 \in \mathbb{R}$. A one-pole solution to the set of Eqs. (15), (23)–(27) has the form

$$E(\tau, \chi) = \frac{-2|\sin\phi_1|\exp[i\gamma_1 - i\phi_1/2]}{|\cosh[4\sin\phi_1\theta + \gamma_2 - i\phi_1/2]|}, \quad (28)$$

where

$$\theta = \tau - \frac{a\chi}{2\sqrt{r^2\cos^2(\phi_1/2) + \sin^2(\phi_1/2)}},$$

$$\gamma_1 = \arg\frac{-ic_1}{2a'(\xi_1)}, \quad \gamma_2 = \ln\left|\frac{c_1}{2a'(\xi_1)}\right|.$$

Note that no limitations on the range of $\xi_{1,2}$ values arise for the two-pole solution corresponding, e.g., to the spectral parameters $\xi_1^2 = \eta$ and $\xi_2^2 = -\eta^{-1}$.

At large (or small) ξ values, one can pass to the above-mentioned isotropic case. In the limit $r \longrightarrow 1$, $\xi \longrightarrow \infty$, one has $\sqrt{1-r^2}(\xi - \xi^{-1})(2r)^{-1} \longrightarrow \lambda$ and $\xi E^* + \xi^{-1}E \longrightarrow \lambda(E_x - iE_y)$. Accordingly, one should replace dn, cn $\longrightarrow \lambda$ and sn$^2 \longrightarrow 1 - \lambda^2$ in the Lax representation (7), (8). The ISP equations presented above (except for symmetry property (12)) remain valid after the following modification. In Eq. (16), we omit the terms with $m = 1, 2$ powers of ξ^{-m}. Then, in the set of Marchenko Eqs. (23)–(26), only Eqs. (23) and (25) without the last integrands on the right-hand sides are retained.

Instead of relations (19) and (20), one then gets

$$\partial_\tau\mu(\tau, \chi) = 2|K_1(\tau, \tau, \chi)|^2, \quad (29)$$

$$\tilde{E}^*(\tau, \chi) = -2K_1^*(\tau, \tau, \chi)\exp(-2i\mu), \quad (30)$$

where $\tilde{E}^* = E_x - iE_y$.

The one-soliton solution corresponding to a single eigenvalue $\lambda_1 = |\lambda_1|e^{i\alpha_1}$ lying in the first (third) quadrant in the λ plane has the form

$$\tilde{E}_c(\tau, \chi) = \frac{-2\text{Im}\lambda_1^2 e^{[i(\text{Re}\lambda_1^2\tau + W\chi + \gamma_1 - \alpha_1 - 2\mu)]}}{|\lambda_1|\cosh[\text{Im}\lambda_1^2(\tau - \chi/V) + \beta_1 + i\alpha_1]}, \quad (31)$$

where

$$V = (1 - \text{Re}\lambda_1^2)^2 + (\text{Im}\lambda_1^2)^2,$$

$$W = [\text{Re}\lambda_1^2(1 - \text{Re}\lambda_1^2) - (\text{Im}\lambda_1^2)^2]V^{-1},$$

$$\beta_1 = \ln|(\lambda_1 c_1)/(4\text{Im}\lambda_1^2 a'(\lambda_1))|,$$

$$\mu = -\arctan\left\{\cot\alpha_1\coth\left[\text{Im}\lambda_1^2\left(\tau - \frac{\chi}{V}\right) + \beta_1\right]\right\}$$

$$\times \frac{2\text{Im}\lambda_1^2}{|\lambda_1^2|\sin(2\alpha_1)}.$$

Let us compare solitonic solution (31) for a circularly polarized wave with the familiar solution for the analogous linearly polarized solitary electromagnetic wave propagating through a two-level medium. The corresponding solitonic solution to the RMB equations (see, e.g., [10]) is

$$\tilde{E}_l(\tau, z) = \frac{2\text{Im}\eta_1}{\cosh[\text{Im}\eta_1(\tau - \tau_0 - z/V_0)]}, \quad (32)$$

where $(\text{Im}\eta_1)^{-1}$ is the soliton duration, $(c^{-1} + V_0^{-1})^{-1}$ is its group velocity, and τ_0 is the position at zero time. Let us take, for the sake of comparison, the same durations for solitons (31) and (32): $\eta_1 = \lambda_1^2$ and $|\lambda_1| = 1$. An analysis of the corresponding solution showed that, if $\text{Im}\lambda_1^2 \ll \text{Re}\lambda_1^2$, the soliton amplitudes are close. For $\text{Im}\lambda_1^2 = \text{Re}\lambda_1^2$, the maximal intensity I_c of soliton (31) is twice as high as the maximal intensity I_l of soliton (32). For $\text{Im}\lambda_1^2 \gg \text{Re}\lambda_1^2$, it was found that $I_c \gg I_l$ (Fig. 2).

Therefore, it has been shown that σ transitions and circularly polarized electromagnetic pulses can be used to generate pulses with an intensity that is appreciably higher than for linearly polarized pulses of the same
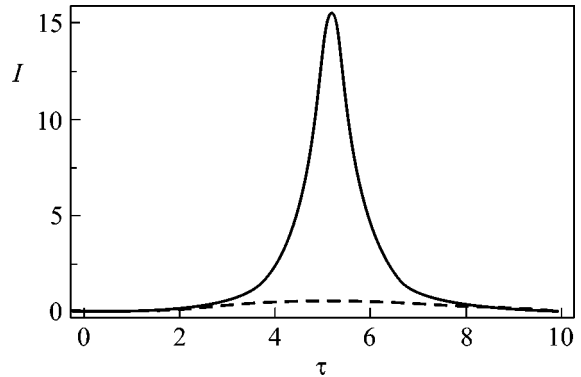

Fig. 2. Soliton intensity $I = |E|^2$ as a function of τ for (solid line) circularly and (dashed line) linearly polarized light; $\lambda_1 = (0.2 + i)/1.04$.

duration. The reverse statement is also true: the duration of circularly polarized pulses is shorter than the duration of linearly polarized pulses with the same maximal amplitude. To produce pulses with such characteristics, it is necessary that the phase of the initial pulse be close to $\alpha_1 \approx \pi/2$. The required parameters of a pulse injected into the medium can easily be determined by solving Eq. (9).

To observe the pulses, the requirements imposed, e.g., on the NUSP intensity, are at least two orders of magnitude less stringent than for the USPs [5–7]. Due to the narrower NUSP spectrum, the requirements on the applicability of a two-level medium are also milder than for USPs.

Note in conclusion that the new integrable model and the ISP apparatus suggested in this work can be used for the description of transverse acoustic waves in a paramagnetic crystal containing impurities with spin 1/2 and for the description of pulse dynamics of a transverse magnetic field in a crystalline magnet with low spin density and orthorhombic symmetry.

REFERENCES

1. T. Brabec and F. Krausz, Rev. Mod. Phys. **72**, 545 (2000).

2. A. I. Maĭmistov, Kvantovaya Élektron. (Moscow) **30**, 287 (2000).

3. D. You, D. R. Dykaar, and P. H. Bucksbaum, Opt. Lett. **18**, 290 (1993).

4. M. Wittmann, A. Nazarkin, and G. Korn, Opt. Lett. **26**, 5 (2001).

5. É. M. Belenov, P. G. Kryukov, A. V. Nazarkin, *et al.*, Pis'ma Zh. Éksp. Teor. Fiz. **47**, 442 (1988) [JETP Lett. **47**, 523 (1988)].

6. É. M. Belenov, A. V. Nazarkin, and V. A. Ushchapovskiĭ, Zh. Éksp. Teor. Fiz. **100**, 762 (1991) [Sov. Phys. JETP **73**, 422 (1991)].

7. S. V. Sazonov and E. V. Trifonov, J. Phys. A: Math. Gen. **27**, L7 (1994).

8. A. Yu. Parkhomenko and S. V. Sazonov, Zh. Éksp. Teor. Fiz. **114**, 1393 (1998) [JETP **87**, 864 (1998)].

9. V. E. Zakharov, S. V. Manakov, S. Novikov, and L. P. Pitaevskiĭ, *Theory of Solitons: the Inverse Scattering Method* (Nauka, Moscow, 1980; Consultants Bureau, New York, 1984).

10. J. D. Gibbon, P. J. Coudrey, J. K. Eilbeck, and R. K. Bullough, J. Phys. A: Math. Gen. **6**, 1237 (1973).

11. L. Allen and J. H. Eberly, *Optical Resonance and Two-Level Atoms* (Wiley, New York, 1975; Atomizdat, Moscow, 1978).

12. D. J. Kaup and A. C. Newell, J. Math. Phys. **19**, 798 (1978).

13. E. A. Kuznetsov and A. V. Mikhaĭlov, Teor. Mat. Fiz. **30**, 303 (1977).

14. A. A. Zabolotskiĭ, Zh. Éksp. Teor. Fiz. **107**, 1100 (1995) [JETP **80**, 614 (1995)].

Translated by V. Sakun

Amplification of Two-Mode Squeezed Light in the Einstein–Podolsky–Rosen State

V. N. Gorbachev and A. I. Trubilko

Laboratory of Quantum Information and Calculations, St. Petersburg State University of Aerospace Instrument Engineering, Bol'shaya Morskaya ul. 67, St. Petersburg, 190000 Russia

Received April 3, 2003

Two schemes for amplifying two-mode squeezed light in the Einstein–Podolsky–Rosen state, where quantum correlations are conserved due to the presence of integrals of motion, while the power of each wave can increase, are considered. The first scheme is based on the parametric three-photon interaction in a transparent nonlinear medium. The second scheme is a variant of the resonance interaction with an atomic ensemble. © 2003 MAIK "Nauka/Interperiodica".

PACS numbers: 42.50.Dv; 42.50.Gy; 03.65.Ud

INTRODUCTION

The nonclassical states of light represent optical implementation of entangled states, which are at the basis of quantum information processes. In particular, the well-known two-mode squeezed light in quantum optics is a continuous analogue of the Einstein–Podolsky–Rosen (EPR) state of a pair [1]. This light possesses quantum correlation which can easily be destroyed by interactions. Because of this, only certain transformations can conserve its properties. In particular, it is difficult to amplify nonclassical light. An ordinary linear amplifying medium was shown to destroy the squeezed state owing to the noise induced by spontaneous radiation [2, 3]. This is also true for nonlinear amplification [4] and light propagation through an amplifying communication channel [5]. At the same time, nonclassical light can be converted from one frequency to another [6].

In this work, we consider the possibility of amplifying two-mode squeezed light in the continuous-variable EPR state, which can be obtained using an optical parametric oscillator. This is precisely the light that was used as a quantum channel for the teleportation of a coherent state of an electromagnetic field [7], for dense coding [8], and for spectroscopy with nonclassical light [9]. The light intensity in these experiments was low. The main idea of amplification is based on the existence of certain integrals of motion in the light interaction with a medium. Since the entangled or squeezed states can be eigenstates of operators that, in turn, are integrals of motion, the degree of entanglement or the character of quantum correlation is conserved, whereas the light intensity can increase. An example of the interaction conserving certain properties of squeezed light upon amplification was given in [10]. A special thermostat with a collective resulting in the atomic entangled state and, hence, conserving it, was considered in [11].

At the same time, if light propagates in a quantum channel with a phase-sensitive environment, where squeezed vacuum plays the role of a thermostat, the degradation of entangled states is not retarded [12].

In this work, two schemes for amplifying two-mode squeezed light in the entangled state are considered. The first scheme is based on the parametric three-photon interaction in a transparent nonlinear medium. The second scheme is based on the resonance interaction with an atomic ensemble. A distinguishing feature of these schemes is that they do not create entangled states but conserve the degree of correlation or entanglement between modes. In this case, light intensity can increase. This is a direct consequence of the existence of integrals of motion due to which two problems—conservation of certain properties and amplification—are solved. In this work, we use the time description for the evolution. However, this approach can be immediately extended to the propagation process by using, e.g., quantum formalism of transport theory, which was presented in [13], where, in particular, it was discussed what information can be gained from the integrals of motion in the multiphoton parametric processes.

This paper is organized as follows. We first discuss the definition of the EPR entangled state of a pair for the case of continuous variables and its implementation by two-mode squeezed light and then consider the schemes with parametric interaction in a transparent medium and resonance interaction with an atomic ensemble.

2. TWO-MODE SQUEEZED LIGHT AND ENTANGLED STATE

In the case of continuous variables, there are two possible definitions of a state of the EPR-pair type. First, it is defined as the eigenfunction of the operators

of the total momentum P and the coordinate difference Q of the two subsystems. Second, it is specified in terms of the Heisenberg P and Q operators at the exit of an optical parametric oscillator. For optical implementation, where the measured quantities, such as dispersions of the P and Q observables, are important, both approaches lead to a two-mode squeezed light.

The operators of the relative positions and the total momentum of two subsystems or two particles can be defined as

$$Q = x_1 - \epsilon x_2, \quad P - p_1 + (1/\epsilon)p_2, \qquad (1)$$

where x_m and p_m are the canonical operators of the coordinate and momentum of the mth particle ($m = 1$ and 2), respectively, and ϵ is a real number. The observables P and Q have a common complete set of eigenfunctions known as Bell continuous states [14]:

$$Q|\Psi_{PQ}\rangle = \mathcal{Q}|\Psi_{PQ}\rangle, \quad P|\Psi_{PQ}\rangle = \mathcal{P}|\Psi_{PQ}\rangle. \qquad (2)$$

If the eigenvalues are equal to zero, a continuous analogue of the entangled EPR pair arises:

$$|\Psi_{00}\rangle = |EPR\rangle. \qquad (3)$$

A simple model of a nondegenerate parametric oscillator can be described by the effective Hamiltonian $H = i\chi\hbar(a_1^\dagger a_2^\dagger - \text{h.c.})$, where χ is the coupling constant proportional to the squared susceptibility of the nonlinear medium and $a_m^\dagger$ and a_m ($m = 1, 2$) are the operators of creation and annihilation of the mth mode, respectively. The solution to the problem for the operators $Z = P$ and Q in the Heisenberg representation has the form $Z = Z_0\exp(-\epsilon r)$, where $\epsilon = \pm 1$, Z_0 are the output operators of the parametric oscillator and r is the squeezing parameter. Independently of the state of a field generated at the entry, the EPR pair arises if $r \longrightarrow \infty$. It can be defined in terms of the properties of the P and Q operators, for which

$$Q \longrightarrow 0, \quad P \longrightarrow 0. \qquad (4)$$

This state corresponds to an ideal EPR pair, which is not implemented experimentally because r takes a certain fixed value. Two independent sources generating independent quadrature-squeezed fields in the process of the degenerate parametric transformation described by the Hamiltonian $H = ik\hbar(a^{\dagger 2} - \text{h.c.})$ can be used as another model of a source of an entangled photon pair with similar properties [15]. The EPR state arises upon mixing such light fields in a beamsplitter.

Light in quantum optics is often described using the quadrature operator

$$X(\theta) = a^\dagger\exp(i\theta) + \text{h.c.} = 2(x\cos\theta + p\sin\theta), \quad (5)$$

where $a = x + ip$ is the photon annihilation operator, $[a; a^\dagger] = 1$, and $[x; p] = i/2$. The properties of light can be determined from the set of its correlation functions, in particular, from the dispersions of the quadrature operator $\langle(\Delta X)^2\rangle = \langle X^2\rangle - \langle X\rangle^2$, whose measurement is a

well-known procedure. In particular, $\langle(\Delta X)^2\rangle = 1$ for a coherent state minimizing the uncertainty relation and serving as a boundary between classical and nonclassical (or quantum) states of an electromagnetic field.

However, if

$$\langle(\Delta X(\theta))^2\rangle < 1, \qquad (6)$$

light is called squeezed. More precisely, such a state is squeezed over coordinate or amplitude if $\theta = 0$ and is squeezed over momentum or phase if $\theta = \pi/2$. The limiting squeezing corresponds to $\langle(\Delta X(\theta))^2\rangle = 0$. The terms "amplitude" and "phase" are used in considering the properties of light in the phase space and not for the observables of the amplitude and phase type.

The introduced quadrature operator is measured in the scheme of heterodyne reception. In this scheme, the signal under investigation mixes with the reference wave in a semitransparent mirror, whereupon the difference photocurrent i from two detectors is measured. If the quantum efficiencies of both detectors are the same and equal to unity, the spectrum of the photocurrent or light noises is determined through the dispersion of the quadrature operator

$$i^2(\omega) = \int_{-\infty}^{\infty} d\tau \langle i(t)i(t+\tau)\rangle \exp(i\tau\omega)$$

$$= \int_{-\infty}^{\infty} d\tau \langle X(t)X(t+\tau)\rangle \exp(i\tau\omega). \qquad (7)$$

In many quantum-optical models, the spectrum of low-frequency noise is determined by the expression

$$i^2(\omega \approx 0) = 1 + \langle:(\Delta X(\theta))^2:\rangle, \qquad (8)$$

where 1 corresponds to the shot noise level or to the standard quantum limit and the colon means the normal ordering of operators. As follows from Eqs. (6) and (8), the noise level of squeezed light is lower than for the shot noise, which can, in principle, be suppressed almost completely. This is one of the known basic properties of this state, which makes it attractive for, e.g., precision measurements.

The operators of the total momentum P and relative positions Q defined by Eq. (1) can be represented in terms of the quadrature operators X_m for two modes ($m = 1$ and 2) of the electromagnetic field as

$$Q = (1/2)[X_1(0) - \epsilon X_2(0)],$$
$$P = (1/2)[X_1(\pi/2) + (1/\epsilon)X_2(\pi/2)]. \qquad (9)$$

Both observables P and Q can be measured by the use of a beamsplitter mixing two modes followed by the measurement of the canonical momentum and coordinates of two outgoing beams [7]. As follows from Eqs. (2) and (4), the dispersions of the observables P and Q are equal to zero. Therefore, according to Eqs. (6) and (8), the Bell continuous states $|\Psi_{PQ}\rangle$ or the states at the

exit of a parametric oscillator are squeezed with respect to the coordinate difference and the total momentum with suppressed shot noise. Thus, squeezed states are entangled. However, squeezing or the presence of a nonclassical state of fields is only the necessary condition. At the same time, if the state is entangled, the level of shot-noise suppression can be taken as a measure of entanglement.

3. AMPLIFICATION IN A TRANSPARENT MEDIUM WITH QUADRATIC NONLINEARITY

Let the interaction between two modes be described by the Hamiltonian

$$V = \hbar k P Q, \qquad (10)$$

where k is the real coupling constant. In this case, the operators of the total momentum P and the relative position Q, as well as any functions of these variables, are integrals of motion. Let the initial light state be specified by the EPR pair, which can be obtained using a parametric oscillator. For this pair, $Z(t = 0) = Z_0\exp(-\epsilon r)$, where $Z = P$ and Q. Therefore, $Z(t) = Z(0)$. At the same time, any eigenfunctions of the integrals of motion $Z = P$ and Q also do not change. In particular, entangled states $|\Psi_{PQ}\rangle$ are conserved because their evolution reduces to the multiplication by the phase factor:

$$\exp(-i\hbar^{-1}Vt)|\Psi_{PQ}\rangle = \exp(-ik\mathcal{P}\mathcal{Q}t)|\Psi_{PQ}\rangle.$$

The conservation of quantum correlation does not hinder the variations of the state of each mode during the process of interaction. To describe the mode evolution, we use the Heisenberg equations of motion. In the interaction representation, these equations for the operators of momenta and coordinates have the form

$$\frac{\partial}{\partial t}x_1 = \frac{1}{2}kQ, \quad \frac{\partial}{\partial t}p_1 = -\frac{1}{2}kP,$$

$$\frac{\partial}{\partial t}x_2 = \frac{1}{2\epsilon}kQ, \quad \frac{\partial}{\partial t}p_2 = \frac{\epsilon}{2}kP.$$

Using these equations, one can easily obtain the following equations for the operators of the number of photons ($n_m = x_m^2 + p_m^2 - 1/2$) in the waves:

$$\frac{\partial}{\partial t}n_1 = k(Qx_1 - Pp_1), \quad \frac{\partial}{\partial t}n_2 = k\left(Q\frac{x_2}{\epsilon} + \epsilon Pp_2\right). (11)$$

Solutions to Eqs. (11) have the form

$$n_1(t) = n_{10} + \mu^2(Q^2 + P^2) + 2\mu(Qx_{10} + Pp_{10}),$$

$$n_2(t) = n_{20} + \mu^2\left(\frac{Q^2}{\epsilon^2} + P^2\epsilon^2\right) + 2\mu\left(Q\frac{x_{20}}{\epsilon} + Pp_{20}\epsilon\right),$$

where Y_{m0} ($m = 1$ and 2) are the operators at the initial time and $\mu = kt/2$.

If the maximally squeezed and entangled state specified by Eq. (4) is present at the entry, amplification

does not arise. In other cases, amplification proportional to μ^2 can occur. We illustrate this by the examples of model sources based on an optical parametric oscillator with the initial vacuum states. Under real experimental conditions, the squeezing parameters of the parametric oscillator take a certain finite value r. Then, the average number of photons in the entangled waves incident on the amplifying medium is given by $\langle n_{m0}\rangle = \sinh^2 r$, and the dispersions of the coordinate and momentum are given by the expressions $\langle(\Delta Q(0))^2\rangle = \langle(\Delta P(0))^2\rangle = 1/2\exp(-2r)$. The gain $K = (\langle n_m(t)\rangle/\langle n_{m0}\rangle)$ is expressed as $K = 1 + 4\mu^2(\exp(2r) - 1)^{-2}$. For the ideal case, $r \longrightarrow \infty$ and the amplification does not occur ($K \longrightarrow 1$). In this case, the medium serves as an ideal quantum repeater, which can be important for ensuring the properties of the propagated EPR pair, because the interaction with environment destroys it. In a real case, r is fixed, and the smaller the squeezing parameter, the larger the gain. At $r \longrightarrow 0$, the amplifier transforms to a field generator from the vacuum state. However, this generator does not generate EPR pairs or two-mode light squeezed in P and Q. The dispersions of the vacuum input state $\langle(\Delta P)^2\rangle = \langle(\Delta Q)^2\rangle = 1/2$ is conserved in time, although the mean numbers of photons in the modes are $\langle n_m(t)\rangle = \mu^2 \neq 0$.

However, the question arises as whether Hamiltonian (10) describe any real processes or not. To answer this question, we write the Hamiltonian in terms of the operators of mode creation and annihilation:

$$\begin{aligned} V = i\frac{k}{4}[&a_1^{\dagger 2} - a_1^2 - a_2^{\dagger 2} + a_2^2 \\ &+ (1/\epsilon)(a_1^\dagger a_2^\dagger - a_1 a_2)(1 - \epsilon^2) \\ &+ (1/\epsilon)(a_1 a_2^\dagger - a_1^\dagger a_2)(1 + \epsilon^2)]. \end{aligned} \qquad (12)$$

For $\epsilon = \pm 1$, Hamiltonian (12) describes three-photon parametric interactions in a transparent medium with quadratic nonlinearity. Indeed, this formula presents three processes of frequency conversion. Two of them are frequency division in a classical pumping field $\Omega_m = \omega_m + \omega_m$ and one process is the frequency up-conversion $\Omega + \omega_1 = \omega_2$, where Ω_m and Ω are the frequencies of the classical pumping waves and ω_m are the frequencies of the $m = 1$, 2 modes. For these three interactions to be efficient, the phase-matching conditions must be satisfied, which can be ensured in nonlinear periodic media discussed in [16]. Following [17], we estimate the intensity of the classical field used to pump the processes under consideration. The squeezing parameter in real experiments corresponds to the value $\exp(2r) \approx 5$. Let the gain be $K = 10$; under these conditions, the dimensionless parameter is $\mu = 6$. These can be achieved in crystals with a length of several centimeters if the wavelength of the amplified light is, e.g., $\lambda = 0.5$ μm and the pump power is $I \approx 10^4$ W/cm², which is experimentally quite realizable.

4. AMPLIFICATION IN THE RESONANCE MEDIUM

We consider the resonance interaction of N identical two-level atoms with the electromagnetic field. This interaction is described by the effective Hamiltonian

$$H = i\hbar\vartheta, \quad \vartheta = S_{10}B - S_{01}B^{\dagger}. \tag{13}$$

Here, the atomic operators are determined by the expression

$$S_{xy} = \sum_a s_{xy}(a), \quad s_{xy}(a) = |x\rangle_a\langle y|, \quad x, y = 0, 1,$$

where $|0\rangle_a$ and $|1\rangle_a$ are the ground and excited levels of atom a, respectively, and the field enters through the operators B and $B^{\dagger}$.

Let three modes with frequencies $\omega_m (m = 1, 2, \text{ and } 3)$ described by the operators a_m interact with the atomic transition. The frequencies are related to the transition frequency ω as $\omega_1 = \omega_0$ and $\omega_3 - \omega_2 = \omega_0$. In this case, $B = ga_1 - fa_3 a_2^{\dagger}$, where g and f are the coupling constants. Let the ω_3 mode be classical. Then, $B = g(a_1 + \nu a_2^{\dagger})$, where $\nu = fa_3/g$. Taking $\nu = \epsilon = \pm 1$, we obtain

$$B = g(a_1 - \epsilon a_2^{\dagger}) = Q + iP,$$
$$B^{\dagger} = g(a_1^{\dagger} - \epsilon a_2) = Q - iP. \tag{14}$$

For this interaction, where $\epsilon^2 = 1$, P and Q are integrals of motion. Therefore, the quantum correlation of the EPR pair is conserved.

To determine the possibility of amplification, we write the kinetic equation for the density matrix ρ of electromagnetic field. In the lowest order with respect to interaction, this equation has the form

$$\frac{\partial}{\partial t}\rho = -\frac{N_0}{\gamma_{\perp}}(B^{\dagger}B\rho - B\rho B^{\dagger} + \text{h.c.})$$
$$-\frac{N_1}{\gamma_{\perp}}(BB^{\dagger}\rho - B^{\dagger}\rho B + \text{h.c.}), \tag{15}$$

where N_0 and N_1 are the populations of the lower and upper working levels, respectively, and $\gamma_{\perp}$ is the transverse-relaxation constant. The equations

$$\frac{\partial}{\partial t}\langle n_1\rangle = \frac{g^2}{\gamma_{\perp}}(N_1 - N_0)(\langle n_1\rangle - \langle n_2\rangle + \langle BB^{\dagger}\rangle)$$
$$+ \frac{g^2}{\gamma_{\perp}}(N_0 + N_1), \tag{16}$$

$$\frac{\partial}{\partial t}\langle n_1\rangle - \frac{\partial}{\partial t}\langle n_2\rangle = \frac{2g^2}{\gamma_{\perp}}(N_1 - N_0)\langle BB^{\dagger}\rangle$$

for the average numbers of photons follow from Eq. (15). Here, two amplification regimes are also possible. In particular, if $N_1 = N_0$, then, independently of the presence of initial correlations between the incident waves, the interaction of the incident waves in the medium results in the amplification at the inversionless working transition. In this case, the average number of

photons in each wave increases proportionally to the total number of atoms, and the difference of the numbers of photons is conserved. Due to the existence of quantum-correlated waves such as the EPR pair, for which relations (4) are fulfilled, the condition $\langle BB^{\dagger}\rangle = 0$ is met. In this case, light is amplified in each component of the overall light field. The average number of photons in these components is determined by the expression $\langle n_m\rangle = \langle n_{m0}\rangle + (g^2t/\gamma_{\perp})((N_1 - N_0)(\langle n_{10}\rangle - \langle n_{20}\rangle)) + N_1 + N_0)$. Therefore, if the initial numbers of photons are identical, each wave is amplified, and the correlation between waves is conserved.

In this work, two schemes for amplifying two-mode squeezed light with quantum intermode correlation are presented. The initial EPR-type quantum correlations are conserved due to the existence of integrals of motion. We emphasize that these schemes are close to the current experiments but are nontrivial because they themselves do not generate the EPR-type correlated light modes.

REFERENCES

1. A. Einstein, B. Podolsky, and N. Rosen, Phys. Rev. **47**, 777 (1935).
2. C. M. Caves, Phys. Rev. D **26**, 1817 (1982).
3. M. I. Kolobov and I. V. Sokolov, Opt. Spektrosk. **63**, 958 (1987) [Opt. Spectrosc. **63**, 562 (1987)].
4. V. N. Gorbachev and A. I. Trubilko, Zh. Éksp. Teor. Fiz. **102**, 1441 (1992) [Sov. Phys. JETP **75**, 781 (1992)].
5. M. Paris, J. Opt. B **4**, 442 (2002).
6. V. N. Gorbachev and A. I. Trubilko, Zh. Éksp. Teor. Fiz. **103**, 1931 (1993) [JETP **76**, 956 (1993)].
7. A. Furusawa, J. L. Sorensen, S. L. Braunstein, *et al.*, Science **282**, 706 (1998).
8. X. Li, Q. Pan, J. Jing, *et al.*, quant-ph/0107068.
9. B. E. A. Saleh, B. M. Jost, H.-B. Fei, and M. C. Teich, Phys. Rev. Lett. **80**, 3483 (1998).
10. V. N. Gorbachev and A. I. Trubilko, Opt. Spektrosk. **84**, 970 (1998) [Opt. Spectrosc. **84**, 879 (1998)].
11. A. M. Basharov, Zh. Éksp. Teor. Fiz. **121**, 1249 (2002) [JETP **94**, 1070 (2002)].
12. D. Wilson, Jinhyong Lee, and M. S. Kim, quant-ph/0206197 (2001).
13. V. N. Gorbachev and A. I. Zhiliba, J. Phys. A: Math. Gen. **33**, 371 (2000).
14. S. L. Brauntstein and H. J. Kimble, Phys. Rev. Lett. **80**, 869 (1998).
15. P. van Loock and S. L. Braunstein, Phys. Rev. Lett. **84**, 3482 (1998).
16. A. S. Chirkin, V. V. Volkov, G. D. Laptev, and E. Yu. Morozov, Kvantovaya Élektron. (Moscow) **30**, 847 (2000).
17. A. V. Nikandrov and A. S. Chirkin, Pis'ma Zh. Éksp. Teor. Fiz. **76**, 333 (2002) [JETP Lett. **76**, 275 (2002)].

Translated by R. Tyapaev

Overheated Plasma at the Surface of a Target with a Periodic Structure Induced by Femtosecond Laser Radiation

R. V. Volkov, D. M. Golishnikov, V. M. Gordienko, and A. B. Savel'ev

International Laser Center, Moscow State University, Vorob'evy gory, Moscow, 119992 Russia

Received March 24, 2003

A periodic structure is induced at the surface of a metal target exposed to a series of *p*-polarized 200-femtosecond laser pulses with intensity close to the melting threshold of the target material. The period of the structure is determined by the interference between the incident pump wave and the surface electromagnetic wave. Exposure of the obtained structure to the same laser pulse, but with an intensity of $\sim 10^{16}$ W/cm^2, provides resonant excitation of the surface electromagnetic waves at the plasma–vacuum interface. This leads to an increase in the X-ray output and the temperature of plasma hot electrons. © *2003 MAIK "Nauka/Interperiodica".*

PACS numbers: 52.50.Jm; 52.38.-r; 52.25.Os

1. The plasma produced at the surface of a solid target by superstrong laser radiation with an intensity $I \sim 10^{16}$–10^{17} W/cm^2 is a source of subpicosecond hard X-ray bursts with the energy spectrum determined by the temperature of plasma hot electrons. The energy of X-ray quanta can reach 0.1 MeV [1]. It was shown in [2, 3] that the use of special targets made it possible to enhance the conversion efficiency of femtosecond laser radiation into X-ray emission and increase the temperature of hot electrons without increasing the intensity of heating radiation. In particular, this can be achieved using diffraction gratings or other periodic surface structures as a target. The exposure of such targets to femtosecond laser pulses results in the excitation of surface electromagnetic waves (SEWs) at the plasma–vacuum interface [4]. The reason is that the plasma exposed to an ultrashort pulse has no time to expand, so that the plasma boundary remains rather sharp. The SEW excitation is accompanied by the enhancement of a local electromagnetic field at the target surface, which is equivalent to an increase in the heating radiation intensity. This, in turn, leads to the amplification of various effects nonlinear in intensity, in particular, to an increase in the energy of the second harmonic generated by the superintense radiation reflected from the plasma surface [5]. The X-ray emission from plasma is also expected to undergo a considerable increase in the conversion efficiency Y_x and a shift toward higher energies due to an increase in the hot-electron temperature T_{hot}, because both of these quantities are proportional to the laser intensity [6].

Since the efficiency of conversion to X-ray emission increases with increasing atomic number of the target material [7], it is best to use gratings produced in materials with a high atomic number. However, conventional methods cannot produce diffraction gratings at an arbitrary material. The exposure of a target to laser radiation with intensity slightly exceeding the melting threshold can result in the generation of periodic structures at the target surface [8]. In particular, such structures were observed in dielectrics, semiconductors, and semimetals exposed to femtosecond pulses [9–11].

Interference at the target surface between the SEW excited by vacuum pump wave and the pump itself is one of the mechanisms for generating periodic surface structures [8]. Because of this, the interference pattern produced on the target surface has a period that provides resonant SEW excitation by the same vacuum wave. For metal and plasma, the difference between the SEW wave vectors is insignificant [5]. Therefore, a periodic structure produced by low-intensity laser radiation is also resonant for the superintense laser radiation used for producing plasma and exciting SEW at its boundary, provided that the wavelength, polarization, and the angle of incidence on the target do not change.

The goal of this work was to show that femtosecond laser radiation can be used for generating periodic structures on the surface of a metal target. It was also shown that the X-ray output and the hot-electron temperature increase upon the resonant SEW excitation on the periodic structures obtained at the plasma–vacuum interface.

2. The intensity of femtosecond laser radiation with an energy of several hundreds of μJ was reduced in our experiments by defocusing to a level that was slightly higher than the target melting threshold. A series of laser pulses gave rise to a periodic structure at the target surface. Then, the laser radiation was again tightly focused to produce plasma at the surface of the resulting structure.

The scheme of experimental setup is shown in Fig. 1. A Johansson plate with the iron surface as a target was placed into a vacuum chamber pumped down to a residual pressure of 10^{-2} Torr. *p*-Polarized laser pulses
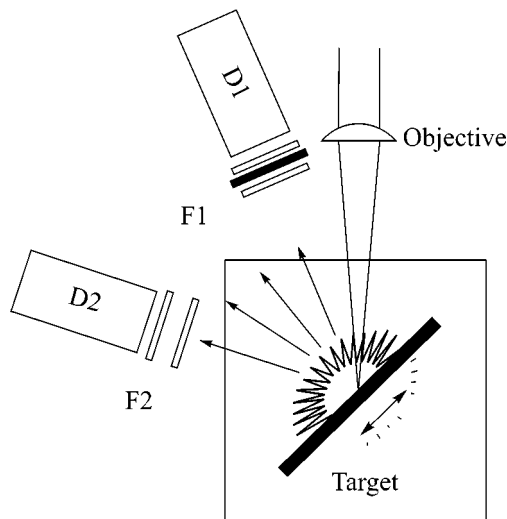
VOLKOV *et al.*

Fig. 1. Scheme of the experimental setup. Laser radiation with a duration of 200 fs and an energy of ~300 μJ was focused on a metal target using an aberration-free objective lens. The plasma X-ray emission was measured by detectors $D1$ and $D2$. Sets of X-ray filters $F1$ and $F2$ were used to select the range of measured X-ray output.

with a wavelength of 610 nm, an energy of 300 μJ, and a duration of 200 fs were focused by an aberration-free objective lens. To produce the periodic structures, the focus of the objective lens was shifted by 300 μm from the target surface, so that the radiation intensity became ~10^{12} W/cm^2. The angle of incidence on the target was 45°. The results of 15 successive irradiations of a fixed target are shown in Fig. 2. The period of the structure obtained was approximately 330 nm. Profilometric measurements showed that the grating amplitude ranged from 40 to 80 nm.

The periodic structure was exposed to the same laser radiation focused to an intensity of ~10^{16} W/cm^2. X-ray

detectors $D1$ and $D2$ (Fig. 1) and sets of X-ray filters $F1$ (100 μm of beryllium and 100 μm of Al) and $F2$ (100 μm of beryllium, 300 μm of Al, and 13 μm of Ta) were used to measure the X-ray output in different spectral ranges and estimate the hot-electron temperature for each laser pulse by the filter method [7]. The results of these measurements are shown in Figs. 3 and 4. The same results, but for a flat target, are also shown in these figures. It is seen that, for the grating, the X-ray output in the energy range above 7 keV is two to three times greater than for the flat target. In the range above 20 keV, the grating provides a fourfold increase in the X-ray output. This indicates an increase in the temperature of hot electrons that are responsible for the generation of hard X-ray radiation (Fig. 4).

3. The period of the structure is determined by the interference between the SEW generated by vacuum pump wave and the pump light itself at the target surface [8]. The surface electromagnetic waves are excited due to the diffraction of pump radiation by the original rough surface of the target. The period d of the interference pattern at the target surface is

$$d = 2\pi/(k_p \pm k_0 \sin\theta), \tag{1}$$

where k_p and k_0 are the SEW and pump wave vectors, respectively, and θ is the pump incidence angle. The period d provides resonant SEW excitation by the same vacuum wave. The sign in Eq. (1) depends on the diffraction order. If the pump intensity exceeds the melting threshold, the amplitude of resonant periodic structure increases with each successive irradiation because of a considerable loss of the target material at the sites of interference maxima. In our case, the period of the structure is equal to the smaller of the two possible values determined by Eq. (1), because the structure with a smaller period has a greater growth increment [12].

The measured increase in the X-ray output and the hot-electron temperature on a periodic structure, com-
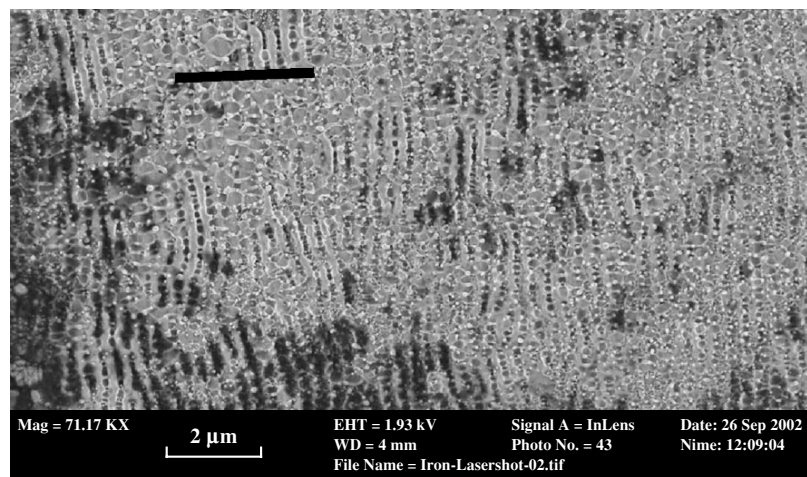

Fig. 2. Image of the laser-induced grating obtained using a LEO1550 electron microscope. The black line indicates the approximate direction of the projection of the pump-wave electric-field vector on the target surface.

pared to the usual flat target, allows the estimation of the increase in a local field induced by SEW excitation. Indeed, the conversion efficiency into X-ray emission in the spectral range measured in the experiment is proportional to the squared laser intensity: $Y_x \sim I^2 \sim L^4 I_0^2$ [6]. Here, I is the laser intensity at the target surface. It is related to the pump wave intensity by $I = L^2 I_0$, where L is the local-field amplification factor. Thus, the factor L can be estimated by the formula $L \sim (Y_x(\text{grating})/Y_x(\text{flat}))^{1/4}$, where $Y_x(\textit{grating})$ is the X-ray output obtained by irradiation of plasma produced at the periodic structure and $Y_x(\textit{flat})$ is the X-ray output obtained by irradiation of a flat target. The experimental data give $L \sim 3^{1/4} \sim 1.3$.

Measurements of the increase in hot-electron temperature with increasing laser intensity showed that $T_{\text{hot}} \sim I^\alpha$, where $\alpha = 0.4 \pm 0.1$ (Fig. 4). Taking into account this dependence, one can conclude that the local-field enhancement calculated from the measured increase in T_{hot} is

$$L \sim \left(\frac{T_{\text{hot}}(\text{grating})}{T_{\text{hot}}(\text{flat})}\right)^{1/0.4 \times 2} \sim (1.4)^{1/0.4 \times 2} \sim 1.5.$$

This value is close to the one derived from the X-ray output data and agrees with the theoretical estimates of the local-field enhancement. For the plasma expanded over a distance Δz much shorter than the wavelength λ of the p-polarized laser radiation and for the optimal groove height, the local-field amplification factor can be estimated by the following equation [13]:

$$L_{p,\max} = \sqrt{\frac{\cos\theta}{n/(n^2 + m^2) + \pi \cdot \eta \cdot k_0}}; \qquad (2)$$

where $\eta = (d|\text{Re}(\varepsilon)|/dz)^{-1} \sim (|\text{Re}(\varepsilon)|/\Delta z)^{-1}$, ε is the plasma dielectric constant, n is the real part of the refractive index, and m is its imaginary part. If the plasma temperature is $T_e \sim 300$ eV, the degree of ionization is $Z \sim 20$, $|\text{Re}(\varepsilon)| \sim 11$, and the plasma expansion into vacuum is $\Delta z \sim 200$ Å (which corresponds to the heating radiation intensity $I \sim 10^{16}$ W/cm² and a pulse duration of 200 fs [14]), the local-field amplification factor $L_{p,\max}$ is approximately 1.8.

The local-field amplification factor calculated from the results of measuring hard X-ray output is smaller than expected. A possible reason is that the amplitude of the obtained periodic structure is not optimal. The optimal groove height for SEW generation at the surface of plasma produced in the experiment is 80 nm [13]. In addition, Eq. (2) is valid for a sinusoidal grating, whereas the actual relief of the periodic structure is far from sinusoidal (Fig. 2). This leads to additional losses due to the radiation scattering by the nonresonant Fourier components of the surface relief. As a result, the local-field amplification factor is reduced.
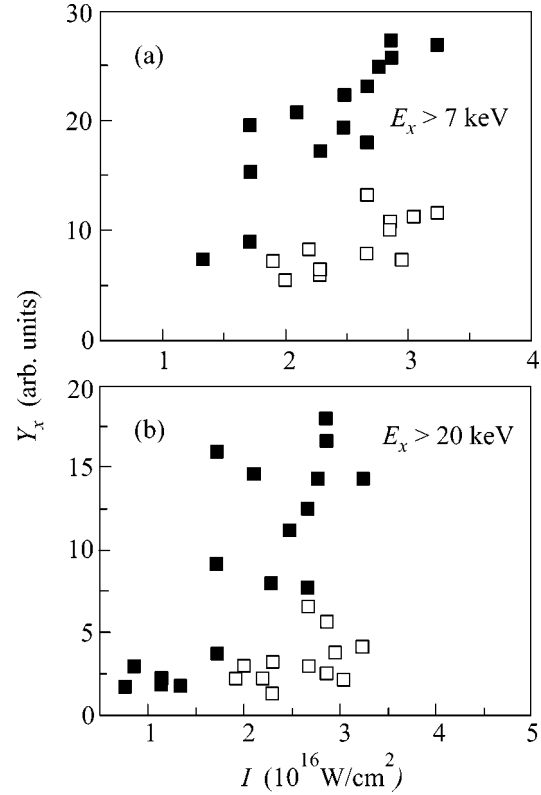
Fig. 3. Conversion efficiency of the laser radiation into X-ray emission in different ranges of X-ray spectrum: above (a) 7 and (b) 20 keV for (open squares) flat target and (filled squares) laser-induced grating.
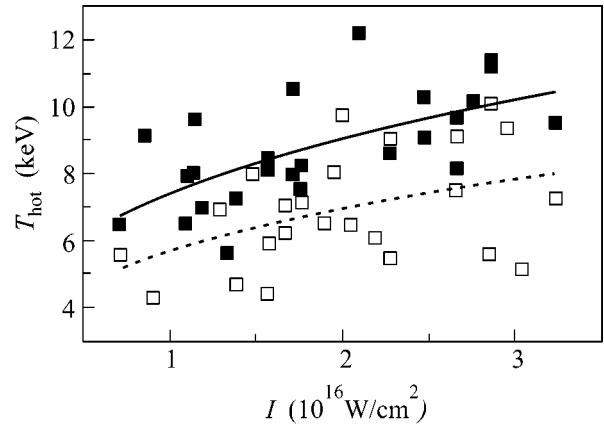

Fig. 4. Dependence of the hot-electron temperature on the intensity for (open squares) flat target and (filled squares) laser-induced grating. The experimental data both for the grating (solid line) and the flat target (dashed line) are best approximated by a power law $T_{\text{hot}} \sim I^\alpha$, where $\alpha = 0.4 \pm 0.1$.

The obtained increase in the hot-electron temperature can be used to increase the excitation efficiency for low-lying nuclear levels. For example, in the case of 14-keV Fe[57] transition, it can be shown, following [15],

that an increase in the hot-electron temperature from 7 to 10 keV brings about a twofold increase in the excitation efficiency. It should also be noted that the maximal energy of protons emitted by the plasma produced from the femtosecond laser radiation with intensity $I \sim 10^{16}$ W/cm^2 can be enhanced to 50 keV, because it increases in proportion to T_{hot} [16].

REFERENCES

1. A. V. Andreev, V. M. Gordienko, and A. B. Savel'ev, Kvantovaya Élektron. (Moscow) **31**, 941 (2001).

2. J. Gauthier, S. Bastiani, P. Audebert, *et al.*, Proc. SPIE **2523**, 242 (1995).

3. R. V. Volkov, V. M. Gordienko, M. S. Dzhidzhoev, *et al.*, Kvantovaya Élektron. (Moscow) **24**, 1114 (1997).

4. R. V. Volkov, V. M. Gordienko, M. S. Dzhidzhoev, *et al.*, Kvantovaya Élektron. (Moscow) **23**, 539 (1996).

5. R. V. Volkov, V. M. Gordienko, A. B. Savel'ev, *et al.*, Laser Phys. **6**, 1158 (1996).

6. A. Varanavichyus, T. V. Vlasov, R. V. Volkov, *et al.*, Kvantovaya Élektron. (Moscow) **30**, 523 (2000).

7. R. V. Volkov, V. M. Gordienko, P. M. Mikheev, and A. B. Savel'ev, Kvantovaya Élektron. (Moscow) **30**, 896 (2000).

8. F. Keilmann and Y. H. Bai, Appl. Phys. A **29**, 9 (1982).

9. D. Ashkensi, A. Rosenfeld, H. Varel, *et al.*, Appl. Surf. Sci. **120**, 65 (1997).

10. J. Bonse, J. M. Wrobel, J. Kruger, and W. Kautek, Appl. Phys. A **72**, 89 (2001).

11. M. B. Agranat, S. I. Anisimov, S. I. Ashitkov, *et al.*, Zh. Éksp. Teor. Fiz. **115**, 675 (1999) [JETP **88**, 370 (1999)].

12. S. A. Akhmanov, V. I. Emel'yanov, N. I. Koroteev, and V. N. Seminogov, Usp. Fiz. Nauk **147**, 675 (1985) [Sov. Phys.–Usp. **28**, 1084 (1985)].

13. R. V. Volkov, D. M. Golishnikov, V. M. Gordienko, and A. B. Savelev, *Materials of Deutsch–Russisches Laser-symposium*, Pommersfelden, Germany (2002).

14. V. T. Platonenko, Laser Phys. **2**, 852 (1992).

15. A. V. Andreev, R. V. Volkov, V. M. Gordienko, *et al.*, Zh. Éksp. Teor. Fiz. **118**, 1343 (2000) [JETP **91**, 1163 (2000)].

16. R. V. Volkov, V. M. Gordienko, I. M. Lachko, *et al.*, Pis'ma Zh. Éksp. Teor. Fiz. **76**, 171 (2002) [JETP Lett. **76**, 139 (2002)].

Translated by K. Chamorovskiĭ

Decay of the Monochromatic Capillary Wave[¶]

A. I. Dyachenko[1], A. O. Korotkevich[1, *], and V. E. Zakharov[1, 2]

[1] *Landau Institute for Theoretical Physics, Russian Academy of Sciences, Moscow, 119334 Russia*
**e-mail: kao@landau.ac.ru*
[2] *University of Arizona, Department of Mathematics, Tucson, USA*
Received March 31, 2003

It was demonstrated by direct numerical simulation that, in the case of weakly nonlinear capillary waves, one can get resonant waves interaction on the discrete grid when resonant conditions are never fulfilled exactly. The waves's decay pattern was obtained. The influence of the mismatch of resonant condition was studied as well. © 2003 MAIK "Nauka/Interperiodica".

PACS numbers: 47.35.+i

Nonlinear waves on the surface of a fluid are one of the most well known and complex phenomena in nature. Mature ocean waves and ripples on the surface of the tea in a pot, for example, can be described by very similar equations. Both these phenomena are substantially nonlinear, but the wave amplitude is usually significantly less than the wavelength. Under this condition, waves are weakly nonlinear.

To describe processes of this kind, weak turbulence theory was proposed [1, 2]. It results in Kolmogorov spectra as an exact solution of the Hasselman–Zakharov kinetic equation [3]. Many experimental results are in great accordance with this theory. In the case of gravity surface waves, the first confirmation was obtained by Toba [4], and the most recent data by Hwang [5] were obtained as a result of lidar scanning of the ocean surface. Recent experiments with capillary waves on the surface of liquid hydrogen [6, 7] are also in good agreement with this theory. On the other hand, some numerical calculations have been made to check the validity of the weak turbulent theory [8–10].

In this letter, we study one of the keystones of weak turbulent theory, the resonant interaction of weakly nonlinear waves. The question under study is the following:

How does a discrete grid for wavenumbers in numerical simulations affect the resonant interaction?

Can a nonlinear frequency shift broad resonant manifold to make discreteness unimportant?

We study this problem for nonlinear capillary waves on the surface of an infinitely depth incompressible ideal fluid. Direct numerical simulation can make the situation clear.

Let us consider a nonrotating flow of an ideal incompressible fluid of infinite depth. For the sake of

simplicity, let us suppose fluid density $\rho = 1$. The velocity potential ϕ satisfies the Laplace equation

$$\Delta\phi = 0 \tag{1}$$

in the fluid region bounded by

$$-\infty < z < \eta(\mathbf{r}), \quad \mathbf{r} = (x, y), \tag{2}$$

with the boundary conditions for the velocity potential

$$\frac{\partial\eta}{\partial t} + \frac{\partial\phi}{\partial x}\frac{\partial\eta}{\partial x} + \frac{\partial\phi}{\partial y}\frac{\partial\eta}{\partial y} = \frac{\partial\phi}{\partial z}\bigg|_{z=\eta},$$

$$\left(\frac{\partial\phi}{\partial t} + \frac{1}{2}(\nabla\phi)^2\right)\bigg|_{z=\eta} + \sigma(\sqrt{1+(\nabla\eta)^2}-1) = 0 \tag{3}$$

on $z = \eta$ and

$$\phi_z|_{z=-\infty} = 0 \tag{4}$$

on $z \longrightarrow -\infty$. Here $\eta = \eta(x, y, t)$ is the surface displacement. In the case of capillary waves, the Hamiltonian has the form

$$H = T + U,$$

$$T = \frac{1}{2}\int d^2r \int_{-\infty}^{\eta} (\nabla\phi)^2 dz, \tag{5}$$

$$U = \sigma\int(\sqrt{1+(\nabla\eta)^2}-1)d^2r, \tag{6}$$

where σ is the surface tension coefficient. In [11], it was shown that this system is Hamiltonian. The Hamiltonian variables are the displacement of the surface $\eta(x, y, t)$ and velocity potential on the surface of the fluid $\psi(x, y; t) = \phi(x, y, \eta(x, y; t); t)$. The Hamiltonian equations are

$$\frac{\partial\eta}{\partial t} = \frac{\delta H}{\delta\psi}, \quad \frac{\partial\psi}{\partial t} = -\frac{\delta H}{\delta\eta}. \tag{7}$$

[¶] This article was submitted by the authors in English.

Using the weak nonlinearity assumption [3], one can expand the Hamiltonian in the powers of surface displacement:

$$H = \frac{1}{2}\int(\sigma|\nabla\eta|^2 + \psi\hat{k}\psi)d^2r$$

$$+ \frac{1}{2}\int\eta[|\nabla\psi|^2 - (\hat{k}\psi)^2]d^2r. \qquad (8)$$

The third order is enough for three-wave interactions.

Here, $\hat{k}$ is the linear operator corresponding to multiplication of Fourier harmonics by the modulus of the wavenumber $\mathbf{k}$. Using (7), one can get the following system of dynamical equations:

$$\dot{\eta} = \hat{k}\psi - \mathrm{div}(\eta\nabla\psi) - \hat{k}[\eta\hat{k}\psi],$$

$$\dot{\psi} = \sigma\Delta\eta - \frac{1}{2}[(\nabla\psi)^2 - (\hat{k}\psi)^2]. \qquad (9)$$

The properties of the $\hat{k}$ operator suggest exploiting the equations in Fourier space for Fourier components of η and ψ,

$$\psi_{\mathbf{k}} = \frac{1}{2\pi}\int\psi_{\mathbf{r}}e^{i\mathbf{kr}}d^2r, \quad \eta_{\mathbf{k}} = \frac{1}{2\pi}\int\eta_{\mathbf{r}}e^{i\mathbf{kr}}d^2r.$$

Let us introduce the canonical variables $a_{\mathbf{k}}$ as shown below:

$$a_{\mathbf{k}} = \sqrt{\frac{\omega_k}{2k}}\eta_{\mathbf{k}} + i\sqrt{\frac{k}{2\omega_k}}\psi_{\mathbf{k}}, \qquad (10)$$

where

$$\omega_k = \sqrt{\sigma k^3}. \qquad (11)$$

With these variables, the Hamiltonian (8) acquires the form

$$H = \int\omega_k|a_{\mathbf{k}}|^2d\mathbf{k}$$

$$+ \frac{1}{6}\frac{1}{2\pi}\int E^{\mathbf{k}_0}_{\mathbf{k}_1\mathbf{k}_2}(a_{\mathbf{k}_1}a_{\mathbf{k}_2}a_{\mathbf{k}_0} + a^*_{\mathbf{k}_1}a^*_{\mathbf{k}_2}a^*_{\mathbf{k}_0})$$

$$\times\delta(\mathbf{k}_1 + \mathbf{k}_2 + \mathbf{k}_0)d\mathbf{k}_1d\mathbf{k}_2d\mathbf{k}_0 \qquad (12)$$

$$+ \frac{1}{2}\frac{1}{2\pi}\int M^{\mathbf{k}_0}_{\mathbf{k}_1\mathbf{k}_2}(a_{\mathbf{k}_1}a_{\mathbf{k}_2}a^*_{\mathbf{k}_0} + a^*_{\mathbf{k}_1}a^*_{\mathbf{k}_2}a_{\mathbf{k}_0})$$

$$\times\delta(\mathbf{k}_1 + \mathbf{k}_2 - \mathbf{k}_0)d\mathbf{k}_1d\mathbf{k}_2d\mathbf{k}_0.$$

Here,

$$E^{\mathbf{k}_0}_{\mathbf{k}_1\mathbf{k}_2} = V^{k_0}_{\mathbf{k}_1\mathbf{k}_2} + V^{k_1}_{\mathbf{k}_0\mathbf{k}_2} + V^{k_2}_{\mathbf{k}_0\mathbf{k}_1},$$

$$M^{\mathbf{k}_0}_{\mathbf{k}_1\mathbf{k}_2} = V^{k_0}_{\mathbf{k}_1\mathbf{k}_2} - V^{k_1}_{-\mathbf{k}_0\mathbf{k}_2} - V^{k_2}_{-\mathbf{k}_0\mathbf{k}_1},$$

$$V^{k_0}_{\mathbf{k}_1\mathbf{k}_2} = \sqrt{\frac{\omega_{k_1}\omega_{k_2}k_0}{8k_1k_2\omega_{k_0}}}L_{\mathbf{k}_1\mathbf{k}_2}, \qquad (13)$$

$$L_{\mathbf{k}_1\mathbf{k}_2} = (\mathbf{k}_1\mathbf{k}_2) + |k_1||k_2|.$$

The dynamic equations in these variables can be easily obtained by variation of Hamiltonian:

$$\dot{a}_{\mathbf{k}} = -i\frac{\delta H}{\delta a^*_{\mathbf{k}}} = -i\omega_k a_{\mathbf{k}}$$

$$- \frac{i}{2}\frac{1}{2\pi}\int M^{\mathbf{k}}_{\mathbf{k}_1\mathbf{k}_2}a_{\mathbf{k}_1}a_{\mathbf{k}_2}\delta(\mathbf{k}_1 + \mathbf{k}_2 - \mathbf{k})d\mathbf{k}_1d\mathbf{k}_2$$

$$- \frac{i}{2\pi}\int M^{\mathbf{k}_0}_{\mathbf{k}\mathbf{k}_2}a^*_{\mathbf{k}_2}a_{\mathbf{k}_0}\delta(\mathbf{k} + \mathbf{k}_2 - \mathbf{k}_0)d\mathbf{k}_2d\mathbf{k}_0 \qquad (14)$$

$$- \frac{i}{2}\frac{1}{2\pi}\int E^{\mathbf{k}}_{\mathbf{k}_1\mathbf{k}_2}a^*_{\mathbf{k}_1}a^*_{\mathbf{k}_2}\delta(\mathbf{k}_1 + \mathbf{k}_2 + \mathbf{k})d\mathbf{k}_1d\mathbf{k}_2.$$

Each term in this equation has its own clear physical meaning. The linear term gives a periodic evolution of the initial wave. The first nonlinear term describes a merging of two waves $\mathbf{k}_1$ and $\mathbf{k}_2$ in $\mathbf{k}$. The second describes decay of the wave $\mathbf{k}_0$ to the waves $\mathbf{k}$ and $\mathbf{k}_2$. And the last term corresponds to the second harmonic generation process. It is useful to eliminate the linear term with the substitution

$$a_{\mathbf{k}} = A_{\mathbf{k}}e^{i\omega_k t}. \qquad (15)$$

In these variables, the dynamical equations take the form

$$\dot{A}_{\mathbf{k}} = -\frac{i}{2}\frac{1}{2\pi}\int M^{\mathbf{k}}_{\mathbf{k}_1\mathbf{k}_2}A_{\mathbf{k}_1}A_{\mathbf{k}_2}e^{i\Omega^k_{k_1k_2}t}$$

$$\times\delta(\mathbf{k}_1 + \mathbf{k}_2 - \mathbf{k}_0)d\mathbf{k}_1dk_2$$

$$- \frac{i}{2\pi}\int M^{\mathbf{k}_0}_{\mathbf{k}\mathbf{k}_2}A^*_{\mathbf{k}_2}A_{\mathbf{k}_0}e^{-i\Omega^{k_0}_{kk_2}t} \qquad (16)$$

$$\times\delta(\mathbf{k} + \mathbf{k}_2 - \mathbf{k}_0)d\mathbf{k}_2d\mathbf{k}_0,$$

where

$$\Omega^{k_0}_{k_1k_2} = \omega_{k_1} + \omega_{k_2} - \omega_{k_0}. \qquad (17)$$

Here we do not consider the harmonic generation term. The remaining terms give us the following conditions of resonance:

$$\Omega^k_{k_1k_2} = \omega_{k_1} + \omega_{k_2} - \omega_k = 0, \quad \mathbf{k}_1 + \mathbf{k}_2 - \mathbf{k} = 0. \qquad (18)$$

All this theory is well known in the literature [3].

Now let us turn to the discrete grid. Also, from this point we assume periodic boundary conditions in x and

y with lengths L_x and L_y. One can easily obtain equations similar to (16):

$$\dot{A}_{\mathbf{k}} = -\frac{i}{2}\frac{2\pi}{L_xL_y}\sum_{\mathbf{k}_1\mathbf{k}_2}M^{\mathbf{k}}_{\mathbf{k}_1\mathbf{k}_2}A_{\mathbf{k}_1}A_{\mathbf{k}_2}e^{i\Omega^{\mathbf{k}}_{k_1k_2}t}\Delta_{(\mathbf{k}_1+\mathbf{k}_2),-\mathbf{k}}$$

$$-\frac{i2\pi}{L_xL_y}\sum_{\mathbf{k}_2\mathbf{k}_0}M^{\mathbf{k}_0}_{\mathbf{k}\mathbf{k}_2}A^*_{\mathbf{k}_2}A_{\mathbf{k}_0}e^{-i\Omega^{k_0}_{kk_2}t}\Delta_{(\mathbf{k}+\mathbf{k}_2),-\mathbf{k}_0},$$

(19)

where $\Delta_{\mathbf{k}_1,\mathbf{k}_2}$ is the Kronecker delta—the discrete analogue of the Dirac delta function.

Consider the decay of a monochromatic capillary wave $A_{\mathbf{k}_0}$ on two waves

$$\dot{A}_{\mathbf{k}_0} = -\frac{i}{2}\frac{2\pi}{L_xL_y}M^{\mathbf{k}_0}_{\mathbf{k}_1\mathbf{k}_2}A_{\mathbf{k}_1}A_{\mathbf{k}_2}e^{i\Omega^{k_0}_{k_1k_2}t},$$

$$\dot{A}_{\mathbf{k}_1} = -i\frac{2\pi}{L_xL_y}M^{\mathbf{k}_0}_{\mathbf{k}_1\mathbf{k}_2}A^*_{\mathbf{k}_2}A_{\mathbf{k}_0}e^{-i\Omega^{k_0}_{k_1k_2}t}, \qquad (20)$$

$$\dot{A}_{\mathbf{k}_2} = -i\frac{2\pi}{L_xL_y}M^{\mathbf{k}_0}_{\mathbf{k}_1\mathbf{k}_2}A^*_{\mathbf{k}_1}A_{\mathbf{k}_0}e^{-i\Omega^{k_0}_{k_1k_2}t}.$$

Let $A_{\mathbf{k}_1}$, $A_{\mathbf{k}_2}$ be small ($|A_{\mathbf{k}_0}| \gg \max(|A_{\mathbf{k}_1}|, |A_{\mathbf{k}_2}|)$) at $t = 0$). In this case, the equations can be linearized. The solution of linearized (20) has the form ($A_{\mathbf{k}_0} \sim$ const)

$$A_{\mathbf{k}_{1,2}}(t) = A_{\mathbf{k}_{1,2}}(0)e^{\lambda t}, \qquad (21)$$

where

$$\lambda = -\frac{i}{2}\Omega^{k_0}_{k_1k_2} + \sqrt{\left|\frac{2\pi}{L_xL_y}M^{\mathbf{k}_0}_{\mathbf{k}_1\mathbf{k}_2}A_{\mathbf{k}_0}\right|^2 - \left(\frac{1}{2}\Omega^{k_0}_{k_1k_2}\right)^2}. \quad (22)$$

In the case of a continuous media, resonant conditions (18) can be satisfied exactly. But on the grid, there is always a frequency mismatch $\Omega^{k_0}_{k_1k_2} \neq 0$ although if the amplitude of the initial wave is high enough there are resonances even on a discrete grid. But the width of this resonance is very important.

System of equations (9) can be solved numerically. This system is nonlocal in coordinate space due to the presence of the $\hat{k}$ operator. The origin of this operator gives us a hint to solve (9) in wavenumber space (K space). In this case, we can effectively use the fast Fourier transform algorithm. Omitting the details of this numerical scheme, we reproduce only the final results of calculations.

We have solved system of equations (9) numerically in the dimensionless periodic domain $2\pi \times 2\pi$ (the wavenumbers k_x and k_y are integer numbers in this case). Correspondingly, all other variables also become dimensionless. It is convenient to use the surface tension $\sigma = 1$. The size of the grid was chosen as
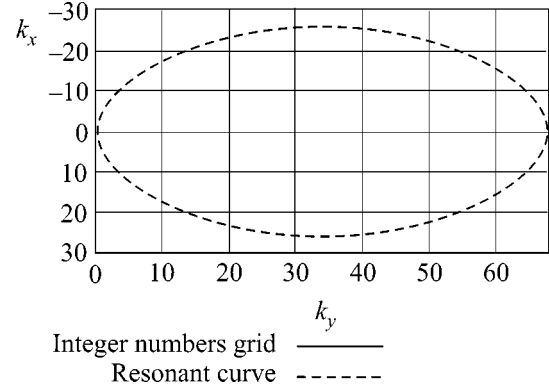
Fig. 1. The resonant manifold for $k_0 = 68$.

512×512 points. We have also included damping for waves with large wavenumbers. In K space, the damping terms for $\eta_{\mathbf{k}}$ and $\psi_{\mathbf{k}}$, respectively, were the following: $\gamma_{\mathbf{k}}\eta_{\mathbf{k}}$ and $\gamma_{\mathbf{k}}\psi_{\mathbf{k}}$, where $\gamma_{\mathbf{k}}$ was of the form

$$\gamma_{\mathbf{k}} = 0, \quad |\mathbf{k}| < \frac{1}{2}|\mathbf{k}_{\max}|,$$

$$\gamma_{\mathbf{k}} = -\gamma_0\left(|\mathbf{k}| - \left|\frac{1}{2}\mathbf{k}_{\max}\right|\right)^2, \quad |\mathbf{k}| \geq \frac{1}{2}|\mathbf{k}_{\max}|,$$

(23)

where γ_0 is some constant.

As an initial condition we used one monochromatic wave of sufficiently large amplitude with wavenumbers $\mathbf{k}_0$ ($k_{0x} = 0$, $k_{0y} = 68$). Along with that, there was a small random noise in all other harmonics.

Resonant manifold (18) for decaying waves

$$\mathbf{k}_0 = \begin{pmatrix} 0 \\ k_0 \end{pmatrix},$$

$$\mathbf{k}_1 = \begin{pmatrix} -k_x \\ k_0 - k_y \end{pmatrix}, \quad \mathbf{k}_2 = \begin{pmatrix} k_x \\ k_0 + k_y \end{pmatrix}$$

(24)

is given in Fig. 1. Since the wavenumbers are integers, the resonant curve never coincides with grid points exactly. A detailed picture is given in Fig. 2. It is clear that some points are closer to the resonant manifold than others. This difference might be important in numerals.

In the beginning, one can observe exponential growth of resonant harmonics in accordance with (21) and (22). This is shown in Figs. 3 and 4. Here one can clearly see that some harmonics are in resonance and others are not.

Then almost all harmonics in the resonant manifold become involved in the decay process (Fig. 5). Later, the harmonics that are the closest to the resonant manifold (compare with Fig. 2) reach the maximum level, while the secondary decay process develops. Waves
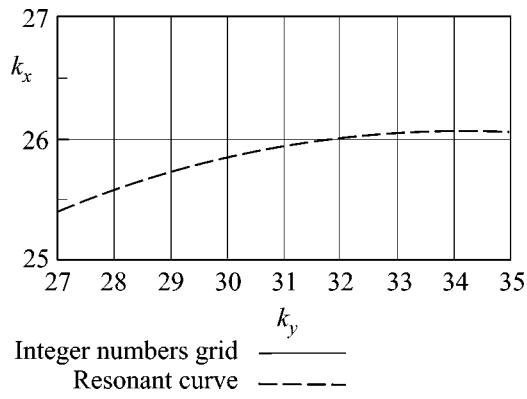
Integer numbers grid ⎯⎯⎯
Resonant curve ⎯ ⎯ ⎯

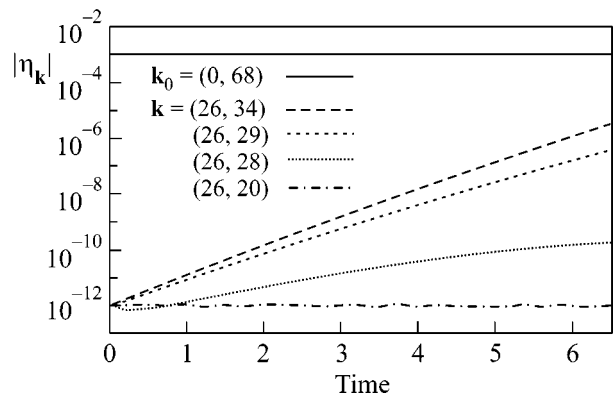**Fig. 2.** Different mismatch is seen at different grid points.

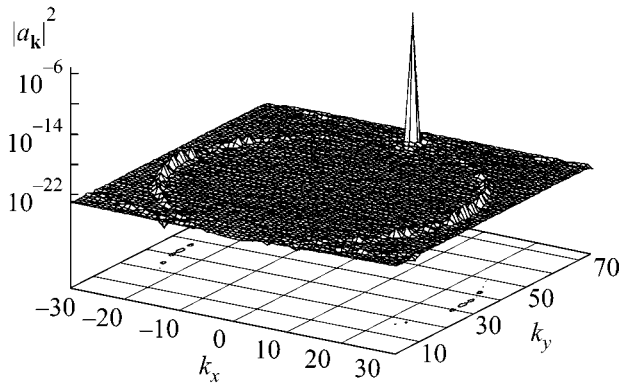**Fig. 3.** Evolution of various harmonics for decaying wave $\mathbf{k}_0 = (0, 68)$.

Fig. 4. Resonant harmonics starting to grow. At the basement there is a contour line for level $|a_{\mathbf{k}}|^2 = 10^{-22}$. Time $t = 1.4$.
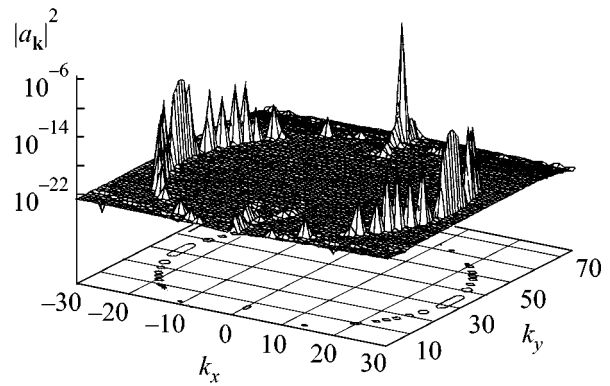

Fig. 5. Secondary decays start. At the basement there is a contour line for level $|a_{\mathbf{k}}|^2 = 10^{-22}$. Time $t = 11$.
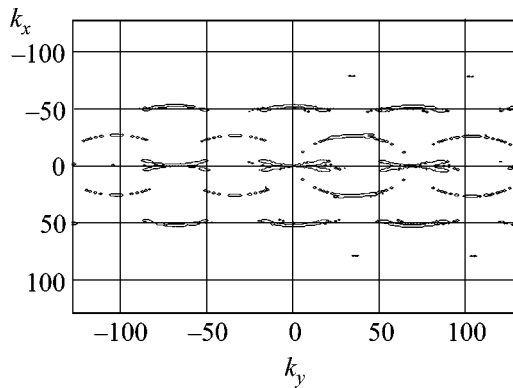

Fig. 6. The contour lines for $|a_k|^2 = 10^{-21}$. Secondary decays are clearly seen. Time $t = 14$.
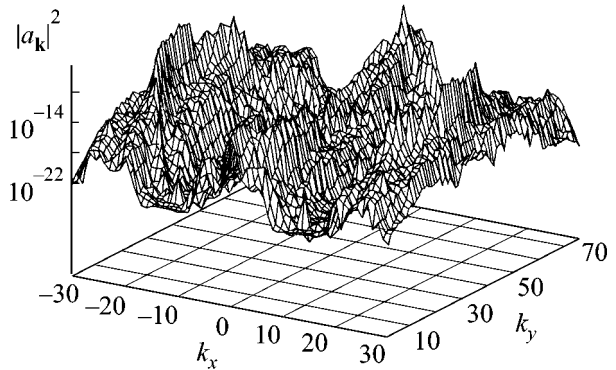

Fig. 7. Wavenumber spectrum at time $t = 57$.

amplitudes become significantly different. The largest amplitudes are for those waves with the maximum growth rate. One can see the regular structure generated by the $\mathbf{k}_0$ wave in Fig. 6. After a while, the whole $\mathbf{k}$ space is filled by decaying waves, as shown in Fig. 7.

Direct numerical simulation has demonstrated that the finite width of the resonance makes the discrete grid very similar to a continuous one. Of course, this is true only if the amplitude of the wave is large enough, so that according to (22)

$$\left| \frac{2\pi}{L_x L_y} M_{\mathbf{k}_1 \mathbf{k}_2}^{\mathbf{k}_0} A_{\mathbf{k}_0} \right| > \left| \frac{1}{2} \Omega_{k_1 k_2}^{k_0} \right|. \tag{25}$$

As regards numerical simulation of the turbulence, namely, weak turbulence, condition (25) is very important. $A_{\mathbf{k}_0}$ has to be treated as the level of turbulence.

REFERENCES

1. V. E. Zakharov and N. N. Filonenko, Dokl. Akad. Nauk SSSR **170**, 1292 (1966) [Sov. Phys. Dokl. **11**, 881 (1966)].
2. V. E. Zakharov and N. N. Filonenko, J. Appl. Mech. Tech. Phys. **4**, 506 (1967).
3. V. E. Zakharov, G. Falkovich, and V. S. Lvov, *Kolmogorov Spectra of Turbulence*, Vol. 1: *Wave Turbelence* (Springer, Berlin, 1992).
4. Y. Toba, J. Oceanogr. Soc. Jpn. **29**, 209 (1973).
5. P. A. Hwang, D. W. Wang, E. J. Walsh, *et al.*, J. Phys. Oceanogr. **30**, 2753 (2000).
6. M. Yu. Brazhnikov, G. V. Kolmakov, A. A. Levchenko, and L. P. Mezhov-Deglin, Pis'ma Zh. Éksp. Teor. Fiz. **74**, 660 (2001) [JETP Lett. **74**, 583 (2001)].
7. M. Yu. Brazhnikov, G. V. Kolmakov, and A. A. Levchenko, Zh. Éksp. Teor. Fiz. **122**, 521 (2002) [JETP **95**, 447 (2002)].
8. A. N. Pushkarev and V. E. Zakharov, Phys. Rev. Lett. **76**, 3320 (1996).
9. F. Dias, P. Guyenne, and V. E. Zakharov, Phys. Lett. A **291**, 139 (2001).
10. V. E. Zakharov, O. A. Vasilyev, and A. I. Dyachenko, Pis'ma Zh. Éksp. Teor. Fiz. **73**, 68 (2001) [JETP Lett. **73**, 63 (2001)].
11. V. E. Zakharov, J. Appl. Mech. Tech. Phys. **2**, 190 (1968).

Dust Grains in Plasma with Coulomb Collisions

A. G. Leonov[1], A. F. Pal'[2], A. N. Starostin[2], and A. V. Filippov[2],*

[1]*Moscow Institute of Physics and Technology, Institutskiĭ per. 9, Dolgoprudnyĭ, Moscow region, 141700 Russia*
[2]*State Scientific Center "Troitsk Institute for Innovation and Fusion Research,"*
Troitsk, Moscow region, 142190 Russia
*e-mail: fav@triniti.ru
Received March 31, 2003

Dust-grain charging in a dense plasma with electron and ion concentration up to 10^{16} cm^{-3}, where the electron transport cross section is dominated by Coulomb collisions, was investigated. It was established that the charge of an isolated dust grain increases with electron concentration, whereas its potential is almost constant in the range 10^{14}–10^{16} cm^{-3} of electron concentrations studied. It is shown that the self-consistent electric-field potential at moderate and large distances from the dust grain is well approximated by the Debye expression, but the screening radius is appreciably larger than even the electron Debye radius. The region of parameters of a dense photoresonance sodium plasma, where the dust-grain ensemble may crystallize, was established. © *2003 MAIK "Nauka/Interperiodica".*

PACS numbers: 52.27.Lw; 52.25.Vy

INTRODUCTION

Today, increased interest in dust plasma is caused by a number of its unique properties. In such plasmas, an ordered Coulomb crystal may form under certain conditions. The study of this structure is of great interest from both fundamental and applied points of view. At present, investigations of dust plasma are carried out in a weakly ionized low-temperature plasma with the electron density n_e no higher than 10^9–10^{12} cm^{-3}. According to modern concepts, the charge of an isolated dust grain is virtually independent of n_e. However, as the plasma density increases, the electron mobility is controlled more and more by the Coulomb collisions with ions, so that, in the analytic theory of hydrodynamic charging regime, the dust-grain charge decreases logarithmically with increasing plasma concentration [1, 2]. It should also be noted that the Debye radius at low electron and ion densities is large, allowing the condition for dust-component crystallization in weakly ionized plasma to be satisfied at reasonable values of experimental parameters (see, e.g., [3]). At higher densities of the charged plasma particles, the Debye radius decreases, thereby weakening the interaction between the grains and, at first glance, preventing the formation of ordered structures. However, it was found both in the experiments and in numerical calculations that, under real experimental conditions of low-temperature plasma, the screening radius characterizing the spatial dependence of dust-grain potential may appreciably differ from its classical value (see [3] for details) and the screening radius may become larger than even the electron Debye radius upon an increase in the electron and ion density. This follows from the fact that the linearized Debye–Hückel theory does not apply to the open systems exemplified by dust plasma. Because the dust grains continuously absorb electrons and ions, such plasma can exist only if energy is continuously fed to generate new charge carriers instead of the absorbed ones. Since the degree of plasma perturbation by a dust grain increases with electron concentration, the deviations from the Debye–Hückel theory also decrease with increasing n_e. This motivated us to study the fundamental processes of nonstationary dust-grain charging and the possibility of Coulomb crystallization in a dense plasma with $n_e \sim 10^{15}$–10^{17} cm^{-3} at a relatively low electron temperature $T_e \sim 0.2$–0.5 eV, which is typical of, e.g., photoresonance plasma [4].

NUMERICAL SIMULATION OF DUST-GRAIN CHARGING

Numerical studies were carried out using a model of nonlocal charging in the hydrodynamic regime [5]. Calculations were carried out with the effective boundary conditions whose applicability was discussed in detail in [3, 5]. The results of simulating the charging process for a solitary dust grain with radius $r_0 = 10$ μm in the argon plasma at room temperature and atomic concentration $N = 2.5 \times 10^{19}$ cm^{-3} are given in Fig. 1. The Ar_2^+ ion, whose dissociative recombination coefficient is given by the expression $\beta_{ei} = 0.85 \times 10^{-6}(300/T_e)^{0.67}$ cm^3/s [6] (the electron temperature is in K, as is adopted in the theory of elementary processes), was assumed to be the bulk ion, and the mobility k_i of a molecular ion was taken to be 2.1 cm^2/(V s) [7]. The fast dissociative recombination of a molecular ion plays an important part in the charging kinetics of dust grains
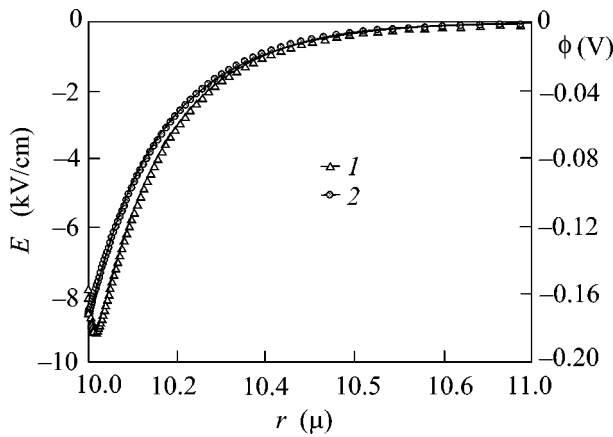
Fig. 1. Radial distributions of the (curve *1*) electric field and (curve *2*) potential of an isolated dust grain in argon plasma for $T_e = 0.4$ eV, $r_0 = 10$ μm, $n_{e\infty} = 10^{16}$ cm^{-3}, and $n_d = 10^8$ cm^{-3}.
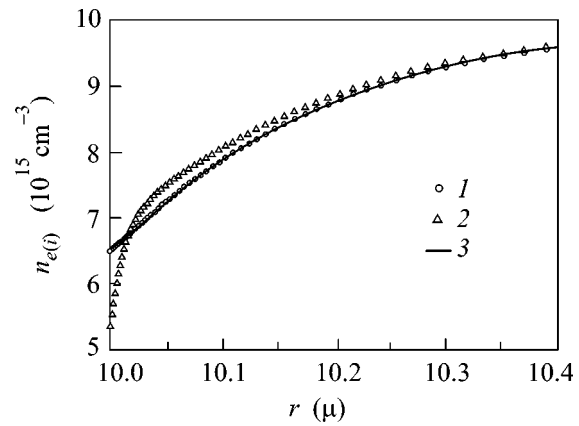

Fig. 2. Radial distributions of the (curve *1*) electron and (curve *2*) ion concentrations in the immediate vicinity of an isolated dust grain in argon for $T_e = 0.4$ eV, $r_0 = 10$ μm, $n_{e\infty} = 10^{16}$ cm^{-3}, and $n_d = 10^8$ cm^{-3}. Curve *3* is for the Boltzmann electron distribution.

[5]. It was assumed that the electron temperature is $T_e = 0.4$ eV and the electron concentration away from the grain is $n_{e\infty} = 10^{16}$ cm^{-3}. One can see in Fig. 1 that the curve for the radial dependence of electric field passes through a minimum, while the radial behavior of the potential is rather regular and monotonic. The fact that the field in the vicinity of a dust grain is nonmonotonic is rather unexpected, so that we will dwell upon this effect in more detail.

Under normal conditions, the Ar_2^+ ion free path is $l_i \approx 0.05$ μm, and the region where the plasma quasi-neutrality is broken is $d \sim 1$ μm, so that the hydrodynamic description of the transport processes is correct for the ion component. The electron free path with respect to the electron–neutral and electron–ion collisions at $n_e = n_i = 10^{16}$ cm^{-3} is $l_{ei} \approx 1.5$ μm, and the total free path with allowance made for all collisions is $l_e \approx 1.1$ μm. One can see that d and l_e are comparable in magnitude, so that the hydrodynamic approach becomes incorrect for the electron component (note that the free path l_e and the distance from the minimum point to the dust grain are given in Fig. 1 on different scales). In this case, the kinetic approach is, generally, required to determine the electron energy distribution function (EEDF). However, the electron–electron collisions in dense plasma give rise to the Maxwellian EEDF, and it is not affected by electric field in a Knudsen layer, where electrons almost do not collide with each other and with other particles. For this reason, the behavior of the electron component is completely described by the lowest (no higher than second-order) moments of EEDF, i.e., by the balance equations for the number of electrons and their energy. Due to the smallness of the ion current and almost total compensation between the drift and diffusional electron fluxes, this also brings about Boltzmann electron distribution in a

self-consistent dust-grain electric field. Indeed, the results of numerical simulation show that the electron distribution is described by the Boltzmann expression with a high accuracy (Fig. 2). In this case, one can show that, for the adopted effective boundary conditions, the electron flux on a dust grain will coincide in the collisionless limit with the flux in the orbit motion limited (OML) approach [8], which is valid at $l_e \gg d$. Because of this, we can conclude that the nonlocal charging model with the effective boundary conditions properly describes the behavior of the electron component under the conditions considered in this work and that the area of its applicability is fully determined by the ion component.

The reason for which the electric field is nonmonotonic becomes clear from Fig. 2, where the electron and ion distributions in the immediate vicinity of a dust grain are shown. One can see that the electron concentration near the dust grain decreases to a value (determined by the electric-field potential and electron concentration and temperature at large distances) that far exceeds the ion concentration (in the hydrodynamic limit $l_i/r_0 \longrightarrow 0$, the ion concentration at the dust-grain surface tends to zero). For this reason, a region of negative space charge appears in the vicinity of a dust grain, as a result of which the electric field becomes nonmonotonic. Of course, one cannot argue that the ion density in the Knudsen layer is properly determined if the effective boundary conditions are used. To describe the ion transport in this layer more accurately, the ion inertia should be taken into account. However, this will increase the ion velocity and, due to flux conservation, lead to even sharper decrease in ion concentration in the Knudsen layer, rendering the observed effect more pronounced.

As was mentioned above, the charge of an isolated dust grain, according to the modern theories of charg-
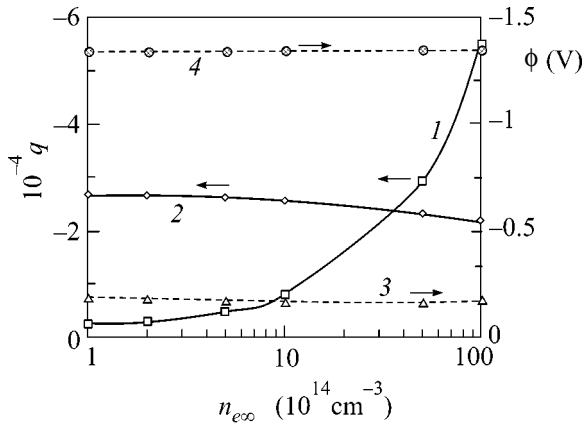
Fig. 3. Charge and potential of an isolated dust grain in an argon plasma with Coulomb collisions vs. electron concentration at a large distance from the grain for $T_e = 0.4$ eV and $r_0 = 10$ μm. Curve *1* is the calculated charge; curve *2* corresponds to the analytic charging theory [1, 2]; curve *3* is the calculated potential; and curve *4* is the OML potential [8].

Fig. 4. Effective Debye screening radius (reduced to the classical electron radius) of an isolated dust grain in (curve *1*) argon and (curve *2*) photoresonance sodium plasma vs. electron concentration at a large distance from the grain for $T_e = 0.4$ eV and $r_0 = 10$ μm. The run of curve *2* reflects the time evolution (passing though a maximum) of the electron temperature and concentration in a photoresonance sodium plasma.

ing [1, 2, 8], is independent of the electron concentration $n_{e\infty}$ away from the grain. The influence of $n_{e\infty}$ on the charge is of fundamental interest, because the applicability of the cited theories is questionable for a dense plasma with the parameters considered in this work. The dust-grain charge and potential in argon plasma with Coulomb collisions are presented in Fig. 3 for various electron concentrations at large distances. One can see that, in contrast to weakly ionized plasma, the charge depends rather strongly on the electron concentration, but the potential virtually does not change upon a change in $n_{e\infty}$ by two orders of magnitude.

With the purpose of determining the character of screening the dust-grain charge, the calculated potential was approximated by the Debye expression:

$$\phi(r) = \frac{eq_a}{r}\exp(-r/R_{D,a}), \qquad (1)$$

where r is the distance from the grain center; q_a and $R_{D,a}$ are, respectively, the approximated charge and screening radius. The results of approximation showed that the calculated potential was rather well described by expression (1). A comparison of the results obtained by approximating the screening radii by the plasma and electron Debye radii is shown in Fig. 4. One can see that $R_{D,a}$ markedly exceeds even the classical electron Debye radius $R_{D,e}$ given by the expression

$$R_{D,e} = \sqrt{\frac{T_e}{4\pi e^2 n_{e\infty}}}. \qquad (2)$$

These data allow the probability of formation of a Coulomb dust-grain crystal to be estimated for the dense-plasma parameters considered in this work. One can see from Fig. 4 that the dust grain in an argon plasma perturbs it only at small distances, so that the interaction
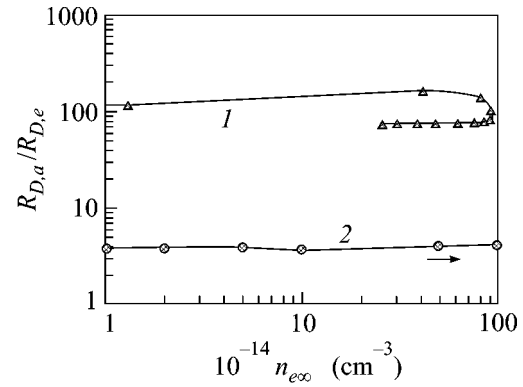
energy of dust grains becomes comparable with their thermal energy only at high dust concentrations exceeding 10^8 cm^{-3}. Taking this into account, one can hardly expect that the dust plasma can crystallize.

In this work, the possibility of dust-plasma crystallization in a sodium photoresonance plasma (PRP) produced by laser pulses (see, e.g., [4]) was also studied. In this plasma, the monatomic Na$^+$ ions, whose decay channel is dominated by three-body recombination (with an electron as a third body), are bulk ions at the electron densities on the order of 10^{15}–10^{16} cm^{-3} [9], with $\beta_3 = 8.75 \times 10^{-27} T_e^{-9/2}$ cm^6/s (T_e is in eV). The mobility of sodium ions was determined from the Langevin formula [7] $k_i = 36/\sqrt{\alpha\mu}$ cm^2/(V s), where α is the polarizability of argon atoms and μ is the reduced mass of ion and neutral particles in atomic units. Due to a low three-body recombination rate (compared to the dissociative recombination rate in argon), the screening radius increases appreciably, because the size of the plasma region disturbed by the dust grain depends on the loss rate of charged particles in plasma bulk [5]. Calculations show (Fig. 4) that the screening radius in a dense sodium plasma may be two orders of magnitude larger than the electron Debye radius given by the classical Debye–Hückel theory. Due to a large screening radius in the sodium PRP considered, the condition for crystallization, in contrast to argon, may not be fulfilled at reasonable dust-grain concentrations $n_d < 10^7$ cm^{-3}, as is seen in Fig. 5, showing the dependence $n_{cr}(t)$ of the critical dust-grain concentration above which the crystallization condition is fulfilled for the photoresonance dust plasma.

It should be noted that the effect of laser radiation with a pulse duration on the order of 10 ns and a peak intensity up to 10^8 W/cm^2 on heating plasma dust com-
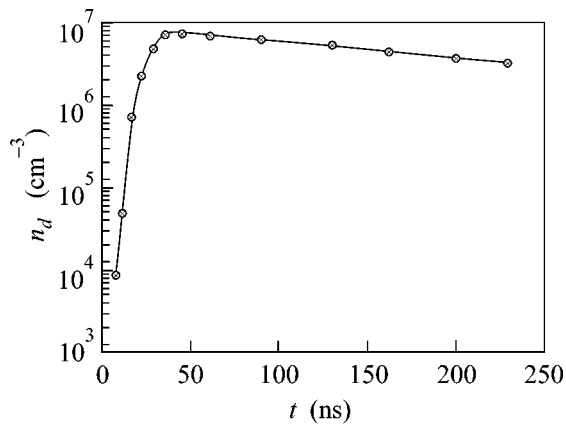
Fig. 5. Time dependence of the critical concentration of dust grains with a radius of 10 μm in a photoresonance sodium plasma.

ponent is immaterial in the case where the grains consist of a transparent material (e.g., alumina powder); accordingly, the influence of a thermoforethic force on the dust-grain levitation is weak. Although the levitation can, in principle, be affected by the pressure of laser radiation, the kinetic energy acquired by the dust grain under the action of a laser pulse with the above-mentioned parameters does not exceed the grain thermal motion energy. Estimates show that the grain heating by the ion flux can also be ignored for the plasma parameters considered. The influence of the photoemission processes induced by visible laser radiation on the charging of dielectric particles is also insignificant.

CONCLUSIONS

The studies carried out in this work have shown that, when passing from a weakly ionized plasma to a rather dense plasma with an electron concentration of $\sim 10^{16}$ cm^{-3}, the charge of a dust grain, as expected, starts to strongly depend on the plasma density because of switching on of the Coulomb collisions. With an increase in the electron density, these collisions start to dominate the drift and diffusional velocities. The results of numerical simulation have also demonstrated that the calculated potential of an isolated dust grain in a dense plasma decreases with distance much more slowly than is predicted by the classical Debye–Hückel theory. The approximation of calculated data gives a value for the screening radius which exceeds the classical electron Debye radius by almost two orders of magnitude. It is established that the dust component may crystallize in a photoresonance sodium plasma.

REFERENCES

1. B. M. Smirnov, Usp. Fiz. Nauk **170**, 495 (2000) [Phys. Usp. **43**, 453 (2000)].
2. V. Yu. Baranov, I. A. Belov, A. V. Dem'yanov, *et al.*, in *Isotopes*, Ed. by V. Yu. Baranov (IzdAT, Moscow, 2000), p. 626.
3. A. F. Pal', D. V. Sivokhin, A. N. Starostin, *et al.*, Fiz. Plazmy (Moscow) **28**, 32 (2002) [Plasma Phys. Rep. **28**, 28 (2002)].
4. A. G. Leonov, A. N. Starostin, and D. I. Chekhov, Zh. Éksp. Teor. Fiz. **111**, 1274 (1997) [JETP **84**, 703 (1997)].
5. A. V. Filippov, N. A. Dyatko, A. F. Pal', and A. N. Starostin, Fiz. Plazmy (Moscow) **29**, 214 (2003) [Plasma Phys. Rep. **29**, 190 (2003)].
6. V. A. Ivanov, Usp. Fiz. Nauk **162**, 35 (1992) [Sov. Phys. Usp. **35**, 17 (1992)].
7. B. M. Smirnov, *Ions and Excited Atoms in Plasma* (Atomizdat, Moscow, 1974).
8. M. S. Barnes, J. H. Keller, J. C. Forster, *et al.*, Phys. Rev. Lett. **68**, 313 (1992).
9. Yu. P. Raĭzer, *The Physics of Gas Discharge* (Nauka, Moscow, 1987).

Translated by V. Sakun

Hall Effect in Nonideal Argon and Xenon Plasmas

N. S. Shilkin*, S. V. Dudin, V. K. Gryaznov, V. B. Mintsev, and V. E. Fortov

Institute of Energy Problems of Chemical Physics, Chernogolovka Branch, Russian Academy of Sciences,
Chernogolovka, Moscow region, 142432 Russia
*e-mail: shilkin@ficp.ac.ru
Received January 10, 2003; in final form, April 2, 2003

The Hall constant and conductivity of nonideal partially ionized argon and xenon plasmas are measured by the probe methods. Plasmas were generated behind the front of powerful shock waves using linear explosive generators. The results are compared with some plasma models. © 2003 MAIK "Nauka/Interperiodica".

PACS numbers: 52.25.Fi; 52.27.Gr; 52.50.Lp; 52.70.Ds

A low-temperature nonideal plasma ($\Gamma = 2e^3(\pi n_e)^{1/2}/(k_B T)^{3/2} > 1$) is the object of steady interest of researchers, both because of the complexity and diversity of the processes occurring in it and due to the possible practical use of dense plasma in some technical devices and energy projects [1].

At present, the comprehensive description of the physical properties of a dense plasma is far from completion because of difficulties of both a theoretical and an experimental character [1]. In the commonly used "chemical" model [2], the calculation of the thermal properties of a nonideal plasma rests on the knowledge of its equilibrium component composition. In the case of strong Coulomb interaction ($\Gamma > 1$), the calculation of the composition is a separate and rather complex problem because of the uncertainty inherent in the chemical model [3], so that the correctness of the corresponding solution requires experimental verification. Direct measurements of electron concentration provide a unique opportunity to check the adequacy of modern theoretical ideas of the properties of dense plasma. Note that the strong interparticle interaction renders the use of the majority of classical methods for measuring electron concentration [4, 5] practically impossible, in spite of their successful use in other areas of physics.

In this work, we report the first data on measuring the electron concentration (10^{16}–10^{20} cm^{-3}) in low-temperature (0.5–1 eV) nonideal (0.01 < Γ < 2.8) partially ionized (degree of ionization $\alpha = 10^{-6}$–10^{-1}) inert gas plasmas. The data were obtained by the four-probe method based on the measurement of the Hall potential difference.

Plasma was generated by the dynamic compression of the gas under study ($P_0 = 0.4$ MPa and $T_0 \sim 300$ K) behind the front of powerful shock waves. This technique is a good tool for the production of spatially uniform plasma formations with the characteristic sizes (~1 cm) sufficient for probe diagnostics. For self-similar flows, the conservation laws at the shock-wave discontinuity are written in a simple algebraic form [6], allowing the thermodynamic parameters of a shock-compressed gas to be calculated from the measured flow hydrodynamic parameters.

The initial gas parameters and shock-front velocities (2–3 km/s) were chosen in such a way as to produce weakly nonideal plasma ($\Gamma \ll 1$) behind the front of the incident shock wave and a nonideal (1 < Γ < 2.8) plasma behind the front of the reflected wave. Behind the front of the incident wave, magnetic field freely penetrated into plasma, while, after reflection, a hydrodynamic flow with a "frozen-in" magnetic field was realized.

Plasma was produced using a linear explosive generator [7] with a ~5-cm-i.d. channel. Ammonite of a bulk density was used as an active explosive charge. The overall charge length was 12–15 cm. The plasma parameters were varied by changing the charge density.

Argon or xenon gas was taken for the investigation. Measurements were performed in the region of partial plasma ionization, because this is precisely the range of parameters where the uncertainty in the description of electron concentration and conductivity is the highest.

The method of determining electron concentration is based on the measurement of the Hall potential difference that arises in a medium if an electric current passing through it is not collinear with an external magnetic field. The Hall field is uniquely related to the current density, magnetic induction, and concentration of charged particles. Therefore, measurements of the currents, voltages, and characteristic sizes of the medium allow the determination of electron concentration with an accuracy of the Hall factor. The method of determining low-frequency conductivity is based on the detection of a voltage drop on the conducting section in the medium and the magnitude of electric current passing through it. The geometric factors of a measurement cell were determined in special experimental runs with a

weakly nonideal helium plasma, where the measured parameters can be calculated with a high accuracy.

The scheme of the experimental setup is shown in Fig. 1. The electrode system was attached to organic-glass block 3 inside the generator channel. The transport current I (0.1–1 kA) was passed through a pair of flat electrodes 4 dipped in plasma, and the Hall potential difference U_H (100 mV–20 V) was taken at the pair of point probes 5. The voltage for determining conductivity was taken at the pair of probes 6. The Hall constant and the conductivity were measured both upon plasma-bunch flying up to the block and at the reflection. The accuracy of determining conductivity was ~30%. The Hall constant was determined with an accuracy of ~50%, and the electron concentration was derived from the measured Hall constants. The Hall factor was calculated with allowance made for the magnetic-field magnitude according to [8]. The energy dependence of the pulse relaxation time $\tau(\varepsilon)$ was assumed to be the same as in the conductivity calculations performed in [9].

A pulsed magnetic field (~5 T) was produced by a discharging capacitor bank, applied on the frame of the explosive generator, through a solenoid. With such a geometry of the explosion device, the plasma bunch was moved parallel to the magnetic lines of force at the solenoid center. For the known solenoid geometry, the magnetic induction at its center was calculated from the electric current flowing through it.

To provide galvanic decoupling of the power and measurement circuits, the signal from the measuring probes was fed to the primary winding of a high-frequency transformer, while the signal from the secondary winding was fed to a system of C9-8 oscilloscopes. The transport current was measured using either the Rogowski loop or a low-inductive shunt. To avoid induction produced by high-intensity electric and magnetic fields, the measuring oscilloscopes were placed in a shielded room. In each experiment, two or three independent oscilloscope recordings were made for each parameter with different sensitivities.

The velocity D of the incident shock front was also determined with an accuracy of 1–3% using the basis electrical contact technique. The plasma-plug thickness was calculated from the inert-gas Hugoniot curves [10, 11] with allowance for the distance from the charge tail to the block with probes.

A typical experimental oscillogram is presented in Fig. 2. The signal appeared as the probes were short-circuited with plasma. Before short-circuiting the power probes, the transport current flew through the shunt. Upon reflection, the plasma conductivity increased and its resistance diminished and became even lower than the shunt resistance, so that the current through the plasma increased. The Hall emf in the reflected wave decreased because of an increase in the electron concentration as a result of further plasma heating and compression. The probe voltage for deter-
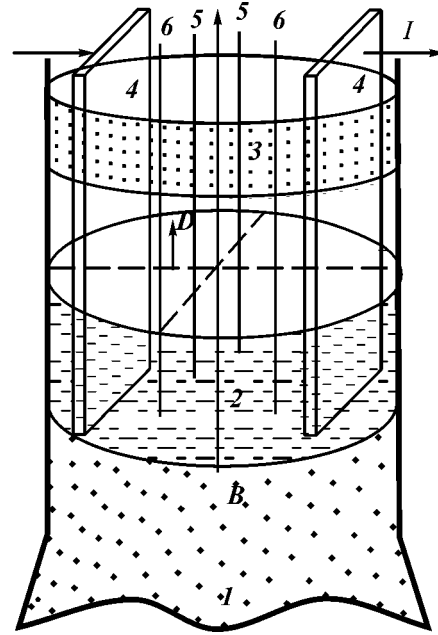

Fig. 1. Scheme of the experiment: (1) detonation products, (2) plasma, (3) block, (4) power probes, (5) probes for measuring the Hall potential difference, and (6) probes for the conductivity measurements.
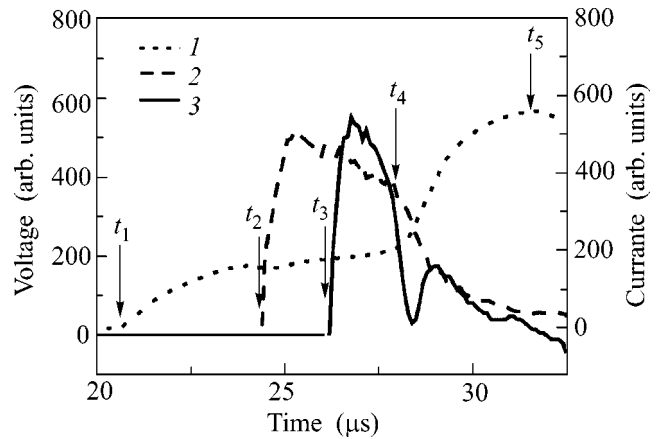

Fig. 2. The typical oscillogram for the experiment with argon plasma: (1) current flowing through plasma, (2) voltage at the probes for determining the conductivity, (3) voltage at the probes for determining the electron concentration, t_1 is the time of plasma arrival at probes 4, t_2 is the time of plasma arrival at probes 6, t_3 is the time of plasma arrival at probes 5, t_4 is the start of reflection, and t_5 is the termination of reflection.

mining the conductivity dropped upon reflection, because the plasma resistance decreased faster than the current increased.

In Fig. 3, the experimental and calculated electron concentrations are compared with each other. The lower groups of curves correspond to the incident wave,
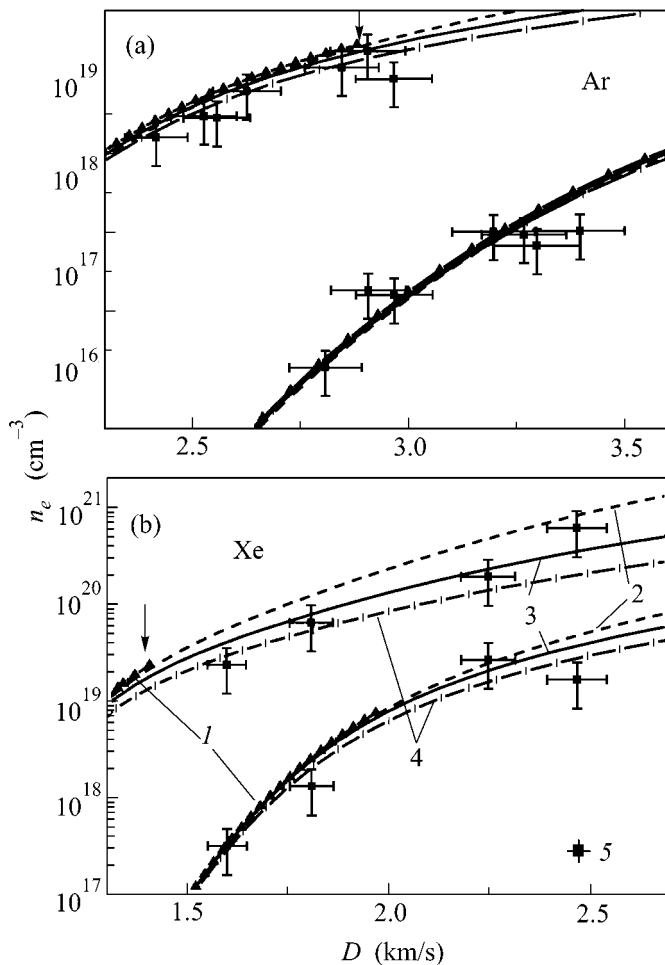
Fig. 3. Electron concentrations in the nonideal argon and xenon plasmas: (*4*) noninteracting-particle approximation with the inclusion of $n = 100$ energy levels in the partition function; (*2*) ring approximation for the grand canonical ensemble with the second-order expansion in Γ and the inclusion of only the ground state in the partition function; (*3*) DGCE with the atomic and ion partition functions calculated for energy levels E_n not exceeding $I - \Delta I$, where ΔI is a drop in the ionization potential; (*1*) Debye–Hückel model; and (*5*) is the experiment.

and the upper curves are for the reflected wave. In the calculations, the effect of Coulomb interaction was described using the following variants of the chemical model [1, 3]: the ideal-plasma model (noninteracting particles); the Debye–Hückel model; and the Debye ring approximation in the grand canonical ensemble (DGCE), which, contrary to the classical Debye–Hückel approximation, is thermodynamically stable at any values of the nonideality parameter (the pressure correction in a Coulomb system does not exceed two thirds of the kinetic part of charged-particle pressure). In addition to various models of Coulomb nonideality, the influence of the bound states on the cumulative thermodynamic quantities and on the calculated electron

concentration n_e was analyzed using several variants of a truncated partition function [3].

In the noninteracting-particle calculations, two variants of the truncated partition function were used. In one of them, up to 100 atomic and ion energy levels were included, and, in another, only the ground state was used. To describe the Coulomb interaction of free charges, the DGCE and the approximation that was close to it but included terms quadratic in the nonideality parameter [12] were used. For both argon and xenon plasmas, the possibilities of Debye–Hückel calculations are limited by the narrow range of low shock-front velocities. The limiting points for which the calculations with this model were made are shown by the arrows in Fig. 3. The higher shock-compression velocities correspond to the larger values of nonideality parameter, for which the model becomes unstable [13] and which are sometimes interpreted as a phase transition [13].

In the range of velocities (2.3–3.5 km/s) and initial pressures (0.400 ± 0.001 MPa) studied, the states behind the front of the incident wave in the shock-compressed argon are moderately nonideal ($\Gamma < 0.3$). In this range of nonideality parameter, the discrepancy between all used theoretical models is small, and they do not contradict the experimental data. After the reflection in argon, Γ reached a value of 1.2 behind the reflected wave. One can see from this comparison that the experimental n_e values behind the front of the reflected wave in argon, on the whole, tend to be smaller than the values obtained with the above-mentioned models. This fact, however, can be explained by the underestimation of the Hall factor, presumably because of the uncertainty in the electron–atom scattering cross sections or the use of incorrect energy dependence for the momentum relaxation time in the calculation of the Hall factor.

The experimental results on measuring n_e in xenon plasma are presented in Fig. 3b. For these studies, the calculated Coulomb nonideality parameter Γ in shock-compressed xenon was as high as 1.3 behind the incident wave and 2.8 behind the reflected wave. Behind the incident wave, the calculated and measured n_e values do not contradict each other. After the reflection, there is a noticeable discrepancy between the calculated and experimental data. One can assume that models 3a and 3b with $\Gamma > 1.5$ overestimate the n_e values, while the DGCE satisfactorily describes the experiment up to $\Gamma = 2.8$.

The choice of a model for the description of transport properties is one of the main problems in the calculation of the conductivity of a partially ionized plasma. In Fig. 4, different methods of calculating the conductivity of a partially ionized xenon and argon plasmas are compared with each other for the thermodynamic model with the DGCE Coulomb interactions. Since the plasma under study was not magnetized (the electron cyclotron frequency $\omega_H \tau < 1$, ω_H), the influ-

This comparison shows that the experimental conductivities are satisfactorily described only by the Frost formula, whereas the other methods overstate the calculated data, compared to the experiment. The curves shown in Fig. 4 retain their shapes also for other thermodynamic models of dense xenon and argon plasmas.

We believe that a more distinct conclusion about the applicability of one or another model can be drawn only after achieving higher accuracy in the determination of experimental data.
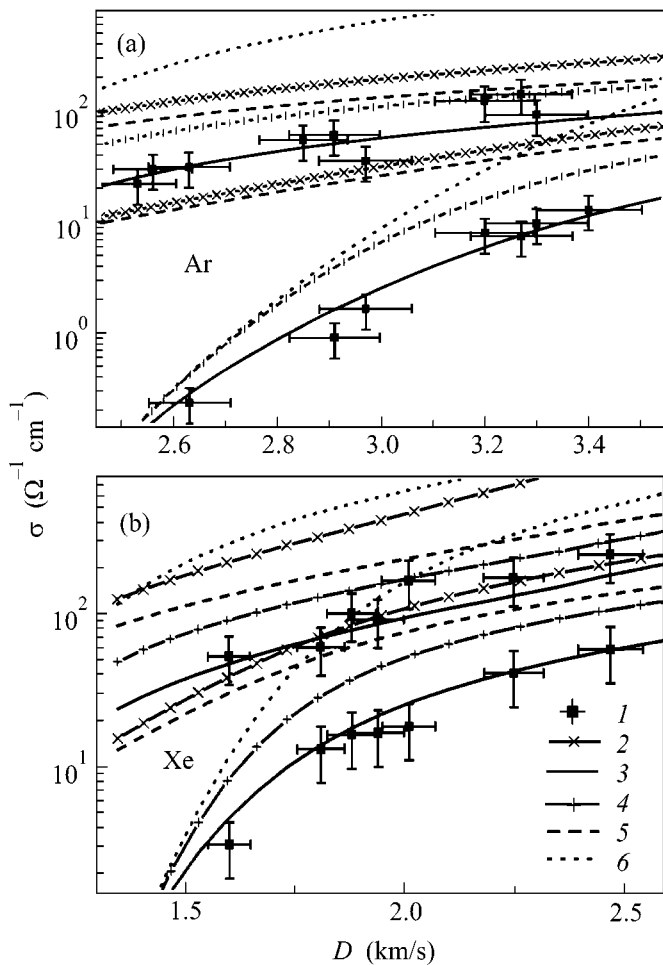
Fig. 4. Conductivity of the nonideal argon and xenon plasmas. Thermodynamic properties correspond to the Debye approximation for the grand canonical ensemble; (*1*) our experimental data; (*2*) calculation by the Spitzer formula; (*3*) calculation by the Frost formula; (*4*) additive approximation; (*5*) Coulomb conductivity component; and (*6*) is the conductivity due to the electron–atom scattering.

ence of a magnetic field on the conductivity was not taken into account in the calculations. Curve *2* corresponds to the calculation of conductivity by the Spitzer formula [14] that was derived for a fully ionized ideal plasma. The result of calculation with the interpolation Frost formula [9] is shown by curve *3*. The electron–atom scattering cross sections were taken from [15]. Curve *4* corresponds to the independent electron scattering by atoms and ions [16]; σ_{ei} is the conductivity Coulomb component corresponding [9] to the electron collisions with ions, σ_{ea} is the conductivity [9] caused by the electron scattering by atoms. The calculations of σ_{ei} and σ_{ea} are represented by curves *5* and *6*. One can see from Fig. 4 that the conductivities calculated in different models of the transport properties of a dense plasma exhibit a considerable scatter.

REFERENCES

1. V. E. Fortov and I. T. Yakubov, *Nonideal Plasma* (Énergoatomizdat, Moscow, 1994).
2. W. Ebeling, Physica (Amsterdam) **43**, 293 (1969).
3. V. K. Gryaznov, I. L. Iosilevskiĭ, Yu. G. Krasnikov, *et al.*, *Thermal Properties of Working Media of Gas-Phase Nuclear Reactor*, Ed. by V. M. Ievlev (Atomizdat, Moscow, 1980).
4. *Plasma Diagnostics*, Ed. by W. Lochte-Holtgreven (North-Holland, Amsterdam, 1968; Mir, Moscow, 1971).
5. *Plasma Diagnostic Techniques*, Ed. by R. H. Huddlestone and S. L. Leonard (Academic, New York, 1965; Mir, Moscow, 1967).
6. Ya. B. Zel'dovich and Yu. P. Raĭzer, *Physics of Shock Waves and High-Temperature Hydrodynamic Phenomena* (Atomizdat, Moscow, 1963; Academic, New York, 1966, 1967), Vols. 1, 2.
7. V. B. Mintsev and V. E. Fortov, Teplofiz. Vys. Temp. **20**, 745 (1982).
8. P. S. Kireev, *Physics of Semiconductors* (Vysshaya Shkola, Moscow, 1969).
9. L. S. Frost, J. Appl. Phys. **32**, 2029 (1961).
10. V. K. Gryaznov, I. L. Iosilevskiĭ, and V. E. Fortov, Prikl. Mekh. Tekh. Fiz. **3**, 70 (1973).
11. V. K. Gryaznov, M. V. Zhernokletov, V. N. Zubarev, *et al.*, Zh. Éksp. Teor. Fiz. **78**, 573 (1980) [Sov. Phys. JETP **51**, 288 (1980)].
12. L. P. Kudrin, *Statistical Physics of Plasma* (Atomizdat, Moscow, 1974).
13. N. N. Kalitkin and L. V. Kuz'mina, Preprint No. 16, IPM AN SSSR (Inst. of Applied Mechanics [or Mathematics], USSR Academy of Sciences, Moscow, 1989).
14. L. Spitzer and R. Harm, Phys. Rev. **89**, 977 (1953).
15. L. S. Frost and A. V. Phelps, Phys. Rev. A **136**, 1538 (1964).
16. S. C. Lin, E. L. Resler, and A. Kantrowitz, J. Appl. Phys. **26** (1), 95 (1955) [Vopr. Raket. Tekh. **1** (31), 13 (1956)].

Translated by V. Sakun

Improvement of Confinement in Tokamaks by Weakening of Poloidal Magnetic Field near Boundary[¶]

V. V. Yankov

Vyoptics, Inc., Allendale, New Jersey, 0767, USA
e-mail: vladimir@vyopticsinc.com
Received April 2, 2003

Theory of turbulent equipartition and experiment indicate that density, pressure, and temperature profiles follow the poloidal magnetic field profile. Therefore, it is suggested to change the magnetic geometry between core and boundary by toroidal conductors and/or plasma current. As a result, density and temperature gradients will become steeper, and stored energy will be higher with low boundary plasma parameters. The suggested new mode of confinement may substantially simplify achieving of ignition. © *2003 MAIK "Nauka/Interperiodica".*

PACS numbers: 52.55.Fa; 52.35.Ra

Turbulent transport remains a major obstacle to achieving controlled nuclear fusion. Despite several decades of experimental and theoretical efforts, even the nature of the transport remains unclear. This paper's suggestion is based on many experimental observations [1–5] and theoretical arguments [6–10] that plasma pressure and density profiles depend on the safety factor profile. Explanation of the dependence on the safety factor profile was reached during the last ten years with the theory of turbulent equipartition (TEP), based on the dominant role of trapped particles [11]. TEP theory describes only a turbulent attractor (density profile and, with lesser accuracy, pressure and temperature profiles) using a Lagrangian invariant (see [6, 7]). TEP theory explains the phenomenon of canonical or resilient profiles in line with [12] and has common features with the concept of marginal stability [13]. TEP theory is limited and says nothing about unstable modes or heat flux, but unstable modes and heat flux are necessary for calculation of profiles, which are given by the TEP attractor directly. TEP is sufficient to design the "turbulent part" of tokamak.

In the first approximation, tokamak plasma is frozen in a poloidal magnetic field only. To be more exact, the theory argued that toroidal and poloidal components of the frozen-in law decay with different rates on the turbulent transport time scale, which makes turbulent convection possible and leads to TEP profiles. Since angular magnetic momentum and angle are drift Hamiltonian canonical variables, TEP density profile is a plateau

$$dN/dM = \text{const} \qquad (1)$$

on the distribution function of the angular magnetic momentum $M = eAr$, where e is a particle charge, A is

the toroidal component of vector potential of poloidal magnetic field, r is radius measured from the main axis of the tokamak, and N is the number of particles inside a magnetic surface $M = \text{const}$. Since particle density is by definition $n = dN/dV$, where V is the volume inside a magnetic surface, the density can be rewritten as

$$n \sim dM/dV. \qquad (2)$$

In small aspect ratio tokamaks, the TEP density profile may be expressed as a function of the well-known safety factor $n \sim 1/q$.

TEP resolved an impressive paradox of particle pinch, long ago observed in all tokamaks. Correlation of the pinching and boundary safety factor was found in [1, 2]. The pinch paradox is that density profiles have a strong maximum at the center, while the source of the particles is at the periphery.

In tokamaks, plasma temperature could be estimated with the empirical 1D adiabatic law

$$T \sim n^2 \sim (dM/dV)^2, \qquad (3)$$

perhaps because electrostatic drift changes mostly longitudinal energy of the trapped particles. Thus, TEP gives the density, temperature, and pressure plasma profiles, while real profiles should be flatter than the ideal TEP profiles. There are many experimental indications that the pressure attractor is more stiff than the density and temperature attractors. This is a natural property of the marginal stability, since instabilities are driven by pressure gradients [13]. Stronger stiffness of the pressure attractor explains the flattening of the density profile during strong central heating in T-10 [14], since density flatness compensates for increased temperature peakedness. It also explains the paradoxical growth of the central temperature during plasma injection at the boundary [15, 16] by compensation of density flatness with temperature peakedness.

[¶] This article was submitted by the author in English.

Experiments indeed have demonstrated that L-mode density and temperature profiles follow the profile of poloidal magnetic flux in every compared tokamak with a consistency almost excluding coincidence [3–5, 7]. Recent comparison of several hundred profiles in TCV tokamak with variable magnetic geometry is especially impressive [4, 5]. While no serious contradictions with theory were found, a more massive comparison of other tokamaks is highly desirable. The basic features of H-mode and reversed shear mode (Internal Transport Barriers) are also in line with the expectations of the TEP theory, since the transport barriers appear where suppression of trapped particle instabilities was predicted [7, 11, 17, 18].

In this paper, we suggest a change in the magnetic geometry, which does not suppress turbulence and does not introduce transport barriers. Instead, turbulence is used to create desirable profiles, to provide a heat and impurity sink, and to tune confinement time. Plasma convection is analogous to the L-mode, but particle and temperature pinch should be stronger [12], providing better isolation of the core plasma. Plasma energy should be higher with the same boundary parameters and energy flux. In accordance with formulas (2) and (3), the ratio of central to boundary pressure is given by the formula

$$\frac{p_c}{p_b} = \frac{(dM_c/dV_c)^3}{(dM_b/dV_b)^3}. \tag{4}$$

As was already mentioned, experiments do not contradict this formula, but it would be useful to extract an empirical power in this ratio from experimental data. The reason is that TEP theories [7–10] differ in the treatment of passing particles and therefore predict slightly different powers. The above ratio grows with weakening of the average boundary poloidal magnetic field, since $B_p \sim dM/dV$. There are two possibilities to improve turbulent pinch, to change plasma current or external coils currents. Both were actually used, without reliance on TEP physics. In TFTR Supershots [19] the ratio (4) was increased by the peakedness of plasma current. The boundary poloidal magnetic field may also be weakened by reversing the toroidal plasma current between core and boundary, but control of the current profile may be difficult. A decrease of $B_p \sim dM/dV$ by external toroidal currents looks more promising. Poloidal bays in an ideally conducting vacuum chamber decrease the average poloidal magnetic field, since it is evidently weaker in the bays. The same magnetic geometry can be provided by coils instead of chamber currents. Poloidal magnetic fields of the bays may or may not include X-points. X-points lead to a logarithm divergency of dV/dM near the separatrix, where the model is not valid. Divertor tokamaks have weakened poloidal magnetic field near the X-point of the separatrix, and therefore JET experiments exhibit strong L-mode plasma gradients near the separatrix [20], in accordance with the above formulas. A stronger effect

may be achieved with a directed design of coils, but this requires a numerical code. To weaken the magnetic field even more, the cross-section of the vacuum chamber may have several bays, the number of the bays being a multiple in dV_b/dM_b.

Peakedness of the toroidal core current may be combined with bays, while excessive current peaking leads to MHD instability. Improvement of confinement by weakening of the poloidal magnetic field near the boundary was observed in the TFTR current ramp-down experiment [21]. While the improvement is not sustainable, it supports the suggested tokamak design.

To calculate energy confinement time, we have all but the connection of boundary plasma parameters with the energy flux. The gain coefficient for core plasma pressure against conventional L-mode could be introduced, according to ratio (4). If boundary parameters are the same, energy confinement time is proportional to the gain coefficient. The same coefficient describes lowering pressure at the edge if central core parameters are fixed. The suggested bays may improve energy confinement several times, but more reliable number requires simulation of poloidal magnetic field with a 2D code. In the presented ideal model, the theoretical gain (4) is unlimited, while after some improvements TEP should be violated by sharp gradients or something else. Note that the discussed effects were theoretically studied in a dipole trap more rigorously [13], because convection in a dipole trap can be described by MHD. Any improvements at the camera wall, such as the use of lithium [22], are complimentary to the suggested improvement.

CONCLUSIONS

Experiment and theory point to plasma pressure dependence on the safety factor. While the exact dependence is not known, TEP profiles of the L-mode can be made more peaked with additional toroidal conductors and a corresponding change of shape of the vacuum chamber. The suggested new mode of confinement is beneficial in several ways: (1) it improves plasma isolation, thus lowering the auxiliary heating and the size of the facility necessary to reach ignition; (2) TEP profiles are resilient and therefore more predictive than transport barriers; (3) turbulent mixing prevents accumulation of helium and impurities in the core plasma, simultaneously delivering hydrogen to the core; (4) turbulence provides a controlled heat sink in ignited plasma; and (5) this new mode of confinement does not require substantially new equipment.

While the idea of improving magnetic confinement by weakening of the magnetic field looks paradoxical, it deserves experimental testing.

The same idea may be applied to a quasihelical (quasisymmetrical) stellarator.

REFERENCES

1. M. Murakami *et al.*, Plasma Phys. Controlled Fusion **28**, 17 (1986).

2. Yu. V. Esipchuk and K. A. Razumova, Plasma Phys. Controlled Fusion **28**, 1253 (1986).

3. D. R. Baker, M. R. Wade, C. C. Petty, *et al.*, Nucl. Fusion **40**, 1003 (2000).

4. H. Weisen and E. Minardi, Europhys. Lett. **56**, 542 (2001).

5. H. Weisen, I. Furno, S. Alberti, *et al.*, Nucl. Fusion **42**, 136 (2002).

6. V. V. Yankov, Nycander, Phys. Plasmas **4**, 2907 (1997).

7. V. V. Yankov, Usp. Fiz. Nauk **167**, 499 (1997) [Phys. Usp. **40**, 477 (1997)].

8. M. B. Isichenko, A. V. Gruzinov, P. H. Diamond, and P. N. Yushmanov, Phys. Plasmas **3**, 1916 (1996).

9. D. R. Baker and M. N. Rosenbluth, Phys. Plasmas **5**, 2936 (1998).

10. I. A. Ivonin, V. P. Pavlenko, and H. Persson, Phys. Plasmas **6**, 3163 (1999).

11. B. B. Kadomtsev and O. P. Pogutse, in *Reviews of Plasma Physics*, Ed. by M. A. Leontovich (Gosatomizdat, Moscow, 1967), Vol. 5.

12. Yu. N. Dnestrovskij, S. E. Lysenko, and K. N. Tarasyan, Nucl. Fusion **35**, 1047 (1995).

13. V. P. Pastukhov and V. N. Chudin, Fiz. Plazmy (Moscow) **27**, 963 (2001) [Plasma Phys. Rep. **27**, 907 (2001)].

14. V. F. Andreev, Yu. N. Dnestrovskij, K. A. Razumova, and A. V. Sushkov, Fiz. Plazmy (Moscow) **28**, 403 (2002) [Plasma Phys. Rep. **28**, 367 (2002)].

15. M. W. Kissick, E. D. Fredrickson, J. D. Callen, *et al.*, Nucl. Fusion **34**, 349 (1994).

16. K. W. Gentle, R. V. Bravenec, G. Cima, *et al.*, Phys. Plasmas **2**, 2292 (1995).

17. H. L. Berg and A. A. Galeev, Phys. Fluids **10**, 441 (1967).

18. A. A. Galeev, R. Z. Sagdeev, and H. V. Wong, Phys. Fluids **10**, 1535 (1967).

19. J. D. Strachan, M. Bitter, A. T. Ramsey, *et al.*, Phys. Rev. Lett. **58**, 1004 (1987).

20. P. H. Rebut, J. R. Bickerton, and B. E. Keen, Nucl. Fusion **25**, 1011 (1985).

21. M. C. Zarnstorff, C. W. Barnes, P. C. Efthimion, *et al.*, in *Proceedings of 13th International Conference on Plasma Physics and Controlled Nuclear Fusion Research, Washington, DC, 1990* (IAEA, Vienna, 1991), Vol. 1, p. 109.

22. L. E. Zakharov, Phys. Rev. Lett. **90**, 045001 (2003).

Theory of the Vertical Hall Effect
in a Dimensionally Quantized System

L. I. Magarill and M. V. Éntin

Institute of Semiconductor Physics, Siberian Division, Russian Academy of Sciences, Novosibirsk, 630090 Russia
e-mail: entin@isp.nsc.ru
Received March 19, 2003

The transverse redistribution of carriers that occurs in a 2D system under the effect of a tangential electric field and a magnetic field possessing a tangential component is studied. It is shown that the redistribution of carriers gives rise to a Hall voltage across isolated electrodes positioned above and under the quantum film. This voltage is determined by the 2D conductivity tensor and the transverse static electric polarizability of the 2D layer. The additional contribution that appears in the vertical Hall voltage because of the electron spin orientation induced by magnetic field and the spin–orbit interaction of electrons with the quantum well potential is determined. © 2003 MAIK "Nauka/Interperiodica".

PACS numbers: 73.50.Jt; 73.63.Hs; 71.70.Ej

INTRODUCTION

Normally, the Hall voltage in a 2D system is directed along the surface and appears under the effect of the normal component of magnetic field. However, it is evident that the tangential component of magnetic field together with the bias electric field may redistribute the electrons across the quantum layer and give rise to a transverse voltage. This effect is relatively weak, because the action of the longitudinal magnetic field on the electrons is reduced due to their quantization. In addition, the arising potential difference cannot be measured as an electromotive force because of the isolation of the system along the quantization axis. Nevertheless, the vertical Hall voltage can be measured by capacitance methods.

The problem of the Hall emf that appears along the inhomogeneity direction in a classical electron gas confined in a parabolic potential well was studied years ago [1]. However, we do not know of any relevant publications considering size-quantized systems. In this paper, we determine the vertical Hall voltage in an arbitrary quantum layer in a tilted magnetic field.

We also study the specific Hall effect caused by the electron spin and the spin–orbit interaction. This effect occurs because the wave functions of electrons with different spin directions and a given longitudinal momentum have different localizations in the vertical direction.

The geometry of the effect under consideration is shown in the figure. We seek the linear response of the potential difference V between the upper and lower electrodes to a homogeneous longitudinal bias electric field $\mathbf{E}$. In the first approximation with respect to the magnetic field $\mathbf{B}$, in an isotropic medium, the response has the form

$$V = \lambda[\mathbf{nB}]\mathbf{E}. \qquad (1)$$

Here, $\mathbf{n} = (0, 0, 1)$ is the normal to the plane of the system, $\mathbf{E} = (E_x, E_y, 0)$, and $\mathbf{B} = (\mathbf{B}_\parallel, B_z)$. If the magnetic field is not small, the symmetry with respect to the reflection of coordinates and rotation of the (x, y) plane yields the phenomenological expression

$$V = \mathbf{\Lambda}\mathbf{E} = \lambda_1([\mathbf{nB}]\mathbf{E}) + \lambda_2(\mathbf{Bn})(\mathbf{BE}), \qquad (2)$$

where the coefficients $\lambda_{1,2}$ are functions of B_z^2 and $B_\parallel^2$. The coefficient λ_1 changes sign under the time reversal and, hence, is related to dissipation, while λ_2 remains unchanged and, in the general case, is unrelated to scattering.

BASIC EXPRESSIONS FOR THE RESPONSE

We assume that the electron interaction is weak and only the lower subband of the transverse quantization is filled. The first condition requires that the inequality $N_s a_B^a \gg 1$ be satisfied, where N_s is the surface electron
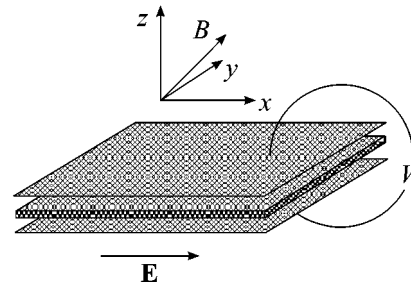

Fig. 1.

concentration and $a_B = me^2/\kappa$ is the effective Bohr radius ($-e$ and m are the electron charge and mass and κ is the dielectric constant of the medium). The second condition is satisfied when $\pi N_s/m < \varepsilon_1 - \varepsilon_0$, where ε_n is the nth level of the transverse quantization.

To determine the correction to the charge density $\rho(z)$ in the linear approximation with respect to $\mathbf{E}$, one can use the Kubo formula [2]. The Poisson equation yields the expression for the induced potential difference V between the upper and lower boundaries of the film:

$$V = \frac{4\pi}{\kappa} \int_{-\infty}^{\infty} z\rho(z)dz. \tag{3}$$

From Eq. (3) with the use of the Kubo formula, we obtain the following expression for the vector $\mathbf{\Lambda}$:

$$\mathbf{\Lambda} = \frac{4\pi e^2}{\kappa S}\mathrm{Re}\int_{-\infty}^{\infty}d\varepsilon\int_{-\infty}^{\infty}\frac{d\varepsilon'}{\delta + i(\varepsilon - \varepsilon')}\frac{f(\varepsilon) - f(\varepsilon')}{\varepsilon' - \varepsilon}\mathbf{D}(\varepsilon, \varepsilon'),$$

$$(\delta \longrightarrow +0), \tag{4}$$

$$\mathbf{D} = \langle\mathrm{Sp}(z\delta(\varepsilon - \mathcal{H})\mathbf{v}\delta(\varepsilon' - \mathcal{H}))\rangle, \tag{5}$$

where $\mathbf{v}$ is the electron velocity operator, S is the area of the system, $f(\varepsilon) = 1/(\exp((\varepsilon - \zeta)/T) + 1)$ is the Fermi function, and $\hbar = 1$. The angular brackets denote averaging over impurities. The Hamiltonian $\mathcal{H}$ of the system includes the quantum well potential $U(z)$, the interaction with scatterers $U_{im}(\mathbf{r})$, and the spin–orbit interaction with the walls of the well H_{SO}:

$$\mathcal{H} = \frac{(\mathbf{p} + e/c\mathbf{A})^2}{2m} + U(z)$$

$$+ U_{im}(\mathbf{r}) - g\mu_B\mathbf{Bs} + H_{SO} = H + H_{SO}. \tag{6}$$

Here, $\mathbf{p}$ is the momentum operator, $\mathbf{s}$ is the spin operator, g is the Landé factor, and μ_B is the Bohr magneton. The interaction with magnetic field is determined by the vector potential $\mathbf{A} = \mathbf{A}_\perp + \mathbf{A}_\parallel$, where $\mathbf{A}_\perp = (0, B_z x, 0)$ and $\mathbf{A}_\parallel = z[\mathbf{B}_\parallel \mathbf{n}]$. The spin–orbit interaction of electrons with the quantum well potential $U(z)$ is determined by the expression

$$H_{SO} = 2\alpha F[\mathbf{sn}](\mathbf{p} + e/c\mathbf{A}), \tag{7}$$

where $F(z) = \partial U/\partial z$. With allowance for the spin–orbit interaction, the velocity operator has the form

$$\mathbf{v} = (\mathbf{p} + e\mathbf{A}/c)/m + 2\alpha[\mathbf{sn}]F.$$

We assume that the distance between the size-quantized levels is great compared to the cyclotron frequency and the scattering frequency. Then, the effect of the longitudinal component of magnetic field on the electron motion in the plane of the system can be taken into account only in the linear approximation: $H \approx \bar{H} + ze(\mathbf{v}[\mathbf{B}_\parallel \mathbf{n}])/c$, where $\bar{H}$ does not involve the longitudi-

nal component of magnetic field. The spin–orbit interaction is also assumed to be weak and is taken into account through a correction that is linear in α. At the same time, the effect of the normal component of magnetic field B_z and the splitting of the spin states are described exactly. The spin-flip scattering is ignored in our calculations.

THE VERTICAL HALL EFFECT IN THE ABSENCE OF SPIN–ORBIT INTERACTION

First, we determine the transverse voltage without regard for the spin–orbit interaction. Performing the expansion in the longitudinal component of magnetic field, we obtain

$$D_i = \frac{e}{4\pi^2 mc}[\mathbf{nB}_\parallel]_j$$

$$\times\langle\mathrm{Sp}\{2m[G^a(\varepsilon')v_j zG^a(\varepsilon') - G^r(\varepsilon')v_j zG^r(\varepsilon')] \tag{8}$$

$$\times z(G^a(\varepsilon) - G^r(\varepsilon))v_i$$

$$+ z(G^a(\varepsilon') - G^r(\varepsilon'))z(G^a(\varepsilon) - G^r(\varepsilon))\}\rangle.$$

Here, $G^{r,a} = (\varepsilon - \bar{H} \pm i\delta)^{-1}$ and $\mathbf{v} = (\mathbf{p} + e\mathbf{A}_\perp/c)/m$ is the velocity operator in the absence of both spin–orbit interaction and longitudinal magnetic field. Without loss of generality, we can measure the z coordinate with respect to the mean value of the ground state in the quantum well; i.e., we set $z_{00} = 0$. On the assumption that the scattering is weak compared to the transverse level spacing (the smallness parameter is the ratio of the subband-nondiagonal matrix elements $(U_{im}(\mathbf{r}))_{nm}$ to the level spacing), the Green's functions can be considered as diagonal in the transverse states: $G_{nm}(\varepsilon) \approx \delta_{nm}G_n(\varepsilon)$. The typical term in the trace in Eq. (8) has the form

$$G_n(\varepsilon')v_j z_{nm}G_m(\varepsilon')z_{mn}G_n(\varepsilon)v_i.$$

The characteristic energies entering the final result lie in the lower subband of the transverse quantization, under the chemical potential. The principal terms are those with $n = 0$, in which the Green's functions are localized near the poles. The presence of the transverse coordinate in the trace in Eq. (8) results in $G_m(\varepsilon')$ being far from the pole. Since the difference in the transverse energies exceeds the interaction with magnetic field, the Green's function $G_m(\varepsilon')$ can be replaced by $1/(\varepsilon_0 - \varepsilon_m)$. As a result, after some simplification, we arrive at the expression

$$\Lambda_i = \frac{8\pi e}{\kappa c}[\mathbf{nB}_\parallel]_k\sigma_{ki}\sum_{n\neq 0}\frac{z_{0n}^2}{\varepsilon_n - \varepsilon_0}, \tag{9}$$

where σ_{ki} is determined by the formula

$$\sigma_{ki} = \frac{e^2}{S}\mathrm{Re}\int\limits_{-\infty}^{\infty}d\varepsilon\int\limits_{-\infty}^{\infty}\frac{d\varepsilon'}{\delta + i(\varepsilon - \varepsilon')}\frac{f(\varepsilon) - f(\varepsilon')}{\varepsilon' - \varepsilon}$$

$$\times \langle\mathrm{Sp}\{\delta(\varepsilon' - \overline{H})v_k\delta(\varepsilon - \overline{H})v_i\}\rangle. \tag{10}$$

One can readily see that σ_{ik} coincides with the conductivity tensor of the 2D system in magnetic field. The sum in Eq. (10) can be related to the transverse polarizability of the quantum layer per one electron [3]:

$$\chi = 2e^2\sum_{n\neq 0}\frac{|z_{n0}|^2}{\varepsilon_n - \varepsilon_0}.$$

In the case of a parabolic quantum well with the potential $U(z) = m\Omega^2z^2/2$, the aforementioned polarizability has the form $\chi = e^2/m\Omega^2$; for a rectangular quantum well of width d with infinite walls, we obtain $\chi = e^2md^4(15 - \pi^2)/12\pi^4$.

In terms of the current density $j_i = \sigma_{ij}E_j$, the voltage is expressed as

$$V = \frac{4\pi\chi}{\kappa}\frac{1}{ec}[\mathbf{nB}]\mathbf{j}. \tag{11}$$

According to Eq. (11), the transverse Hall voltage is completely determined by the parameters of the quantum well, the longitudinal current, and the planar component of magnetic field that is perpendicular to this current.

In the particular case of a parabolic potential, for a strictly longitudinal magnetic field, Eq. (11) leads to a result coinciding with that obtained in [1] (Eq. (20) from [1]) for a classical electron gas.

Formula (11) is valid without any limitations imposed on the value of B_z. In particular, it can be used both at $B_z = 0$ and in the quantum Hall regime. The longitudinal component must satisfy the condition $eB_\parallel d^2/c \ll 1$.

For a quantum well on the basis of GaAs/AlGaAs with the thickness $d = 5\times 10^{-7}$ cm, the voltage in a longitudinal magnetic field is estimated as V [V] $\approx 3\times 10^{-6} B$ [T] j [A/cm]. A transverse voltage measurement makes sense when the corresponding electric field exceeds the bias field; otherwise, a small "bias" of the structure will give rise to a transverse electric field in the absence of magnetic field. At $B_z = 0$, the analytical estimate of the ratio of these electric field components yields the quantity $V/dE \sim N_Sd^2\omega_H\tau d/a_B$, where $\omega_H = eB/mc$ and τ is the electron relaxation time. In a sufficiently strong magnetic field, this parameter may exceed unity.

In the quantum Hall regime, at the plateau, the following expression is obtained from Eq. (11): $V = \mathbf{B}_\parallel EN(e^2/h)(4\pi\chi/\kappa ec)$, where N is the filling factor of the Landau levels.

SPIN HALL EFFECT

Although the spin–orbit interaction is weak, the correction due to this interaction may be considerable, because the orbital contribution decreases with the layer thickness owing to the transverse quantization.

Let us consider the physical origin of the spin Hall effect. If the influence of magnetic field on the orbital motion is neglected, the states in the quantum well may be classified according to the spin projection $s = \pm 1/2$ on the direction of the magnetic field $\mathbf{B}$. The averaging of the spin–orbit interaction Hamiltonian over the state with a given s determines the effective potential energy $U(z) + 2\alpha sdU/dz(\mathbf{p}[\mathbf{Bn}])/B \approx U(z + 2\alpha s\mathbf{p}[\mathbf{Bn}]/B)$. This means that the potential wells for electrons with the spin projections $s = \pm 1/2$ are shifted in the vertical and the shift depends on the longitudinal momentum of the electron. The magnetic field determines the spin orientation, and the bias electric field determines the momentum orientation. As a result, a vertical redistribution of charge carriers takes place.

In the lowest order with respect to the small parameters, the terms that contain the spin–orbit interaction constant and do not involve the effect of the longitudinal magnetic field on the in-plane motion are combined with the orbital contribution determined above. In what follows, we take into account the spin–orbit interaction of electrons accurate to the first order in the constant α. Corrections appear because of both the expansion of the δ functions from Eq. (4) in terms of H_{SO} and the spin–orbit correction to the velocity operator. Performing the expansion, we determine the contribution to the quantity $\mathbf{D}$ that is caused by the spin–orbit interaction:

$$D_i^{SO} = \frac{\alpha}{2\pi^2B^2}[\mathbf{nB}_\parallel]_j\langle\mathrm{Sp}\{\mathbf{sB}[2m(G^a(\varepsilon')v_jFG^a(\varepsilon')$$

$$- G^r(\varepsilon')v_jFG^r(\varepsilon'))z(G^a(\varepsilon) - G^r(\varepsilon))v_i \tag{12}$$

$$+ F(G^a(\varepsilon') - G^r(\varepsilon'))z(G^a(\varepsilon) - G^r(\varepsilon))]\}\rangle.$$

After some simplification as in Eq. (9), we use the identity $\sum_{n\neq 0}z_{0n}F_{0n}(\varepsilon_n - \varepsilon_0)^{-1} = 1/2$ to obtain the expression

$$V^{SO} = \frac{2m\pi\alpha}{\kappa B}[\mathbf{nB}_\parallel]_i$$

$$\times(\sigma_{ik}^0(\zeta + \omega/2) - \sigma_{ik}^0(\zeta - \omega/2))E_k. \tag{13}$$

Here, $\omega = g\mu_BB$, and $\sigma_{ik}^0(\zeta)$ is the conductivity tensor in the absence of spin splitting. The latter tensor is considered as a function of the chemical potential and is related to the conductivity in the presence of splitting by the finite-difference relation $2\sigma_{ik}(\zeta) = \sigma_{ik}^0(\zeta + \omega/2) +$

$\sigma^0_{ik}(\zeta - \omega/2)$. If the spin splitting is small, the expression for the voltage takes the form

$$V^{SO} = \frac{2\pi\alpha mg\mu_B}{\kappa}[\mathbf{nB}_\parallel]_i\frac{\partial\sigma_{ik}}{\partial\zeta}E_k. \qquad (14)$$

We stress that the results obtained above do not use the assumptions about the absence of electron scattering or about the classical range of magnetic field. The product of the cyclotron frequency by the relaxation time $\omega_H\tau$ and the parameters $\zeta\tau$ and ω_H/ζ are assumed to be arbitrary. The impurity scattering is assumed to be small only compared to the distance between the transverse quantization levels, but this parameter is assumed to be small in any case when a system is considered as two-dimensional. Except for this limitation, the formulas obtained above are exact. They are applicable in both the linear regime in magnetic field and the quantum Hall regime in a transverse magnetic field.

At the same time, our results take into account the finite thickness of the quantum layer. The trace of the transverse wave functions remains in only one parameter, namely, in the transverse polarizability of the 2D layer in the external homogeneous electric field. Other quantities do not depend on the structure of the transverse wave function.

REFERENCES

1. L. I. Magarill and A. V. Chaplik, Zh. Éksp. Teor. Fiz. **74**, 2196 (1978) [Sov. Phys. JETP **47**, 1143 (1978)].

2. R. Kubo, J. Phys. Soc. Jpn. **12**, 570 (1957).

3. L. D. Landau and E. M. Lifshitz, *Course of Theoretical Physics*, Vol. 3: *Quantum Mechanics: Non-Relativistic Theory*, 4th ed. (Nauka, Moscow, 1989; Pergamon, New York, 1977).

Translated by E. Golyamina

Observation of Plasmon–Polariton Modes in Two-Dimensional Electron Systems

I. V. Kukushkin[1, *], D. V. Kulakovskiĭ[1, 2], S. A. Mikhaĭlov[2], J. H. Smet[2], and K. von Klitzing[2]

[1] *Institute of Solid-State Physics, Russian Academy of Sciences, Chernogolovka, Moscow region, 142432 Russia*
[2] *Max-Planck-Institut für Festkörperforschung, 70569 Stuttgart, Germany*
*e-mail: kukush@issp.ac.ru
Received March 24, 2003

A manifestation of retardation effects, which were predicted theoretically more than 35 years ago, is revealed for the first time in the plasma excitation spectrum of a two-dimensional electron system with a high electron mobility. It is shown that a significant decrease in the resonant plasma frequency due to a hybridization of the plasma and light modes is observed in zero magnetic field. An unusual dependence of the frequency of the hybrid cyclotron–plasmon mode on the magnetic field has been observed in a perpendicular magnetic field. The experimental results are in good quantitative agreement with the theory. © 2003 MAIK "Nauka/Interperiodica".

PACS numbers: 71.36.+c; 73.20.Mf

Natural plasma oscillations in two-dimensional electron systems were predicted by Stern in 1967 [1] and were observed experimentally approximately 10 years later in the electron system on the surface of liquid helium [2] and in silicon metal–insulator–semiconductor structures [3, 4]. These and numerous subsequent experiments (see the reviews [5, 6]) quantitatively confirmed the phonon dispersion predicted in [1, 7]

$$\omega_p^2(q) = \frac{2\pi n_s e^2}{m^* \epsilon(q)} q, \qquad (1)$$

where n_s and m^* are the concentration and the effective mass of two-dimensional electrons and $\epsilon(q)$ is the permittivity of the surrounding medium. Plasma excitations in a variety of semiconductor structures, such as silicon metal–insulator–semiconductor structures or GaAs/AlGaAs heterojunctions, were detected by IR spectroscopy. The plasmon wave vector (with a typical magnitude of 10^4 cm^{-1}) in these experiments was specified by the period of the metal lattice, which provided the interaction between plasma excitations and the electromagnetic field.

The plasmon spectrum described by Eq. (1) was obtained within the quasielectrostatic approximation. The electrodynamic effects on the spectrum of plasma oscillations were studied theoretically in the work by Stern and also in the subsequent publications [8–11]. Retardation effects become essential at small quasimomenta of plasmons, when their phase velocity approaches the velocity of light. For the typical parameters of GaAs/AlGaAs heterostructures, this occurs at $q = 10$ cm^{-1} and a frequency of 10–30 GHz. Some years

ago, two-dimensional plasmons could not be observed at such low frequencies, because the quality of the structures was poor and, for this reason, the linewidth of plasma resonances was about 100 GHz. In the last ten years the quality of the samples has been improved significantly: the mobility of two-dimensional electrons has been enhanced by several orders of magnitude, and the linewidth of plasma resonances has decreased down to 2–10 GHz. These improvements allow the plasma resonance to be studied at low frequencies and at small quasimomenta and open up possibilities for studying retardation effects. The theory [9] predicts that a system of high-mobility two-dimensional electrons must exhibit weakly damped hybrid plasmon–polariton modes (bound states of plasmons with light). However, these hybrid modes have not been observed experimentally until the present time. In this work, we report the observation of these plasmon–polariton modes and a study of their dispersion and properties in a perpendicular magnetic field.

We studied several single GaAs/AlGaAs quantum wells with both large and small concentrations of two-dimensional electrons (from 0.2×10^{11} cm^{-2} to 6.6×10^{11} cm^{-2}). In all the structures, the well width was 25 nm, and the mobility of electrons varied from 0.3 to 5×10^6 cm^2 V^{-1} s^{-1}. The linewidths of resonant microwave absorption in all the structures studied did not exceed 5 GHz and were 1 GHz in the best structures. This allowed us to measure the plasmon–cyclotron resonance at record low microwave frequencies (10–50 GHz). In order to measure the dimensional plasma resonance, we manufactured circular disks with diameters of 0.1, 0.2, 0.3, 0.4, 0.5, 0.6, 1, 2, and 3 mm [12, 13] and used the optical detection method based on the high
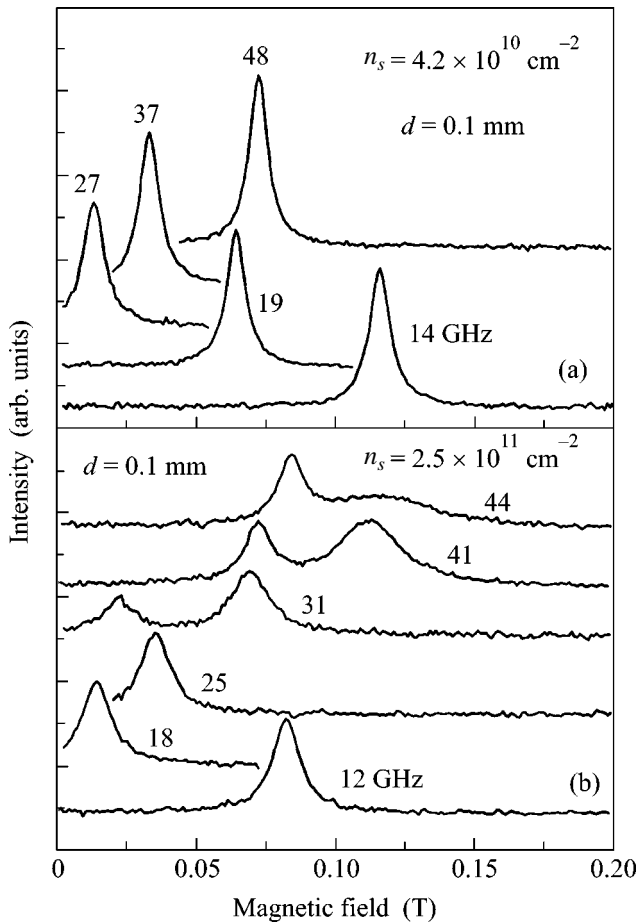
Fig. 1. Optically detected dimensional magnetoplasma resonance spectra of a two-dimensional electron gas measured at various microwave excitation frequencies for mesa structures with diameters (a) $d = 0.1$ mm and (b) $d = 1$ mm in a GaAs/AlGaAs quantum well with a well width of 250 Å.

sensitivity of luminescence spectra to heating of the two-dimensional electron system [14, 15]. The luminescence spectra were recorded using a CCD camera and a dual spectrometer, which provided a spectral resolution of 0.03 meV. A stabilized semiconductor laser with a wavelength of 750 nm and a power of 0.1 mW was used for photoexcitation. An HP-83650B generator was used as a source of microwave radiation in the range 10–50 GHz. The samples were placed at a maximum of the microwave electric field inside a 16-mm waveguide, which was short-circuited near the sample by a movable metal plug. The output microwave radiation power of the generator varied from 10 nW to 0.2 mW. The other experimental details can be found elsewhere [12, 13, 15]. Characteristic resonant absorption spectra for samples differing in the electron density and the mesa diameter are displayed in Fig. 1. The spectra exhibit both an edge magnetoplasmon (observed at low frequencies $\omega < \omega_p$) and a bulk magnetoplasmon (at $\omega > \omega_p$). The two-dimensional electron density was measured by the sensitive spectroscopic method, which

allowed the concentration to be measured to better than 10^{-3}. This was provided by an exceptionally small peak width in the spectrum of luminescence noise appearing in the quantum Hall effect regime at integer filling factors [16].

The magnetic-field dependence of the resonant absorption frequency measured for samples differing in the electron density and the mesa diameter is shown in Figs. 2a and 2b. When measuring the resonant absorption contour, we preferred to sweep the magnetic field at a fixed frequency rather than the reverse, because it was impossible to provide the constancy of the microwave power in the case of frequency sweep. The results obtained for two samples with a relatively small concentration of two-dimensional electrons (0.46×10^{11} cm^{-2}) and for small disk diameters (0.1 and 0.2 mm) are presented in Fig. 2a. The spectra measured demonstrate a typical pattern [17–20] of magnetoplasma absorption consisting of two modes, which were described in detail theoretically [17, 18, 21–24]. The frequency of the upper mode, which corresponds to the bulk magnetoplasmon, asymptotically tends to the cyclotron frequency in the limit of an infinite magnetic field. The frequency of the lower mode, which corresponds to the edge magnetoplasmon, tends to zero in the limit of strong magnetic fields. At $B = 0$, the frequencies of both modes coincide, and this frequency markedly differs from the frequency $\omega_0 = (2\pi n_s e^2/m^* R\epsilon)^{1/2}$ (shown by an arrow in the figure), which follows from Eq. (1) if q in this equation is replaced by $1/R$.

The situation changes markedly if the dimensional magnetoplasma resonance is studied in samples with a high concentration of electrons and with a large mesa diameter. The results measured for a sample with $n_s = 2.54 \times 10^{11}$ cm^{-2} and $d = 1$ mm are shown in Fig. 2b. In this figure, it is evident that several new features are observed at these parameters: (a) the resonance frequency measured at $B = 0$ is markedly lower than ω_0; (b) the slope $|d\omega_\pm/d\omega_c|$ at $B \longrightarrow 0$ is significantly smaller than the standard value 1/2; and (c) at a certain finite value of the magnetic field, the upper magnetoplasma mode intersects the line corresponding to the cyclotron resonance and demonstrates a strange zigzag behavior, which is accompanied by the appearance of one more high-frequency mode. After crossing the cyclotron resonance line, the width of the absorption line starts to increase markedly, as is evident in Fig. 1. A further increase in the electron density and (or) in the mesa diameter leads to an even stronger manifestation of the above features [25].

A simple qualitative analysis allowed us to suggest that the observed phenomena are associated with retardation effects. Actually, the dimensionless parameter $A = \omega_0 \sqrt{\epsilon} R/c$, defined as the ratio of the plasmon frequency to the frequency of light with the same wave vector $q = 1/R$, can serve as an indicator of the degree
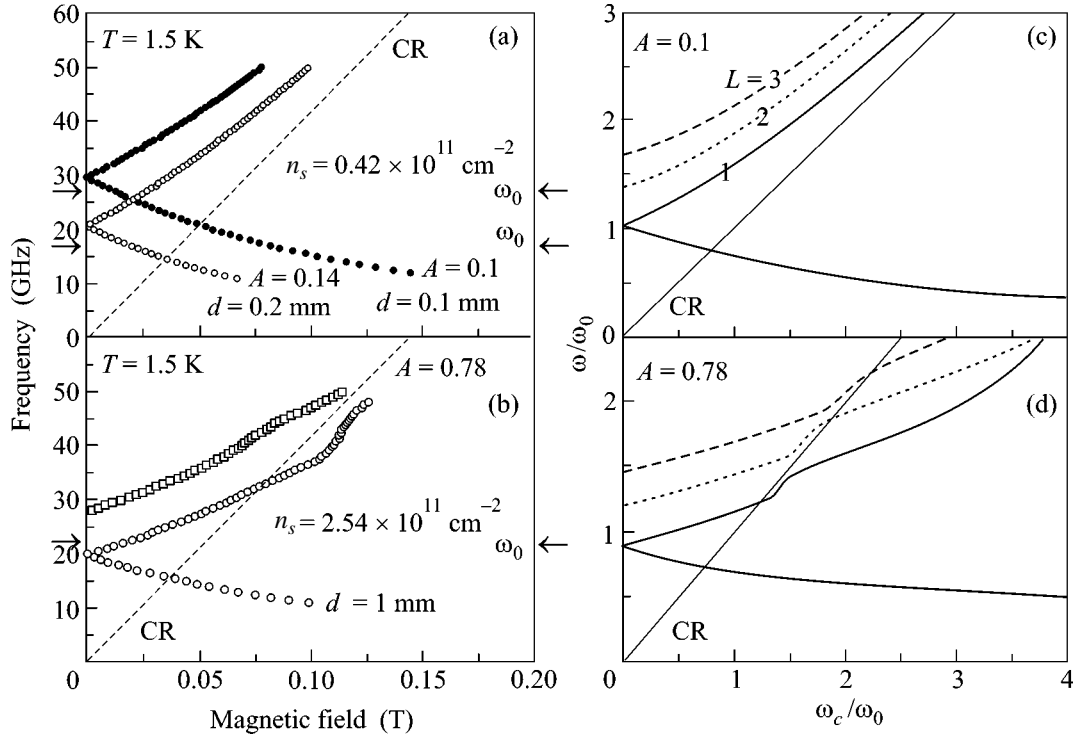
Fig. 2. Field dependence of magnetoplasma resonances: (a) and (b) experimental results obtained for samples with different electron densities and different mesa diameters; (c) and (d) theoretical calculations of the lowest ($n = 1$) modes with $L = 1, 2$, and 3 for parameters A obtained experimentally. Edge magnetoplasma modes for $L = 2$ and 3 are not shown on the plots.

of importance of retardation effects. This parameter grows with increasing n_s and R, because $A \sim \sqrt{n_s R}$, and it has never exceeded 0.1–0.15 in all the previous experimental studies. For the two samples shown in Fig. 2a, parameter A equaled 0.1 and 0.14 for diameters $d = 0.1$ and $d = 0.2$ mm, respectively, so that no manifestation of the finite velocity of light could be expected in the spectra. On the contrary, for the case shown in Fig. 2b, parameter A equaled 0.78; therefore, it was reasonable to associate the observed phenomena with retardation effects. In order to corroborate this assumption, we carried out calculations of the resonant magnetoplasma modes in a two-dimensional disk.

The electrostatic potential $\varphi(\mathbf{r}, z)$ and the vector potential $\mathbf{A}(\mathbf{r}, z)$ over all space must obey the Maxwell equations

$$\Delta \mathbf{A}(\mathbf{r}, z) - \frac{1}{c^2}\frac{\partial^2 \mathbf{A}(\mathbf{r}, z)}{\partial t^2} = -\frac{4\pi}{c}\mathbf{j}(\mathbf{r})\delta(z),$$

$$\Delta\varphi(\mathbf{r}, z) - \frac{1}{c^2}\frac{\partial^2\varphi(\mathbf{r}, z)}{\partial t^2} = -4\pi\rho(\mathbf{r})\delta(z). \tag{2}$$

Let us make the Fourier transformation with respect to variables $(\mathbf{r}, t)$. Using the known relations between the current in a two-dimensional electron gas, the electron density, and the total electric field in the plane $z = 0$

$$j_\alpha(r, \theta) = \sigma_{\alpha\beta}(r, \theta)E_\beta^{\text{tot}}(r, \theta),$$

$$\partial\rho/\partial t + \text{div}\,\mathbf{j} = 0, \tag{3}$$

for the cylindrically symmetric case, when the eigenmodes of the system are characterized by the angular momentum l and the radial quantum number n (see [18, 22, 26–28]), we obtain the following system of equations from Eqs. (2):

$$E_{r,l}^{\text{ind}}(r) = \frac{2\pi i\omega}{c^2}\int_0^\infty \frac{qdq}{\chi_{q\omega}}J_{|l|}(qr)\int_0^\infty r'dr' J_{|l|}(qr')$$

$$\times [\sigma_{rr}(r')E_{r,l}^{\text{tot}}(r') + \sigma_{r\theta}(r')E_{\theta,l}^{\text{tot}}(r')]$$

$$-\frac{2\pi}{i\omega}\frac{\partial}{\partial r}\int_0^\infty \frac{qdq}{\chi_{q\omega}}J_{|l|}(qr)\int_0^\infty r'dr' J_{|l|}(qr')$$

$$\times \left\{\frac{1}{r'}\frac{\partial}{\partial r'}(r'[\sigma_{rr}(r')E_{r,l}^{\text{tot}}(r') + \sigma_{r\theta}(r')E_{\theta,l}^{\text{tot}}(r')])\right.$$

$$\left. + \frac{il}{r'}[\sigma_{\theta r}(r')E_{r,l}^{\text{tot}}(r') + \sigma_{\theta\theta}(r')E_{\theta,l}^{\text{tot}}(r')]\right\}, \tag{4}$$

$$E_{\theta,l}^{\text{ind}}(r) = \frac{2\pi i\omega}{c^2}\int_0^\infty \frac{qdq}{\chi_{q\omega}}J_{|l|}(qr)\int_0^\infty r'dr' J_{|l|}(qr')$$
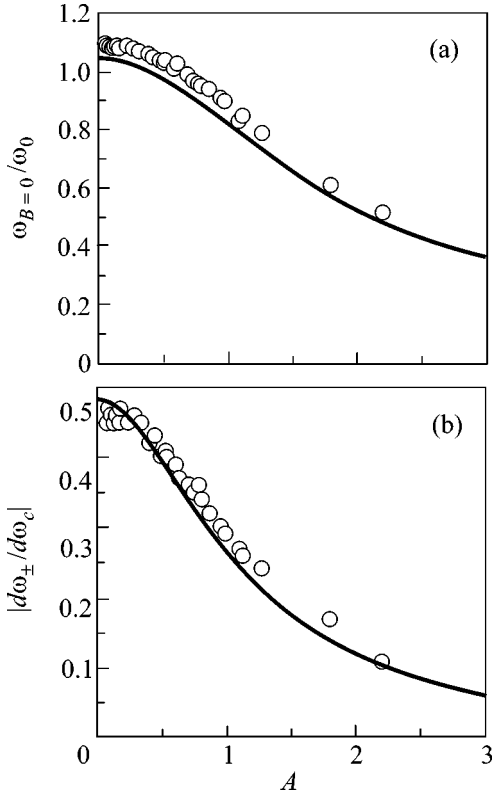
Fig. 3. (a) Normalized resonance frequency $\omega_{B=0}/\omega_0$ at $B = 0$ and (b) its slope $|d\omega_\pm/d\omega_c|$ at $B \longrightarrow 0$ as functions of the dimensionless parameter $A = \omega_0 \sqrt{\epsilon}\, R/c$, $\omega_0 = (2\pi n_s e^2/m^* R \epsilon)^{1/2}$. Experimental data are shown by circles, and theoretical data are shown by a solid line.

$$\times \left[\sigma_{\theta r}(r') E_{r,l}^{\mathrm{tot}}(r') + \sigma_{\theta\theta}(r') E_{\theta,l}^{\mathrm{tot}}(r') \right]$$

$$- \frac{2\pi}{i\omega}\frac{il}{r}\int\limits_0^\infty \frac{q\,dq}{\chi_{q\omega}} J_{|l|}(qr) \int\limits_0^\infty r'dr' J_{|l|}(qr')$$

$$\times \left\{ \frac{1}{r'}\frac{\partial}{\partial r'}(r'[\sigma_{rr}(r')E_{r,l}^{\mathrm{tot}}(r') + \sigma_{r\theta}(r')E_{\theta,l}^{\mathrm{tot}}(r')]) \right.$$

$$\left. + \frac{il}{r'}[\sigma_{\theta r}(r')E_{r,l}^{\mathrm{tot}}(r') + \sigma_{\theta\theta}(r')E_{\theta,l}^{\mathrm{tot}}(r')] \right\},$$

with the accessory condition for the radial current component at the disk edge

$$j_r = \sigma_{rr}(R)E_{r,l}^{\mathrm{tot}}(R) + \sigma_{r\theta}(R)E_{\theta,l}^{\mathrm{tot}}(R) = 0. \qquad (5)$$

By analogy with [22], we solved the system of Eqs. (4) with the additional condition (5) by the method of decompositing the unknown components of the total electric field $E_{r,l}^{\mathrm{tot}}(r)$ and $E_{\theta,l}^{\mathrm{tot}}(r)$ in an orthonormalized basis set and determined the magnetic-field depen-

dences for the magnetoplasmon energies in a disk with a stepped potential profile. The lowest ($n = 1$) mode with $L \equiv |l| = 1$, 2, and 3 for the parameters A obtained experimentally is presented in Figs. 2c and 2d. It is evident that the theory and experiment are in good agreement. A quantitative comparison of the measured and calculated frequencies allowed us to infer that the upper bulk magnetoplasma mode observed at $A = 0.78$ was the mode with the higher angular momentum $L = 2$ and the lowest $n = 1$ (modes with $n > 1$ have high frequencies).

Further we will concentrate on the quantitative analysis of our results in the region of small magnetic fields $B \longrightarrow 0$. The dependence of the ratio $\omega_{B=0}/\omega_0$ on the parameter A measured for seven samples with various concentrations and radii is presented in Fig. 3a. This ratio starts from 1.1 at small values of A and decreases down to 0.5 as A increases up to 2.20. The solid line in the figure represents the results of theoretical calculations. At $A = 0$, our result coincides with the result obtained by Fetter [22] in the quasistatic approximation. The theory and experiment are in good agreement, and the small (~4%) discrepancy can be related to the inaccuracy of the determination of the effective dielectric constant $\bar{\epsilon}$ of the medium, which in the real system can depend on the size of the sample, the presence of the waveguide, etc. Figure 3b demonstrates the dependence of the slope $|d\omega_\pm/d\omega_c|$ at $B \longrightarrow 0$ on the parameter A. It is readily seen that the slope is even more sensitive to an enhancement of retardation effects. An increase in the dimensionless parameter from 0 to 2.2 leads to a decrease in the slope by a factor of 4. The theoretical results shown in this figure with a solid line are in very good agreement with the experiment.

Finally, we will analyze our experimental data in order to qualitatively verify the two-dimensional plasmon dispersion $\omega(q)$ predicted in the pioneering work by Stern [1]. According to this work, the dispersion with regard to retardation effects takes the form

$$q^2 = \epsilon \omega^2/c^2 + \left(\frac{\omega^2}{2\pi n_s e^2/m^* \bar{\epsilon}} \right)^2. \qquad (6)$$

Knowing the relation between the wave vector and the disk diameter ($q = 2.4/d$, see [25]), we can now obtain the resonance frequency as a function of the inverse mesa diameter. Such curves are shown in Figs. 4a and 4b for two different electron densities ($n_s = 6.6 \times 10^{11}$ cm^{-2} and $n_s = 2.5 \times 10^{11}$ cm^{-2}). For comparison, we also depicted the dispersion of light $\omega = 2\pi f = cq/\sqrt{\epsilon}$ and the two-dimensional plasmon dispersion defined by Eq. (1). This figure confirms the validity of Eq. (6), because the dispersion of the hybrid mode at low concentrations primarily corresponds to the purely two-dimensional plasmon dispersion and approaches the dispersion of light at high densities in the region of small wave vectors. This fact is in perfect agreement
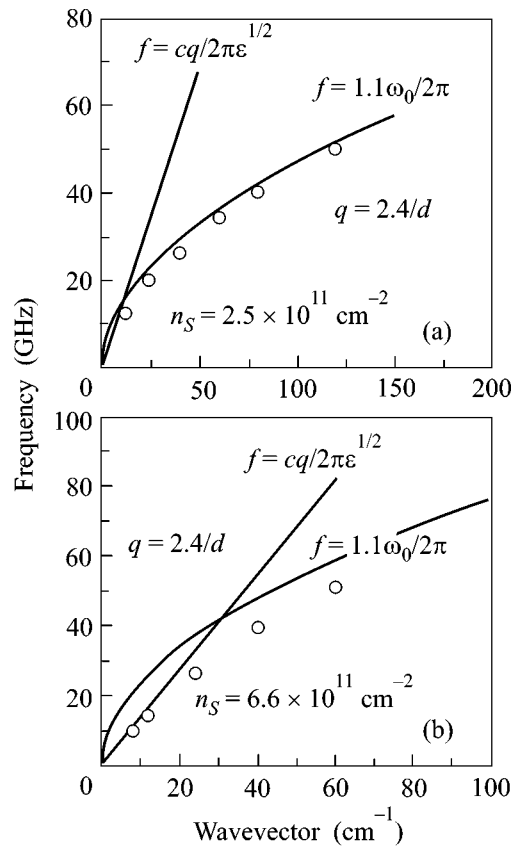
Fig. 4. Circles show the two-dimensional plasmon–polariton dispersion obtained from experimental data for two samples with different electron densities: (a) $n_s = 2.5 \times 10^{11}$ cm^{-2} and (b) $n_s = 6.6 \times 10^{11}$ cm^{-2}. The dispersion of light is depicted by a straight line, and the two-dimensional plasmon dispersion is presented in the quasistatic approximation (Eq. (1)).

with the results obtained in [1, 9], in which it was shown that mixing between the plasma and light modes occurs only at high electron concentrations.

In this work, the absorption spectra of two-dimensional magnetoplasmons were studied at small wave vectors and in the region of low frequencies, where retardation effects must be manifested. The features associated with these effects were observed experimentally and explained theoretically. It should be noted separately that an anomalous hybrid magnetoplasma mode with a very unusual field dependence was observed in the region of finite perpendicular magnetic fields. The experimental results were compared with theoretical predictions for 2D plasmon–polaritons in an infinite two-dimensional electron gas at $B = 0$ and also for a disk-shaped sample in zero and finite magnetic fields. These calculations describe the experimental results well.

REFERENCES

1. F. Stern, Phys. Rev. Lett. **18**, 546 (1967).
2. C. C. Grimes and G. Adams, Phys. Rev. Lett. **36**, 145 (1976).
3. S. J. Allen, Jr., D. C. Tsui, and R. A. Logan, Phys. Rev. Lett. **38**, 980 (1977).
4. T. N. Theis, J. P. Kotthaus, and P. J. Stiles, Solid State Commun. **26**, 603 (1978).
5. T. N. Theis, Surf. Sci. **98**, 515 (1980).
6. D. Heitmann, Surf. Sci. **170**, 332 (1986).
7. A. V. Chaplik, Zh. Éksp. Teor. Fiz. **62**, 746 (1972) [Sov. Phys. JETP **35**, 395 (1972)].
8. K. W. Chiu and J. J. Quinn, Phys. Rev. B **9**, 4724 (1974).
9. V. I. Fal'ko and D. E. Khmel'nitskiĭ, Zh. Éksp. Teor. Fiz. **95**, 1988 (1989) [Sov. Phys. JETP **68**, 1150 (1989)].
10. A. O. Govorov and A. V. Chaplik, Zh. Éksp. Teor. Fiz. **95**, 1976 (1989) [Sov. Phys. JETP **68**, 1143 (1989)].
11. S. A. Mikhaĭlov, Pis'ma Zh. Éksp. Teor. Fiz. **57**, 570 (1993) [JETP Lett. **57**, 586 (1993)].
12. S. I. Gubarev, I. V. Kukushkin, S. V. Tovstonog, *et al.*, Pis'ma Zh. Éksp. Teor. Fiz. **72**, 469 (2000) [JETP Lett. **72**, 324 (2000)].
13. M. Y. Akimov, I. V. Kukushkin, S. I. Gubarev, *et al.*, Pis'ma Zh. Éksp. Teor. Fiz. **72**, 662 (2000) [JETP Lett. **72**, 460 (2000)].
14. B. M. Ashkinadze and V. I. Yudson, Phys. Rev. Lett. **83**, 812 (1999).
15. I. V. Kukushkin, J. H. Smet, K. von Klitzing, and W. Wegscheider, Nature **415**, 409 (2002).
16. O. V. Volkov, I. V. Kukushkin, M. V. Lebedev, *et al.*, Pis'ma Zh. Éksp. Teor. Fiz. **71**, 558 (2000) [JETP Lett. **71**, 383 (2000)].
17. S. J. Allen, Jr., H. L. Störmer, and J. C. M. Hwang, Phys. Rev. B **28**, 4875 (1983).
18. D. C. Glattli, E. Y. Andrei, G. Deville, *et al.*, Phys. Rev. Lett. **54**, 1710 (1985).
19. T. Demel, D. Heitmann, P. Grambow, and K. Ploog, Phys. Rev. Lett. **64**, 788 (1990).
20. W. Hansen, J. P. Kotthaus, and U. Merkt, Semicond. Semimet. **35**, 279 (1992).
21. R. P. Leavitt and J. W. Little, Phys. Rev. B **34**, 2450 (1986).
22. A. L. Fetter, Phys. Rev. B **33**, 5221 (1986).
23. V. A. Volkov and S. A. Mikhaĭlov, Zh. Éksp. Teor. Fiz. **94**, 217 (1988) [Sov. Phys. JETP **67**, 1639 (1988)].
24. S. A. Mikhailov, Phys. Rev. B **54**, 10335 (1996).
25. I. V. Kukushkin, J. H. Smet, S. A. Mikhailov, and D. V. Kulakovskii, Phys. Rev. Lett. (in press).
26. S. S. Nazin and V. B. Shikin, Fiz. Nizk. Temp. **15**, 227 (1989) [Sov. J. Low Temp. Phys. **15**, 127 (1989)].
27. V. Shikin, S. Nazin, D. Heitmann, and T. Demel, Phys. Rev. B **43**, 11903 (1991).
28. Z. L. Ye and E. Zaremba, Phys. Rev. B **50**, 17217 (1994).

Translated by A. Bagatur'yants

Observation of Domain Boundaries in a TbNi$_2$B$_2$C Single Crystal

L. Ya. Vinnikov[1], *, J. Anderegg[2], S. L. Bud'ko[2], P. C. Canfield[2], and V. G. Kogan[2]

[1] *Institute of Solid-State Physics, Russian Academy of Sciences, Chernogolovka, Moscow region, 142432 Russia*
* e-mail: vinnik@issp.ac.ru
[2] *Ames Laboratory DOE and Department of Physics, Iowa State University Ames, Iowa 50011, USA*
Received March 26, 2003

The domain structure of TbNi$_2$B$_2$C was studied by the finest ($\simeq 0$ nm) magnetic-particle decoration below 13 K. The twin domain boundaries caused by magnetoelastic stresses were observed in the {110} planes. © *2003 MAIK "Nauka/Interperiodica".*

PACS numbers: 75.50.Ee; 75.60.Ch

The family of borocarbides RNi$_2$B$_2$C (R = rare-earth ion) were synthesized less than ten years ago and, since then, have attracted attention because of the unique possibility to obtain various combinations of electric and magnetic properties by changing the rare-earth ions [1]. Of particular interest is the competition of magnetic ordering and superconducting state at low temperatures. As the "magnetism" of rear-earth ion strengthens (the de Gennes factor increases [1]) in the order of R = Lu, Tm, Er, Ho, Dy, Tb, Gd, the superconducting transition temperature (T_C) decreases from 16 K for LuNi$_2$B$_2$C to 0 K for TbNi$_2$B$_2$C and GdNi$_2$B$_2$C, whereas the antiferromagnetic transition temperature (Néel temperature T_N) increases from 0 K for LuNi$_2$B$_2$C to 15 K for TbNi$_2$B$_2$C and 20 K for GdNi$_2$B$_2$C [1]. In addition, the magnetization in TbNi$_2$B$_2$C was found to be anisotropic in the basal plane (perpendicular to the c axis [001]), and the compound was assumed to be a weak antiferromagnet below 8 K [2]. The magnetic properties in the superconducting state showed some anomalies that were caused by the antiferromagnetic transitions at T_N = 6 and 5 K for ErNi$_2$B$_2$C and HoNi$_2$B$_2$C, respectively [3, 4]. Recently, vortex structures were observed in ErNi$_2$B$_2$C by the decoration technique and interpreted as being due to the vortex pinning along the antiferromagnetic domain boundaries (110) and (1$\bar{1}$0) at the (001) observation plane [5]. In this work, an attempt is undertaken to observe the domain structure in the normal (nonsuperconducting) state of TbNi$_2$B$_2$C by the finest magnetic-particle decoration technique [6].

Earlier, the decoration technique was successfully used for the visualization of the vortex structure in traditional and high-T_C superconductors [6]. This method is based on the segregation of magnetic particles at the surface of a superconductor or magnet in the regions of nonuniform magnetic-field penetration. The subsequent visualization of the magnetic particle distribution provides information about the vortex or domain structure. A high resolution of the method (better than 100 nm [7]) is provided by the small size ($\simeq 10$ nm) of magnetic particles in a powder prepared directly upon the evaporation of a magnetic material (iron in our case) in the atmosphere of a buffer helium gas at a low pressure of $\simeq 10^{-2}$ torr in a low-temperature experiment.

The original (001) growth surface of a TbNi$_2$B$_2$C single crystal of size $\simeq 3 \times 5$ mm^2 and thickness $\simeq 0.5$ mm was studied. Crystals were grown from a Ni$_2$B melt as described in [8]. Experiments were carried out in the frozen-flux regime in a magnetic field ($\simeq 20$ or $\simeq 200$ Oe) parallel to the c axis [001]. The sample temperature was controlled by a resistance thermometer placed at a massive copper base near the sample holder. The sample was cooled in a magnetic field to a temperature of 4.2 K, which increased to 7–8 K in the course of decoration. The samples could be heated to a temperature of 15–20 K by a heater, which was used in the magnetic-particle decoration through feeding a tungsten evaporator with low power that was insufficient for Fe evaporation. To monitor the decoration process, YNi$_2$B$_2$C single crystals were placed in the immediate vicinity of the TbNi$_2$B$_2$C single crystal and used as control samples. After the decoration, the samples were examined in a scanning electron microscope.

A typical pattern of magnetic structure revealed by the decoration at the (001) surface is shown in Fig. 1. The $\langle 110 \rangle$-directed light stripes with a width of about 1 μm and a periodicity of few microns intersect the step at the surface of TbNi$_2$B$_2$C single crystal without visible distortions. The fact that the contrast in Fig. 1a is produced by small magnetic particles (bright points) is clearly seen at high magnification in Fig. 1b. Such patterns were never observed in the original (before deco-
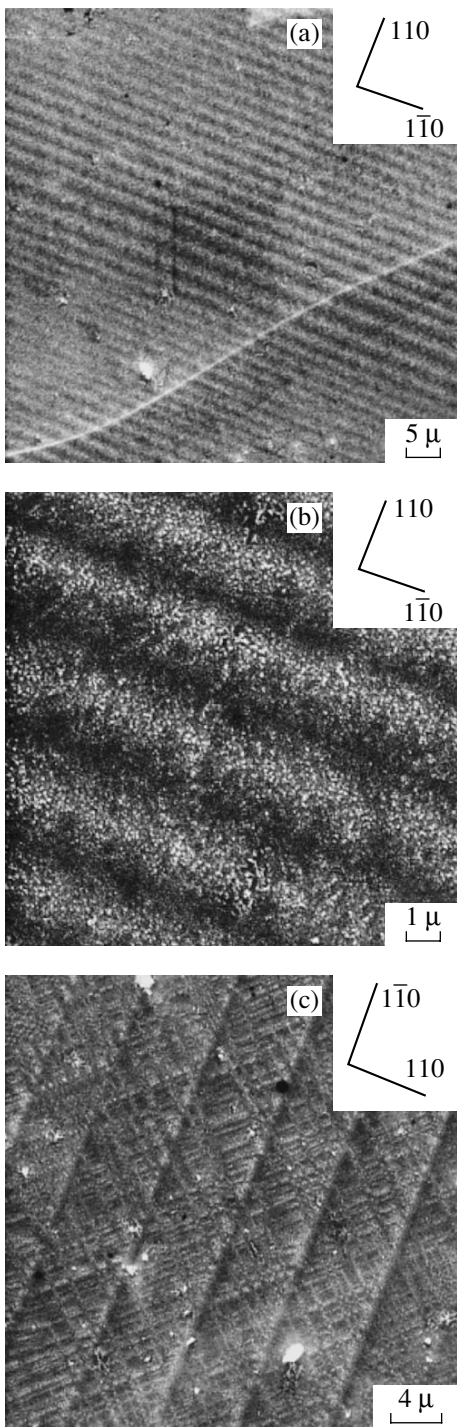
Fig. 1. (a) Typical decoration pattern at the (001) plane of a TbNi$_2$B$_2$C single crystal in a magnetic field of 190 Oe at a temperature of 8.5 K. (b) Magnified central part of (a). (c) Region with a more complicated structure.

Fig. 2. Decoration pattern at the (001) plane in the same experiment for (a) TbNi$_2$B$_2$C and (b) YNi$_2$B$_2$C single crystals in a magnetic field of 18 Oe and a temperature of 12.7 K.

$\langle 110 \rangle$ direction, fine structure is seen in the directions close to $\langle 100 \rangle$. These structures were observed at temperatures below 13 K. It is seen in Fig. 2a that the contrast produced by magnetic particles at the TbNi$_2$B$_2$C sample almost completely disappears at a temperature of 13 K (the particles are uniformly distributed), whereas the vortex structure is clearly seen in the adjacent control YNi$_2$B$_2$C single crystal with T_C = 15 K. This result suggests that the absence of contrast in Fig. 2a is not caused by the adverse experimental conditions, so that one can assert that the patterns shown in Figs. 1 and 2a reflect the magnetic-flux structure in TbNi$_2$B$_2$C.

Since the temperature range in which the magnetic structure exhibits unusual macroscopic features coincides with the temperature range of the antiferromagnetic state in TbNi$_2$B$_2$C [1], one may naturally consider the observed patterns as a manifestation of the domain structure. Nevertheless, it is desirable to clarify why the normal component of magnetic-field gradient is non-

ration) samples. Although, at the greater part of the (001) crystal surface, the light stripes were observed in both $\langle 110 \rangle$ directions, more complicated structures were observed in a small area of the sample (Fig. 1c), where, along with the main system of stripes in the
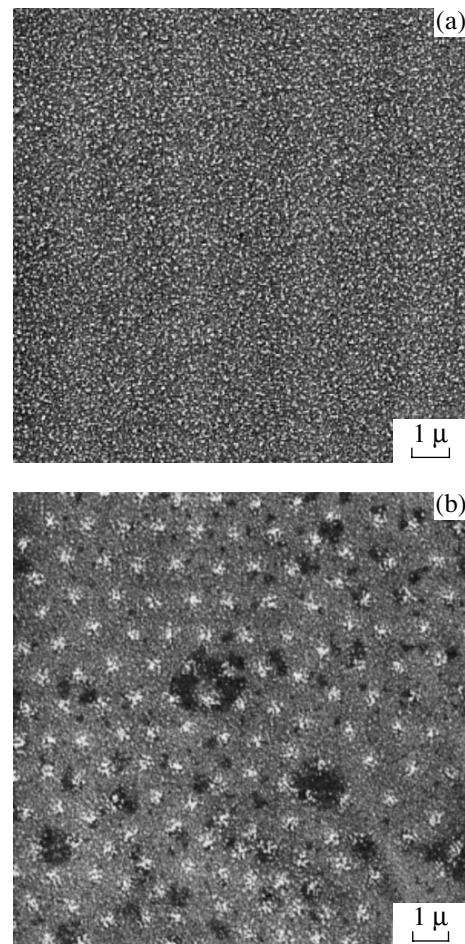
zero at the antiferromagnetic domain walls (this is a necessary condition for the visualization of the domain boundaries by decoration) and also to elucidate the reason for the appearance of the domains themselves. This may be due to the magnetoelastic (magnetostrictive) stresses that arise below the temperature T_N and transform the initial tetragonal structure into the orthorhombic $TbNi_2B_2C$ [10]. According to [10], the degree of orthorhombicity increases with lowering temperature and reaches $a/b - 1 = 0.55\%$ at a temperature of 8.6 K. Thus, one can imagine that the twin structure in a $TbNi_2B_2C$ single crystal is formed at $T < T_N$, much as it occurs in YBCO [9]. According to [12], the crystallographic-distortion and magnetic-moment vectors directed, respectively, along [010] and [100] dictate the orientation of the twin and domain boundaries along the (110) or ($1\bar{1}0$) plane. On the whole, the experimental data (Fig. 1a) conform to this crystal geometry, although they do not explain some features of the domain structure (Fig. 1c). The appearance of a crystallographic twin boundary in the (110) or ($1\bar{1}0$) plane because of a difference in the lattice parameters a and b alone cannot provide the magnetic contrast. The latter arises due to the nonzero gradient of the magnetic-induction component normal to the (001) surface of the sample, which is demonstrated by the decoration technique. One can assume that, in the temperature range 8–15 K, the observed boundaries are the Bloch walls that separate the antiferromagnetic domains with mutually perpendicular directions of a longitudinally polarized $\langle 100 \rangle$-directed spin-density wave in the basal (001) plane [11]. At temperatures below 8 K, these walls can function as boundaries between the domains with a weak ferromagnetism. The magnetic contrast probably appears due to the domain boundary with an uncompensated magnetic moment along the c axis, although the microscopic reason for its appearance still remains to be clarified.

The neutron diffraction data suggest [11] that the magnetic structures in $TbNi_2B_2C$ and $ErNi_2B_2C$ are similar, because their spin-density waves both are directed along [100] and the crystal-distortion vectors are directed along [010] coinciding with the tetragonal-to-orthorhombic magnetoelastic-transformation direction in the basal plane [12]. This fact may explain the crystallographic similarity of the domain structure observed in $TbNi_2B_2C$ with the magnetic-flux structure in $ErNi_2B_2C$ [5], thereby favoring our interpretation of the origin of domain boundaries.

REFERENCES

1. K.-H. Müller, G. Fuchs, S.-L. Drechsler, and V. N. Narozhnyi, in *Handbook of Magnetic Materials*, Vol. 14: *Magnetic and Superconducting Properties of Rare Earth Borocarbides of the Type RNi_2B_2C*, Ed. by K. H. J. Buschow (North-Holland, Amsterdam, 2002).

2. B. K. Cho, P. C. Canfield, and D. C. Johnston, Phys. Rev. B **53**, 8499 (1996).

3. C. D. Dewhurst, R. A. Doyle, E. Zeldov, and D. McK. Paul, Phys. Rev. Lett. **82**, 827 (1999).

4. C. D. Dewhurst, R. A. Doyle, Y. Paltiel, *et al.*, Phys. Rev. B **63**, 060501 (2001).

5. N. Saha, R. Surdeanu, M. Marchevsky, *et al.*, Phys. Rev. B **63**, 020502 (2000).

6. L. Ya. Vinnikov, I. V. Grigor'eva, and L. A. Gurevich, Springer Ser. Mater. Sci. **23**, 89 (1993).

7. L. Ya. Vinnikov, T. L. Barkov, P. C. Canfield, *et al.*, Phys. Rev. B **64**, 220508 (2001).

8. M. Xu, P. Canfield, J. Ostenson, *et al.*, Physica C (Amsterdam) **227**, 321 (1994).

9. L. Ya. Vinnikov, L. A. Gurevich, G. A. Emelchenko, and Yu. A. Ossipyan, Solid State Commun. **67**, 421 (1988).

10. C. Song, Z. Islam, L. Lottermoser, *et al.*, Phys. Rev. B **60**, 6223 (1999).

11. J. W. Lynn, S. Skanthakumar, Q. Huang, *et al.*, Phys. Rev. B **55**, 6584 (1997).

12. A. Kreyssig, A. Schneiwind, M. Lowenhaupt, *et al.*, *Rare Earth Transition Metal Borocarbides (Nitrides): Superconducting, Magnetic and Normal State Properties*, Ed. by K.-H. Müller and V. N. Narozhnyi (Kluwer Academic, Dordrecht, 2001), NATO Science, Vol. 14.

Translated by V. Sakun

Spectral Representations and Description of a Superconducting State with *S*-Type Order Parameter Δ(k)

V. V. Val'kov[1, 2, 3, *], D. M. Dzebisashvili[1, 3], and A. S. Kravtsov[1, 3]

[1]*Kirenskiĭ Institute of Physics, Siberian Division, Russian Academy of Sciences,*
Akademgorodok, Krasnoyarsk, 660036 Russia
* *e-mail: vvv@iph.krasn.ru*
[2]*Krasnoyarsk State Technical University, Krasnoyarsk, 660074 Russia*
[3]*Krasnoyarsk State University, Krasnoyarsk, 660075 Russia*
Received March 24, 2003

The inclusion of a singular contribution to the spectral intensity of the anomalous correlation function is shown to regain the sum rule and remove the unjustified forbidding of the *S*-symmetry order parameter in superconductors with strong correlations. For the order parameter of this symmetry, the solution to the self-consistency equation is analyzed beyond the nearest-neighbor approximation. © *2003 MAIK "Nauka/Interperiodica"*.

PACS numbers: 74.20.Fg; 71.27.+a

1. Among the models describing the main features of a superconducting transition through the nonphonon Cooper pairing mechanism in an electron system with strong correlations, the Hubbard model and the *t*–*J* model obtained on its basis are most frequently used. It was the Hubbard model that was invoked in [1] to discover a kinematic pairing mechanism for the formation (at $U \longrightarrow \infty$) of a superconducting phase with the order parameter Δ_0 independent of quasimomentum. However, more recently, the possibility of forming such a state was questioned by some theorists, because the solution to the self-consistent equation for the order parameter $\Delta(\mathbf{k}) = \Delta_0$ violates, in their opinion, the requirement that the on-site anomalous mean $\langle X_f^{0\sigma} X_f^{0\bar{\sigma}} \rangle$ of the product of Hubbard operators must be zero.

In this communication, the above statement is analyzed using the spectral representations of the time-dependent anomalous correlation functions. The new point is that the spectral intensity of the anomalous correlation function constructed from Hubbard operators contains, apart from the usual regular part, an additional singular component. It is shown that, after the inclusion of the singular component, the necessary requirements for one-time on-site correlations are fulfilled, on the one hand, and, on the other, neither the equations of motion for the Green's functions nor the self-consistent equation for the superconducting order parameter are affected. The *S*-type superconducting phase will be considered in the non-nearest-neighbor approximation, and it will be shown that the superconducting order parameter (OP) with this symmetry may, in principle, go to zero.

2. In the standard notation, the Hubbard Hamiltonian has the form [2]

$$H = \sum_{f\sigma} (\varepsilon - \mu) a_{f\sigma}^+ a_{f\sigma}$$

$$+ \sum_{fm} t_{fm} a_{f\sigma}^+ a_{m\sigma} + U \sum_f \hat{n}_{f\uparrow} \hat{n}_{f\downarrow}, \quad (1)$$

The scattering amplitude in the strong-correlation regime was calculated for model (1) in [3]. It was found that, in the Cooper scattering channel, this amplitude has a singularity corresponding to the instability against the superconducting transition (Zaĭtsev kinematic mechanism). A set of four equations for the normal and anomalous Green's functions describing the superconducting state in model (1) with a finite U was obtained and solved in [4]. In [4], the pairing was caused not only by the electron motion in the lower Hubbard band but also by the electron transitions from the lower to the upper Hubbard subband and by the charge-carrier motion in the upper subband.

At the same time, the superconducting phase with strong correlations can be studied using the effective Hamiltonian [5] constructed in the operator form of the perturbation theory for a small parameter $|t_{fm}|/U \ll 1$. It is known that the corresponding Hilbert space $\tilde{L}$ for H_{eff} does not contain binary states. As a result, only the anomalous means $\langle X_f^{0\sigma} X_m^{0\bar{\sigma}} \rangle$ appear in the theory of superconducting state, and they must go to zero for the coinciding site indices. The opinion that this phase could not be realized rested on the difficulties caused by the necessity of satisfying this requirement in a superconducting phase with the *S*-symmetry OP.

Leaving aside the physical interpretation of the "strangeness" of the above-mentioned forbidding, we rather analyze the mathematical aspect of the problem. For this purpose, we consider the spectral representations of the temporal anomalous correlation functions and their relation to the Fourier transform of the anomalous two-time Green's function.

First of all, there is a fundamental difference between the anomalous Green's functions in the BCS theory and in the theory of high-T_c superconductivity with the electronic pairing mechanism. The anomalous Green's function of the standard Fermi second-quantization operators

$$F_{\sigma\bar{\sigma}}(ft; gt') = -i\theta(t-t')\langle\{a^+_{f\sigma}(t), a^+_{g\bar{\sigma}}(t')\}\rangle$$

is zero at $t = t' + \delta$ ($\delta \longrightarrow +0$). This is caused by the fact that the creation operators anticommute at the coinciding times. At the same time, the means $\langle a^+_{f\sigma}(t)a^+_{g\bar{\sigma}}(t)\rangle$ and $\langle a^+_{g\bar{\sigma}}(t)a^+_{f\sigma}(t)\rangle$ are nonzero in the superconducting phase even for $f = g$:

$$\langle a^+_{f\sigma}a^+_{f\bar{\sigma}}\rangle = \eta(\sigma)\langle X^{20}_f\rangle, \quad \langle a^+_{f\bar{\sigma}}a^+_{f\sigma}\rangle = -\eta(\sigma)\langle X^{20}_f\rangle.$$

A different situation occurs for the anomalous Green's function with the Hubbard operators:

$$\langle\langle X^{\bar{\sigma}0}_f(t)|X^{\sigma 0}_g(t')\rangle\rangle$$
$$= -i\theta(t-t')\langle\{X^{\bar{\sigma}0}_f(t), X^{\sigma 0}_g(t')\}\rangle. \tag{2}$$

In this case at $t \longrightarrow t' + 0$, the means $\langle X^{\bar{\sigma}0}_f X^{\sigma 0}_g\rangle$ and $\langle X^{\sigma 0}_g X^{\bar{\sigma}0}_f\rangle$ are identical zeros for the coinciding site indices. It is essential that this is so not due to the properties of the physical system but due to the multiplication algebra for Hubbard operators. The fact that Eq. (2) is valid regardless of the particular physical system allows it to be explicitly taken into account using the spectral representation.

With this property in mind, the spectral intensity $\tilde{J}^{\sigma\bar{\sigma}}_{gf}(\omega)$ in the spectral representation

$$\langle X^{\sigma 0}_g(t')X^{\bar{\sigma}0}_f(t)\rangle = \int d\omega \exp\{-i\omega(t-t')\}\tilde{J}^{\sigma\bar{\sigma}}_{gf}(\omega) \tag{3}$$

can be written in the form

$$\tilde{J}^{\sigma\bar{\sigma}}_{gf}(\omega) = \tilde{J}^{\sigma\bar{\sigma}}_{gf} - \delta(\omega)\delta_{fg}\int d\omega_1 J^{\sigma\bar{\sigma}}_{gf}(\omega_1)\exp(-i\omega_1\delta),$$
$$\delta \longrightarrow +0, \tag{4}$$

providing a zero value for the right-hand side of Eq. (3) at $t = t' + \delta$ ($\delta \longrightarrow +0$) if $f = g$. This is the main distinction between the introduced spectral representation and the representation used in the theory of two-time temperature Green's functions [6].

The following fact is of fundamental importance. The singular component of the spectral intensity cannot be determined solely from the known Fourier transform

of the analytic continuation of the anomalous Green's function in the upper complex half plane. This fact provides one more example of the known problem of ambiguous reproduction of the spectral intensity of correlation function from the spectral theorem. The discussion of particular examples of this kind is given, e.g., by Yu.G. Rudoĭ in [7] and in original works [8, 9]. In practice, the inclusion of the singular component is necessary for obtaining the correct limiting values for the correlators.

To prove this statement, we use Eq. (3) to construct the spectral representation for the anomalous correlation function $\langle X^{\bar{\sigma}0}_f(t)X^{\sigma 0}_g(t')\rangle$. After the cyclic permutation of operators under the trace sign, one obtains from Eq. (3)

$$\langle X^{\bar{\sigma}0}_f(t)X^{\sigma 0}_g(t')\rangle = \int d\omega \exp\{-i\omega(t-t')\}$$
$$\times \{J^{\sigma\bar{\sigma}}_{gf}(\omega)\exp(\beta\omega) - \delta(\omega)\delta_{fg}S^{\bar{\sigma}\sigma}_{fg}\}, \tag{5}$$

where

$$S^{\bar{\sigma}\sigma}_{gf} = \int d\omega_1 J^{\sigma\bar{\sigma}}_{gf}(\omega_1)\exp(\beta\omega_1)\exp(-i\omega_1\delta),$$
$$\beta = 1/T, \quad \delta \longrightarrow +0. \tag{6}$$

One can see that the right-hand side turns to zero at $t \longrightarrow t' + 0$ and $f = g$, as it must, and $\langle X^{\bar{\sigma}0}_f X^{\sigma 0}_f\rangle = 0$.

By using spectral representations (3) and (5), one obtains the following expression for the average value of the anticommutator appearing in the definition of the anomalous Green's function:

$$\langle\{X^{\bar{\sigma}0}_f(t), X^{\sigma 0}_g(t')\}_+\rangle = \int d\omega \exp\{-i\omega(t-t')\}$$
$$\times \{J^{\sigma\bar{\sigma}}_{gf}(\omega)[\exp(\beta\omega) + 1] - \delta(\omega)\delta_{fg}\Sigma^{\sigma\bar{\sigma}}_{gf}\}, \tag{7}$$

where

$$\Sigma^{\sigma\bar{\sigma}}_{gf} = \int d\omega_1 J^{\sigma\bar{\sigma}}_{gf}(\omega_1)[\exp(\beta\omega_1) + 1]\exp(-i\omega_1\delta),$$
$$\delta \longrightarrow +0. \tag{8}$$

From definition (2) and using Eq. (7), one gets for the Fourier transform of the anomalous Green's function:

$$\langle\langle X^{\bar{\sigma}0}_f|X^{\sigma 0}_g\rangle\rangle_\omega = \int \frac{d\omega_1}{\omega - \omega_1 + i\delta}$$
$$\times \{J^{\sigma\bar{\sigma}}_{gf}(\omega)\exp((\beta\omega) + 1) - \delta(\omega)\delta_{fg}\Sigma^{\sigma\bar{\sigma}}_{gf}\}. \tag{9}$$

Consequently, the spectral theorem [6] in our case takes the form of the integral equation for $J^{\sigma\bar{\sigma}}_{gf}(\omega)$:

$$-\frac{1}{\pi}\frac{\mathrm{Im}\langle\langle X^{\bar{\sigma}0}_f|X^{\sigma 0}_g\rangle\rangle_{\omega+i\delta}}{\exp(\beta\omega) + 1} = J^{\sigma\bar{\sigma}}_{gf}(\omega) - \frac{\delta(\omega)\delta_{fg}}{\exp(\beta\omega) + 1}$$
$$\times \int d\omega_1 J^{\sigma\bar{\sigma}}_{gf}(\omega_1)[\exp(\beta\omega_1) + 1]\exp(-i\omega_1\delta). \tag{10}$$

One can readily verify that

$$J_{gf}^{\sigma\bar\sigma}(\omega) = R_{gf}^{\sigma\bar\sigma}(\omega) + \delta(\omega)\delta_{fg}\frac{A_{ff}^{\sigma\bar\sigma}}{\exp(\beta\omega)+1}, \quad (11)$$

with

$$R_{gf}^{\sigma\bar\sigma}(\omega) = -\frac{1}{\pi}\frac{\mathrm{Im}\langle\langle X_f^{\bar\sigma0}|X_g^{\sigma0}\rangle\rangle_{\omega+i\delta}}{\exp(\beta\omega)+1}$$

satisfies the integral equation for an arbitrary $A_{ff}^{\sigma\bar\sigma}$. Here, it is taken into account that the equality

$$\int d\omega \exp(-i\omega\delta)\mathrm{Im}\langle\langle X_f^{\bar\sigma0}|X_g^{\sigma0}\rangle\rangle_{\omega+i\delta} = 0, \quad (12)$$

being the particular case of a more general relation

$$\langle\langle X_f^{\bar\sigma0}(t)|X_g^{\sigma0}(t')\rangle\rangle_{(t\to t'+\delta)}$$
$$= \int d\omega \exp(-i\omega\delta)\langle\langle X_f^{\bar\sigma0}|X_g^{\sigma0}\rangle\rangle_{\omega+i\delta} = 0, \quad (13)$$

$$\delta \longrightarrow +0,$$

is valid. The uncertainty in $A_{ff}^{\sigma\bar\sigma}$ is immaterial, because the total spectral intensity $\tilde{J}_{gf}^{\sigma\bar\sigma}(\omega)$ is independent of $A_{ff}^{\sigma\bar\sigma}$. Indeed, substituting solution (11) into definition (4), one obtains

$$\tilde{J}_{gf}^{\sigma\bar\sigma}(\omega) = R_{gf}^{\sigma\bar\sigma}(\omega)$$
$$- \delta(\omega)\delta_{fg}\int d\omega_1 R_{gf}^{\sigma\bar\sigma}(\omega_1)\exp(-i\omega_1\delta). \quad (14)$$

Thus, the analytically continued Fourier transform of the anomalous Green's function determines only the regular part $R_{gf}^{\sigma\bar\sigma}(\omega)$ of the total spectral intensity $\tilde{J}_{gf}^{\sigma\bar\sigma}(\omega)$. In turn, its singular component is uniquely expressed through $R_{gf}^{\sigma\bar\sigma}(\omega)$, providing the correct values for the correlators in the limiting cases.

This analysis demonstrates that the above-mentioned forbidding of the superconducting phase with the S-symmetry OP is caused by ignoring the singular component of the correlation function, and not by any physical principle. The inclusion of the singular part removes this forbiddenness without changing the form of all equations obtained in the theory of superconducting state in strongly correlated systems.

To confirm the statement about the invariability of the self-consistent equations, we note that Eq. (3) leads to the following expression for the one-time correlators:

$$\langle X_f^{0\sigma}X_g^{0\bar\sigma}\rangle = S_{gf}^{\bar\sigma\sigma} - \delta_{fg}S_{gf}^{\bar\sigma\sigma}$$
$$= \frac{1}{N}\sum_q \exp\{iq(f-g)\}\left\{S_q^{\bar\sigma\sigma} - \frac{1}{N}\sum_k S_k^{\bar\sigma\sigma}\right\}. \quad (15)$$

This means that, in the quasimomentum representation,

$$\langle X_{q\sigma}X_{-q\bar\sigma}\rangle = \sum_{(f-g)} \exp\{-iq(f-g)\}\langle X_f^{0\sigma}X_g^{0\bar\sigma}\rangle$$
$$= S_q^{\bar\sigma\sigma} - \frac{1}{N}\sum_k S_k^{\bar\sigma\sigma}.$$

It follows that the equation for the superconducting order parameter in the t–J^* model (three-center interactions are taken into account) [10, 11]

$$\Delta_{\mathbf{k}} = \frac{1}{N}\sum_{\mathbf{q}}\left\{2t_{\mathbf{q}} + \frac{n}{2}(J_{\mathbf{k}+\mathbf{q}} + J_{\mathbf{k}-\mathbf{q}})\right.$$
$$\left. + 4\left(1-\frac{n}{2}\right)\frac{t_{\mathbf{k}}t_{\mathbf{q}}}{U} - n\left(\frac{t_{\mathbf{q}}^2}{U} - \frac{J_0}{2}\right)\right\}\langle X_{q\sigma}X_{-q\bar\sigma}\rangle \quad (16)$$

does not change its form after the singular component of spectral intensity is taken into account, because

$$\frac{1}{N}\sum_{\mathbf{q}}\left\{\left[2t_{\mathbf{q}} + \frac{n}{2}(J_{\mathbf{k}+\mathbf{q}} + J_{\mathbf{k}-\mathbf{q}}) + 4\left(1-\frac{n}{2}\right)\frac{t_{\mathbf{k}}t_{\mathbf{q}}}{U}\right.\right.$$
$$\left.\left. - n\left(\frac{t_{\mathbf{q}}^2}{U} - \frac{J_0}{2}\right)\left[\frac{1}{N}\sum_{\mathbf{p}}S_p^{\bar\sigma\sigma}\right]\right]\right\} \equiv 0.$$

Let us consider the solution to Eq. (16) for the S-symmetry OP. Beyond the nearest-neighbor approximation (with the three nonzero hopping parameters), one has

$$t_{\mathbf{k}} = t_1 S_1(\mathbf{k}) + t_2 S_2(\mathbf{k}) + t_3 S_3(\mathbf{k}),$$
$$J_{\mathbf{k}} = J_1 S_1(\mathbf{k}) + J_2 S_2(\mathbf{k}) + J_3 S_3(\mathbf{k}), \quad (17)$$
$$J_i = 2t_i^2/U.$$

Here, $S_i(\mathbf{k})$ are the square-lattice invariants:

$$S_1(\mathbf{k}) = (\cos k_x a + \cos k_y a)/2,$$
$$S_2(\mathbf{k}) = \cos(k_x a)\cos(k_y a),$$
$$S_3(\mathbf{k}) = (\cos 2k_x a + \cos 2k_y a)/2.$$

Taking into account the relation

$$\langle X_{q\sigma}X_{-q\bar\sigma}\rangle = \left(\frac{\Delta_{\mathbf{q}}}{2E_{\mathbf{q}}}\right)\tanh\left(\frac{E_{\mathbf{q}}}{2T}\right),$$

one finds that the quasimomentum dependence of the OP in the S phase has the form

$$\Delta_{\mathbf{k}} = \Delta_0 + \Delta_1 S_1(\mathbf{k}) + \Delta_2 S_2(\mathbf{k}) + \Delta_3 S_3(\mathbf{k}). \quad (18)$$
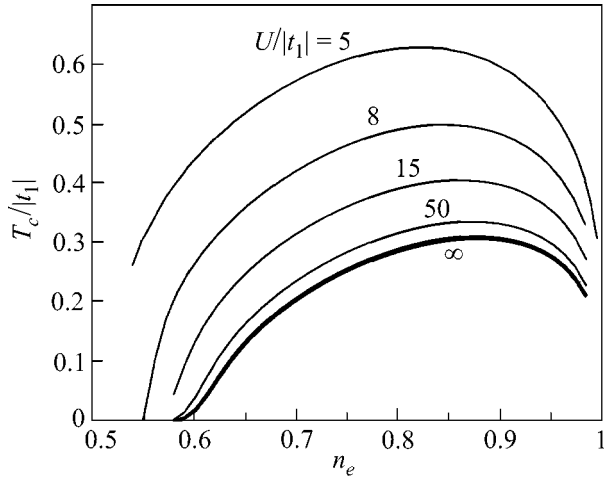
Fig. 1. Concentration dependence of the critical temperature for the superconducting transition to the *S* phase with allowance for three hopping integrals.
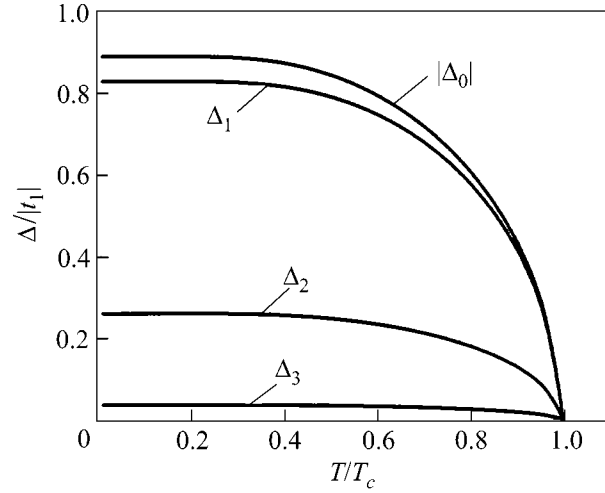

Fig. 2. Temperature dependence of the amplitudes Δ_i ($i = 0$, 1, 2, 3) of the *S*-symmetry order parameter $\Delta(\mathbf{k})$.

The coefficients Δ_i ($i = 0, 1, 2, 3$) are found from the solution to the following set of four equations:

$$\Delta_0 = \sum_{l=0}^{3}\left\{\sum_{j=1}^{3} 2G_{lj}T_j + \frac{n}{2}J_0 G_l - \frac{n}{U}\sum_{i,j=1}^{3} G_{lij}T_i T_j\right\}\Delta_l$$

$$(T_j = -4t_j, \quad j = 1, 2, 3),$$

$$\Delta_m = 4\sum_{l=0}^{3}\left\{nJ_m G_{ml} + (1 - n/2)T_m\sum_{i=1}^{3} G_{li}T_i/U\right\}\Delta_l, \quad (19)$$

$$m = 1, 2, 3,$$

where

$$G_i = G_{i00}, \quad G_{ij} = G_{ij0},$$

and

$$G_{ijl} = \frac{1}{N}\sum_{\mathbf{q}} S_i(\mathbf{q})S_j(\mathbf{q})S_l(\mathbf{q})\Psi_{\mathbf{q}},$$

$$\Psi_{\mathbf{q}} = \frac{\tanh(E_{\mathbf{q}}/2T)}{2E_{\mathbf{q}}}, \quad S_0(\mathbf{k}) = 1.$$

The results of the numerical analysis of the superconducting transition temperature as a function of electron concentration is shown in Fig. 1 for various values of the Coulomb repulsion parameter U. For finite U, the superconducting state is formed through both the Zaĭtsev kinematic [3, 1] and magnetic pairing mechanisms. As U increases, the region of superconducting state diminishes (the magnetic pairing mechanism is suppressed). In the limit of large U, only the kinematic mechanism is retained (thick curve). In the calculations, the following values of hopping integrals were used: $t_2/|t_1| = -0.35$ and $t_3/|t_1| = -0.05$.

The temperature behavior of the parameters Δ_i ($i = 0, 1, 2, 3$) is demonstrated in Fig. 2 for the same values of hopping integrals, $U/|t_1| = 5$, and $n_e = 0.82$. The chosen electron concentration corresponded to the optimal doping ($T_c/|t_1| = 0.64$). One can see that the absolute values of Δ_0 and Δ_1 are close and nearly compensate each other ($\Delta_0 < 0$). In such a situation, the third term in $\Delta_{\mathbf{k}}$ comes into play. Note also that, due to a complex quasimomentum dependence of $\Delta_{\mathbf{k}}$ and the close values of parameters Δ_i ($i = 0, 1, 2, 3$), $\Delta_{\mathbf{k}}$ turns to zero at certain lines in the Brillouin zone. This fact is of interest because it opens up the possibility to obtain the spectrum of elementary excitations in the superconducting phase with the *S*-type symmetry of order parameter and a narrow, or even zero, energy gap. Our preliminary calculations corroborate this assumption; however, because of limited space, the corresponding results will be reported elsewhere.

REFERENCES

1. R. O. Zaĭtsev and V. A. Ivanov, Pis'ma Zh. Éksp. Teor. Fiz. **46**, 140 (1987) [JETP Lett. **46**, S116 (1987)].
2. J. C. Hubbard, Proc. R. Soc. London, Ser. A **276**, 238 (1963).
3. R. O. Zaĭtsev, Zh. Éksp. Teor. Fiz. **70**, 1100 (1976) [Sov. Phys. JETP **43**, 574 (1976)].

4. R. O. Zaĭtsev, V. A. Ivanov, and Yu. V. Mikhaĭlova, Fiz. Met. Metalloved. **68**, 1108 (1989).

5. Yu. A. Izyumov, Usp. Fiz. Nauk **167**, 465 (1997) [Phys. Usp. **40**, 445 (1997)].

6. D. N. Zubarev, *Nonequilibrium Statistical Thermodynamics* (Nauka, Moscow, 1971; Consultants Bureau, New York, 1974).

7. *Statistical Physics and the Quantum Theory of Field*, Ed. by N. N. Bogolyubov (Nauka, Moscow, 1973).

8. H. Callen, R. H. Swendsen, and R. Tahir-Kheli, Phys. Lett. A **25**, 505 (1967).

9. P. E. Bloomfield and N. Nafari, Phys. Rev. A **5**, 806 (1972).

10. V. Yu. Yushankhay, G. M. Vujicic, and R. B. Zakula, Phys. Lett. A **151**, 254 (1990).

11. V. V. Val'kov, T. A. Val'kova, D. M. Dzebisashvili, and S. G. Ovchinnikov, Pis'ma Zh. Éksp. Teor. Fiz. **75**, 450 (2002) [JETP Lett. **75**, 378 (2002)].

Translated by V. Sakun

Triplet Proximity Effect in FSF Trilayers[¶]

Ya. V. Fominov[1, 2], A. A. Golubov[2], and M. Yu. Kupriyanov[3]

[1] *Landau Institute for Theoretical Physics, Russian Academy of Sciences, Moscow, 117940 Russia*
[2] *Department of Applied Physics, University of Twente, 7500 AE Enschede, The Netherlands*
[3] *Nuclear Physics Institute, Moscow State University, Moscow, 119992 Russia*
e-mail: fominov@landau.ac.ru, a.golubov@tn.utwente.nl, mkupr@pn.sinp.msu.ru
Received March 27, 2003

We study the critical temperature T_c of FSF trilayers (F is a ferromagnet, S is a singlet superconductor), where the triplet superconducting component is generated at noncollinear magnetizations of the F layers. An exact numerical method is employed to calculate T_c as a function of the trilayer parameters, in particular, mutual orientation of magnetizations. Analytically, we consider limiting cases. Our results determine the conditions necessary for the existence of recently investigated odd triplet superconductivity in SF multilayers. © 2003 MAIK "Nauka/Interperiodica".

PACS numbers: 74.45.+c; 74.78.Fk; 75.70.Cn

A striking feature of the proximity effect between singlet superconductors and nonhomogeneous ferromagnets is the possibility of generating the triplet superconducting component [1, 2]. Recently, it was shown that the triplet component also arises in the case of several homogeneous but differently oriented ferromagnets [3]. Physically, the generating of the triplet component in SF systems [1–3] is similar to the case of magnetic superconductors [4].

In [3], the Josephson effect was studied, keeping in mind that the superconductivity in the system is not suppressed by the ferromagnets. However, this issue requires separate study.

Although the SF (F is ferromagnet, S is singlet superconductor) proximity effect is rather well studied, the influence of the mutual orientation of F-layer magnetizations (exchange fields) on T_c of layered SF structures has been mostly considered based on the cases of parallel (P) and antiparallel (AP) alignment [5–10]. At the same time, those are the only cases when the triplet component is absent.

A FSF trilayer with homogeneous but noncollinear magnetizations of the F layers is the simplest example of a layered structure in which the triplet component is generated. The triplet component (correlations between quasiparticles with parallel spins) arises as a result of interplay between the Andreev reflections at the two SF interfaces. This mechanism is similar to the one described in [2], with the difference that instead of local magnetic inhomogeneity we deal with magnetic inhomogeneity of the structure as a whole.

The critical temperature of the noncollinear FSF system was studied in [11]. However, in that work the

triplet component was not taken into account. Thus, calculation of T_c in the noncollinear FSF trilayer is still an open question.

In this letter, we study the critical temperature of a FSF trilayer at an arbitrary angle between the in-plane magnetizations (see Fig. 1), which makes it necessary to take the triplet component into account. We reduce the problem to a form that allows us to apply general numerical methods developed in [12, 13]. This form also leads to some general conclusions about T_c and allows analytical progress in limiting cases.

1. General description. We consider the dirty limit, which is described by the Usadel equations. Near the T_c, the Usadel equations are linearized and contain only the anomalous Green's function $\hat{F}$ [1]:

$$\frac{D}{2}\frac{d^2\hat{F}}{dx^2} - |\omega_n|\hat{F} + \Delta\hat{\sigma}_3 - \frac{i}{2}\mathrm{sgn}\,\omega_n(\hat{F}\hat{H}^* + \hat{H}\hat{F}) = 0,$$

$$\hat{F} = \begin{pmatrix} f_{\uparrow\downarrow} & f_{\uparrow\uparrow} \\ f_{\downarrow\downarrow} & f_{\downarrow\uparrow} \end{pmatrix}. \tag{1}$$

Here, D is the diffusion constant (D_s and D_f for the S and F layers), $\omega_n = \pi T(2n + 1)$ are the Matsubara frequencies, and $\hat{\sigma}_3$ is the third Pauli matrix. The function $\hat{F}$ is a matrix in the spin space. The $f_{\uparrow\uparrow}$ and $f_{\downarrow\downarrow}$ components describe the triplet superconducting correlations. In the P and AP cases, it is sufficient to consider only the scalar equation for the singlet component $f_{\uparrow\downarrow}$.

Equation (1) is written in the general case when both pair potential and exchange field are present. In our sys-

tem, in the F layers the pair potential is absent, $\Delta = 0$, while

$$\hat{H} = h(\hat{\sigma}_2 \sin\alpha + \hat{\sigma}_3 \cos\alpha) \qquad (2)$$

at the exchange field $\mathbf{h} = h(0, \sin\alpha, \cos\alpha)$. h is the exchange energy, and α describes the direction of the in-plane magnetization.

In the S layer, the exchange energy is zero, while the pair potential obeys the self-consistency equation

$$\Delta \ln\frac{T_{cs}}{T} = \pi T \sum_{\omega_n} \left(\frac{\Delta}{|\omega_n|} - f_{\uparrow\downarrow} \right), \qquad (3)$$

where T_{cs} is the critical temperature of the S material. In the case of a single S layer, Δ can be chosen real.

The boundary conditions at the outer surfaces of the trilayer are

$$d\hat{F}_f/dx = 0, \qquad (4)$$

while at the SF interfaces

$$\xi_s(d\hat{F}_s/dx) = \gamma\xi_f(d\hat{F}_f/dx), \quad \gamma = \rho_s\xi_s/\rho_f\xi_f, \qquad (5)$$

$$\pm\xi_f\gamma_b(d\hat{F}_f/dx) = \hat{F}_s - \hat{F}_f, \quad \gamma_b = R_b\mathscr{A}/\rho_f\xi_f. \qquad (6)$$

Here, $\xi_{s(f)} = \sqrt{D_{s(f)}/2\pi T_{cs}}$ and $\rho_{s(f)}$ are the coherence lengths and the normal state resistivities of the S and F metals, R_b is the total resistance of the SF boundary, and $\mathscr{A}$ is its area. The $\pm$sign on the l.h.s. of Eq. (6) refers to the left and right SF interface, respectively. The above boundary conditions were derived for SN interfaces [14] (N is a normal metal); their use in the SF case is justified by the small parameter $h/E_F \ll 1$ (E_F is the Fermi energy).

We expand the Green's function $\hat{F}$ in the basis of the Pauli matrices $\hat{\sigma}_i$, $i = 1, 2, 3$, and the unity matrix $\hat{\sigma}_0$. It can be shown that the solution has the form

$$\hat{F} = f_0\hat{\sigma}_0 + f_1\hat{\sigma}_1 + f_3\hat{\sigma}_3. \qquad (7)$$

The f_0 component is imaginary, while f_1 and f_3 are real. The relations $f_0(-\omega_n) = -f_0(\omega_n)$, $f_1(-\omega_n) = -f_1(\omega_n)$, $f_3(-\omega_n) = f_3(\omega_n)$ make it sufficient to consider only positive Matsubara frequencies.

The f_1 component describes a special type of triplet condensate [1, 3], odd in frequency $[f_1(-\omega_n) = -f_1(\omega_n)]$ and even in momentum, which is similar to the one proposed by Berezinskii [15]. It is the independence of the momentum direction that allows the triplet condensate to survive in the diffusive limit.

Equation (1) yields three coupled scalar equations (we consider $\omega_n > 0$):

$$\frac{D}{2}\frac{d^2f_0}{dx^2} - \omega_n f_0 - ihf_3\cos\alpha = 0,$$

$$\frac{D}{2}\frac{d^2f_1}{dx^2} - \omega_n f_1 + hf_3\sin\alpha = 0, \qquad (8)$$

$$\frac{D}{2}\frac{d^2f_3}{dx^2} - \omega_n f_3 - ihf_0\cos\alpha - hf_1\sin\alpha + \Delta = 0.$$

Analyzing the symmetries implied by Eqs. (8) and the geometry of the system, we conclude that $f_0(x) = f_0(-x)$, $f_1(x) = -f_1(-x)$, $f_3(x) = f_3(-x)$. Thus, we can consider only one half of the system, say $x < 0$, while the boundary conditions at $x = 0$ are

$$df_0/dx = 0, \quad f_1 = 0, \quad df_3/dx = 0. \qquad (9)$$

Below, we shall use the following wave vectors:

$$k_f = \sqrt{2\omega_n/D_f}, \quad k_h = \sqrt{h/D_f},$$
$$\tilde{k}_h = \sqrt{k_f^2 + 2ik_h^2}, \quad k_s = \sqrt{2\omega_n/D_s}. \qquad (10)$$

The solution in the left F layer, satisfying the boundary condition (4), has the form

$$\hat{F}_f = C_1(i\hat{\sigma}_0\sin\alpha + \hat{\sigma}_1\cos\alpha)\cosh[k_f(x + d_s + d_f)]$$

$$+ C_2(\hat{\sigma}_0\cos\alpha + i\hat{\sigma}_1\sin\alpha + \hat{\sigma}_3)\cosh[\tilde{k}_h(x + d_s + d_f)] \qquad (11)$$

$$+ C_3(\hat{\sigma}_0\cos\alpha + i\hat{\sigma}_1\sin\alpha - \hat{\sigma}_3)\cosh[\tilde{k}_h^*(x + d_s + d_f)].$$

The matrix boundary condition (6) yields three scalar equations, which allow us to express the coefficients C_1, C_2, C_3 in terms of the components f_0, f_1, f_3 of the Green's function on the S side of the FS interface:

$$C_1 = (-if_0\sin\alpha + f_1\cos\alpha)/(1 + \gamma_b A_f),$$

$$C_2 = (f_0\cos\alpha - if_1\sin\alpha + f_3)/2(1 + \gamma_b A_h), \qquad (12)$$

$$C_3 = (f_0\cos\alpha - if_1\sin\alpha - f_3)/2(1 + \gamma_b A_h^*),$$

where we have introduced the following notations:

$$A_f = k_f\xi_f\tanh(k_f d_f), \quad A_h = \tilde{k}_h\xi_f\tanh(\tilde{k}_h d_f),$$
$$V_f = \gamma A_f/(1 + \gamma_b A_f), \quad V_h = \gamma A_h/(1 + \gamma_b A_h). \qquad (13)$$

Then boundary condition (5) yields three scalar equations that entangle f_0, f_1, and f_3. Thus, the Green's function of the F layer is eliminated, and we obtain equations for the S layer only. Moreover, we can proceed further, because in the S layer the unknown function $\Delta(x)$ only enters the equation for the f_3 component [see Eqs. (8)]. At the same time, taking boundary conditions (9) into account, we can write $f_0 = B_0\cosh(k_s x)$, $f_1 = B_1\sinh(k_s x)$. Excluding B_0 and B_1, we arrive at the effective boundary condition for f_3:

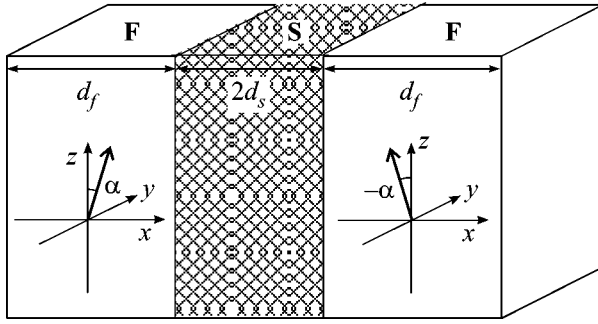$$\xi_s(df_3/dx) = Wf_3, \qquad (14)$$

Fig. 1. FSF trilayer. The system is the same as in [11]. The thickness of the S layer is $2d_s$, of each F layer—d_f. The center of the S layer corresponds to $x = 0$. The thick arrows in the F layers denote the exchange fields **h** lying in the (y, z) plane. The angle between the in-plane exchange fields is 2α.
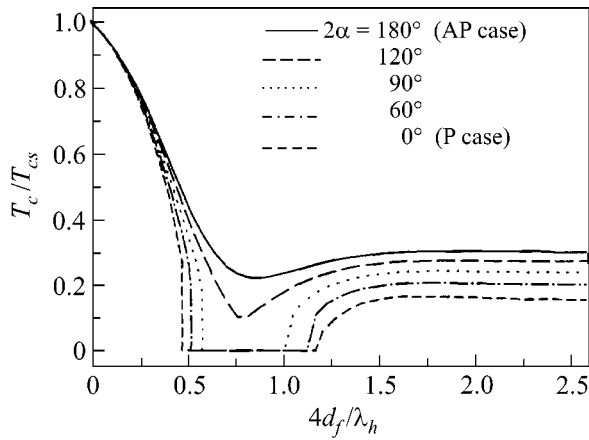

Fig. 2. Critical temperature T_c vs. thickness of the F layers d_f, which is normalized on the wavelength of the singlet component oscillations $\lambda_h = 2\pi/k_h$. Parameters $d_s/\xi_s = 1.2$, $h/\pi T_{cs} = 6.8$, $\gamma = 0.15$, $\gamma_b = 0.02$ correspond to [13]. The curves are calculated at different angles 2α between the in-plane exchange fields in the F layers.

where

$$W = \mathrm{Re}\,V_h + \frac{(\mathrm{Im}\,V_h)^2}{k_s\xi_s A(\alpha) + \mathrm{Re}\,V_h}, \tag{15}$$

and the angular dependence is determined by

$$A$$
$$= \frac{k_s\xi_s\tanh(k_s d_s) + V_f[\sin^2\alpha + \tanh^2(k_s d_s)\cos^2\alpha]}{k_s\xi_s[\cos^2\alpha + \tanh^2(k_s d_s)\sin^2\alpha] + V_f\tanh(k_s d_s)}. \tag{16}$$

Effectively, we obtain the following problem:

$$\Delta\ln\frac{T_{cs}}{T} = 2\pi T\sum_{\omega_n > 0}\left(\frac{\Delta}{\omega_n} - f_3\right), \tag{17}$$

$$\frac{D_s}{2}\frac{d^2 f_3}{dx^2} - \omega_n f_3 + \Delta = 0, \tag{18}$$

$$\xi_s\frac{df_3(-d_s)}{dx} = W(\omega_n)f_3(-d_s), \quad \frac{df_3(0)}{dx} = 0. \tag{19}$$

This is exactly the problem that was solved in [12, 13]. Inserting the new function W, we can use the methods developed in those works. At $\alpha = 0$, Eq. (15) reproduces W from [12, 13].

All information about the F layers is contained in a single function W, and all information about the misorientation angle is in its part $A(\alpha)$. Knowledge of W is already sufficient to draw several general conclusions about the behavior of T_c. First, if the S layer is thick, i.e., $d_s \gg \xi_s$, then $\tanh(k_s d_s) \approx 1$ at characteristic frequencies, and T_c does not depend on α. Qualitatively, this happens because the effect of mutual orientation of the F layers is due to "interaction" between the two SF interfaces, which is efficient only in the case of a thin S layer. Second, T_c does not depend on d_f if $d_f \gg \max(\xi_f, k_h^{-1})$. Qualitatively, this is due to the fact that quasiparticles penetrate from the S to F layer only on the scale $\max(\xi_f, k_h^{-1})$.

The triplet component is "nonmonotonic" as a function of α: it vanishes at $\alpha = 0$ and $\alpha = \pi/2$ (P and AP case, respectively) and arises only between the two boundary values. However, the $T_c(\alpha)$ dependence is always monotonic. It can be directly proven from the monotonic behavior of $A(\alpha)$ and, hence, W. This rigorously derived conclusion disproves the result obtained by the approximate single-mode method in [7], where it was claimed that T_c in the AP configuration can be smaller than in the P case.

Numerical results obtained by the methods developed in [12, 13] are shown in Figs. 2, 3. A question arises: why is there a pronounced angular dependence in the case $d_s > \xi_s$, when the S layer is not thin? The answer is that the condition $d_s \ll \xi_s = \sqrt{D_s/2\pi T_{cs}}$ is a sufficient condition of thin S layer, whereas the necessary condition is weaker: $d_s \ll \xi = \sqrt{D_s/2\pi T_c}$, since the characteristic energy for a particular system is πT_c with its own value of T_c. The two conditions become essentially different if T_c is notably suppressed, and in this case T_c can exhibit a pronounced angular dependence at $d_s \ll \xi$, while it is possible to have $d_s > \xi_s$.

Experimentally, the conditions for observing the angular dependence of T_c are more easily met when T_c is substantially (but not completely) suppressed. Accordingly, the effect of α on $T_c(d_f)$ dependence is most pronounced near the re-entrant behavior. Experimental detection of such behavior was reported in [16].

2. Thin S layer. If $d_s \ll \xi_s$, then Δ is constant. The Usadel equation (18) can be solved, and the equation determining T_c takes the form

$$\ln\frac{T_{cs}}{T_c} = 2\pi T_c \sum_{\omega_n > 0} \left(\frac{1}{\omega_n} - \frac{1}{\omega_n + W\pi T_{cs}\xi_s/d_s}\right), \quad (20)$$

where W is given by Eq. (15) with simplified function $A(\alpha)$:

$$A = \frac{k_s^2\xi_s d_s + V_f[\sin^2\alpha + (k_s d_s)^2\cos^2\alpha]}{k_s\xi_s[\cos^2\alpha + (k_s d_s)^2\sin^2\alpha] + V_f k_s d_s}. \quad (21)$$

For the P and AP alignments, under the additional assumption of strong ferromagnetism ($h \gg \pi T_{cs}$), we obtain

$$\ln\frac{T_{cs}}{T_c^P} = \operatorname{Re}\psi\left(\frac{1}{2} + \frac{V_h\xi_s}{2}\frac{T_{cs}}{d_s}\frac{T_{cs}}{T_c^P}\right) - \psi\left(\frac{1}{2}\right), \quad (22)$$

$$\ln\frac{T_{cs}}{T_c^{AP}} = \psi\left(\frac{1}{2} + \frac{W\xi_s}{2}\frac{T_{cs}}{d_s}\frac{T_{cs}}{T_c^{AP}}\right) - \psi\left(\frac{1}{2}\right), \quad (23)$$

where ψ is the digamma function, V_h is determined by Eqs. (13) with $\tilde{k}_h = (1 + i)k_h$, and, in the region of parameters where $T_c \neq 0$ [the corresponding conditions can be extracted from the results for the critical thickness; see Eqs. (25), (26) below], we may write

$$W = \operatorname{Re}V_h + (\operatorname{Im}V_h)^2 d_s/\xi_s. \quad (24)$$

Due to symmetry, the result for the P case (22) reproduces that for the SF bilayer with S layer of thickness d_s [13]. In the AP case, if the second terms on the r.h.s. of Eq. (24) can be neglected (e.g., at $k_h d_f \gg 1$ in the region of parameters where $T_c \neq 0$), then $W = \operatorname{Re}V_h$ and we reproduce the result of [8]. However, the second term becomes essential in the Cooper limit, defined by $d_s \ll \sqrt{D_s/2\omega_D}$, $d_f \ll \min(\sqrt{D_f/2\omega_D}, k_h^{-1})$, $\gamma_b = 0$, with ω_D the Debye energy of the S material. In this case, $\operatorname{Re}V_h = 0$ and Eqs. (23), (24) reproduce the result of Tagirov [5].

The critical thickness d_{sc} of the S layer, below which the superconductivity vanishes, immediately follows from Eqs. (22), (23) for the P and AP cases:

$$d_{sc}^P/\xi_s = 2e^C|V_h|, \quad d_{sc}^{AP}/\xi_s = 2e^C W \quad (25)$$

at

$$d_{sc}/\xi_s \ll 1. \quad (26)$$

Here, $C \approx 0.577$ is Euler's constant. Condition (26) is necessary for applicability of Eqs. (25). If this condition is not satisfied, then Eqs. (25) only tell us that at $d_s/\xi_s \ll 1$ the superconductivity is certainly absent, i.e., $T_c = 0$. According to the monotonic growth of $T_c(\alpha)$, the function $d_{sc}(\alpha)$ decreases monotonically, hence $d_{sc}^P >$
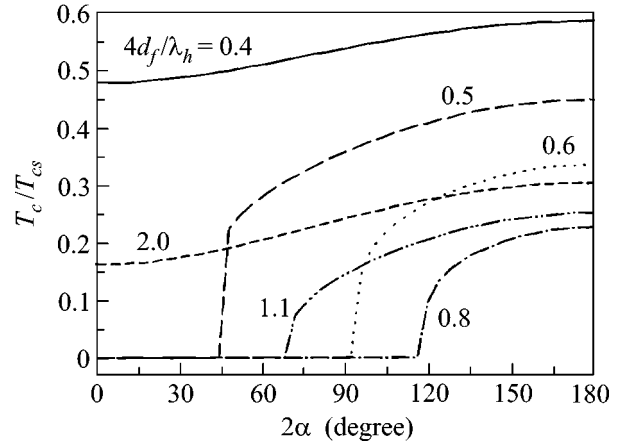
Fig. 3. T_c vs. misorientation angle 2α. The curves correspond to different thicknesses of the F layers d_f. The parameters are the same as in Fig. 2.

d_{sc}^{AP}. At $\gamma_b = 0$, $k_h d_f \gg 1$, Eqs. (25) reproduce the results of [11] for the P and AP cases.

The $T_c(\alpha)$ dependence can be most easily studied in the Cooper limit. In this case, a simple analysis (see, e.g., Appendix Al in [13]) can be performed on the level of the Usadel equations, and the system is described as a uniform layer with the effective exchange energy[1]

$$h_{\text{eff}} = (\tau_f/\tau_s)h\cos\alpha, \quad (27)$$

where $\tau_{s(f)} = 2d_{s(f)}R_b\mathcal{A}/\rho_{s(f)}D_{s(f)}$. The accuracy of this result is limited to the first order over h, which becomes insufficient in the vicinity of $\alpha = \pi/2$. At $\alpha = \pi/2$, the first-order effect of h vanishes, while a more accurate analysis ([5] and Eqs. (23), (24)) reveals the second-order effect of h on T_c.

Let us now consider the same limit as in [11]:

$$d_s \ll \xi_s, \quad k_h d_f \gg 1, \quad h \gg \pi T_{cs}, \quad \gamma_b = 0, \quad (28)$$

$$\gamma k_h\xi_f d_s/\xi_s \ll 1. \quad (29)$$

The condition to have superconductivity at least at some orientations has the form $d_{sc}^{AP} < d_s \ll \xi_s$, and, in the case under discussion, Eqs. (25), (26) yield

$$2e^C\gamma k_h\xi_f < d_s/\xi_s \ll 1. \quad (30)$$

Hence, condition (29) becomes redundant.

Starting from Eqs. (15), (20), and (21), we finally obtain the following equation for T_c:

$$\ln\frac{T_{cs}}{T_c} = Q\psi\left(\frac{1}{2} + \frac{\Omega_1}{2\pi T_c}\right) + R\psi\left(\frac{1}{2} + \frac{\Omega_2}{2\pi T_c}\right) - \psi\left(\frac{1}{2}\right), (31)$$

---

[1] Since ω_n was neglected in comparison with h in the Usadel equation, the result of the Cooper limit is valid only at $\tau_s \gg \tau_f$.
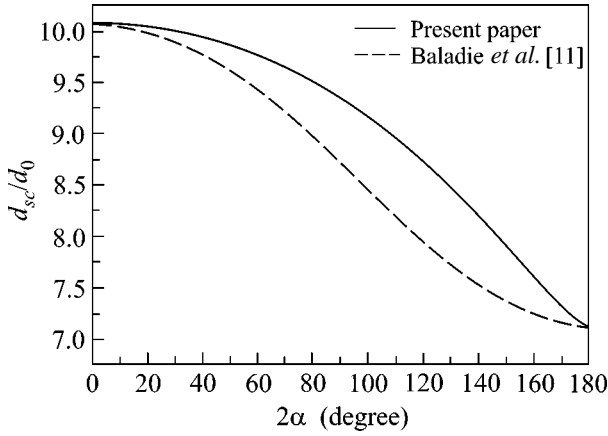
Fig. 4. Critical thickness of the S layer d_{sc} vs. misorientation angle 2α. Dashed line is the result of [11], obtained without account of the triplet component.

where

$$Q = \frac{1}{2} + \frac{\sin^2\alpha}{2\sqrt{\sin^4\alpha - 4\cos^2\alpha}}, \quad R = 1 - Q,$$

$$\Omega_{1,2} = \frac{d_0}{d_s}\pi T_{sc}(1 + \cos^2\alpha \pm \sqrt{\sin^4\alpha - 4\cos^2\alpha}), \quad (32)$$

$$d_0 = \gamma k_h \xi_f \xi_s / 2.$$

In the P and AP cases, where the triplet component is absent, Eqs. (31), (32) reproduce the results of [6, 11]. At the same time, at a noncollinear alignment the results are clearly different.

The critical thickness is found from Eqs. (31), (32):

$$d_{sc}(\alpha)/d_0 = 4\sqrt{2}e^C\cos\alpha$$

$$\times \left(\frac{1 + \cos^2\alpha + \sqrt{\sin^4\alpha - 4\cos^2\alpha}}{1 + \cos^2\alpha - \sqrt{\sin^4\alpha - 4\cos^2\alpha}}\right)^{\frac{\sin^2\alpha}{2\sqrt{\sin^4\alpha - 4\cos^2\alpha}}} \quad (33)$$

Although the square root in this expression can become imaginary, the whole expression remains real (z^i is real if $|z| = 1$). Figure 4 illustrates the result (33).

Now we turn to analyze the conditions of applicability for the results reported in [3]. A noncollinear FSF trilayer is a unit cell of the multilayered structure studied in that work. The main result of [3], the Josephson current due to the long-range triplet component, requires that the S layer be thin $d_s \ll \xi_s$, while the F layers are thick for the singlet component and moderate for the triplet one: $k_h^{-1} \ll \xi_f < d_f$ [3]. In this case, the condition that superconductivity is not completely sup-

pressed at least in the vicinity of the AP alignment (Eqs. (25), (26)) takes the form

$$4e^C\gamma k_h\xi_f\frac{1 + 2\gamma_b k_h\xi_f}{(1 + 2\gamma_b k_h\xi_f)^2 + 1} < \frac{d_s}{\xi_s} \ll 1. \quad (34)$$

At $\gamma_b = 0$ (as was assumed in [3]), this yields $2e^C\gamma k_h\xi_f < d_s/\xi_s \ll 1$, which is a rather strong condition for γ, since $k_h\xi_f \gg 1$. Finite interface transparency relaxes this condition: even at $\gamma_b \sim 1$, Eq. (34) yields $2e^C\gamma/\gamma_b < d_s/\xi_s \ll 1$.

The condition that superconductivity exists at all orientations has a form similar to Eq. (34) but with the corresponding expression for d_{sc}^P instead of d_{sc}^{AP} on the l.h.s. This only leads to a minor difference, since the two critical thicknesses are of the same order: $d_{sc}^P = \sqrt{2}d_{sc}^{AP}$ at $\gamma_b = 0$, while $d_{sc}^P = d_{sc}^{AP}$ at $\gamma_b > 1$.

In conclusion, we have studied T_c of a FSF trilayer as a function of its parameters, in particular, the angle between magnetizations of the F layers. The angular dependence becomes pronounced when the S layer is thin and can lead to switching between superconducting and nonsuperconducting states as the angle is varied. Our results directly apply to multilayered SF structures, where a FSF trilayer is a unit cell. We have formulated the conditions necessary for the existence of recently investigated odd triplet superconductivity in SF multilayers [3].

REFERENCES

1. F. S. Bergeret, K. B. Efetov, and A. I. Larkin, Phys. Rev. B **62**, 11872 (2000); F. S. Bergeret, A. F. Volkov, and K. B. Efetov, Phys. Rev. Lett. **86**, 4096 (2001).

2. A. Kadigrobov, R. I. Shekhter, and M. Jonson, Europhys. Lett. **54**, 394 (2001); Fiz. Nizk. Temp. **27**, 1030 (2001) [Low Temp. Phys. **27**, 760 (2001)].

3. A. F. Volkov, F. S. Bergeret, and K. B. Efetov, Phys. Rev. Lett. **90**, 117006 (2003).

4. L. N. Bulaevskii, A. I. Rusinov, and M. Kulić, J. Low. Temp. Phys. **39**, 255 (1980).

5. L. R. Tagirov, Phys. Rev. Lett. **83**, 2058 (1999).

6. A. I. Buzdin, A. V. Vedyayev, and N. V. Ryzhanova, Europhys. Lett. **48**, 686 (1999).

7. M. G. Khusainov, Yu. A. Izyumov, and Yu. N. Proshin, Pis'ma Zh. Éksp. Teor. Fiz. **73**, 386 (2001) [JETP Lett. **73**, 344 (2001)].

8. I. Baladié and A. Buzdin, Phys. Rev. B **67**, 014523 (2003).

9. G. Deutscher and F. Meunier, Phys. Rev. Lett. **22**, 395 (1969).

10. J. Y. Gu, C.-Y. You, J. S. Jiang, *et al.*, Phys. Rev. Lett. **89**, 267001 (2002).

11. I. Baladié, A. Buzdin, N. Ryzhanova, and A. Vedyayev, Phys. Rev. B **63**, 054518 (2001).

12. Ya. V. Fominov, N. M. Chtchelkatchev, and A. A. Golubov, Pis'ma Zh. Éksp. Teor. Fiz. **74**, 101 (2001) [JETP Lett. **74**, 96 (2001)].

13. Ya. V. Fominov, N. M. Chtchelkatchev, and A. A. Golubov, Phys. Rev. B **66**, 014507 (2002).

14. M. Yu. Kupriyanov and V. F. Lukichev, Zh. Éksp. Teor. Fiz. **94** (6), 139 (1988) [Sov. Phys. JETP **67**, 1163 (1988)].

15. V. L. Berezinskiĭ, Pis'ma Zh. Éksp. Teor. Fiz. **20**, 628 (1974) [JETP Lett. **20**, 287 (1974)].

16. I. A. Garifullin, D. A. Tikhonov, N. N. Garif'yanov, *et al.*, Phys. Rev. B **66**, 020505 (2002).

Duality and Effective Conductivity
of Random Two-Phase Flat Systems[¶]

S. A. Bulgadaev

Landau Institute for Theoretical Physics, Russian Academy of Sciences, Chernogolovka, Moscow region, 142432 Russia
e-mail: sabul@dio.ru
Received December 19, 2002; in final form, April 3, 2003

The possible functional forms of the effective conductivity σ_e of randomly inhomogeneous two-phase systems at arbitrary values of concentrations are discussed. Two explicit approximate expressions for effective conductivity are found using a duality relation, a series expansion of σ_e in the inhomogeneity parameter z, and some additional conjectures about the functional form of σ_e. They differ from the effective medium approximation, satisfy all necessary requirements, and reproduce the known formulas for σ_e in the weakly inhomogeneous case. This can also signify that σ_e of the two-phase randomly inhomogeneous systems may be a nonuniversal function, depending on some details of the structure of the random inhomogeneities. © *2003 MAIK "Nauka/Interperiodica".*

PACS numbers: 73.61.-r; 73.50.Bk

The electrical transport properties of the disordered systems have an important practical interest. For this reason, they are intensively studied theoretically as well as experimentally. In this region, there is one classical problem about the effective conductivity σ_e of an inhomogeneous (randomly or regularly) heterophase system which is a mixture of N ($N \geq 2$) different phases with different conductivities σ_i, $i = 1, 2, \ldots, N$. We confine ourselves here to the simplest case of two-dimensional heterophase systems with $N = 2$. Despite its relative simplicity, only a few general exact results have been obtained so far. There is a general expression for σ_e in the case of a weakly inhomogeneous isotropic medium, when the conductivity fluctuations $\delta\sigma$ are smaller than the average conductivity $\langle\sigma\rangle$ [1]

$$\sigma_e = \langle\sigma\rangle\left(1 - \frac{\langle(\delta\sigma)^2\rangle}{D\langle\sigma\rangle^2}\right) = \langle\sigma\rangle\left(1 - \frac{\langle\sigma^2\rangle - \langle\sigma\rangle^2}{D\langle\sigma\rangle^2}\right), \quad (1)$$

where D is the dimension of the system. In our case of two-dimensional two-phase system $\langle\sigma\rangle = x\sigma_1 + (1 - x)\sigma_2$, $\langle\sigma^2\rangle - \langle\sigma\rangle^2 = 4x(1 - x)\sigma_-^2$, where x is a concentration of the first phase, $\sigma_- = (\sigma_1 - \sigma_2)/2$, and (1) takes the form

$$\sigma_e = \sigma_+(1 + 2(x - 1/2)z - 2x(1 - x)z^2), \quad (2)$$

where $\sigma_+ = (\sigma_1 + \sigma_2)/2$, and a new variable $z = \sigma_-/\sigma_+$, characterizing an inhomogeneity of the system is introduced.

The further progress in the solution of this problem is connected with the discovery of a dual transforma-

tion, interchanging the phases [2, 3]. This transformation allows one to find an exact formula for σ_e in the case of systems with equal concentrations of the phases $x = x_c = 1/2$ [3]:

$$\sigma_e = \sqrt{\sigma_1\sigma_2}. \quad (3)$$

This remarkable formula is very simple and universal, since it does not depend on the type of the inhomogeneous structure of the two-phase system. For systems with unequal phase concentrations, a dual transformation gives a relation between effective conductivities at adjoint concentrations x and $1 - x$ or in terms of a new variable $\epsilon = x - x_c$ ($-1/2 \leq \epsilon \leq 1/2$) at ϵ and $-\epsilon$:

$$\sigma_e(x, \sigma_1, \sigma_2)\sigma_e(1 - x, \sigma_1, \sigma_2) = \sigma_1\sigma_2$$
$$= \sigma_e(\epsilon, \sigma_1, \sigma_2)\sigma_e(-\epsilon, \sigma_1, \sigma_2). \quad (4)$$

Relation (4) means that the product of the effective conductivities at adjoint concentrations is an invariant. Due to this relation, one can consider σ_e only in the regions $x \geq x_c$ ($\epsilon \geq 0$) or $x \leq x_c$ ($\epsilon \leq 0$).

However, an explicit formula for the effective conductivity at arbitrary phase concentrations and z attracts the main interest in this problem. One such formula was obtained many years ago in the so-called effective medium (EM) approximation [4], which turned out to be a good approximation for random resistor networks not only in the weakly inhomogeneous case [5]. In this paper, using a duality relation and a series expansion in the inhomogeneity parameter z, we will find two explicit approximate expressions for the effective conductivity of two-phase systems, differing from the EM approximation. The physical models corresponding to

---

[¶] This article was submitted by the author in English.

them are introduced in other papers, where their properties are discussed in detail [6, 7].

Let us start our investigation of the isotropic classical random two-phase system in the case of arbitrary concentrations with a general analysis of the possible functional form of the effective conductivity. Due to the linearity of the defining equations [1, 3], the effective conductivity of the random systems must be a homogeneous function of degree one of σ_i, $i = 1, 2, \ldots, N$. In the case of $N = 2$, it is convenient to use, instead of σ_i ($i = 1, 2$), the variables σ_+ and z ($-1 \le z \le 1$) and, instead of x, a new variable $\epsilon = x - 1/2$ ($-1/2 \le \epsilon \le 1/2$). Then the effective conductivity can be represented in the following form, symmetrical relative to both phases:

$$\sigma_e(\epsilon, \sigma_+, \sigma_-) = \sigma_+ f(\epsilon, \sigma_-/\sigma_+) = \sigma_+ f(\epsilon, z), \quad (5)$$

where $\sigma_e(\epsilon, \sigma_+, \sigma_-)$ and $f(\epsilon, z)$ must have the next boundary values

$$\sigma_e(1/2, \sigma_+, \sigma_-) = \sigma_1, \quad \sigma_e(-1/2, \sigma_+, \sigma_-) = \sigma_2,$$

$$f(1/2, z) = 1 + z, \quad f(-1/2, z) = 1 - z, \quad (5')$$

$$f(\epsilon, 0) = 1.$$

The duality relation in these variables takes the form

$$f(\epsilon, z) f(-\epsilon, z) = 1 - z^2, \quad (6)$$

from which it follows that at critical concentration $\epsilon = 0$

$$f(0, z) = \sqrt{1 - z^2}. \quad (3')$$

Strictly speaking, the form of duality relation (6) is also a consequence of another exact relation for the effective conductivity, taking place at arbitrary concentrations for systems with similar random structures of both phases of the system,

$$\sigma_e(\epsilon, \sigma_1, \sigma_2) = \sigma_e(-\epsilon, \sigma_2, \sigma_1). \quad (7)$$

This means that the effective conductivity of the random two-phase system must be invariant under substitution of these phases ($\sigma_1 \longleftrightarrow \sigma_2$) with the corresponding change of their concentrations $x \longleftrightarrow 1 - x$ (or $\epsilon \longrightarrow -\epsilon$). In the new variables, this means that

$$f(\epsilon, z) = f(-\epsilon, -z), \quad f(-\epsilon, z) = f(\epsilon, -z). \quad (8)$$

For this reason, the duality relation can also be written in the form

$$f(\epsilon, z) f(\epsilon, -z) = 1 - z^2. \quad (9)$$

It follows from (8) that the even (f_s) and odd (f_a) parts of $f(\epsilon, z)$ relative to ϵ coincide with the even (f^s) and odd (f^a) parts of $f(\epsilon, z)$ relative to z. Consequently, $f(\epsilon, z)$ has the functional form

$$f(\epsilon, z) = f(\epsilon z, \epsilon^2, z^2). \quad (10)$$

One can see from (10) that (1) $f(0, z)$ is an even function of z (i.e., symmetric in $\sigma_{1,2}$) and (2) an expansion of $f(\epsilon, z)$ near the point $\epsilon = z = 0$ does not contain terms

linear in ϵ and z separately. Analogously, the odd part f_a can be represented in the form

$$f_a(\epsilon, z) = 2\epsilon z \Phi(\epsilon, z), \quad (11)$$

where Φ is an even function of ϵ and z (the coefficient 2 in front of ϵz is chosen for further convenience).

At first sight, the duality relation (11) alone is not enough for the complete determination of f in the general case. It only connects f at adjoint concentrations or f_a and f_s:

$$f_s^2 - f_a^2 = 1 - z^2. \quad (12)$$

This means that f_a and f_s considered at fixed z as the functions of ϵ satisfy the hyperbolic relation with a constant depending on z. Relation (12) allows one to express $f(\epsilon, z)$ through its even or odd parts

$$f(\epsilon, z) = f_a + \sqrt{f_a^2 + 1 - z^2} = f_s \pm \sqrt{f_s^2 - 1 + z^2}. \quad (13)$$

For this reason, it is enough to know only one of these two parts. Usually, one prefers to choose an antisymmetric part as a more simple one. It follows from (2) that, in the weakly inhomogeneous case, the odd part coincides with the odd part of $\langle \sigma \rangle$ and has the simplest form (compatible with (11)):

$$f_a(\epsilon, z) = 2\epsilon z. \quad (14)$$

As is well known, the effective conductivity in the EM approximation can be obtained by substitution of (14) into (13):

$$\sigma_e(\epsilon, z) = \sigma_+[2\epsilon z + \sqrt{(2\epsilon z)^2 + 1 - z^2}]. \quad (15)$$

We will call this expression, continued on arbitrary concentrations $x = \epsilon + 1/2$ and inhomogeneities z, the EM approximation for σ_e.

However, systems with a dual symmetry usually have some additional hidden properties, permitting one to obtain more information about the function under question. Moreover, in some cases these properties can help to solve the problem exactly (see, for example, [8]). Having this in mind, we will try to investigate the duality relation in more detail. For every fixed $z \ne 1$ (it is enough to consider only the region $0 \le z \le 1$), a function f must be a monotonic function of ϵ. Since the homogeneous limit $z \longrightarrow 0$ is a regular point of f, it will be very useful to expand f in a series in z:

$$f(\epsilon, z) = \sum_0^\infty f_k(\epsilon) z^k / k!, \quad (16)$$

where, due to the boundary conditions (5'),

$$f_0 = 1, \quad f_1(\epsilon) = 2\epsilon. \quad (17)$$

It is worth noting here that expansion (16) differs from the weak-disorder expansion of σ_e in series on the averaged powers of the conductivity fluctuations $\delta\sigma/\langle\sigma\rangle$ (see, for example, [9]). Expansion (16) is simpler, since

it deals with variables z and ϵ separately, while the expansion in powers of $\delta\sigma/\langle\sigma\rangle$ is an expansion on the rather complicated functions of z and ϵ. Of course, both expansions are connected, but expansion (16) is more convenient for our analysis of possible functional forms.

Substituting expansion (16) into (6), one obtains the following results:

(1) in the second order on z, it reproduces universal formula (2); thus, the latter can be considered as a consequence of the duality relation;

(2) in higher orders, there are recurrent relations between f_{2k} and f_{2k-1}, corresponding to connection (12);

(3) $f_{2k+1}(\epsilon)$ are odd polynomials in ϵ of degree $2k+1$ and $f_{2k}(\epsilon)$ are even polynomials in ϵ of degree $2k$ in agreement with (10).

Taking into account boundary conditions (5') and an exact value (3'), one can show that the coefficients f_k must have the next form

$$f_{2k+1}(\epsilon) = \epsilon(1-4\epsilon^2)g_{2k-2}(\epsilon), \quad k \geq 1,$$
$$f_{2k}(\epsilon) = (1-4\epsilon^2)h_{2k-2}(\epsilon), \quad k \geq 1,$$
(18)

where g_{2k-2} and h_{2k-2} are some even polynomials of the corresponding degree and free terms of h_{2k-2} coincide with the coefficients in the expansion of (3'):

$$\sqrt{1-z^2} = 1 - z^2/2 - z^4/8 - z^6/16$$
$$- z^8/128 - z^{10}/256 + \ldots.$$
(19)

It follows from (18) that f_3 is completely determined up to overall factor number g_0. Since f_4 is determined through lower f_k $(k = 1, 2, 3)$,

$$f_4 = 4f_1 f_3 - 3f_2^2 = (1-4\epsilon^2)[(8g_0+12)\epsilon^2 - 3], \quad (20)$$

it is also determined by the coefficient g_0. Expansion (16) in the EM approximation has a very simple form, since all $g_{2k-2} = 0$ $(k \geq 1)$ and $f_{2k}(\epsilon) \sim (1-4\epsilon^2)^k$. Thus, we see that, in the general case, the arbitrariness of f is strongly reduced by boundary conditions and by exact value (3) and that the third and fourth orders are determined only up to one constant. One can see from the EM approximation that any additional information about function f can determine this constant or even the whole function. For this reason, one needs to know what kind of functions can satisfy the duality relation (6) except general functions from (12), (13). In order to answer this question, it is convenient in the case $z \neq 1$ to pass from f to $\tilde{f} = f/\sqrt{1-z^2}$. Then

$$\tilde{f}(\epsilon, z)\tilde{f}(-\epsilon, z) = 1 = \tilde{f}(\epsilon, z)\tilde{f}(\epsilon, -z). \quad (6')$$

The duality relation gives some constraints on the possible functional form of $\tilde{f}(\epsilon, z)$. For example, assuming a functional form (10), one can write out the next simple expression

$$\tilde{f}(\epsilon, z) = \exp(\epsilon z \phi(\epsilon, z)), \quad (21)$$

where $\phi(\epsilon, z)$ is some even function of its arguments. Another possible form of $\tilde{f}$ is

$$\tilde{f}(\epsilon, z) = B(\epsilon, z)/B(-\epsilon, z).$$

It is easy to see that they automatically satisfy Eq. (6').

Let us now consider two simple ansatzes for a function ϕ. In case (a), we suppose that $\phi(\epsilon, z)$ depends only on z. This means an exponential dependence on concentration, which sometimes takes place in disordered systems [10]. In case (b), we will suppose that $\phi(\epsilon, z)$ depends only on the combination ϵz. This can signify, for example, that f depends only on mean conductivity $\langle\sigma\rangle$ and/or on mean resistivity $\langle\sigma^{-1}\rangle$, since $\langle\sigma^{\pm1}\rangle \sim (1 \pm 2\epsilon z)$. Expanding the corresponding functions $\tilde{f}$ in series, one can check after some algebra that it is now possible to determine all polynomial coefficients unambiguously! For example, one finds for f_a in the third and fifth orders

$$g_0 = -1, \quad g_2 = -(11+4\epsilon^2) \quad \text{case (a)},$$

$$g_0 = -3, \quad g_2 = -15(1+12\epsilon^2) \quad \text{case (b)}.$$

Another way to see this is to apply boundary conditions directly to the function (21). In case (a), one obtains

$$\phi(z) = 1/z \ln\frac{1+z}{1-z}, \quad \tilde{f}(\epsilon, z) = \left(\frac{1+z}{1-z}\right)^\epsilon. \quad (22)$$

It is interesting to note that, in terms of concentration x and partial conductivities σ_i, one obtains in case (a)

$$\sigma_e = \sigma_1^x \sigma_2^{1-x}. \quad (22')$$

This corresponds to the self-averaging of $\ln\sigma$:

$$\sigma_e = \exp\langle\ln\sigma\rangle, \quad \langle\ln\sigma\rangle = x\ln\sigma_1 + (1-x)\ln\sigma_2,$$

noted first by Dykhne for equal phase concentrations [3] and established later in the theory of weak localization [11].

In case (b), when ϕ depends only on the combination ϵz, one finds

$$\phi(\epsilon z) = \frac{1}{2\epsilon z}\ln\frac{1+2\epsilon z}{1-2\epsilon z}, \quad \tilde{f}(\epsilon, z) = \left(\frac{1+2\epsilon z}{1-2\epsilon z}\right)^{1/2}. \quad (23)$$

In terms of x and σ_i, it has the next simple form

$$\sigma_e = \sqrt{\langle\sigma\rangle/\langle\sigma^{-1}\rangle}. \quad (23')$$

Series expansions of (22) and (23) coincide exactly with the corresponding expansions mentioned above. They differ from the EM approximation even in the third order.

For a general form of $\phi(\epsilon, z)$, admitting a double series expansion in z^2 and ϵ^2,

$$\phi(\epsilon, z) = \sum_0^\infty \phi_k(\epsilon) z^{2k}/k!, \quad \phi_k(\epsilon) = \sum_0^\infty \phi_{kl} \epsilon^{2l}/l!,$$

one can show that now f_3 and f_4 again contain one free parameter ϕ_{10} : $g_0 = 6(\phi_{10} - 1)$. Consequently, one needs additional information or a more complicated ansatz for a determination of ϕ in the general case. This will be considered in another paper.

Thus, we have found two explicit functions (22) and (23), which satisfy all required properties. In particular, they reproduce Eq. (2) in the weakly inhomogeneous limit $z \ll 1$. These functions can be considered as regular solutions of the duality relation, since they are represented by convergent series in z for $0 \le z \le 1$ except the small region $z \longrightarrow 1$, $\epsilon \longrightarrow 1/2$.

The systems having the effective conductivity just of the two forms found above and their properties are considered in [6] (see also [7]). We give here their brief description.

The first model represents randomly inhomogeneous systems with compact inclusions of the second phase with finite maximal scale l_m of inhomogeneities. This scale can depend on concentration of the second phase $l_m(1 - x)$ (one can consider only the case $1 - x \le 1/2$). The stable effective conductivity $\sigma_e(x, \{\sigma\})$ (here $\{\sigma\} = (\sigma_1, \sigma_2)$), depending only on x and not depending on the scale on which the averaging is performed, can be obtained only after averaging over scales $l > l_m(x)$. This $\sigma_e(x, \{\sigma\})$ as a function of x must satisfy the next functional equation, generalizing duality relation (4):

$$\sigma_e(x', \{\sigma\})\sigma_e(x'', \{\sigma\}) = \sigma_e^2(x, \{\sigma\}), \qquad (24)$$

where $x = (x' + x'')/2$. The solution of equation (24), satisfying boundary conditions (5'), coincides with (22) and corresponds to the finite maximal scale averaging approximation [6, 7].

The second model of a random inhomogeneous systems has a hierarchical, two-level structure. On the first level, it consists of squares with random phase layers with a mean conductivity $\langle\sigma\rangle$ if the direction of layers is parallel to the applied electrical field E or with a conductivity $\langle\sigma^{-1}\rangle^{-1}$ if this direction is perpendicular to E. On the second level, these squares form a random parquet (or a lattice), which contains with equal probabilities ($p = 1/2$) squares with both orientations. Then, using universal formula (3), one can write the next approximate expression for σ_e:

$$\sigma_e(x, \{\sigma\}) = \sqrt{\langle\sigma\rangle\langle\sigma^{-1}\rangle^{-1}}, \qquad (25)$$

which coincides with (23).

For a comparison of the different expressions for effective conductivity (Eqs. (15), (22), and (23)), we have constructed three plots of the corresponding func-
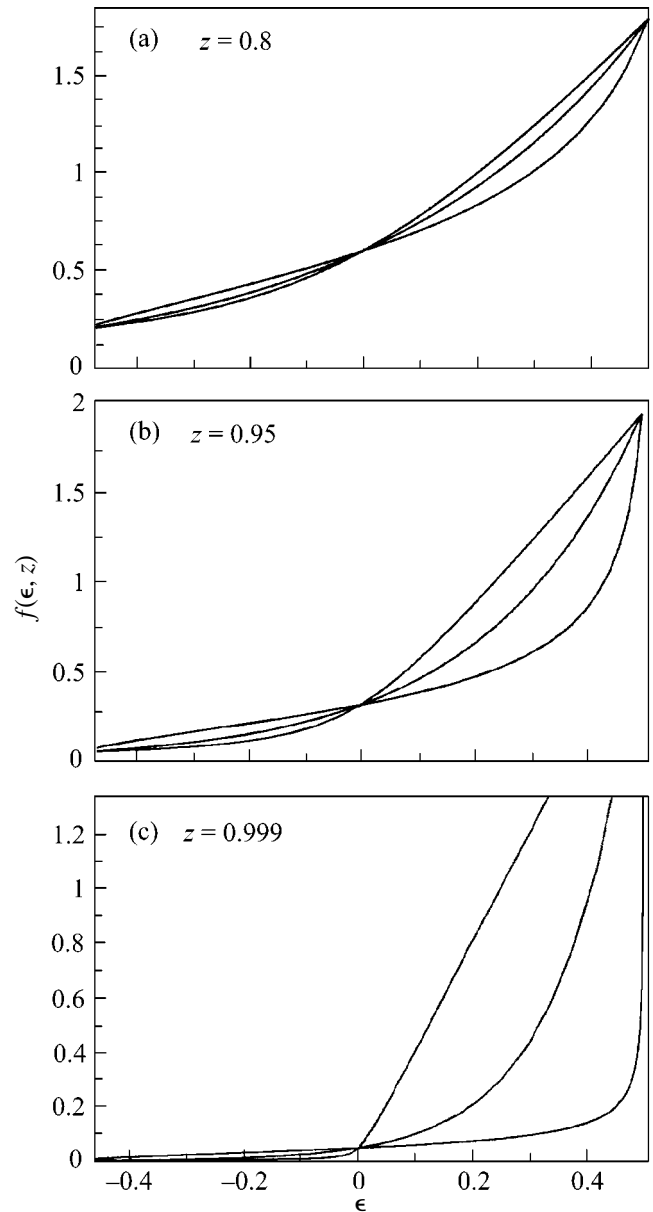

Fig. 1. Plots of various expressions for $f(\epsilon, z)$ at different values of z.

tions $f(\epsilon, z)$ at $z = 0.8$, 0.95, 0.999 (Fig. 1) (their full 3D plots are presented in [7]). The lower branch in the region $\epsilon > 0$ corresponds to f from (23), the upper branch to the EM approximation, and the middle branch to f from (22). It appears that all three formulas for $f(\epsilon, z)$, despite their various functional forms, differ from each other very weakly for $z \lesssim 0.5$ due to very restrictive boundary conditions (5') and the exact Keller–Dykhne value. This range of z corresponds approximately to the ratio $\sigma_2/\sigma_1 \sim 1/3$. For smaller ratios, the differences between these functions become distinguishable (for $\epsilon > 0$), growing significantly only for ratios $\sigma_2/\sigma_1 \lesssim 10^{-1}$.

One can see from formulas (22), (23) that, in both cases, one gets $\sigma_e \longrightarrow 0$ in the limit $\sigma_2 \longrightarrow 0$, except the small region near $x = 1$ and $z = 1$. This means that these formulas are not valid in the percolation limit $\sigma_2 \longrightarrow 0$ ($z \longrightarrow 1$) for $\epsilon > 0$ [10, 12]. One can show that such behavior is a consequence of the assumptions made about the form of the function ϕ and/or of the structure of the corresponding models [7].

It also follows from the plots that EM approximation overestimates the usual σ_e of the percolating systems [10, 12], and both the other formulas underestimate it in the region $z \longrightarrow 1$, $\epsilon > 0$. We hope to investigate this limit in detail later.

Thus, we have discussed possible functional forms of the effective conductivity of random two-phase systems at arbitrary values of concentrations. It was shown that the duality relation and some additional assumptions about the possible functional form of $f(\epsilon, z)$ can give its explicit expression, differing from the EM approximation. They automatically satisfy the duality relation and reproduce all known formulas for f in the weakly inhomogeneous limit $z \ll 1$.

Though the additional assumptions we made are approximate, the results obtained (and especially the existence of the corresponding models [6, 7]) can be interpreted also as if σ_e of the two-phase randomly inhomogeneous systems were a nonuniversal function, depending on some details of the structure of the random inhomogeneities. An analogous conclusion was made earlier for three-phase *regular* systems in [13], where the possibility of finding a generalization of the Keller–Dykhne formula (3) for the case $N = 3$ was studied numerically.

REFERENCES

1. L. D. Landau and E. M. Lifshitz, *Course of Theoretical Physics*, Vol. 8: *Electrodynamics of Continuous Media*, 2nd ed. (Nauka, Moscow, 1982; Pergamon, New York, 1984).
2. J. B. Keller, J. Math. Phys. **5**, 548 (1964).
3. A. M. Dykhne, Zh. Éksp. Teor. Phys. **59**, 110 (1970) [Sov. Phys. JETP **32**, 63 (1971)].
4. D. A. G. Bruggeman, Ann. Phys. (Leipzig) **24**, 636 (1935); R. Landauer, J. Appl. Phys. **23**, 779 (1952).
5. S. Kirkpatrick, Phys. Rev. Lett. **27**, 1722 (1971).
6. S. A. Bulgadaev, Europhys. Lett. (2003) (in press).
7. S. A. Bulgadaev, cond-mat/0212104.
8. R. J. Baxter, *Exactly Solved Models in Statistical Mechanics* (Academic, New York, 1982; Mir, Moscow, 1985).
9. J. M. Luck, Phys. Rev. B **43**, 3933 (1991).
10. B. I. Shklovskii and A. L. Éfros, *Electronic Properties of Doped Semiconductors* (Nauka, Moscow, 1979; Springer, Berlin, 1984).
11. P. W. Anderson, D. J. Thouless, E. Abrahams, and D. S. Fisher, Phys. Rev. B **22**, 3519 (1980).
12. S. Kirkpatrick, Rev. Mod. Phys. **45**, 574 (1973).
13. L. G. Fel, V. Sh. Machavariani, I. M. Khalatnikov, and D. J. Bergman, Preprint (Tel Aviv Univ., 2000).

Resonant Raman Scattering in Superconducting Ba$_{1-x}$K$_x$BiO$_3$

A. P. Menushenkov[1, *], I. A. Troyan[2], and M. I. Eremets[3]

[1] *Moscow Engineering Physics Institute (State University), Moscow, 115409 Russia*
e-mail: menushen@htsc.mephi.ru
[2] *Vereshchagin Institute of High Pressure Physics, Russian Academy of Sciences, Troitsk, Moscow region, 142092 Russia*
[3] *Max-Planck Institut für Chemie, 55020 Mainz, Germany*
Received April 8, 2003

The effect of the photon energy of the exciting laser radiation on the Raman spectra of Ba$_{1-x}$K$_x$BiO$_3$ with $x =$ 0.25, 0.40, and 0.50 is studied. An increase in the laser wavelength from 488 to 750 nm scarcely affects the amplitudes and frequencies of the spectral lines in the Raman spectra of the nonsuperconducting compound with $x = 0.25$. For the optimally doped ($x = 0.40$) and overdoped ($x = 0.50$) superconducting compounds, a substantial increase in the line intensity and a considerable shift of the characteristic frequencies are observed. This result suggests that, in the whole range of superconducting compositions $0.37 \leq x \leq 0.50$, the local symmetry of the Ba$_{1-x}$K$_x$BiO$_3$ crystal lattice differs from the perfect cubic symmetry, which should take place according to the literature data. The fact that resonance phenomena are observed when the laser photon energy is shifted toward the optical gap testifies to the presence of local electron pairs in the whole range of superconducting compositions $0.37 \leq x \leq 0.50$ and is evidence in favor of the superconductivity mechanism proposed for Ba$_{1-x}$K$_x$BiO$_3$ on the basis of the X-ray absorption studies in our previous paper. © 2003 MAIK "Nauka/Interperiodica".

PACS numbers: 74.25.Gz; 78.30.-j

The Raman spectra of the dielectric BaBiO$_3$ compound, which is the starting material for the preparation of BaPb$_{1-x}$Bi$_x$O$_3$ (BPBO) and Ba$_{1-x}$K$_x$BiO$_3$ (BKBO) superconducting oxides, exhibit the phonon mode $\omega_b \simeq 570$ cm^{-1} with a very high intensity exceeding the intensities of other modes by more than an order of magnitude [1–3]. The unusual feature of this mode is the resonance character of its excitation, which manifests itself in the anomalously high amplitude when the photon energy of the exciting laser, $h\nu$, coincides with the optical gap width $E_g \simeq 1.9$ eV [2, 3]. Initially, the existence of this mode was attributed to the breathing-mode-type static distortion of the BaBiO$_3$ cubic lattice in the form of an ordered alternation of small (with a radius R_S) and large (with a radius R_L) oxygen octahedra with Bi ions at their centers. The combination of the breathing and rotational (rotation of the octahedra about the [110] pseudocubic axes) static distortions results in a monoclinic distortion of the BaBiO$_3$ lattice. This distortion corresponds to the $I2/m$ space group and reduces the lattice symmetry, which initially was a perfect cubic one [4]. The observation of active phonon modes in the Raman spectra of BaBiO$_3$ is a direct consequence of this symmetry reduction [3, 5].

When BaBiO$_3$ is doped with potassium, the aforementioned static lattice distortions disappear near the insulator-to-metal phase transition at $x \approx 0.37$, after which the material becomes superconducting. As a result, according to the neutron scattering data [6], the superconducting BKBO compounds with $x \geq 0.37$ have a $Pm3m$ symmetry of a perovskite-like perfect cubic lattice, which, according to the symmetry group analysis, must have no Raman active modes [5, 7]. At the same time, experiments reveal the presence of rather intense Raman modes in the optimally doped ($x = 0.4$) superconducting BKBO compounds [3, 5, 7, 8]. This is explained by the reduction of symmetry of the simple cubic lattice because of either the effect of doping and defect structure [5] or the presence of local structural distortions in the superconducting compounds [7]. For overdoped superconducting BKBO compounds, no active phonon modes were observed in the Raman spectra, and, on the basis of this result, the conclusion was made that the compounds with $x \geq 0.45$ have a perfect perovskite-like lattice without distortions and, hence, the conventional BCS mechanism of superconductivity is realized in the Ba$_{1-x}$K$_x$BiO$_3$ cubic perovskites [3].

However, the X-ray absorption (EXAFS) studies [9–11] showed that the BKBO lattice is locally distorted in the whole interval of potassium contents corresponding to superconductivity: $0.37 \leq x \leq 0.50$. These distortions are of a dynamic character and manifest themselves as oscillations of oxygen ions, which simultaneously belong to two types of octahedra with different electron fillings, in an anharmonic double-well potential. From the model that was proposed in [10] and developed in [11–13] for describing the interrelation between the local electronic and crystal structures
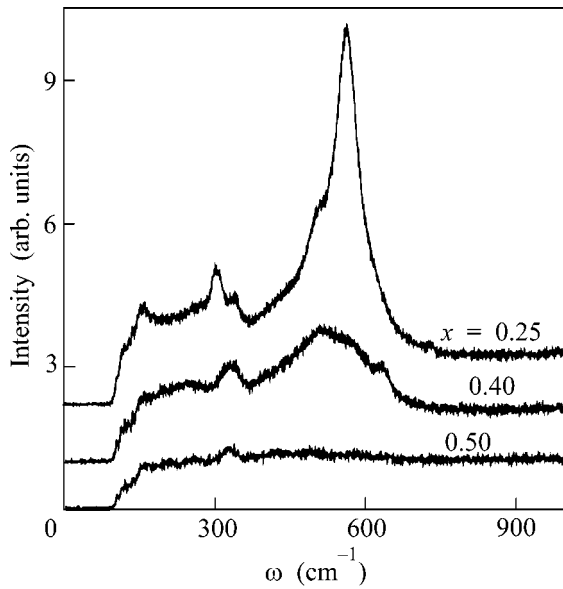
Fig. 1. Raman spectra of BKBO samples: the excitation by an Ar$^+$ laser with a wavelength of 488 nm.
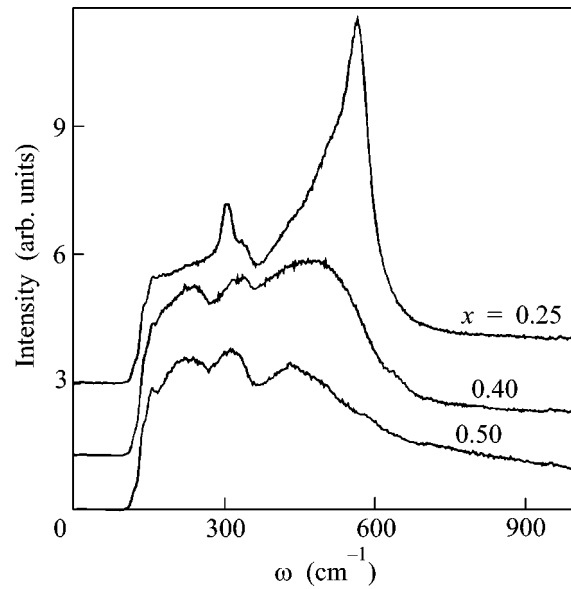

Fig. 2. Raman spectra of BKBO samples: the excitation by a Ti-sapphire laser with a wavelength of 750 nm.

of BKBO, it follows that, in the whole range of superconducting compounds $0.37 \leq x \leq 0.50$ including the overdoped compositions with $x \geq 0.45$, the resonance excitation by a laser radiation with $h\nu = E_g$ should give rise to active phonon modes in the Raman spectra. In our opinion, the fact that these modes were absent in the spectra obtained for overdoped samples with $x \geq 0.45$ by using an argon laser [3] is explained not by the absence of local distortions of the cubic lattice but by the absence of resonance between the laser photon energy $h\nu$ and the optical gap E_g. The point is that the doping of $BaBiO_3$ with potassium leads to a decrease in the optical gap in the superconducting metallic phase down to $E_g \simeq 0.5$ eV [14]. This value is much smaller than the photon energy of the Ar$^+$ laser: $h\nu \simeq 2.4$ eV. Lasers with greater wavelengths were not used for this kind of measurement until now.

In our previous publication [12], we predicted the growth of the Raman scattering intensity for superconducting compounds with $x \geq 0.37$ when the laser photon energy approaches the value of the optical gap. In this paper, we present the results obtained from the experimental study of the effect of the laser photon energy on the Raman spectra of the superconducting $Ba_{1-x}K_xBiO_3$ compounds with the aim to verify the predictions made on the basis of the aforementioned model [12].

The Raman spectra were recorded in the range within 100–2500 cm^{-1} at room temperature by a Jobin Yvon HR-640 spectrometer with a nitrogen cooled CCD detector. To suppress the reflected laser radiation, a set of holographic filters was used. We studied single-crystal samples of $Ba_{1-x}K_xBiO_3$ of three different

types: with $x = 0.25$ (nonsuperconducting composition), 0.40 ($T_c = 26$ K), and 0.50 ($T_c = 16$ K). The samples were grown as described in [15]. The exciting lasers were an Ar$^+$ laser ($\lambda = 488$ nm) and a Ti-sapphire one ($\lambda = 700$ and 750 nm) pumped by the argon laser. The laser radiation was focused to a spot about 50 μm in diameter on a freshly cleaved sample surface. The measurements were performed with low power levels of about 1 mW to avoid the situation when local heating may cause oxygen to leave the surface. The absence of the latter effect was confirmed by the absence of changes in the spectral curves obtained from multiply repeated recording procedures. The spectral curves were normalized to unity in the short-wave region (~1500 cm^{-1}), where the Raman intensity is practically frequency-independent.

Figures 1 and 2 show the Raman spectra of BKBO compounds with $x = 0.25$, 0.40, and 0.50, which were measured with two laser wavelengths: $\lambda = 488$ and 750 nm. The spectral curves obtained with the use of the Ar laser are identical with those obtained by other authors for ceramic samples [8], single crystals [5, 7], and epitaxial thin films [3, 16]. From the comparison of the curves shown in Figs. 1 and 2, one can see that, for a nonsuperconducting sample with $x = 0.25$, the amplitude and frequency patterns of the Raman spectra are practically independent of the laser wavelength. At the same time, for the superconducting compositions ($x = 0.40$ and 0.50), the shift of the laser photon energy toward the value corresponding to the optical gap leads to a frequency shift of the phonon modes and to an increase in their amplitudes. The effect of the laser wavelength on the Raman spectra manifests itself most strongly for the overdoped sample with $x = 0.50$

(Fig. 3). In this case, the spectrum obtained at $\lambda = 488$ nm exhibits a single weak line ($\omega \simeq 330$ cm^{-1}), while at $\lambda = 750$ nm, pronounced maxima are observed at the frequencies 440, 320, 230, and 160 cm^{-1}. This suggests that the features of the Raman spectra obtained for BKBO in the superconducting metallic phase are determined not by the defect structure or the inhomogeneities of the samples, as was assumed earlier [3, 5, 8], but by fundamental physical mechanisms related to the properties of the local electronic structure of BKBO compounds.

We begin the analysis of the experimental results by explaining the resonance in the initial compound BaBiO$_3$. This compound is an unusual semiconductor, because it is characterized by two energy gaps: the optical gap $E_g \simeq 1.9$ eV and the activation energy $E_a \simeq 0.24$ eV. The activation energy does not manifest itself in such experimental data as infrared reflection spectra, optical conductivity spectra, or photoacoustic data. The only possible mechanism that does not contradict the experiment was proposed in [17], where the presence of this gap was explained by the two-particle (bipolaron) conductivity. The optical gap does not have the shape of the absorption edge characteristic of semiconductors and is observed as a resonance peak of optical conductivity or infrared reflection at the energies near $h\nu \simeq 1.9$ eV [3, 14, 17]. This gap is usually attributed to the charge density wave in BaBiO$_3$ [18]. However, the small spectral width of the resonance peak $\Delta \approx 0.8$ eV [3, 14] points to the local character of the excited level rather than to the band absorption.

Earlier, we explained the nature of the two energy gaps by the local electronic structure of BaBiO$_3$, which is determined by the ordered alternation of oxygen octahedra with different electron filling: the BiO$_6$ and BiL^{2}O$_6$ complexes, where L^2 denotes the presence of a hole pair in the Bi6s-O2p$_{\sigma*}$ antibonding molecular orbital of the octahedral complex [10–13]. In other words, the electronic structure of the initial BaBiO$_3$ represents an ordered alternation of electron and hole pairs localized in real space by the neighboring octahedral complexes. In this system, free fermions are absent, and the conductivity, as in [17], is possible only at the expense of the pair (two-particle) excitation through the activation gap $2E_a \simeq 0.48$ eV, which is the pair localization energy. Since a photon cannot excite an electron pair as a whole, this gap does not manifest itself in optical experiments.

A photon can break a pair by transferring one of the electrons from a BiO$_6$ octahedron to a free level in the neighboring BiL^{2}O$_6$ octahedron. However, this process requires a much higher energy $E_g = 2E(\text{BiL}^1\text{O}_6) - E(\text{BiL}^2\text{O}_6 + \text{BiO}_6) = E_b + 2E_a$, where E_b is the pair coupling energy [12, 13]. In this case, a local deformation of the lattice takes place in the form of the transformation of two different octahedra, BiL^{2}O$_6$ and BiO$_6$, into
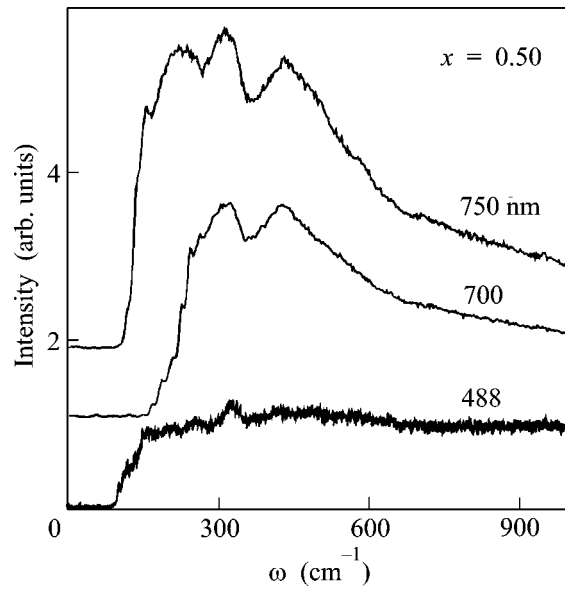

Fig. 3. Dependence of the Raman spectra of a Ba$_{0.5}$K$_{0.5}$BiO$_3$ overdoped sample on the laser wavelength.

two identical BiL^{1}O$_6$ octahedra, each of which has a single hole in the Bi6s-O2p$_{\sigma*}$ antibonding molecular orbital. At the resonance coincidence of the laser photon energy with the optical gap of the initial BaBiO$_3$, the aforementioned deformation is so strong that it generates a breathing mode in the Raman spectra with $\omega_b \simeq 570$ cm^{-1}. The intensity of this mode is rather high, so that the observation of up to five its harmonics is possible [2].

The doping of BaBiO$_3$ with potassium leads to the replacement of part of the BiO$_6$ complexes by BiL^{2}O$_6$, which results in their spatial overlapping. The pair localization energy (the activation energy) vanishes at the insulator-to-metal phase transition, when $x \geq 0.37$. At the same time, according to the infrared reflection data [14], the optical gap E_g, which at $E_a = 0$ coincides with the pair coupling energy, decreases without vanishing, so that local electron pairs are retained in the metallic phase. The local pairs can move freely in real space under the dynamic exchange BiO$_6 \longleftrightarrow$ BiL^{2}O$_6$, and, as shown in [12, 13], their coherent motion at the temperatures $T \leq T_c$ determines the transition to the superconducting state. The optical absorption maximum is shifted from $E_g \approx 1.9$ eV in BaBiO$_3$ to $E_g \approx 0.5$ eV in Ba$_{1-x}$K$_x$BiO$_3$, and its spectral width increases from $\Delta \approx 0.8$ to 1.6 eV [14] because of the delocalization of the previously localized states.

Thus, when the Raman spectra are measured with the Ar laser ($h\nu \approx 2.4$ eV), the optical resonance condition $h\nu = E_g$ is violated, and the amplitudes of phonon modes observed for the optimally doped sample ($x = 0.40$) are much smaller, as compared to the case of $x = 0.25$; in the case of the overdoped composition ($x = $
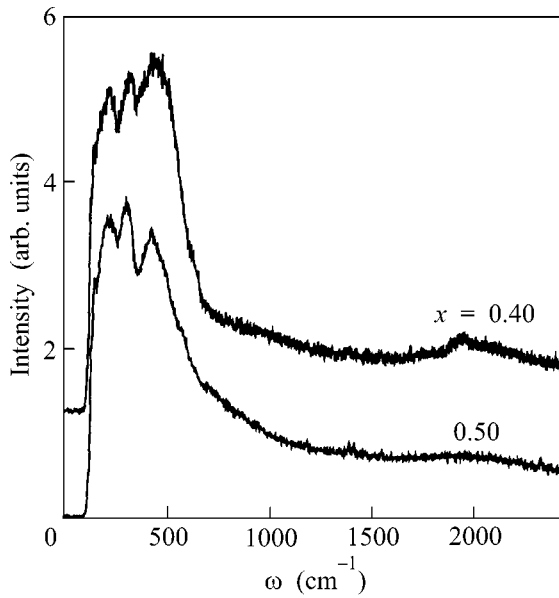
Fig. 4. Raman spectra of the optimally doped ($Ba_{0.6}K_{0.4}BiO_3$) and overdoped ($Ba_{0.5}K_{0.5}BiO_3$) superconducting compounds in the short-wave region; the excitation by a Ti-sapphire laser with a wavelength of 750 nm.

0.50), these modes are virtually absent (see Fig. 1). The use of the Ti-sapphire laser with a wavelength of 750 nm ($h\nu \simeq 1.65$ eV) allowed us to approach, although not too closely, the optical conductivity maximum ($E_g \approx 0.5$ eV). This relatively small shift proved to be sufficient to obtain the resonance excitation of the local lattice distortion accompanying the breakup of electron pairs and to observe intense phonon modes in the spectra of superconducting samples (see Figs. 2, 3). According to [14], at $h\nu \simeq 1.65$ eV for $x = 0.40$, the optical conductivity amplitude makes up less than 20% of the maximum amplitude corresponding to approximately 0.5 eV, and, hence, it should be still smaller for $x = 0.50$. Then, for the Raman spectra of overdoped superconducting samples with $x > 0.45$, we can predict a more than fivefold increase in the phonon mode amplitudes in the case of a closer approach to the resonance conditions, which can be achieved by using lasers with wavelengths ($\lambda \approx 2000$ nm) longer than that of the Ti-sapphire laser.

Another important result of our study is the observation of the considerable background Raman intensity forming a continuous spectrum in the short-wave region. The presence of this Raman continuum in high-T_c superconducting cuprates has been interpreted as evidence of an unconventional mechanism of superconductivity [19]. According to [3], the absence of the Raman continuum in BKBO compounds testifies to the conventional superconductivity mechanism in Bi-based cubic perovskites, which means that their properties are different from those of cuprates. The authors of the cited publication [3] explain the observation of the

Raman continuum in the experiment [20] by the possible defect structure and inhomogeneity of the samples. Our measurements performed with a wavelength of 750 nm (Fig. 4) reveal the presence of a considerable background intensity in the Raman spectra of superconducting samples in the region 1500–2500 cm^{-1}, and this background intensity is comparable to that of the Raman continuum observed in cuprates. This fact suggests that the mechanism of superconductivity in $Ba_{1-x}K_xBiO_3$ is unconventional, i.e., differs from the BCS mechanism, and possibly is similar to the superconductivity mechanism realized in Bi- and Cu-based oxides.

Thus, our study of the Raman spectra of superconducting BKBO samples with the use of the Ti-sapphire laser ($\lambda = 750$ nm) showed that the main conclusions formulated in the analogous study [3], which was performed with a shorter-wavelength Ar$^+$ laser ($\lambda = 514.5$ nm), fail. Specifically, these conclusions include (a) the absence of the optical gap in the superconducting phase of BKBO; (b) the presence of an ideal perovskite-like cubic structure for $x \geq 0.37$; and (c) the realization of the conventional BCS superconductivity mechanism in $Ba_{1-x}K_xBiO_3$, which is different from the superconductivity mechanism in cuprates.

We obtained new independent evidence in support of the concept that the superconducting BKBO compounds with $x \geq 0.37$ do not have an ideal cubic structure (as stated in the literature) but are characterized by considerable local lattice distortions, even in the case of the overdoped compound with $x = 0.50$. According to the model described in [12], the lattice distortions are related to the retention of local electron pairs under the doping procedure: the coupling energy of these pairs manifests itself as the optical gap and guarantees their existence in the whole range of superconducting compositions $0.37 \leq x \leq 0.50$. The observation of the resonance phenomena in the experiment with the longer laser wavelength confirms that the optical gap is present in the superconducting phase and adds support to the superconductivity mechanism proposed for $Ba_{1-x}K_xBiO_3$ in our previous papers [12, 13]. The presence of a considerable background intensity in the short-wave region of the Raman spectra of superconducting BKBO samples is an additional argument in favor of the similarity of the superconductivity mechanisms in Bi- and Cu-based oxides.

REFERENCES

1. S. Sugai, S. Uchida, K. Kitazawa, *et al.*, Phys. Rev. Lett. **55**, 426 (1985).

2. S. Sugai, Phys. Rev. B **35**, 3621 (1987).

3. S. Tajima, M. Yoshida, N. Koshizuka, *et al.*, Phys. Rev. B **46**, 1232 (1992).

4. D. E. Cox and A. W. Sleight, Solid State Commun. **19**, 969 (1976).

5. B. Lederle, C. Thomsen, C. Escribe-Filippini, *et al.*, Physica C (Amsterdam) **235–240**, 2523 (1994).

6. Shiyou Pei, J. D. Jorgensen, B. Dabrowski, *et al.*, Phys. Rev. B **41**, 4126 (1990).

7. N. V. Anshukova, A. I. Golovashkin, V. S. Gorelik, *et al.*, J. Mol. Struct. **219**, 147 (1990).

8. K. F. McCarty, H. B. Radousky, D. G. Hinks, *et al.*, Phys. Rev. B **40**, 2662 (1989).

9. A. P. Menushenkov, K. V. Klement'ev, P. V. Konarev, and A. A. Meshkov, Pis'ma Zh. Éksp. Teor. Fiz. **67**, 977 (1998) [JETP Lett. **67**, 1034 (1998)].

10. A. P. Menushenkov, Poverkhnost **12**, 58 (1999).

11. A. P. Menushenkov and K. V. Klementev, J. Phys.: Condens. Matter **12**, 3767 (2000).

12. A. P. Menushenkov, K. V. Klementev, A. V. Kuznetsov, and M. Yu. Kagan, Zh. Éksp. Teor. Fiz. **120**, 700 (2001) [JETP **93**, 615 (2001)].

13. A. P. Menushenkov, K. V. Klementev, A. V. Kuznetsov, and M. Yu. Kagan, Physica B (Amsterdam) **312–313**, 31 (2002).

14. S. H. Blanton, R. T. Collins, K. H. Kelleher, *et al.*, Phys. Rev. B **47**, 996 (1993).

15. N. V. Anshukova, A. I. Golovashkin, L. I. Ivanova, *et al.*, Zh. Éksp. Teor. Fiz. **108**, 2132 (1995) [JETP **81**, 1163 (1995)].

16. H. Sato, T. Ido, S. Ushida, *et al.*, Phys. Rev. B **48**, 6617 (1993).

17. S. Uchida, K. Kitazawa, and S. Tanaka, Phase Transit. **8**, 95 (1987).

18. L. F. Mattheiss and D. R. Hamann, Phys. Rev. B **28**, 4227 (1983).

19. C. M. Varma, S. Schmitt-Rink, and E. Abrahams, Phys. Rev. Lett. **63**, 1996 (1989).

20. S. Sugai, Y. Enomoto, and T. Murakami, Solid State Commun. **72**, 1193 (1989).

Translated by E. Golyamina

Electron Paramagnetic Resonance of Yb³⁺ Ions in a Concentrated YbRh₂Si₂ Compound with Heavy Fermions

V. A. Ivan'shin[1, *], L. K. Aminov[1], I. N. Kurkin[1], J. Sichelschmidt[2], O. Stockert[2], J. Ferstl[2], and C. Geibel[2]

[1] *Department of Physics, Kazan State University, ul. Kremlevskaya 18, Kazan, 420008 Tatarstan, Russia*
* e-mail: Vladimir.Ivanshin@ksu.ru
[2] *Max-Planck-Institut für Chemische Physik fester Stoffe, D-01187 Dresden, Germany*
Received April 10, 2003

The EPR signal from localized ytterbium ions was observed in an undoped YbRh$_2$Si$_2$ compound with heavy fermions in the temperature range from 1.5 to 25 K. The exponential contribution dominating the temperature dependence of EPR line width at temperatures above 15 K was shown to be caused by the random transitions from the ground to the first excited Stark sublevel of the Yb^{3+}($4f^{13}$) ion with the activation energy Δ = 115 K. © 2003 MAIK "Nauka/Interperiodica".

PACS numbers: 76.30.Da; 75.20.Hr; 71.27.+a

1. Single crystals of a YbRh$_2$Si$_2$ material exhibiting the properties of a so-called non-Fermi liquid were synthesized recently in [1]. The resistivity and specific-heat measurements have shown that the antiferromagnetic transition temperature of this material is very low, T_N = 70 mK, and that the localized Yb^{3+} moments are ordered perpendicularly to the crystallographic c axis in the easy plane [1, 2]. Moreover, YbRh$_2$Si$_2$ is one of a few ytterbium-based stoichiometric Kondo systems that have a low residual resistivity ($\rho_0 \sim 2.5~\mu\Omega$ cm [3]) and a comparatively high characteristic Kondo temperature T_K (spin-fluctuation temperature): $T_K \simeq 24$ K was estimated from entropy change [1], and $T_K \simeq 15$ K was obtained from NMR measurements [3]. The presence of local Yb^{3+} moments is evidence that there is a basic possibility to use the EPR method for studying crystal properties, in particular, for directly detecting the Kondo effect [4]. The ions exhibiting this effect are ordinarily introduced as impurities into alloys and intermetallic compounds. The Kondo effect observed in the EPR experiments on a diluted Au:Yb system [5] manifests itself in the characteristic logarithmic temperature dependences of the g factor and relaxation rate [6]. The interaction of conduction electrons with the localized $4f$ moments also plays an important part. As a rule, the observation of EPR in concentrated insulators is hampered because of a strong EPR line broadening. We are aware of only two experimental observations of rather broad (more than 1 kOe) EPR lines in the undoped ytterbium compounds. In the cubic phase of the Kondo system YbH$_x$, the broadening is explained by the spin-glass ordering of Yb^{3+} ions in the absence of heavy fermions [7], and, in the superconducting phase of a high-T_c superconductor Yb$_x$Y$_{1-x}$Ba$_2$Cu$_3$O$_y$ (x = 1.0,

0.5), it is ascribed to the exchange narrowing [8]. In this communication, we report the results of studying the EPR spectra of YbRh$_2$Si$_2$ single crystals with a dense regular arrangement of the Yb^{3+} ions in the temperature range from 1.5 to 25 K.

2. High-quality single crystals of YbRh$_2$Si$_2$ (symmetry group $I4/mmm$; ThCr$_2$Si$_2$-type structure) were prepared as thin (~0.5 mm) platelets from indium melt by the method described earlier in [9, 10]. To avoid ytterbium evaporation, the YbRh$_2$Si$_2$ single crystals were grown in sealed thallium crucibles. The orientation of crystals and their correspondence to the structural type were determined by the Laue method and X-ray structural analysis. In addition, a high quality of the crystals was confirmed by the presence of a sharp specific-heat peak corresponding to the antiferromagnetic transition. The muon spin-resonance studies of the samples prepared by the same method showed that the compound was homogeneous and that the spin-glass phase was absent in it [11]. The X-band (~9.39 GHz) and Q-band (~34.1 GHz) EPR experiments were accomplished in magnetic fields up to 1.7 T on a Bruker ELEXSYS E500 spectrometer equipped with a helium cryostat (OXFORD). The major EPR measurements were made in the orientation corresponding to the minimal resonance field. The EPR line width was also minimal, while the static magnetic field was perpendicular to the crystal axis c.

3. The EPR signal with a clearly defined Dyson lineshape ($\Delta H \sim 200$–600 Oe) and the g factors typical of the Yb^{3+}($4f^{13}$) ion ($g_\perp \approx 3.55$ and $g_\parallel < 0.4$ at T = 5 K) was observed in the temperature range from 1.5 to 15 K (Fig. 1), where the EPR line width increased linearly with temperature following the Korringa mechanism.
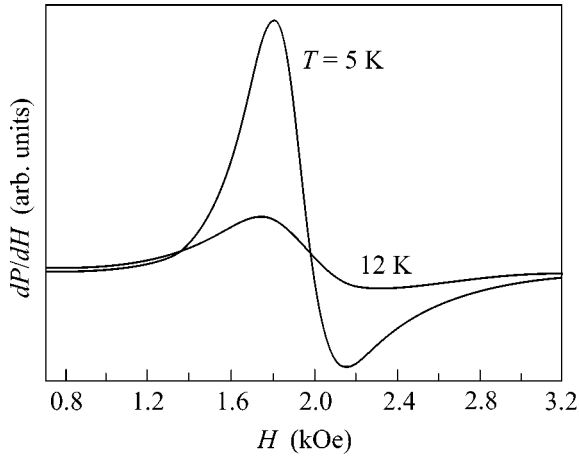
Fig. 1. Derivatives of the Yb^{3+} EPR signal for an $YbRh_2Si_2$ single crystal at 5 and 12 K. Magnetic field is directed perpendicular to the crystal axis c.

On further rise in temperature, the EPR lineshape was noticeably distorted, and this was accompanied by even faster (close to exponential) increase in its width ($\Delta H \sim$ 1200 Oe at 20 K). The EPR signal fully disappeared above 25 K. For both frequencies, the temperature dependence of EPR line width is well described by the formula

$$\Delta H_{pp} = A + BT + C\exp(-\Delta/T), \qquad (1)$$

where $B = 27$ Oe/K, $C = 167\,000$ Oe $\equiv 4 \times 10^{12}$ s^{-1}, and $\Delta = 115$ K $\equiv 9.91$ meV (Fig. 2). The term A, presumably, accounts for the spin–spin interactions and inhomogeneous broadening. It changes approximately from 100 to 180 Oe upon passing from the X-band to the Q-band measurements. Note that Eq. (1) is similar to

the expressions for the EPR line width and the spin–lattice relaxation rate in diluted paramagnetic dielectric systems containing RE ions [12]. In those expressions, the term linear in T is assigned to the single-phonon relaxational transitions, while the exponential term is related to the phonon resonance fluorescence processes. However, the values of B and C appreciably exceed the values typical of the phonon mechanisms. The BT term in Eq. (1) likely accounts for the Korringa contribution to the width, while the exponential term is caused by the random transitions (induced by the magnetic dipole–dipole and exchange interactions with environment) from the ground Kramers doublet of the Yb^{3+} ion to its first excited Stark sublevel with activation energy Δ. The thermal fluctuations of electronic states have already been considered in the literature (see, e.g., review [13]) as mechanisms of nuclear spin–spin and spin–lattice relaxation in the magnetic RE ions and impurity paramagnetic centers in van Vleck paramagnets (vVPs). The correlation frequency estimated for this process in the $LiTmF_4$ vVP (characterized by approximately the same spacing between the RE ions as in $YbRh_2Si_2$) was found to be $\approx 10^{12}$ s^{-1}, i.e., close to the parameter C in Eq. (1). The temperature dependence of the g factor (Fig. 3) at temperatures higher than 15 K is also typical of the above-mentioned electronic thermal fluctuation mechanism. The contribution of this mechanism to the effective g factors is analogous to the one described earlier in the theory of vVP NMR spectra [13]; it can be approximately calculated by the formula

$$g_\alpha(T) = g_0(\alpha) + \Delta g_\alpha^0 \exp(-\Delta/T),$$
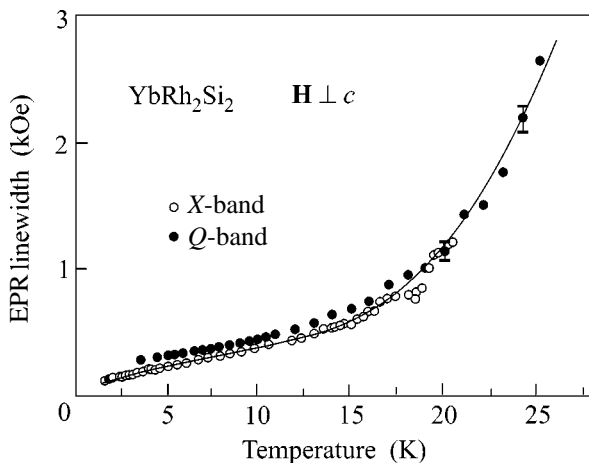$$\Delta g_\alpha^0 = g_\alpha^{exc} - g_\alpha(0), \qquad (2)$$

Fig. 2. Temperature dependence of the EPR line width in $YbRh_2Si_2$: (○) experimental data for a frequency of 9.39 GHz; (●) 34.1 GHz; the solid line is for the theoretical calculation by Eq. (1) with fitting parameters $A = 96.6$ Oe, $B = 27$ Oe K^{-1}, $C = 167\,000$ Oe, and $\Delta = 115$ K.
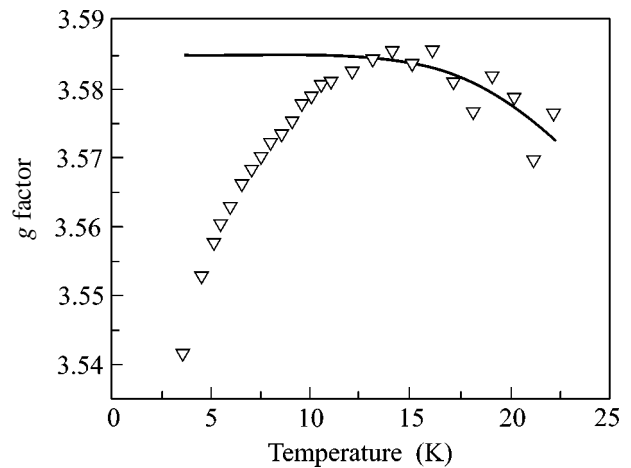

Fig. 3. Temperature dependence of the g factor from the EPR measurements at a frequency of 34.1 GHz: (▽) experimental data and the solid line is for the theoretical calculation by Eq. (2).
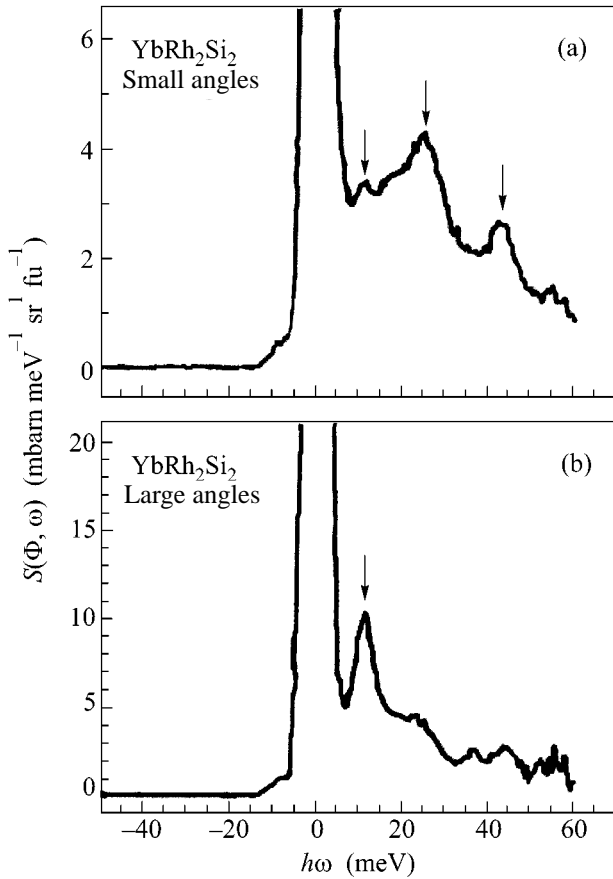
Fig. 4. Inelastic neutron scattering spectrum of the poly-crystalline $YbRh_2Si_2$ samples for (a) small and (b) large scattering angles at a temperature of 1.5 K.

where $g_\alpha(0)$ and g_α^{exc} are the effective g factors in the ground and first excited doublets of the ytterbium ion. Function (2) with $\Delta g_\perp^0 = -2.58$ (i.e., $g_\perp^{exc} \simeq 1.0$) and the same $\Delta = 115$ K as in Eq. (1) is shown in Fig. 3 by the solid line. The tetragonal crystal field splits the ground multiplet of the Yb^{3+} ion ($4f^{13}$, $J = 7/2$) into four Kramers doublets. The value of Δ can be correlated with the data obtained for the Yb^{3+} Stark splitting in $YbRh_2Si_2$ in the inelastic neutron scattering study at the Laue–Langevin Institute (Grenoble, France), according to which the energies of excited Stark sublevels are at 42 and 27 meV and in the vicinity of 10–15 meV (Fig. 4). A more accurate determination of the position of the first excited Stark sublevel was hampered by the presence of a strong phonon signal near 13 meV. Note that the overlap between the broad (smeared) Yb^{3+} Stark sublevels and optical phonons was already observed in the inelastic neutron scattering spectra of the $YbPO_4$ compound [14], where the energy of the first excited state was found to be equal to 12 meV. In this connection, it is worthy of note that, in studying the temperature dependence of the heat capacity of $YbRh_2Si_2$ [1], a peak was

observed at approximately 60 K, which corresponds to the energy $\Delta \simeq 160$ K $\equiv 13.8$ meV of the first excited state in Yb^{3+}. Moreover, in a crystallographically and magnetically close $YbNi_2B_2C$ compound, the first excited Stark sublevel is situated at 7.9 meV [15]. Although the optical and local (quasilocal) phonon modes can also be responsible for the exponential dependence of the spin-lattice relaxation time and, hence, of the EPR line width [16], the pre-exponential factors in this mechanism are appreciably smaller (by approximately two orders of magnitude) than the parameter C in Eq. (1). For this reason, one can naturally assume that it is precisely the first Stark sublevel that is situated near 10–15 meV, although in the spectrum shown in Fig. 4 it is masked by the stronger phonon signal.

4. The temperature-independent term A changes with frequency from 100 Oe (X band) to 180 Oe (Q band). This allows the frequency-dependent (proportional to frequency) inhomogeneous contribution A_1 caused by the scatter of crystal-field parameters to be separated from the frequency-independent contribution A_2 due to the spin–spin broadening. This gives $A = A_1 + A_2$, with $A_1 = 27$ Oe (X band), $A_1 = 108$ Oe (Q band), and $A_2 = 73$ Oe for both frequencies. Whereas the resulting A_1 value is typical of the inhomogeneous broadening, A_2 is appreciably smaller than the dipole–dipole EPR line width $\Delta\omega_{dip}$ in insulators with the concentration of paramagnetic centers as high as in our case. The corresponding estimate of $\Delta\omega_{dip}$ by the formula [17] $\Delta\omega_{dip} = 3.8g^2\beta^2\hbar^{-1}n$ yields $\Delta\omega_{dip} \approx 1600$ E $\equiv 4.9 \times 10^{10}$ s^{-1} for the Yb^{3+} concentration $n = 1.26 \times 10^{22}$ cm^{-3} and g factor $g = 3.55$. It is conceivable that such an abnormal decrease in the dipole–dipole line width in $YbRh_2Si_2$ is a consequence of the specific properties of this compound. Note that we have failed to observe EPR absorption in the related non-Kondo ytterbium-based $Yb_4Rh_7Ge_6$ and $YbFe_2Ge_2$ compounds with heavy fermions.

5. Equation (1) does not account for some features of the experimental curves presented in Fig. 2. In particular, it does not explain the presence of a short flattened section at 17–19 K that was observed for both frequencies. Below 15 K, the temperature dependence of the g factor (Fig. 3) qualitatively resembles the Kondo-type behavior in the EPR experiments with Au:Yb [18]. In the temperature range of our measurements, the crystal field is approximately an order of magnitude more efficient than the Kondo interactions [15], and, in all likelihood, the latter have no strong effect on the EPR spectra at $T > 1.5$ K because of their comparative weakness. A detailed analysis of the possible manifestation of the Kondo effect in the EPR of $YbRh_2Si_2$ single crystal will be possible only after performing experiments at lower temperatures.

6. In conclusion, we formulate the main results of this work. An anomalously narrow EPR signal was

observed from the Yb^{3+} ($4f^{13}$) ions in a concentrated Kondo system $YbRh_2Si_2$ with heavy fermions. The temperature dependence of the EPR line width in the temperature range from 1.5 to 15 K is explained using the Korringa mechanism of interaction between the local ytterbium magnetic moments and conduction electrons. A dramatic broadening of the EPR line at higher temperatures is due to the thermal fluctuations of the Yb^{3+} electronic states, which induce random transitions from the ground Kramers doublet of these ions to the first excited Stark sublevel with energy $\Delta \approx 10$ meV.

REFERENCES

1. O. Trovarelli, C. Geibel, S. Mederle, *et al.*, Phys. Rev. Lett. **85**, 626 (2000).

2. P. Gegenwart, J. Custers, C. Geibel, *et al.*, Phys. Rev. Lett. **89**, 056402 (2002).

3. K. Ishida, K. Okamoto, Y. Kawasaki, *et al.*, Phys. Rev. Lett. **89**, 107202 (2002).

4. H. J. Spencer and S. Doniach, Phys. Rev. Lett. **18**, 994 (1967); M. B. Walker, Phys. Rev. B **176**, 432 (1968).

5. J. Nagel, K. Baberschke, and E. Tsang, J. Magn. Magn. Mater. **15–18**, 730 (1980).

6. B. Elshner and A. Loidl, in *Handbook on the Physics and Chemistry of Rare Earth*, Ed. by K. A. Geschneider, Jr. and L. Eyring (North-Holland, Amsterdam, 1997), Vol. 24, Chap. 162.

7. E. E. Kotel'nikova, N. M. Suleĭmanov, G. G. Khaliullin, *et al.*, Pis'ma Zh. Éksp. Teor. Fiz. **58**, 276 (1993) [JETP Lett. **58**, 284 (1993)].

8. V. Likodimos, N. Guskos, M. Wabia, *et al.*, Phys. Rev. B **58**, 8244 (1998).

9. P. C. Canfield and Z. Fisk, Philos. Mag. B **65**, 1117 (1992).

10. O. Trovarelli, C. Geibel, C. Langhammer, *et al.*, Physica B (Amsterdam) **281–282**, 372 (2000).

11. K. Ishida, D. E. MacLaughlin, O. O. Bernal, *et al.*, Physica B (Amsterdam) **326**, 403 (2003).

12. S. A. Al'tshuler and B. M. Kozyrev, *Electron Paramagnetic Resonance in Compounds of Transition Elements* (Nauka, Moscow, 1972; Halsted, New York, 1975).

13. L. K. Aminov and M. A. Teplov, Usp. Fiz. Nauk **147**, 49 (1985) [Sov. Phys. Usp. **28**, 762 (1985)].

14. C.-K. Loong, M. Loewnhaupt, J. C. Nipko, *et al.*, Phys. Rev. B **60**, R12549 (1999).

15. A. T. Boothroyd, J. P. Barratt, P. Bonville, *et al.*, Phys. Rev. B **67**, 104407 (2003).

16. C. Y. Huang, Phys. Rev. **161**, 272 (1968); D. L. Mills, Phys. Rev. **146**, 336 (1967).

17. A. Abragam, *The Principles of Nuclear Magnetism* (Clarendon Press, Oxford, 1961; Inostrannaya Literatura, Moscow, 1963).

18. Y. von Spalden, E. Tsang, K. Baberschke, *et al.*, Phys. Rev. B **28**, 24 (1983).

Translated by V. Sakun

Solution of Scaling Quantum Networks¶

Yu. Dabaghian and R. Blümel

Department of Physics, Wesleyan University, Middletown, CT 06459-0155, USA
e-mail: ydabaghian@wesleyan.edu
Received February 6, 2003

We show that all scaling quantum graphs are explicitly solvable, i.e., that any one of their spectral eigenvalues E_n is computable analytically, explicitly, and individually for any given n. This is surprising, since quantum graphs are excellent models of quantum chaos (see, e.g., T. Kottos and H. Schanz, Physica E **9**, 523 (2001)). © 2003 MAIK "Nauka/Interperiodica".

PACS numbers: 05.45.Mt; 02.10.Ox

Graphs are networks of bonds and vertices. Figure 1 shows two examples: a three-bond four-vertex star graph (Fig. 1a) and a three-bond four-vertex linear graph (Fig. 1b). A quantum particle moving on the graph turns the graph into a quantum graph [1]. If the quantum particle moves freely on the graph, subjected only to flux conservation at its vertices, we call it a *standard quantum graph*. This is the type of quantum graph most frequently studied in the literature [1–5]. A larger class of quantum graphs, including the standard quantum graphs, are *dressed quantum graphs* [6]. A dressed quantum graph has potentials on its bonds and δ functions on its vertices. The potentials on its bonds are essentially arbitrary as long as they do not introduce turning points on the bonds. But even this case can be dealt with trivially by redefining the topology of the graph.

An important subset of dressed quantum graphs are *scaling quantum graphs* [7–9]. In this case the graph bonds are dressed with scaling potentials and the graph vertices are dressed with scaling δ functions. A scaling potential is one whose strength V_0 scales with the energy E of the quantum particle according to $V_0 = \lambda E$, where λ is a constant. The strength of a scaling δ function scales with $k = \sqrt{E}$. Scaling potentials and δ functions are a natural choice to consider. On the one hand they frequently occur in physical systems [10–15], on the other hand they are mathematically convenient, since they allow studying a quantum system without causing phase-space metamorphoses [16] in the underlying classical system. It has been pointed out before [17] that this is the most natural way of studying quantum systems, in particular quantum chaos [18, 19]. Since quantum graphs are popular and successful models of quantum chaos [1–5], it may come as a surprise that the energy spectrum E_n, $n = 1, 2, \ldots$ of all scaling quantum graphs is explicitly and analytically solvable

in the form $E_n = \ldots$, involving only known quantities on the right-hand side. In many cases the solutions can be stated in closed analytical form.

The spectral function $g^{(0)}(k)$ of a general scaling, dressed quantum graph is of the form [7]

$$g^{(0)}(k) = \cos(S_0 k - \pi\gamma_0) - \sum_{j=1}^{N} a_j^{(0)} \cos(S_j k - \pi\gamma_j), \quad (1)$$

where $S_0 > 0$ is the total reduced action length of the graph [7, 8], $0 < S_j < S_0$ are certain combinations of the reduced bond actions [7, 8], N is the number of action combinations in (1), γ_0, γ_j are constant phases, and $a_j^{(0)}$ are constant amplitudes. The spectrum E_n of the quantum graph is obtained by solving the spectral equation

$$g^{(0)}(k_n^{(0)}) = 0, \quad n = 1, 2, \ldots \quad (2)$$
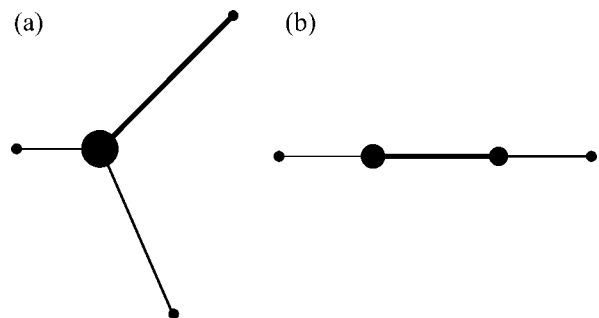
(a)   (b)

Fig. 1. (a) Dressed three-bond star graph and (b) dressed four-vertex chain graph. Different potential strengths on the bonds are indicated by different thickness of the bonds. Different vertex strengths are indicated by different dot sizes representing the vertices.

¶ This article was submitted by the authors in English.

via $E_n = \left(k_n^{(0)}\right)^2$. For the purposes of this paper, we are only interested in the positive solutions of (2) and obtain a well-defined counting index n by defining $k_1^{(0)}$ to be the first positive root of (2). As a first step toward the solution of the general problem, it was shown in [7–9] that (2) can be solved explicitly in the form $k_n^{(0)} = \dots$ if the regularity condition

$$\sum_{j=1}^{N} \left|a_j^{(0)}\right| < 1 \tag{3}$$

is fulfilled. In order to substantiate our claim that (2) is solvable explicitly for *all* scaling quantum graphs, we have to show that (2) is solvable explicitly even if (3) is not fulfilled.

Before we turn our attention to the general case, we introduce our methods with the help of a simple example. Let us consider a scaling quantum graph derived from the three-bond star graph shown in Fig. 1a by putting the scaling potentials $V_l(E) = \lambda_l E$, $0 < \lambda_l < 1$ on its three bonds of length L_l, $l = 1, 2, 3$, require the "Kirchhoff-type" [5] flux conservation condition $\sum_{l=1}^{3} d\psi_l/dx_l = 0$ at its central vertex (ψ_l is the quantum wave function on bond number l of the graph and x_l is the coordinate on bond number l), and require Dirichlet boundary conditions on its three dead-end vertices. The spectral equation is of the form (1) with $N = 3$, $\gamma_1 = \gamma_2 = \gamma_3 = 0$, and

$$S_0 = \alpha_1 + \alpha_2 + \alpha_3, \quad S_1 = -\alpha_1 + \alpha_2 + \alpha_3,$$
$$S_2 = \alpha_1 - \alpha_2 + \alpha_3, \quad S_3 = \alpha_1 + \alpha_2 - \alpha_3, \tag{4}$$

$$a_1^{(0)} = \frac{-\beta_1 + \beta_2 + \beta_3}{\beta_1 + \beta_2 + \beta_3}, \quad a_2^{(0)} = \frac{\beta_1 - \beta_2 + \beta_3}{\beta_1 + \beta_2 + \beta_3},$$
$$a_3^{(0)} = \frac{\beta_1 + \beta_2 - \beta_3}{\beta_1 + \beta_2 + \beta_3}, \tag{5}$$

where

$$\alpha_l = \beta_l L_l, \quad \beta_l = \sqrt{1 - \lambda_l}, \quad l = 1, 2, 3. \tag{6}$$

The amplitudes in (5) do not fulfill the regularity condition (3). In some cases $\sum_{j=1}^{3} \left|a_j^{(0)}\right| = 1$ (for instance for $a_j^{(0)} > 0$, $j = 1, 2, 3$), and in many cases $\sum_{j=1}^{3} \left|a_j^{(0)}\right| > 1$ which strongly violates the regularity condition (3). Since the methods and techniques presented in [7–9] for obtaining the spectrum of a graph explicitly depend crucially on (3), it seems that completely different methods have to be developed for general graphs, such as the three-bond star graph of Fig. 1a, which do not fulfill (3). There is, however, a way to reduce (1) to a form that allows one to bring the powerful theory of regular quantum graphs [7–9] to bear. In order to motivate and to illustrate this method, let us study the case

$\alpha_1 = 1$, $\alpha_2 = 7$, $\alpha_3 = 11$, $\beta_1 = 1/10$, $\beta_2 = 1/5$, $\beta_3 = 1/2$. In this case, $a_1^{(0)} = 3/4$, $a_2^{(0)} = 1/2$, $a_3^{(0)} = -1/4$, $S_0 = 19$, $S_1 = 17$, $S_2 = 5$, $S_3 = -3$, and the spectral equation is given by

$$g^{(0)}(k) = \cos(19k) - \frac{3}{4}\cos(17k) - \frac{1}{2}\cos(5k) + \frac{1}{4}\cos(3k). \tag{7}$$

Since $\left|a_1^{(0)}\right| + \left|a_2^{(0)}\right| + \left|a_3^{(0)}\right| = 3/2 > 1$, this quantum graph is certainly not regular. But let us look at the first derivative of (7). Dividing by S_0, we obtain

$$g^{(1)}(k) = \cos[S_0 k + \pi/2] - \sum_{j=1}^{3} a_j^{(1)} \cos[S_j k + \pi/2] \tag{8}$$
$$= -\sin(19k) + \frac{51}{76}\sin(17k) + \frac{5}{38}\sin(5k) - \frac{3}{76}\sin(3k).$$

This time we have $\sum_{j=1}^{3} \left|a_j^{(1)}\right| = 16/19 < 1$, and, therefore, since (8) is precisely of the form (1) and satisfies (3), it can be solved explicitly using the methods of [7–9]. In particular, it was shown in [7–9] that root number n of a spectral equation that satisfies (3), such as (8), is found in the root interval $[\hat{k}_{n-1}, \hat{k}_n]$, where $\hat{k}_n$ are the root separators [7–9]. It was also shown in [7–9] that the location of the root separators is entirely controlled by the local extrema of the trigonometric function with the largest action argument. Thus, in our case, the root separators of (8) are given by $\hat{k}_n = (2n + 1)\pi/38$. Since according to [7–9] root number n and only root number n is located in the interval $[\hat{k}_{n-1}, \hat{k}_n]$, we can now compute all roots of (8) explicitly and individually according to

$$k_n^{(1)} = \int_{\hat{k}_{n-1}}^{\hat{k}_n} k \left|\frac{dg^{(1)}(k)}{dk}\right| \delta(g^{(1)}(k)) dk. \tag{9}$$

In [20] we show that, because of the hermiticity of the spectral eigenvalue problem on quantum graphs, the locations of the local extrema of $g^{(0)}(k)$ are separators for the roots of $g^{(0)}(k)$. The location of the local extrema of $g^{(0)}(k)$, however, are given by the zeros of $g^{(1)}(k)$, which, up to constants, is the derivative of $g^{(0)}(k)$. Therefore, using the roots $k_n^{(1)}$, explicitly computed in (9), as the root separators of (7), we obtain, again explicitly and individually,

$$k_n^{(0)} = \int_{k_{n-1}^{(1)}}^{k_n^{(1)}} k \left|\frac{dg^{(0)}(k)}{dk}\right| \delta(g^{(0)}(k)) dk. \tag{10}$$

This solves the task of computing the spectrum of our example of the three-bond dressed star graph explicitly.

In general, given a spectral equation (1) that does not fulfill (3), we generate a chain of derivative spectral equations $g^{(m)}(k)$, where $g^{(m)}(k)$ is the mth derivative of (1) divided by S_0^m, explicitly given by

$$g^{(m)}(k) = \cos(S_0 k - \pi\gamma_0 + m\pi/2)$$
$$- \sum_{j=1}^{N} a_j^{(m)} \cos(S_j k - \pi\gamma_j + m\pi/2), \tag{11}$$

where $a_j^{(m)} = a_j^{(0)}(S_j/S_0)^m$. Since $S_0 < S_j$, there always exists an M such that the amplitudes $a_j^{(m)}$ satisfy the regularity condition (3), i.e., $\sum_{j=1}^{N}|a_j^{(M)}| < 1$. Therefore, according to [7–9], root separators $\hat{k}_n^{(M)}$ exist on the level M and the roots $k_n^{(M)}$ of $g^{(M)}(k) = 0$ are explicitly computable via

$$k_n^{(M)} = \int_{\hat{k}_{n-1}^{(M)}}^{\hat{k}_n^{(M)}} k \left| \frac{dg^{(M)}(k)}{dk} \right| \delta(g^{(M)}(k)) dk. \tag{12}$$

Since we now know the roots on the level M, we can go one step backwards to level $M-1$. According to a root-counting argument [20] based on the Weyl formula [18, 19], the root separators $\hat{k}_{n-1}^{(M)}$ on the level $M-1$ are the locations of the local extrema of $g^{(M-1)}(k)$, which are given explicitly by the roots $k_n^{(M)}$, which we know. Therefore, $\hat{k}_n^{(M-1)} = k_n^{(M)}$ and the roots of $g^{(M-1)}(k) = 0$ can now be computed explicitly, according to

$$k_n^{(M-1)} = \int_{k_{n-1}^{(M)}}^{k_n^{(M)}} k S_0 \left| g^{(M)}(k) \right| \delta(g^{(M-1)}(k)) dk. \tag{13}$$

Steps (12) and (13) define a recursive procedure,

$$k_n^{(m-1)} = \int_{k_{n-1}^{(m)}}^{k_n^{(m)}} k S_0 \left| g^{(m)}(k) \right| \delta(g^{(m-1)}(k)) dk,$$
$$m = M, M-1, \ldots, 2, \tag{14}$$

which can be followed until the level 0 is reached and the roots $k_n^{(0)}$, i.e., the spectrum of the quantum graph, is known explicitly.

It is important to notice that (12)–(14) are not just formal solutions. They yield $k_n^{(m)}$, $m = 0, \ldots, M$ explicitly, by quadratures. Thus, (12)–(14) constitute explicit solutions of the problem, very much in the spirit of the

definition of explicit solutions by quadratures in the theory of differential equations [21].

Several special cases require discussion. If the regularity condition (3) is fulfilled, a root k_n lies *strictly inside* of the interval $[\hat{k}_{n-1}, \hat{k}_n]$. However, if (3) is not fulfilled, it is possible that a root $\hat{k}_n^{(m)}$ coincides with one of its separators $\hat{k}_{n-1}^{(m)}$ or $\hat{k}_n^{(m)}$. This is, e.g., the case in our star-graph example above, where $k_{18}^{(0)} = \pi$ is a root and a root separator of (7). In the parameter space of α's and β's, cases like this are extremely rare (nongeneric). But even if such a case occurs, it does not present a problem for our theory. On the contrary, it saves one integration step, since it can always be checked before performing the integration in (14), whether one of the separators $k_{n-1}^{(m)}$ or $k_n^{(m)}$ is a root of $g^{(m-1)}(k)$. If so, the result $k_{n-1}^{(m-1)} = k_{n-1}^{(m)}$, or $k_{n-1}^{(m-1)} = k_n^{(m)}$, respectively, is known in advance, without actually performing the integration.

In other special cases, the roots of $g^{(m)}(k) = 0$ can be obtained in the form of explicit periodic orbit expansions [7, 8]. In order to illustrate this, let us return to our example of the three-bond star graph. We notice that the spectral equation $g^{(1)}(k) = 0$ of the three-bond star graph looks the same as the spectral equation [7]

$$g_{4V-\text{chain}}^{(0)}(k) = \sin(S_0 k)$$
$$+ r_2\sin(S_1 k) + r_2 r_3\sin(S_2 k) - r_3\sin(S_3 k) = 0 \tag{15}$$

of the dressed four-vertex chain graph shown in Fig. 1b, where $r_2 = (\beta_1 - \beta_2)/(\beta_1 + \beta_2)$, $r_3 = (\beta_2 - \beta_3)/(\beta_2 + \beta_3)$ are the reflection coefficients at the vertices number 2 and 3 of the chain graph, and the actions $S_0, \ldots, S_3$ are the same as in (4). If we arrange for the bond actions of the chain graph to equal the bond actions of the three-bond star graph, and furthermore arrange for $a_1^{(1)} = -r_2$, $a_2^{(1)} = -r_2 r_3$, $a_3^{(1)} = r_3$, which is possible if the scaling constants of the three-bond star graph fulfill $\beta_1^2 - \beta_2^2 + \beta_3^2 = 0$, then $g^{(1)}(k)$ of the three-bond star graph is the same as the spectral equation (15) of the associated four-vertex chain graph and the spectral points $k_n^{(1)}$ can be stated immediately and explicitly in the form of convergent, periodic orbit expansions [7, 8], bypassing any integrations that would have been necessary according to the scheme defined in (14).

Although they presented the first examples of explicitly solvable quantum graphs, a major shortcoming of [7] and [8] is the fact that the theory presented in [7] and [8] is only applicable to *regular* quantum graphs, i.e., to quantum graphs that fulfill regularity condition (3). In this paper we showed that the restriction to regular quantum graphs is not necessary: all

scaling quantum graphs can be solved explicitly. Nevertheless, the theory presented in [7–9] provides an indispensable foundation without which the present theory would not be possible.

A conceptual advance is the following. Frequently an operational definition of quantum chaos, or a quantum chaotic regime, is the "loss of quantum numbers." To illustrate, let us consider a Hamiltonian system with Hamiltonian $\hat{H} = \hat{H}_0 + \mu\hat{V}$, where $\hat{H}_0$ is an integrable Hamiltonian, μ is a real parameter, and $\hat{V}$, with respect to and in conjunction with $\hat{H}_0$, is a nonintegrable perturbation. Many quantum systems, for instance the hydrogen atom in a strong magnetic field [10], can be described in this way. For $\mu = 0$, the system is integrable and possesses a complete set of quantum numbers that can be obtained, at least approximately, using EBK quantization [18, 19]. As the parameter μ increases, EBK quantization breaks down and the system makes a transition to quantum chaos. This explains the frequently employed practice of characterizing the onset of quantum chaos by a loss of quantum numbers, since the breakdown of the EBK quantization scheme implies the loss of quantum numbers. The results obtained in this paper, however, show that this is not necessarily a good way to characterize quantum chaos. Although not strictly chaotic in the classical limit (due to ray-splitting [11, 12, 22, 23] the term *stochastic* may characterize the situation better), quantum graphs were shown by many authors [1–5] to be excellent models of quantum chaos. Yet, our results above show that a well-defined quantum number, the counting index n, still exists and produces explicit energy levels in exactly the same spirit as the EBK quantization scheme.

The iteration scheme (14) is perhaps the most interesting feature of our method of explicitly solving quantum graphs. We call the smallest M that "regularizes" a given quantum graph (i.e., the amplitudes of $g^{(M)}$ fulfill (3)) the *order* of the quantum graph. For any given quantum graph, its order is unique. Since the order M of a quantum graph determines the length of the bootstrapping iteration scheme (14), it is possible that the order of a quantum graph is also an indication of the complexity of its spectrum. Quantum iterations similar to (14) were studied before [24] and were found to lead to sensitivity and chaos on the quantum level. This may explain the reason why certain quantum graphs are such good models of quantum chaos [1–5] and the order M of the quantum graph may be an indication of how well a given quantum graph can be described in terms of the usual diagnostic tools of quantum chaos, such as, e.g., random matrix theory [18, 19, 25].

REFERENCES

1. T. Kottos and U. Smilansky, Phys. Rev. Lett. **79**, 4794 (1997); Ann. Phys. (New York) **274**, 76 (1999).
2. H. Schanz and U. Smilansky, Phys. Rev. Lett. **84**, 1427 (2000).
3. T. Kottos and H. Schanz, Physica E (Amsterdam) **9**, 523 (2001).
4. U. Smilansky, in *Mesoscopic Quantum Physics, Les Houches, Session LXI, 1994*, Ed. by E. Akkermans, G. Montambaux, J.-L. Pichard, and J. Zinn-Justin (Elsevier, Amsterdam, 1995), pp. 373–433.
5. P. Kuchment, Waves Random Media **12** (4), R1 (2002).
6. Y. Dabaghian, R. V. Jensen, and R. Blümel, Phys. Rev. E **63**, 066201 (2001).
7. Yu. Dabaghian, R. V. Jensen, and R. Blümel, Pis'ma Zh. Éksp. Teor. Fiz. **74**, 258 (2001) [JETP Lett. **74**, 235 (2001)]; Zh. Éksp. Teor. Fiz. **121**, 1399 (2002) [JETP **94**, 1201 (2002)].
8. R. Blümel, Yu. Dabaghian, and R. V. Jensen, Phys. Rev. Lett. **88**, 044101 (2002); Phys. Rev. E **65**, 046222 (2002).
9. R. Blümel, Yu. Dabaghian, and R. V. Jensen, *Mathematical Foundations of Regular Quantum Graphs* (2003) (in press).
10. H. Friedrich, *Theoretical Atomic Physics*, 2nd ed. (Springer, Berlin, 1998).
11. R. E. Prange, E. Ott, T. M. Antonsen, *et al.*, Phys. Rev. E **53**, 207 (1996).
12. L. Sirko, P. M. Koch, and R. Blümel, Phys. Rev. Lett. **78**, 2940 (1997).
13. M. Keeler and T. J. Morgan, Phys. Rev. Lett. **80**, 5726 (1998).
14. Sz. Bauch, A. Błędowski, L. Sirko, *et al.*, Phys. Rev. E **57**, 304 (1998).
15. R. Blümel, P. M. Koch, and L. Sirko, Found. Phys. **31**, 269 (2001).
16. Y. C. Lai, C. Grebogi, R. Blümel, and M. Ding, Phys. Rev. A **45**, 8284 (1992).
17. A. Kohler and R. Blümel, Phys. Lett. A **238**, 271 (1998).
18. M. C. Gutzwiller, *Chaos in Classical and Quantum Mechanics* (Springer, New York, 1990).
19. H.-J. Stöckmann, *Quantum Chaos* (Cambridge Univ. Press, Cambridge, 1999).
20. Yu. Dabaghian and R. Blümel (in preparation).
21. W. W. Stepanow, *Lehrbuch der Differentialgleichungen* (VEB, Berlin, 1976).
22. L. Couchman, E. Ott, and T. M. Antonsen, Jr., Phys. Rev. A **46**, 6193 (1992).
23. R. Blümel, T. M. Antonsen, Jr., B. Georgeot, *et al.*, Phys. Rev. Lett. **76**, 2476 (1996); Phys. Rev. E **53**, 3284 (1996).
24. R. Blümel, Phys. Rev. Lett. **73**, 428 (1994).
25. F. Haake, *Quantum Signatures of Chaos* (Springer, Berlin, 1991).

On the Geomagnetic Field Inversion Mechanism

S. L. Shalimov

Schmidt Joint Institute of Physics of the Earth, Russian Academy of Sciences,
ul. Bol'shaya Gruzinskaya 10, Moscow, 123995 Russia
e-mail: shalimov@uipe-ras.scgis.ru
Received March 11, 2003

PACS numbers: 91.25.Cw; 47.65.+a

It is well-known that the geomagnetic field is generated and sustained by the motions in the conducting liquid of the Earth's core that rotates together with the planet [1]. At the Earth's surface, which is separated from the liquid core by an extended mantle layer, the major evidence of these motions is given by large-scale magnetic-field variations. They are studied by paleomagnetic recording, i.e., by measuring the external magnetic field in a remanent magnetization of ferromagnetic minerals in the course of their crystallization. Paleomagnetic studies show that, throughout the past few millions of years, the geomagnetic field (to the first approximation a dipole field, because the dipole mode accounts for about 80% of the intensity in the normal state) changed (inverted) its polarity many times (on average, two or three times per 10^6 years) in an irregular way, and, even without inversion, the dipole magnitude fluctuates chaotically with a characteristic time of 10^3–10^4 years (excursions) [2, 3]. At present, the mechanism accounting for these phenomena is unknown.

The first three-dimensional numerical models of geomagnetic field evolution were recently implemented by supercomputer simulation in [4, 5]. The self-consistent set of Navier–Stokes, magnetic induction, and heat conductivity equations was solved in the Boussinesq approximation in a coordinate system rotating together with a conducting fluid. The first computation took 2000 h of CPU time on a CRAY-90 computed. Although the authors succeeded in reproducing some observed characteristics of the geomagnetic field (its morphology, magnitude, and even a few inversions), the duration of the simulated process was only on the order of 4×10^4 years, which is obviously insufficient for comparison with observations.

Furthermore, to provide the stability of numerical schemes, the transport coefficients were taken to be of the "hyperdiffusion" type (i.e., dependent on the wave-number). Such transport coefficients are at least an order of magnitude greater than even the turbulence factors and, hence, are in sharp contradiction with the presumed exceedingly small coefficients of viscosity in the liquid core. Moreover, the calculated magnetic-field structures have never been observed at the Earth's surface. In [5], an attempt was undertaken to depress the influence of the overestimated transport coefficients, primarily by choosing new boundary conditions: instead of a flipless fluid motion at the boundary between the core and mantle, motions with zero shear stresses were chosen. Nevertheless, the results obtained with this scheme were also similar to the results obtained in [4] (including inversion). This fact indicates, in particular, that the boundary conditions in the inversion problem can be chosen in an alternative way.

Although the analytic models might eliminate some of the disadvantages of the numerical approach, no such models have been developed so far for the evolution of geomagnetic field even with the turbulent (without introducing hyperdiffusion) transport coefficients (the electromechanical Rikitake model [6] is not considered here because it does not satisfy the experimental data [7]). Accordingly, the observed intensity variations of the geomagnetic field, both with and without dipole inversion, still remain to be understood. In this work, a simple nonlinear model of the possible inversion and excursion mechanisms is suggested for the Earth's magnetic field.

In the rotating coordinate system, the equations of mean-field magnetohydrodynamics (in the Boussinesq approximation) describing the evolution of geomagnetic field have the form [1, 8]

$$\frac{d\mathbf{V}}{dt} = -\frac{1}{\rho}\nabla p + 2(\mathbf{V} \times \mathbf{\Omega}) + \frac{1}{4\pi\rho}(\nabla \times \mathbf{B}) \times \mathbf{B} + \nu\Delta\mathbf{V} + \mathbf{f}, \tag{1}$$

$$\frac{d\mathbf{B}}{dt} = (\mathbf{B} \cdot \nabla)\mathbf{V} + \nabla \times (\alpha\mathbf{B} - \eta\nabla \times \mathbf{B}), \tag{2}$$

$$\nabla \cdot \mathbf{V} = 0, \quad \nabla \cdot \mathbf{B} = 0. \tag{3}$$

Here, $\mathbf{V}$ and $\mathbf{B}$ are the velocity and magnetic field, respectively; ρ, ν, and η are the mass density, viscosity, and magnetic diffusivity, respectively; $\mathbf{\Omega}$ is the rotation frequency; $\mathbf{f}$ is the sum of Archimedean and centrifugal

accelerations; the coefficient α accounts for the magnetic-field generation α effect; and $d/dt = \partial/\partial t + \mathbf{V} \cdot \nabla$. Although the Archimedean force and the α effect are ordinarily calculated by solving the nonaxisymmetric problem, we will choose them in a certain specified form.

Let us consider an infinite flat layer of a conducting fluid (liquid core) bounded by mutually parallel planes at $z = 0$ (mantle) and $z = h$ (mantle of the conjugate hemisphere) and uniformly rotating about the vertical axis z with angular velocity $\Omega = \text{const}$. Setting $V_z = 0$ and assuming that the stream structure along z is specified, we introduce the stream function $\psi(x, y, z, t)$ such that $\mathbf{V} = (\mathbf{e}_z \times \nabla\psi)$, where $\mathbf{e}_z$ is unit vector along the vertical. The magnitude of the geomagnetic field produced by the $\alpha\omega$-dynamo mechanism is estimated at $B_0 \sim (8\pi\rho\Omega\eta)^{1/2}$ [1]. Assume that the field has the slowly and rapidly varying components $B_{0z}(x, \epsilon t)$, $B_{0x}(z, \epsilon t)$ and $\delta\mathbf{B} = \delta B(x, y, t)\mathbf{e}_z$, respectively. Let us subject Eq. (2) to the curl operator and then project it onto the vertical axis. Ignoring the variations in the slow field component, one finally obtains

$$\frac{\partial\omega}{\partial t} = -\frac{\partial(\psi, \omega)}{\partial(x, y)} + \nu\Delta\omega + \frac{1}{4\pi\rho}\frac{\partial B_{0x}}{\partial z}\frac{\partial b}{\partial y}, \qquad (4)$$

$$\frac{\partial\delta B}{\partial t} = -\frac{\partial(\psi, \delta B)}{\partial(x, y)} + \eta\Delta\delta B + \frac{\partial B_{0z}}{\partial x}\frac{\partial\psi}{\partial x}, \qquad (5)$$

where $\Delta = \partial^2/\partial x^2 + \partial^2/\partial y^2 + \partial^2/\partial z^2$ and $\omega = -(\partial^2/\partial x^2 + \partial^2/\partial y^2)$ is the velocity field vorticity.

The set of magnetohydrodynamic Eqs. (4) and (5) has the form of a set of equations that arises in the problem of convective fluid motion in a Hele–Shaw cell (where one deals with temperature rather than with magnetic field) and refers to the sets of hydrodynamic type [9]. Applying the Galerkin method of finite-dimension approximation to the velocity field and temperature, one obtains, in particular, the convection regimes of the convective-loop and four-vortex types.

To simplify the problem, we assume that the flow along the z axis is uniform (the velocity does not change along this axis). Then the set of Eqs. (4) and (5) formally coincides with the set arising in the problem of heat convection in a flat layer of an ideal fluid heated at the bottom (see, e.g., [10]). We will use this analogy and restrict ourselves to the simplest (for analysis) case of free horizontal boundaries, i.e., assuming that $\psi = \delta B = 0$ and $\partial^2\psi/\partial x^2 = 0$ at $y = \pm d/2$, where d is the characteristic horizontal scale. The approximate solution to set (4), (5) is sought by the Galerkin method in the form

$$\psi = \frac{4\eta}{ab}\sqrt{2}X(\tau)\sin\frac{a\pi x}{d}\sin\frac{\pi y}{d}, \qquad (6)$$

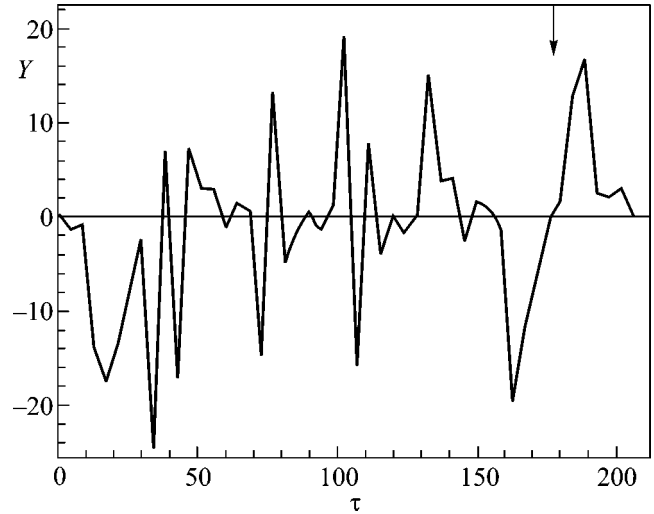**Figure.**

$$\delta B = \frac{\partial B_{0z}}{\partial x}\frac{d}{r\pi}$$

$$\times \left[\sqrt{2}Y(\tau)\cos\frac{a\pi x}{d}\sin\frac{\pi y}{d} - Z(\tau)\sin\frac{2\pi y}{d} \right], \qquad (7)$$

where $\tau = t(4\pi^2\eta/bd^2)$ is the dimensionless time and the constants are taken to be

$$b = \frac{4}{1 + a^2}, \quad r = \frac{Ra}{Ra_c},$$

$$Ra = \frac{1}{4\pi\rho}\frac{\partial B_{0x}}{\partial z}\frac{\partial B_{0z}}{\partial x}\frac{d^4}{\nu\eta}, \quad Ra_c = \frac{64\pi^4}{a^2 b^3}.$$

Substituting Eqs. (6) and (7) into Eqs. (4) and (5) and omitting all harmonics except for those included in Eqs. (6) and (7), one obtains the following set of equations:

$$dX/d\tau = (Y - X)\text{Pr},$$
$$dY/d\tau = rX - Y - XZ, \qquad (8)$$
$$dZ/d\tau = -bZ + XY,$$

where $\text{Pr} = \nu/\eta$ is the Prandtl magnetic number. The set of Eqs. (8) is the well-known Lorentz system [9, 11], which is invariant about the substitution $(X, Y, Z) \longrightarrow (-X, -Y, Z)$. This symmetry arises because of the presence of two unstable stationary flow points and corresponds to two senses of convective rotation (clockwise and counter-clockwise) in the states with opposite signs of the Y mode, which is proportional to the rapidly varying magnetic-field component.

The numerical solution to Eqs. (8) with parameters $Pr = 20$, $r = 28$, $b = 8/3$, and $a^2 = 1/2$ is shown for $Y(\tau)$ in the figure (the same holds for $X(\tau)$). The choice of parameters corresponds to the following estimates [12, 13]: $\eta = 1$ m^2/s, $\partial B_{0x}/\partial z \approx B_{0x}/r_c$, $B_{0x} \approx 0.001$ T, $B_{0z} = $

$B_{0x}/8$, $r_c \approx 3500$ km (core radius), $\rho \approx 10^4$ kg/m³ is the mass density, and $d = 1000$ km is the scale of field variations. The characteristic time is on the order of 2×10^3 years, so that the model duration τ is equal to 4×10^5 years in the dimensional units.

At $r = Ra/Ra_c = 28$, a strange attractor appears in the Lorentz system (see, e.g., [14]). In our case, the Rayleigh number Ra incorporates the product $|\partial B_{0x}/\partial z \, \partial B_{0z}/\partial x|$ of the gradients of slowly varying field components that determine the level above the instability threshold Ra_c. The instability is prevented due to the nonlinear energy transfer from the growing X, Y modes to the decaying Z mode.

The estimates of field-diffusion time in the core yield $r_c^2/\pi^2\eta \sim 4 \times 10^4$ years. Consequently, the polarity of the geomagnetic field is completely reversed (inverted) due to rather prolonged (no shorter than 20τ) oscillations of the fast component about the opposite unstable stationary point. This time suffices for the decay of slow component and the regeneration of an oppositely polarized field through the dynamo mechanism. The model function in the figure has a single inversion (shown by arrow) at the end of the computation, so that one can expect three to four inversions per 10^6 years.

In contrast to the inversions, the field excursions in this model are explained by a relatively short (with a lifetime shorter than 20τ) switching of the rapidly varying magnetic-field component. This is precisely the reason for the fluctuations of field intensity on a time scale of 10^4 years.

A preliminary comparison with the experiment shows that the vorticity in the Earth's liquid core is responsible for the so-called polar vortex, i.e., anticyclonic (for our epoch) displacement of the magnetic-field structures at the Earth's surface [15]. The regions of maximal magnetic-flux concentration, observed by satellites, are considered as regions (two in each hemisphere, separated by approximately 120° in latitude) where the slowly varying field component is distributed nonuniformly, thereby causing the flow instability [16].

Thus, the mechanism suggested in this work for geomagnetic-dipole inversions is based on the assumption that the product of nonuniformly distributed $\partial B_{0x}/\partial z$ and $\partial B_{0z}/\partial x$ components determines the level above the instability threshold for the fluid flow and the rapidly varying magnetic-field component in the core. Their nonlinear interaction brings about flow switching into the state with oppositely directed velocity and, hence, with a magnetic field of opposite polarity.

REFERENCES

1. S. I. Braginskiǐ, Zh. Éksp. Teor. Fiz. **47**, 1084 (1964) [Sov. Phys. JETP **20**, 726 (1964)].
2. J. P. Valet and L. Meynadier, Nature **366**, 234 (1993).
3. G. N. Petrova, T. B. Nechaeva, and G. A. Pospelova, *Typical Variations of the Geomagnetic Field in the Past* (Nauka, Moscow, 1992).
4. G. A. Glatzmaier and P. H. Roberts, Nature **377**, 203 (1995).
5. W. Kuang and J. Bloxham, Nature **389**, 371 (1997).
6. T. Rikitake, Proc. Cambridge Philos. Soc. **54**, 89 (1958).
7. W. Marzocchi, G. Gonzato, and F. Mulargia, Phys. Earth Planet. Inter. **88**, 88 (1995).
8. F. Krause and K.-H. Radler, *Mean-Field Magneto Hydrodynamics and Dynamo Theory* (Akademie, Berlin, 1980; Mir, Moscow, 1984).
9. E. B. Gledzer, F. V. Dolzhanskiǐ, and A. M. Obukhov, *Systems of Hydrodynamic Type* (Nauka, Moscow, 1981).
10. G. Z. Gershuni and E. M. Zhukhovitskiǐ, *Convective Stability of an Incompressible Liquid* (Nauka, Moscow, 1972).
11. E. N. Lorenz, J. Atmos. Sci. **20**, 130 (1963).
12. P. H. Roberts and G. A. Glatzmaier, Rev. Mod. Phys. **72**, 1081 (2000).
13. D. R. Fearn, Rep. Prog. Phys. **61**, 175 (1998).
14. M. I. Rabinovich, Usp. Fiz. Nauk **125**, 123 (1978) [Sov. Phys.–Usp. **21**, 443 (1978)].
15. P. Olson and J. Aurnou, Nature **402**, 170 (1999).
16. D. Gubbins and J. Bloxham, Nature **325**, 509 (1987).

Translated by V. Sakun